A search for pulsed high-energy non-thermal emission from the nova-like variable system AE Aquarii

Hendrik Jacobus van Heerden
M.Sc.

This thesis is submitted as required for the fulfilment
for the degree of

Philosophiae Doctor

in the
Faculty of Natural and Agricultural Sciences
Department of Physics
University of the Free State
South Africa

Promotor: **Prof. P.J. Meintjes**
Date of submission: May 22, 2015

Acknowledgements

The author would like to thank the following persons:

Danelle van Rooyen-van Heerden, his wife, for her love, support, understanding, motivation and patience during the good and the frustrating times of this project.

His promotor, Prof. P.J. Meintjes for his guidance, constructive criticism, ideas, chats and patience over the extent of this project.

Dr. B. van Soelen and Mr. D. Wium for observational data acquired at Boyden Observatory.

Mrs. A. Odendaal for observational data acquired at SAAO.

His father, family and friends for their support.

The UFS Department of Physics and the UFS High Performance Computing Team.

The author is also grateful to the NRF for financial assistance.

And finally to God, our Heavenly Father for the talent, strength and endurance to see this project through.

Abstract

AE Aquarii is an peculiar nova like variable system with emission observable in almost all wavelength regimes. The emission consists of both thermal and non-thermal components. The parameters and models for the non-thermal Synchrotron emission in the radio regime, as well as the optical and UV emission, have been extensively studied and presented since this enigmatic source was first studied in the 1930s. However, the emission processes and parameters towards the higher energies are still not clearly verified. The possibility of non-thermal pulsed emission in the VHE energies was mentioned in previous studies, as well as possible correlations between this pulsed emission and periods of enhanced optical activity.

We searched for non-thermal high energy emission from AE Aquarii using archival data from *Suzaku*, *Fermi* and *AGILE* along with contemporaneous optical photometric data from Boyden Observatory and SAAO. Analysis of the parameters of optical flares resulted in signatures that was used to identify possible correlating features in the *Fermi*-LAT data. In addition, we found that given the presence of a thermal component in conjunction with a power-law towards higher energies in the *Suzaku* X-ray data, as well as a possible low-level pulse signal in the *Fermi*-LAT data at the first harmonic of the white dwarf spin period, the possibility of non-thermal high energy emission from AE Aquarii cannot be excluded. The possible low-level signal in the *Fermi*-LAT data was as a result of a novel peak distribution analysis technique. Finally, an updated spectral energy distribution for AE Aquarii was completed to serve as a reference for future studies.

Key words: - VHE emission, Non-thermal emission, *Fermi* space telescope, *AGILE* space telescope, *Suzaku* space telescope, time series analysis, Multi-wavelength analysis, Photometry, X-ray spectral analysis, Cataclysmic variable star, star - AE Aquarii.

Opsomming

AE Aquarii is 'n eienaardige nova-agtige veranderlike stelsel met emissie wat in amper alle golflengtes waargeneem kan word. Hierdie emissie bestaan uit beide termiese en nie-termiese komponente. Uitgebreide studies rakende die parameters en modelle vir die nie-termiese Synchrotron emissie in die radio-gebied, sowel as die optiese en UV-emissie is al voorheen gebestudeer en aangebied sedert hierdie raaiselagtige stelsel die eerste keer bestudeer is in die 1930s. Die emisse-prosesse en -parameters by hoër energie is daarteenoor nog nie baie goed bevestig nie. Vorige studies het die moontlikheid van nie-termiese gepulseerde emissie in die baie hoë energie-gebied getoon, met moontlike korrelasies ten tye van verhoogde optiese aktiwiteit.

Ons het gebruik gemaak van argief-data verkry vanaf *Suzaku*, *Fermi* en *AGILE* tesame met gelyktydige optiese fotometriese data vanaf Boyden Sterrewag en SAAO om vir nie-termiese hoë-energie-emissie vanaf AE Aquarii te soek. Ontleding van die parameters van optiese uitbarstings het gelei tot aanduidings wat gebruik is om moontlike korrelasie kenmerke in die *Fermi*-LAT data te identifiseer. Bykomend het ons bevind dat 'n termiese komponent tesame met 'n magswet na hoër energieë in die X-straal-data, sowel as die moontlikheid van 'n lae-vlak periodiese sein in die *Fermi*-LAT data by die eerste harmoniek van die wit-dwerg spin-periode teenwoordig kan wees. Daarom kan die moontlikheid van nie-termiese hoë energie emissie vanaf AE Aquarii nie uitgeskakel word nie. Die moontlike lae-vlak sein in die *Fermi*-LAT data was as gevolg van 'n nuwe piek verspreiding analise tegniek. Ten slotte, is 'n opgedateerde spektrale energie verspreiding vir AE Aquarii voltooi, om te dien as 'n verwysing vir toekomstige studies.

Sleutel terme: - Baie hoë energie emissie, nie-termiese emissie, *Fermi* ruimteteleskoop, *AGILE* ruimteteleskoop, *Suzaku* ruimteteleskoop, Tydreeksanalise, Multi-golflengte-analise, Fotometrie, X-straal-spektrum-analise, Kataklismiese veranderlike ster, ster - AE Aquarii.

Contents

List of Figures

List of Tables

Nomenclature

AGILE GAS-map *AGILE* galactic diffuse background map

AGILE OB *AGILE* Observation Blocks

AGILE-GRID *AGILE* Gamma Ray Imaging Detector

Fermi-LAT *Fermi* Large Array Telescope

Swift XRT *Swift* X-ray telescope

AGU Active Galaxy Unknown

ASCA Advanced Satellite for Cosmology and Astrophysics

ASDC ANSI Science Data Center

BI back illuminated CCD

BL Lac BL Lacertae

CALDB calibration database

CCD charge coupled device

CFitsio C based Fits input-output libraries

CNO burning Carbon-Nitrogen-Oxygen burning

CTA Cherenkov Telescope Array

CV cataclysmic variable

Dec Declination

DFT discrete Fourier transform

EM CCD Electron Multiplying CCD

EM spectrum electromagnetic spectrum

ET Ephemeris Time

evclass *Fermi* event class

FFT fast Fourier transform

FI front illuminated CCD

FITS Flexible Image Transport System

FOV field of view

FS-Ratio flare-strength ratio

FSRQ Flat Spectrum Radio Quasar

fwhm full width at half maximum

GCVS General Catalogue of Variable Stars

GMST Greenwich Mean Sidereal Time

GMT Greenwich Mean Time

GPS Global Positioning System

Hα Hydrogen α

H.E.S.S. High Energy Stereoscopic System

HartRAO Hartebeesthoek Radio Astronomy Observatory

HEASARC High Energy Astrophysics Science Archive Research Center

HIPPARCOS High precision parallax collecting satellite

HPC-Cluster High Performance Computing Cluster

HST Hubble Space Telescope

HXD Hard X-ray Detector

IAC Telescope Imaging Atmospheric Cherenkov Telescope

IO commands Input-Output commands

IR infrared

IRAC Infrared Array Camera

IRAF Image Reduction and Analysis Facility

IRS Infrared Spectrograph

ISO Infrared Space Observatory

ISRO Base Indian Space Research Organisation Base

IUE International Ultraviolet Explorer

JD Julian Day

JKT Jacobus Kapteyn Telescope

L1 Lagrangian point 1

LEO Low Earth Orbit

MASS-DIMM multi aperture scintillation sensor - differential image motion monitor

MET Mission Elapsed Time

MHD magneto-hydrodynamic

MIPS Multiband Imaging Photometer for Spitzer

MJD modified Julian date

NASA National Aeronautics and Space Administration

O-C Curve observed-calculated curve

PyRAF Python interface for IRAF

QPO quasi-periodic oscillations

RA Right Ascension

ROI region of interest

S/N Signal versus Noise ratio

SAAO South African Astronomical Observatory

SAST South African Standard Time

SED spectral energy distribution

SHOC Sutherland High-speed Optical Cameras

SKA Square Kilometre Array

TAI International Atomic Time

TDB Barycentric Dynamical Time

TS map test statistic map

TT Terrestrial Time

UBVR ultra-violet, blue, visual and red

UBVRI ultra-violet, blue, visual, red and infrared

UCT University of Cape Town

UT Universal Time

UTC Coordinated Universal Time

UV ultra-violet

VDL van der Laan

VHE very high energy

VLA Very Large Array

WD white dwarf

WHT William Herschel Telescope

XIS X-ray Imaging Spectrometer

Chapter 1

Introduction

In the study of AE Aquarii, some background material must first be considered to give a clear picture in terms of where and how the current model for AE Aquarii applies to our knowledge of variable stars in general and cataclysmic variable stars (CV) in particular. The following concise discussions on variable stars and CV stars is, unless specifically indicated, referenced from the following sources and original references therein: Hellier (2001); Seeds (2001); Van Zyl (2002); Ridpath (1997).

The definition of a variable star is any star that varies in brightness, with two broad categories recognized, i.e., extrinsic variables, which vary for a mechanical reason (e.g. rotation) and intrinsic variables, which undergo a real change in luminosity of either an individual star or some element in a binary system. Certain stars may combine both forms of variation. The standard reference for the classification of types of variable stars and their nomenclature is the *General Catalogue of Variable Stars (GCVS).*

Originally a variable star was classified upon the shape of its light curve, its amplitude, and periodicity (or lack thereof), but today a wider range of reasons for variation is included in the classification. This led to the classification of variable stars into six major groups, each with its own subgroups:

1. Eruptive variables. (Flare stars, R CrB, T. Tau)
2. Pulsating variables. (Cepheid, Mira stars, ZZ Ceti)
3. Rotating variables.
4. Cataclysmic variables (CV). (Novae, dwarf novae, super novae)
5. Eclipsing variables. (Algol stars, Beta Lyrae stars, W Ursae Majoris stars)
6. Optically variable X-ray sources. (AM Hercules stars (polars), HZ Herculis (X-ray pulsars))

The Oxford dictionary of astronomy defines a CV as: "A variable star that exhibits sudden outbursts generally arising from the release of gravitational energy through accretion or from thermonuclear processes". (Ridpath (1997)). For nova being stars or systems that exhibit outburst of energy, sometimes with cataclysmic results, it can be said that basically all nova are one or other type of CV, or vice versa. Thus all supernovae type systems, even if only one star is involved, dwarf-novae, and all close binaries undergoing mass transfer are classified as CV stars. Thus the full list of CV stars include, classical novae, dwarf novae, recurrent novae, nova-like variables, magnetic cataclysmic variables (MCV) and supernovae. AE Aquarii is currently classified as a DQ Hercules type star, and therefore falls under the subgroup of MCV stars.

Binaries are systems consisting of two components, which are gravitationally bound and rotates about a common centre-of-mass (COM). In close binaries the separation distance is comparable to the diameter of the stars. The two components of the system are surrounded by an equipotential surface, with the inner critical surface in the form of a figure of eight, with the two halves called the Roche Lobes. The point at which the Roche Lobes touch is the inner Lagrange point L1, where the effective gravity is zero, with the material to the left belonging to the star on the left and the material to the right belonging to the star on the right, as illustrated in Figure 1.1.

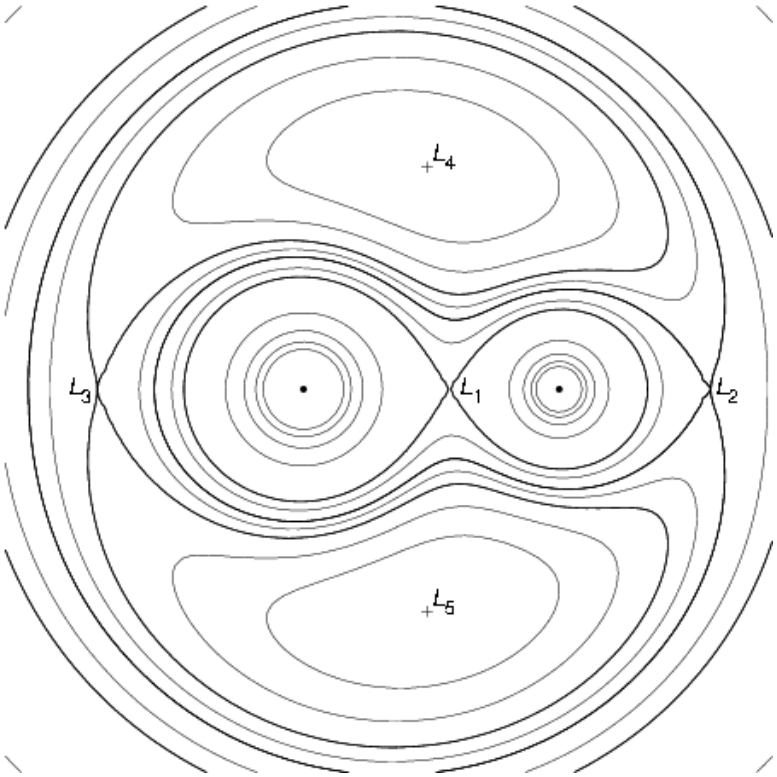

Figure 1.1: Equipotential surfaces about two stars (Adopted from http://inspire hep.net/record/846517/plots).

Cataclysmic binaries are systems that consist of a primary and a secondary star, where there is a mass transfer from the secondary to the primary. The primary is usually a compact object like a white dwarf (WD) or a neutron star. Dwarf-novae are thus systems that consist of a WD as a primary, wherein the transferred mass falls onto the WD via an accretion mechanism, as illustrated for example in Figure 1.2. The flares or outbursts from these CV stars are observed as a sudden brightening or increase in magnitude of the star during observation, and can be the result of a number of different mechanisms.

One of the mechanisms is due to a sudden release of energy at the so called hot spot of the accretion disk of the primary, i.e. where the in-falling gas or matter stream from the secondary interacts with the accretion disk. The variability occurs when there are fluctuations in the rate of mass transfer. The mechanism in dwarf

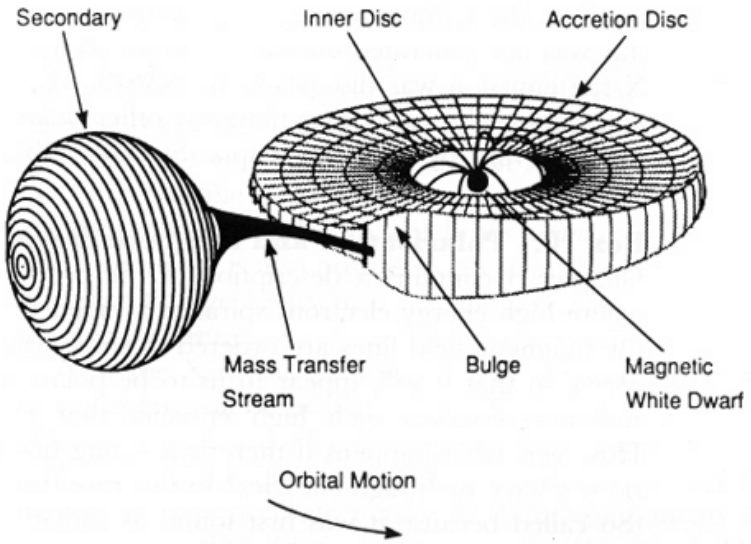

Figure 1.2: Model of a dwarf nova system (Adopted from http://heasarc.gsfc.nasa.gov).

novae, however, differ from that of classical novae in that the eruptions are mainly because of instabilities in the accretion disc, due to variation in the mass transfer, or rate of accretion. These instabilities can thus cause a sudden brightening of the whole disc.

Classical novae explosions are due to thermonuclear runaway. That is, the matter that accreted from the secondary to the primary is, because it comes from a main sequence star, rich in unused fuel in the form of hydrogen. As this fuel accumulates on the surface of the WD through accretion processes, it forms a layer of unprocessed fuel, which as it grows deeper increases in density and temperature until it eventually becomes degenerate. At this stage the pressure-temperature thermostat fails, at which time about 100 earth masses of fuel have accumulated and the temperature at the base of the hydrogen layer has reached sufficient temperatures for proton-proton fusion to begin. The released energy then causes the ignition of the CNO (Carbon-Nitrogen-Oxygen) cycle. The combined energies cause thermonuclear runaway, which results in the gas-degeneracy to be lifted and the gas to expand and the surface layers of the WD to be blown away, resulting in the nova. Fortunately this explosion hardly disturbs the CV system, and mass transfer can

resume as normal, causing again a build-up of a fuel layer, until the next nova.

Another type of mechanism is when the compact object not only has a strong magnetic field, but spins so fast that instead of the in-falling matter being able to form an accretion disc to get rid of the angular momentum, the in-falling matter gets caught in the magnetic field lines, which then drives the in-falling matter out of the system, analogous to a propeller. Because of the mechanisms involved the matter forms "blobs", which are accelerated out of the system by the compact object, with the larger blobs having a smaller velocity because of Newtons second law. Thus when the smaller blobs because of their greater speed crashes into the larger blobs the resulting interaction can thus be observed as a flare. AE Aquarii is one of these systems.

Two important things happen in the accretion disc of the more classical dwarf nova CV. First, the gas in the disc grows very hot, due to friction and tidal forces, secondly, the disc also acts as a brake, ridding the in-falling gas of its angular momentum and allowing it to fall onto the WD. The temperatures of the gas in the inner parts of the accretion disc can exceed one million Kelvin and the gas can emit intense X-rays. These discs consist of a number of important components, the so called "Hot Spot", where the in-falling matter stream hits the accretion disc which results in heating and turbulence and therefore a brightening of the disc at this specific region. The other important component is called the "Inner boundary layer". This is where the accreted matter is fed from the inner edge of the disc through this boundary layer onto the WD. This boundary layer may radiate as much energy as the disc itself.

One of the important consequences of the way in which the gas rotates inside the accretion disc is internal or viscous torque. That is as the gas spirals inward, it loses angular momentum, thus velocity or energy. The internal torque then transfers this energy outward. This mechanism is responsible for the initial ring of accreted matter to be spread out into a disc. Another torque that may influence the system is the so-called spin-up or spin-down torque. This torque is when, because of interactions between the WD and the accretion disc, the WD

receive or loose angular momentum, resulting in a spin-up or spin-down of the WD.

A important component that can influence the accretion process is when the WD has a strong magnetic field. This can lead to even more exotic processes to occur, with these magnetized systems then called magnetic cataclysmic variable (MCV) stars. These magnetic fields can be as strong as 1×10^6 G (100 tesla). These magnetic fields can interact with the mass flow from the secondary onto the WD. Interactions include the interception of the mass flow from the secondary by the magnetic fields, preventing the formation of an accretion disc, or the magnetic fields can also disrupt the accretion disc, preventing it from reaching down to the WD. Another process that may occur is magnetic accretion, wherein the in-falling matter travels along the field line onto the magnetic poles of the WD star.

One of the more important field-fluid interactions is when the magnetic fields causes a drag, i.e. the magnetic fields are frozen not just in the WD, but also in the accretion disc plasma. This drag or torque causes the spin-up or spin-down mentioned previously. That is, there is a critical radius where the WD and the accreting plasma rotate at the same speed, the so-called co-rotational radius. Through Keplerian motion in the accretion disc it is known that the inner matter rotates faster than the outer. Then if the magnetic fields are frozen in the WD as well as the accretion disc, and if the inner edge of the accreting plasma is inside the co-rotational radius, it will rotate faster than the WD and thus through the magnetic field interactions will cause spin-up torque, thus accelerating the WD. The opposite is then also true, if the inner edge of the accreting plasma is outside the co-rotational radius, then the result will be spin-down torque, and the WD will slow down.

MCV stars are subdivided into three categories nl. Polars, Intermediate Polars and DQ Her type stars. The classification is done according to the magnetic field strength of the WD, the degree of synchronism between the WD and companion, the rotation period of the WD and the energy spectrum of the emission (Meintjes (1990)). Only DQ Her type stars will be explored because AE Aquarii can be classified as such a type and is the object of this study.

DQ Her stars are asynchronous systems with spin periods <100 seconds. The orbital periods of between 4.65 and 9.88 hours imply a wide binary separation. This improves the chances of formation of an accretion disc. With the limits of whether a disc will form being $\geq$5 hours and no disc formation being $\leq$5 hours (Meintjes (1990)). If there is a large initial transfer rate then spin-up can occur, following a specific amount of time if there is a significant enough drop in the transfer rate from the secondary, after the WD has been spun-up, the WD will enter a spin-down period. During this time the WD may enter a propeller phase, during which time the magnetic fields act like the blades of a propeller, and push the in-falling gas stream into a ring around the WD, or even out of the system completely. More specifically the fast rotating magnetosphere interacts with the matter flow.

Now through the understanding of the definitions and description of all the different theories involved in Binaries, CV, MCV and DQ Her type stars the current model of AE Aquarii can be described. The most recent model for AE Aquarii is that of a peculiar nova-like variable star, consisting of a highly magnetized fast rotating white dwarf (WD) primary star that is in an ejector state with a propeller mechanism driving the in-falling matter from the secondary star away in the form of interacting blobs (Wynn et al. (1997)). The WD, with a rotation period of $P_{spin} \approx 33$ s, is spinning down at a rate of $\dot{P}_{spin} = 5.64 \times 10^{-14}$ s s^{-1} with a spin down luminosity of $-I\dot{\Omega}\Omega = 6 \times 10^{33} I_{50}$ erg s^{-1}, where $I_{50} = \frac{I}{10^{50} \text{g cm}^{-2}}$. This is a factor of $\sim$ 120 greater than the accretion luminosity, with a considerable fraction of this spin down power available for particle acceleration and non-thermal emission in a wide frequency range (De Jager et al. (1994)). The WD is orbiting a K2-K5 type secondary star about the common centre of mass with an orbital period of $P_{orb} = 9.88$ h. It is a non-eclipsing binary system at an inferred distance of about 100 ± 30 pc, at an orbital inclination of $58^\circ \pm 3^\circ$ and almost no eccentricity (Echevarria et al. (2006)). Lately the proposal has been made by Ikhsanov et al. (2004) and Beskrovnaya and Ikhsanov (2014) that AE Aquarii should be reclassified as its own subclass of cataclysmic variable (CV), that it might be the missing link in the evolution of Polars, and that the WD resembles a recycled pulsar.

The search for non-thermal emission from AE Aquarii in the very high energy (VHE) part of the electromagnetic (EM) spectrum resulted from a suggestion made in a study by Bastian et al. (1988). The study found a case for non-thermal synchrotron emission from interacting spherical clouds containing relativistic MeV electrons. A time averaged power law emission fit, where $S_\nu \propto \nu^{0.35}$, was found to be a result of a superposition of synchrotron emitting flares that occur more or less continuously. The study also compared AE Aquarii to other close X-ray binary sources that exhibit flaring activity, and suggested that AE Aquarii might be a low-power analogue to Cygnus X-3. With high energy γ-rays detected from Cygnus X-3 (as well as Her X-1, for example), it has been suggested that AE Aquarii might be a possible VHE (historically defined as $E \sim 10^{12}$eV, but for this study defined as MeV to GeV) source.

A study by Meintjes et al. (1992) utilizing the Nooitgedacht Mk I Cherenkov telescope, together with coincidental and non-coincidental optical observations of AE Aquarii, found evidence of strong coherent pulsed emission during optical flares at frequencies close to the spin frequency, i.e. $\sim 29.9 - 30$ mHz and a fundamental frequency $F_0 = 30.23$ mHz at the 4σ significance level. The total time-averaged luminosity at a threshold energy of ~ 2.4 TeV was $L_\gamma \sim (1.5 \pm 0.3) \times 10^{32}$ erg s^{-1}, corresponding to a conversion efficiency of 15% of the spin-down power. A noteworthy result was the detection of a pulsed emission during an optical flare at the same 30 mHz frequency. This observation also strengthened a hypothesis that there could exist a correlation between the pulsed optical and VHE γ-ray emission during optical flares as illustrated in Figure 1.3.

A study by Chadwick et al. (1995) using the VHE $\gamma -$ ray telescopes at Narrabi, New South Wales in Australia, found an excess of pulsed VHE γ-rays during an observation on 11 October 1993, lasting ~ 4200 s with a count rate in excess of 4σ. The burst occurred at phase 0.62-0.74 of the 9.88 h orbital period, with a pulse periodicity at 16.5 s (first harmonic of the 33 s spin period). Some evidence was presented of a hardening of the brightness spectrum of Cherenkov events during the burst compared to the background events.

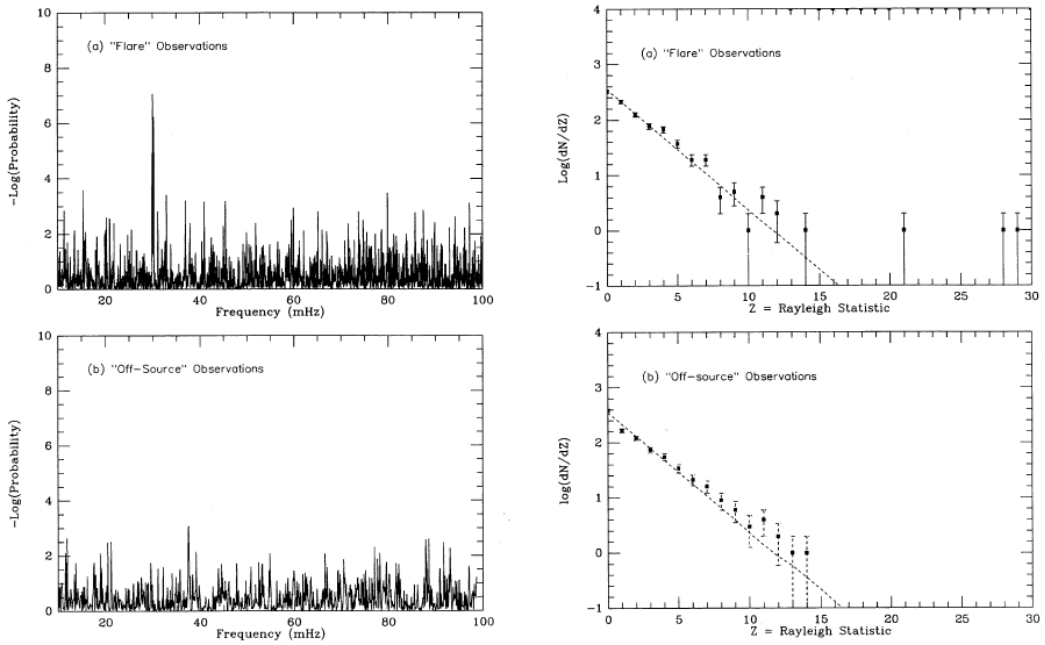

Figure 1.3: Comparison between Rayleigh power spectra from optical data (left) and noise statistics from VHE observations (right) for VHE Flare state and Off state of AE Aquarii (Meintjes et al. (1992)).

Follow-up work by Meintjes et al. (1994) independently confirmed previously identified optical and TeV γ-ray periodicities at a $-\log(\text{probability}) = 3$ level, with the most significant TeV detections confined to the time just before the onset of optical flares. A significant detection of two rapid bursts ($\sim$ 1-3 min) by three independent telescopes, following an optical flare was made, with the strongest flare at a significance of 4.6σ per min. It was suggested that the observed spin-down power ($-\mathrm{I}\dot{\Omega}\Omega \sim 6 \times 10^{33}$ erg s^{-1}) might account for the energy released by a TeV accelerator. A subsequent search for TeV emission using the *Whipple* 10 m telescope was done by Lang et al. (1998), but no evidence was found for any steady, pulsed or episodic emission.

More recent studies by Terada et al. (2007, 2008) using *Suzaku* data found a significant excess above the extrapolated model for the hard X-ray (HXD, $12 - 25$ keV) data. The proposed models for the excess were either a third thermal component

(in concurrence with a two thermal component fit in the soft X-ray spectrum) or a power law with a photon index of $1.12^{+0.63}_{-0.62}$. The non-thermal pulsed hard X-ray radiation was explained by relativistic electrons from an acceleration mechanism in the strong magnetic fields of the fast rotating WD, i.e., synchrotron radiation. These studies sparked renewed interest in AE Aquarii as a potential high-energy source. Oruru and Meintjes (2012) showed that electrons can be accelerated to VHE energies (lorentz factor of $\gamma \sim 10^7$) outside the light cylinder radius of the WD. Here the light cylinder radius of the WD is defined as the radial distance at which the rotational velocity of co-rotating particles equals the speed of light. The resultant proposed $\gamma-$ray emission might then be from up-scattering of soft photons from the K-type secondary star or propeller ejected outflow via inverse Compton processes.

However, studies by Sidro et al. (2008) using the *MAGIC* telescope found no evidence of any steady or pulsed $\gamma-$ray emission, but derived upper limits for steady emission above 350 GeV of $\sim 8.0 \times 10^{-12}$ cm^{-2} s^{-1} and for coherent pulsed (at the first harmonic of WD spin) emission above 4.0×10^{-12} cm^{-2} s^{-1}. Additionally a multi-wavelength campaign was conducted by Lopez-Coto et al. (2013); Aleksić et al. (2014) in 2012. A search in the *MAGIC* data for steady TeV, as well as variable TeV emission during high states and specifically pulsed emission at 33.08 and 16.54 s, did not result in any significant detections. The campaign did however result in improved integral upper limit values at the 95% confidence level for AE Aqr for steady emission of 6.4×10^{-12} cm^{-2} s^{-1} above 200 GeV and 7.4×10^{-13} cm^{-2} s^{-1} above 1 TeV for a Crab-like power-law photon spectral index of Γ=2.6 as well as an upper limit for pulsed emission of 2.6×10^{-12} cm^{-2} s^{-1} for energies above 200 GeV. Aleksić et al. (2014) therefore concluded that AE Aquarii was not an emitter of VHE $\gamma-$rays at levels previously claimed, e.g. $F_\gamma = (2.3 \pm 0.6)7.4 \times 10^{-11}$ cm^{-2} s^{-1} at a threshold energy of 2.4 TeV (Meintjes et al. (1992)).

All of the above-mentioned $\gamma-$ray work was done using Cherenkov radiation detection systems. With the availability of relatively young space-based $\gamma-$ray telescopes (*Fermi* and *AGILE*), the amount of data to analyse for possible detection

of steady, pulsed or episodic non-thermal VHE emission increased. Based on the gap in the spectral energy distribution (SED) of AE Aquarii between hard X-rays and VHE (above 200 GeV) γ-rays, a part of the picture was missing in terms of the non-thermal VHE emission from AE Aquarii, which makes it difficult to define a clear model for the origin of possible VHE non-thermal emission from the system.

The aim of this study will therefore be to search for non-thermal high-energy emission from AE Aquarii using data from the *Suzaku*, *Fermi* and *AGILE* space telescope systems. Data from the *Fermi*-LAT (20 MeV $-$ 300 GeV) and *AGILE*-GRID (30 MeV $-$ 50 GeV) instruments will be analysed for steady, pulsed and/or episodic emission. The primary study of *Fermi*-LAT data will include recommended methods such as binned and unbinned likelihood analyses. Additionally, a search for periodic emission will be conducted using the tools available from the *Fermi* science software center. The validity of the analysis method used in the periodic search will also be tested. Likelihood analysis will also be used in the search for non-thermal VHE emission in *AGILE*-GRID data. *Fermi*-LAT upper limits will be calculated for different energies, and an updated SED for AE Aquarii presented. To help facilitate the search for VHE non-thermal emission around flare events, optical studies will be conducted, as well as analysis of archival X-ray data from the *Suzaku* satellite. This is because of previous studies that have shown correlations between optical flare events and burst-like VHE emission, as well as correlations between the pulsed emission in the different wavelength regimes. A multi-wavelength analysis using aperture photometry of *Fermi*-LAT data in a search for correlations around optical and X-ray flare events will also be performed.

The layout of the thesis will thus be as follows: Chapter 2 will contain a historical overview of AE Aquarii, focusing on the identification of possible signatures allowing a search for VHE non-thermal emission. Chapter 3 will consist of a detailed discussion of the optical photometric observations, analysis and results. This will facilitate the search for possible signatures of VHE non-thermal emission from AE Aquarii, especially around optical flares. Chapter 4 will consist of a detailed discussion of the methodology used, and analyses and results obtained in the characterisation of X-ray emission from AE Aquarii using *Suzaku* archive

data. Chapter 5 will consist of a detailed discussion of the methodology used, the analyses and results obtained in the search through *Fermi*-LAT and *AGILE*-GRID data for VHE non-thermal emission. Chapter 6 will then contain a final discussion and conclusion of the study conducted.

Additionally included are three appendices: Appendix A contains expanded discussions of different time series techniques considered and used during this study, Appendix B contains a concise discussion of different γ-ray production mechanisms and finally Appendix C contains a concise overview of the data acquisition system Spica developed and used during the optical studies conducted at Boyden.

Chapter 2

AE Aquarii - A historical overview

2.1 Introduction

AE Aquarii (General Catalogue of Variable Stars designation) has been studied since the 1930s, with the first observational reports from Wachmann (1931) who classified AE Aquarii as an o Ceti star. It was later reclassified by Zinner (1938) as a T Tauri star (although some of the variations were noted as U Geminorum like), and then by Joy (1954) in his 1943 paper as an SS Cygni star. The flaring was noted by Henize (1949), with the discovery of the binary components of a red dwarf and a hot companion made by Joy (1954). With the identification of the fast rotating highly magnetized white dwarf (WD) in both optical (Patterson (1979)) and X-ray (Patterson et al. (1980)) the system was again reclassified, but this time as an Intermediate Polar (IP) of the DQ Her type. It was also considered as a system with a non-stationary accretion disk until 1984, when a whole series of different studies over the next decade changed the system model to that known today as a peculiar nova-like variable star, that consists of a highly magnetized fast rotating WD primary star in an ejector state with a propeller mechanism driving the in-falling matter from the secondary star away in the form of interacting blobs (Figure 2.1) as modelled by Wynn et al. (1997).

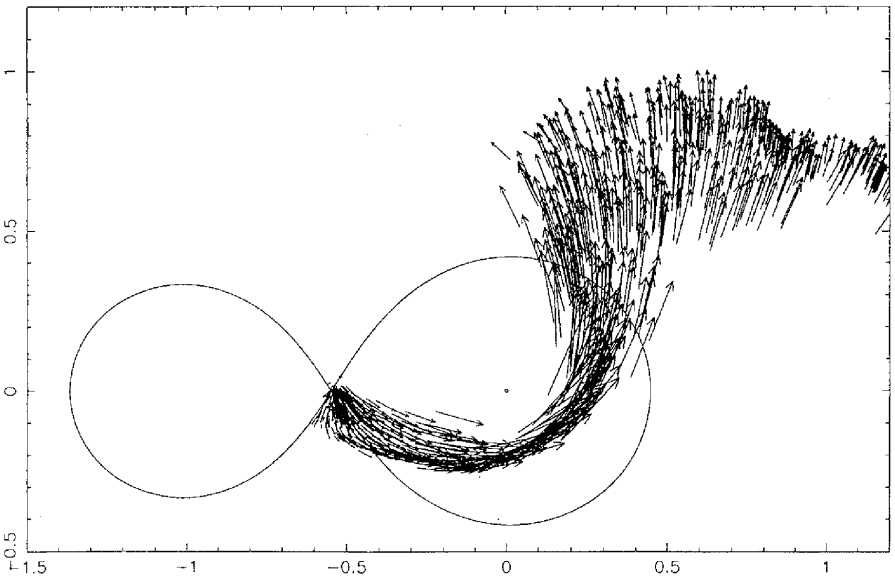

Figure 2.1: Model of the "propeller" state in which the rapidly spinning magnetic field expels the accretion stream from the system (Adopted from Wynn et al. (1997)).

The magnetospheric propeller and accompanying spin down luminosity of the WD of
$L_{sd} \sim 10^{34}$erg s^{-1} provide a huge energy reservoir to drive the multi-wavelength emission from the system over the entire frequency band, from radio to possible VHE $\gamma-$rays. The main properties of AE Aquarii will now be presented.

2.2 Multi-wavelength characteristics

2.2.1 Radio- and IR-studies

The first discovery of radio emission from AE Aquarii was made by Bookbinder and Lamb (1987) using Very Large Array (VLA) observations. Variable multi-frequency emission was detected at 4.9 GHz, with flux densities ranging between 8-16 mJy, and at 1.4 GHz, with flux densities ranging between 3-5 mJy. The short time-scale ($\lesssim$ 5 min) variability as well as effective temperature $T_{eff} > 10^{10}$ K of

the emission detected was best explained through non-thermal synchrotron emission from mildly relativistic electrons.

The case for synchrotron emission from relativistic MeV electrons was strengthened by Bastian et al. (1988) using VLA observations. Observations were performed at frequencies 1.5, 4.9, 15.0 and 22.5 GHz. (See Figure 2.2 for an example of radio variability in AE Aquarii.) As with the previous study performed by Bookbinder and Lamb (1987), the effective temperature in excess of 10^{10} K suggested a non-thermal origin for the emission. The location for the variability was proposed as flare-like events due to accelerated particles that cause disruptions in the accretion disk near the WD, with the flare events idealized as spherical clouds of relativistic electrons that expand adiabatically.

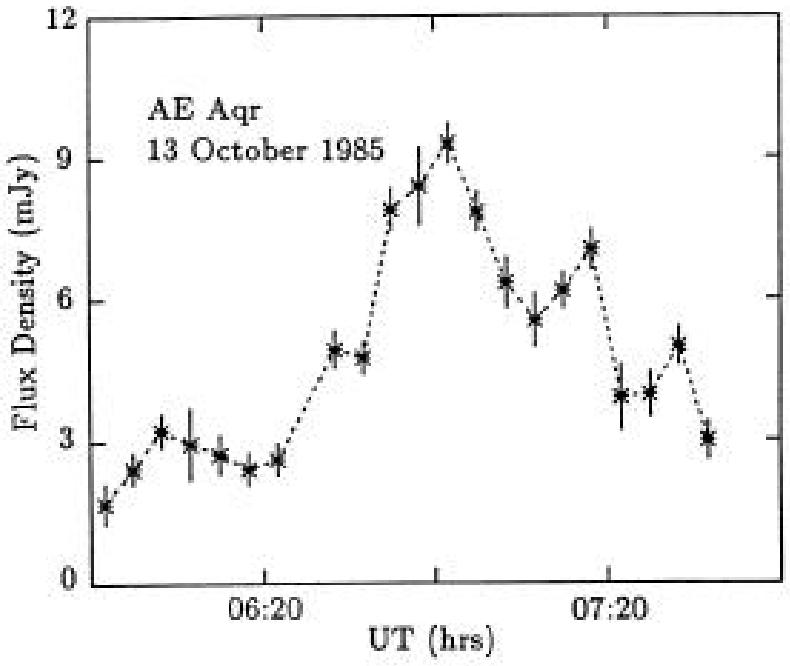

Figure 2.2: Example of radio flares in AE Aquarii at 15 GHz (Adopted from Bastian et al. (1988)).

The average radio spectrum between 1.5 and 22.5 GHz was also shown to increase with frequency as a non-thermal power law where $S_\nu \propto \nu^\alpha$ with a spectral index of

$\alpha \approx 0.35$. A van der Laan (VDL) model was used to determine and characterise the parameters for the flares, with the time-averaged power law emission from the system the result of a superposition of synchrotron emitting flares, in different phases of their evolution, that occur more or less continuously. The suggestion was made that the flux density would increase to millimetre and sub-millimetre wavelengths based on maximum allowable model parameters fitted for an expanding plasmoid cloud with initial values for its magnetic field of $B_0 \sim 25 - 3000$ G and radius of $r_0 \sim 10^9 - 3 \times 10^{10}$cm. A comparison was also made between AE Aquarii and other close X-ray binary sources that also exhibit transient radio emission. These sources have also been modelled in terms of the VDL model. Based on these parameters it was suggested that AE Aquarii might be a low-power version of Cygnus X-3. Additionally, with high-energy $\gamma -$ rays detected from Cygnus X-3 (as well as Her X-1), the suggestion was made that detection of $\gamma -$ rays (specifically TeV) from AE Aquarii might be a possibility (Bastian et al. (1988)).

Studies of AE Aquarii at millimetre wavelengths were performed by Abada-Simon et al. (1993). Radio emission from AE Aquarii was detected at $\lambda = 3.4$ mm on five independent observation runs. Additional detections were also made at $\lambda = 1.25$ mm using the Caltech Sub-millimetre Observatory on Mauna Kea. Observations using the VLA accompanied the previously mentioned observations concurrently. The time averaged spectral data was fitted well by a power law $S_\nu \propto \nu^{0.35-0.60}$ with a spectral turnover above 240.0 GHz. The flux density at millimetre wavelengths also varied on time-scales ≤ 1 h. It has been proposed that the radio emission was the result of dynamic interactions between the in-falling material from the secondary star and the strong ($\gtrsim 100$ G) magnetic field of the WD primary star. This model explained the flares as expanding synchrotron emitting clouds ejected by the fast rotating magneto-hydrodynamic (MHD) propeller. The power-law was explained as the expected spectrum from the superposition of flare-like events, with the frequency distribution of flare intensities or flux densities described by a power law of $f(S_0) \propto S_0^{-\epsilon}$ with a flare frequency index $\epsilon \approx 1.8$, indicating that large flares were less frequent than smaller flares. A magnetic field strength in excess of 250 G was implied for the fitted model parameters.

Further detections from 4.8 to 170 μm in infrared (IR) were reported by Abada-Simon et al. (2002) and Abada-Simon et al. (2005) during a multi-wavelength campaign from radio to visible wavelengths. ISO observations resulted in detections at 7.3, 60 and 90 μm and upper limits at 4.8, 12, 25, 100 and 170 μm were reported. The constraints of the synchrotron radio on far-IR emitting plasmoids were strengthened, as well as the indication of a turning point in the spectrum between 170 and 90 μm. Extended measurements from Near- to Mid-IR were performed by Dubus et al. (2004) using the Keck I telescope. AE Aquarii also showed variability at these wavelengths. Based on a fit to the SED, a "superposition of emitting synchrotron clouds" emission model with an index of 0.5 at the low frequency parts and a characteristic synchrotron cooling with a fitted index of -5/3 that dominates the frequencies between the turning point and Near-IR could be used to explain the spectrum. The results from Dubus et al. (2004) then also strengthened the case for expanding clouds of relativistic electrons thrown from the system by the WD.

To improve the accuracy in the SED of AE Aquarii between 5 and 70 μm, observations were made by Dubus et al. (2007) using the *Spitzer* space telescope. Observations were performed using the IRACs , MIPS and IRS instruments. From these results the inverted radio spectrum can be interpreted as typical of superimposed emission from multiple synchrotron self-absorbed components, i.e. expanding clouds containing accelerated particles. A canonical $E^{-2.4}$ power-law electron spectrum also explained the SED from radio to mid-IR frequencies (Dubus et al. (2007)). See Figure 2.3 for a SED of AE Aquarii between radio and optical, including fitted models explaining the different components.

Based on a blob-like propeller-driven outflow from the system, Meintjes and Venter (2005); Venter and Meintjes (2006) refined the constraints on the parameters surrounding the non-thermal radio to mid-IR emission mechanism. Through a series of calculations based on MHD theory, it was shown that magnetized plasma clouds/blobs with field strengths of $B \sim 300 - 1000$ G could emit synchrotron radiation from electrons accelerated to $\epsilon_e \sim 150 - 10$ MeV. These magnetized clouds/blobs then also confined the population of relativistic electrons. The MHD

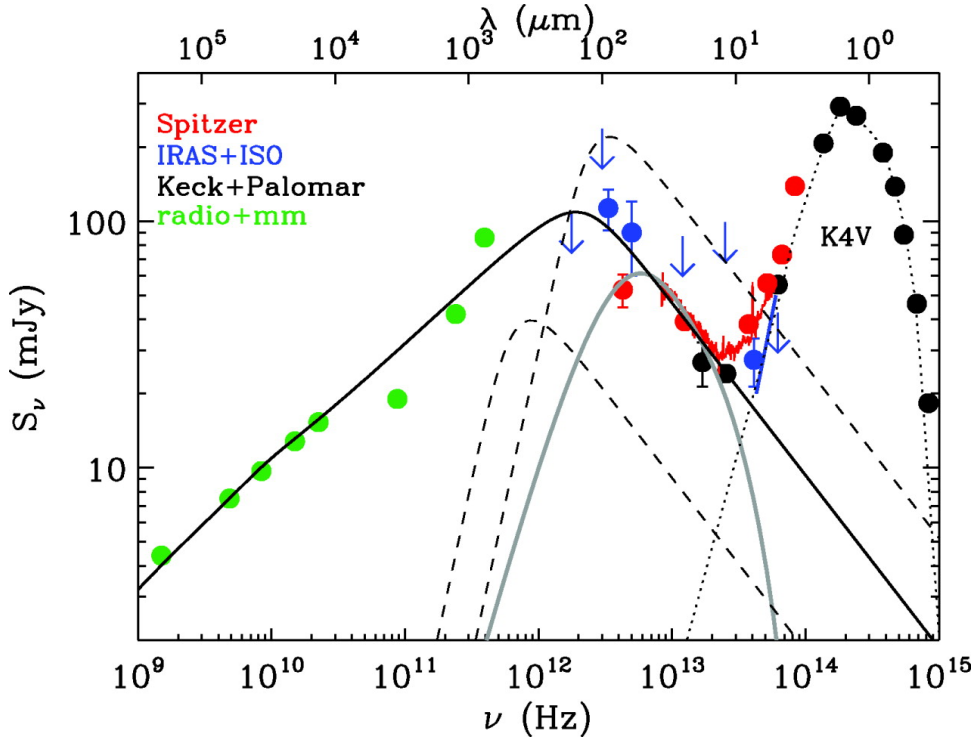

Figure 2.3: SED for AE Aquarii between radio and optical including proposed fitted models as explained and proposed in Dubus et al. (2007) (Adopted from Dubus et al. (2007)).

driven propeller mechanism combined with magnetic reconnection and magnetic pumping (betatron acceleration) were thus responsible for the conversion of the thermal electron population to relativistic electrons with an efficiency of ~ 0.1, required to explain the SED and observational data. This was consistent with the ratio $\beta \sim 0.1$ between the total observed radio to mid-IR synchrotron emission and the total spin-down power of the WD. This mechanism then drove the total observed radio to mid-IR emission, with luminosity $L_{R-IR} \sim 10^{31}$ erg s^{-1}.

Finally it has also been suggested by Venter and Meintjes (2006) that the confluence of the ejected magnetized clouds could result in a radio remnant surrounding AE Aquarii. This cloud would then also be optically thin between frequencies $\nu \gtrsim 100$ MHz $-$ 1 GHz. Thus far this radio remnant has yet to be observed. This might be a scientific case for future Radio telescopes like the Square Kilometre

Array (SKA).

2.2.2 Optical- and UV-studies

The first reports of the optical variability and flaring nature of AE Aquarii were made by Zinner (1938). Later, the now classical spectroscopic studies of AE Aquarii were made by Joy (1954) and Crawford and Kraft (1956). In these studies the discovery and identification of the spectroscopic binary components (K-type secondary and "Blue" companion) led to a basic model for the system wherein a WD primary star and a late K-type secondary star orbits a common centre of mass. The secondary star also fills its Roche-lobe, transferring mass through Roche-lobe overflow across the L1 region, to the primary component.

The first studies of the periodic nature of the WD in AE Aquarii yielded the discovery of a 33.076737 s periodic oscillation in the optical part of the spectrum at an amplitude of 0.2-0.3% (Patterson (1979)). It has been observed (Patterson (1979)) that the pulsed amplitude increases to $\sim 1\%$ during optical flares. Power spectra representing observations displaying flaring also exhibit broadband quasi-periodic oscillations (QPO) activity supplementing the 33.076 s fundamental period ($F_0 = 30.23$ mHz) and its first harmonic at 16.54 s ($2F_0 = 60.46$ mHz) (See Figure 2.4). (This convention for the definition of the fundamental period and its first harmonic for the WD spin as defined by Patterson (1979) will be used throughout this thesis.)[1] Through a pulse timing analysis, Patterson (1979) determined a measurement of the projected orbital velocity, with the resultant velocity curve and additional constraints being used to determine the system properties. Mass estimates of 0.74 ± 0.06 $M_\odot$ for the secondary star and 0.94 ± 0.10 $M_\odot$ for the primary star were determined. The detected QPOs during flares were then also explained for the first time using a model where gaseous blobs were produced by instabilities near the WD accretion zone in the accretion disc. The model also described a highly magnetized WD, with a field strength of $10^6 - 10^7$ G. The polarization of AE Aquarii was measured by Cropper (1986). Circular polarization of

[1]This convention differs from the mathematical description of harmonic theory, wherein the fundamental frequency F_0 has harmonics equal to multiples of F_0, i.e. nF_0 where $n = 1, 2, 3, ...$ The first harmonic n=1 is then F_0, the second n=2 is $2F_0$ and etc.

$0.05 \pm 0.01\%$ was reported, using the University of Cape Town (UCT) Polarimeter at SAAO.

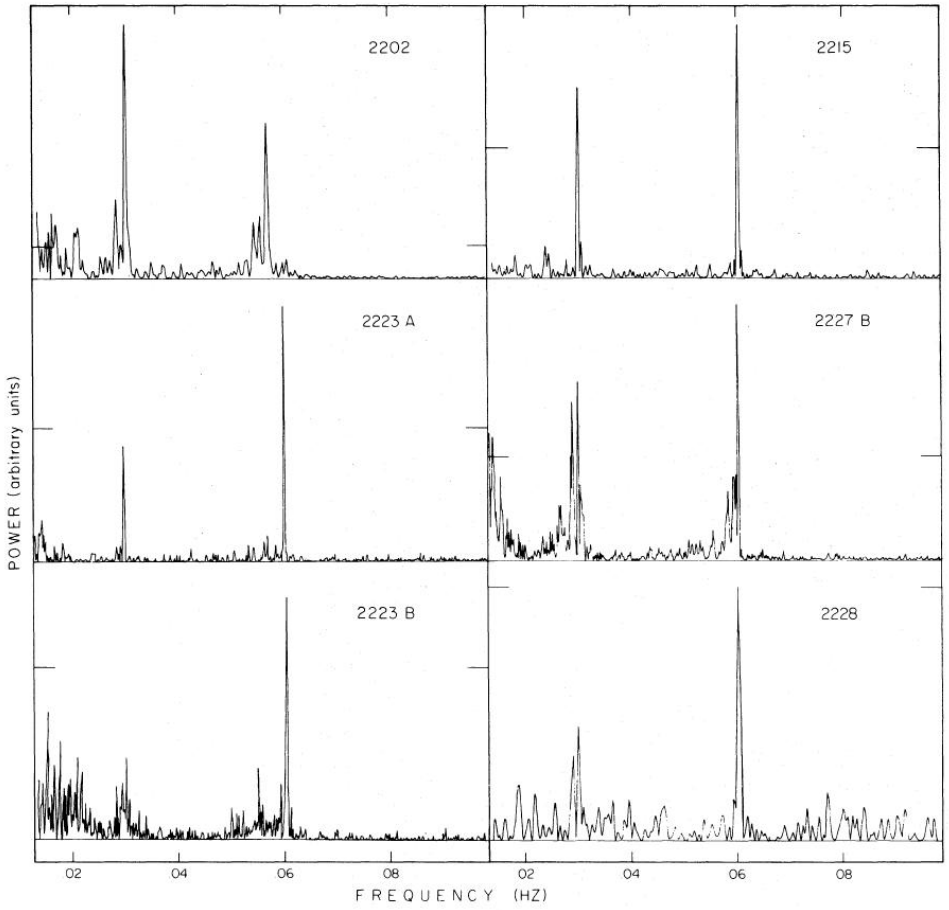

Figure 2.4: Power spectra showing the variable nature of the 16.5 and 33 s oscillations of AE Aquarii (Adopted from Patterson (1979)).

Studies by Robinson et al. (1991) using spectroscopic and photometric data improved the model constraints for AE Aquarii in general and the WD in particular. An improved orbital period of $0.4116580(\pm 2)$ days and radial velocity variation amplitude of $K_{em} = 141 \pm 8$ km s^{-1} were derived. The ephemeris of the 16.5 s component was revised to $T_{max} = \text{BJED}2,445,171.999844(\pm 1) + 0.000191416425(\pm 1)E$, with a pulse timing orbit semi-amplitude of 2.30 ± 0.07 giving $K_{pulse} = 122 \pm 4$ km s^{-1}. From the spectroscopic orbital elements, the masses of the components

were calculated as $M_K \sin^3 i = 0.54 \pm 0.05\ M_\odot$ for the secondary star, and $M_{WD} \sin^3 i = 0.62 \pm 0.05\ M_\odot$ for the WD. This gave a mass ratio of $q = M_{WD}/M_K = 1.13 \pm 0.06$. This study did find an interesting discrepancy of a phase shift of $\sim 60^\circ$ in the oscillation time-delay curve with respect to the emission-line radial velocity curve. An orbital inclination between 63° and 70° was also derived. However, later studies revealed no shift in the phase-profiles (De Jager et al. (1994))

Follow-up work was done by Welsh et al. (1993) using high speed spectroscopy from the Mount Wilson 2.5 m coudé Spectrograph and (bandpass matched) near simultaneous (0.01 ms delay) optical photometry from the Mount Wilson 1.5 m telescope obtained during July 1981. The study found a phase shift of 75° in the emission-line velocities. (Refer to Figure 2.5). The oscillation orbit was however shifted by only $5^\circ \pm 3^\circ$, confirming the theory by Robinson et al. (1991) that the oscillations arose from a region concentric with the WD. The oscillations could therefore be used to determine the apparent orbital velocity of the WD, independent of the emission-line radial velocity measurements. An improved orbital ephemeris was calculated for superior conjunction, i.e. $T_0 = 2439030.7879(\pm 11) + 0.411655601(\pm 56)E$. The study also calculated mass ranges and orbital inclination values for the system of $0.64 < M_{WD}/M_\odot \lesssim 0.91$ and $0.49 < M_K/M_\odot \lesssim 0.70$ using $M_{WD} \sin^3 i = 0.528 \pm 0.017\ M_\odot$ for orbital inclinations of $56^\circ \lesssim i < 70^\circ$, giving a mass ratio of $q = M_K/M_{WD} = 0.773 \pm 0.026$.

The nature of anomalous (~ 1 min) optical bursts and their effects were examined by De Jager and Meintjes (1993) using optical photometer studies conducted at SAAO. Reports of short optical bursts with rise and decay times of a few seconds and durations of ≈ 1 min were recorded. This was contradictory to expected flare rise times of a few hundred seconds and were probably associated with dynamic activities in the WD magnetosphere. Using the Faraday induction equation ($\underline{\nabla} \times \underline{E} = -\frac{1}{c}\partial \underline{B}/\partial t$) for the short time scale of the burst rise time, a potential drop of $\Delta V \gg 10^{12}$ volt may be induced during these events. These short optical bursts and possible associated particle acceleration could be signatures for possible $\gamma -$ ray burst detections, as reported by Meintjes et al. (1992, 1994).

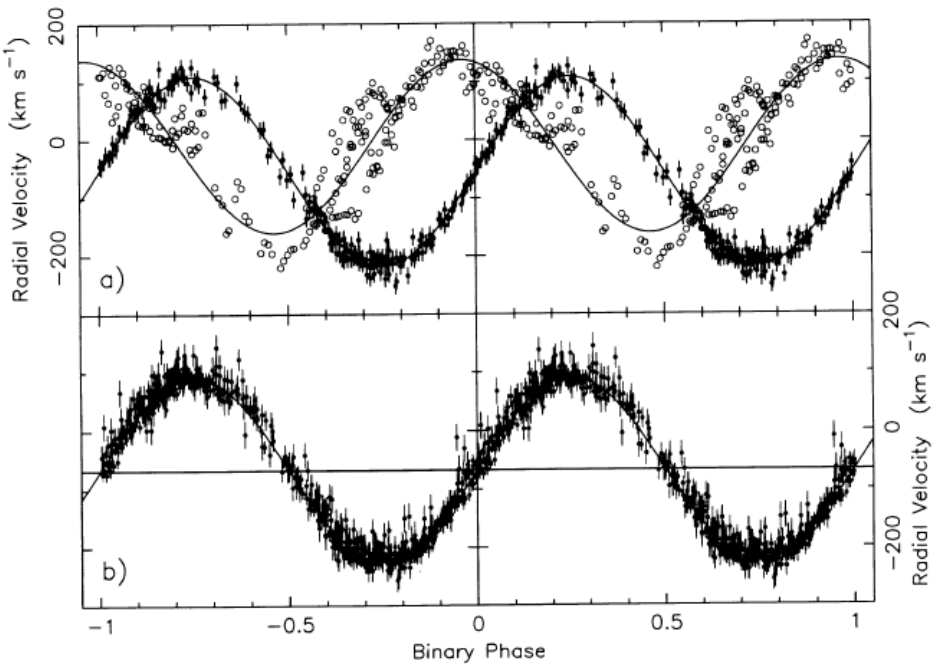

Figure 2.5: Radial velocity curves, with the top panel showing the phase shift between absorption-line (filled circles) and emission-line (open circles) measurements (Adopted from Welsh et al. (1993)).

In an in-depth study covering 14.5 years of observational work, De Jager et al. (1994) discovered a spin-down or $\dot{\mathrm{P}}$ in the spin period of the WD at a rate of 5.64×10^{-14} s s^{-1}. (Refer to Figure 2.6). This study confirmed the orbital ephemeris determined by Welsh et al. (1993), and showed that the absorption-line radial velocity of the secondary star provided the correct phasing for the 33 s oscillations, if the oscillations originate at the WD. A mass of $0.9 - 1.0$ M$_\odot$ for the WD was determined using a pulse-timing delay amplitude of $\mathrm{a_{WD}} \sin \mathrm{i} = 2.04$ s. Additionally the spin-down power of the WD was determined at $-\mathrm{I}\dot{\Omega}\Omega = 6 \times 10^{33}$ $\mathrm{I_{50}}$ erg s^{-1}, which is a factor of ~ 120 greater than the inferred accretion luminosity derived from UV (Eracleous et al. (1994)) and X-ray (Eracleous et al. (1991)) observations. De Jager et al. (1994) also noted that a considerable fraction of the spin-down power may be converted into particle acceleration, thus possibly explaining the radio synchrotron and possible $\gamma -$ ray emission. These authors also stated that the secondary K-star lies above the main sequence, which complied with the required mass-radius ratio.

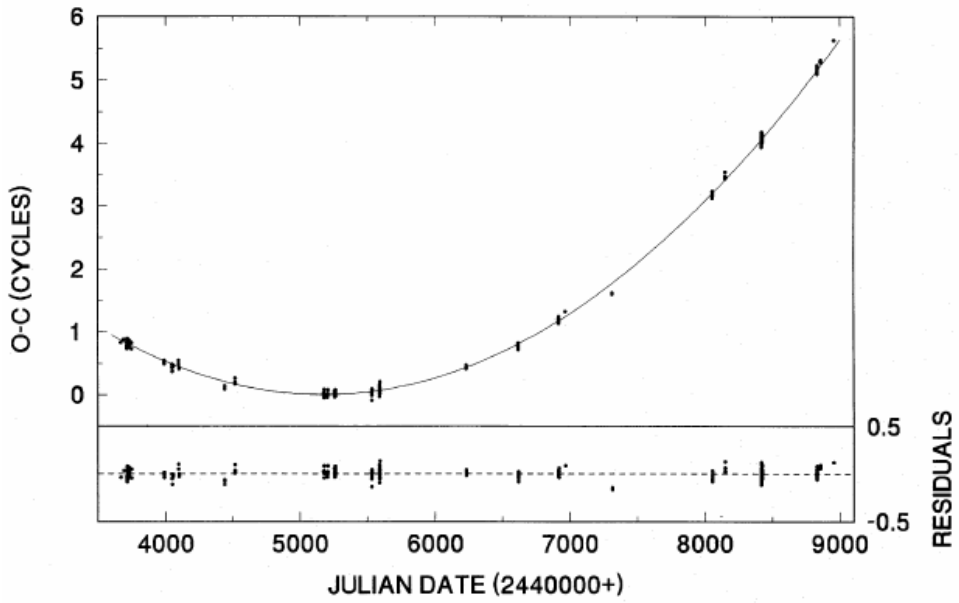

Figure 2.6: O-C Curve for AE Aquarii taking a period derivative into account (Adopted from De Jager et al. (1994)).

The nature of the ultra-violet (UV) emission of AE Aquarii was quantified by Eracleous et al. (1994) in an important study that utilized the Hubble Space Telescope (HST). The study consisted of high time resolution UV spectroscopy using the Faint Object Spectrograph aboard the HST, and simultaneous high speed UBVR photometry using the 82" telescope at McDonald Observatory. It was found that the amplitude of the 33-oscillations in UV was at $\sim 40\%$ of the mean quiescent level (Figure 2.7), and that the mean pulse profile had two broad unequal peaks spaced at half an oscillation cycle. There was also a correlation noted between the optical and UV pulse profiles. With the orbital delay curve of the UV pulses establishing the WD as the origin, the UV and optical spectra were used to describe a WD atmosphere model with a temperature of ~ 26000 K. As with previous studies that found no correlation between the oscillations and the emission line spectra, no oscillations in the UV emission line fluxes or their velocities (down to 800 km.s^{-1}) were found. It was proposed that the 33 s oscillations originate at the X-ray heated magnetic polar caps of the WD. Based on that assumption, the mean

pulse profile was reproduced through the modelling of maximum entropy maps of the brightness distribution on the WD surface. From these maps the fluctuations in the oscillation amplitude were described as small fluctuations in the accretion rate. It was also found that large aperiodic flares did not strongly affect the properties of the pulses, and the argument was made that the flares were not associated with accretion of material onto the WD, nor that their origin was within the WD magnetosphere.

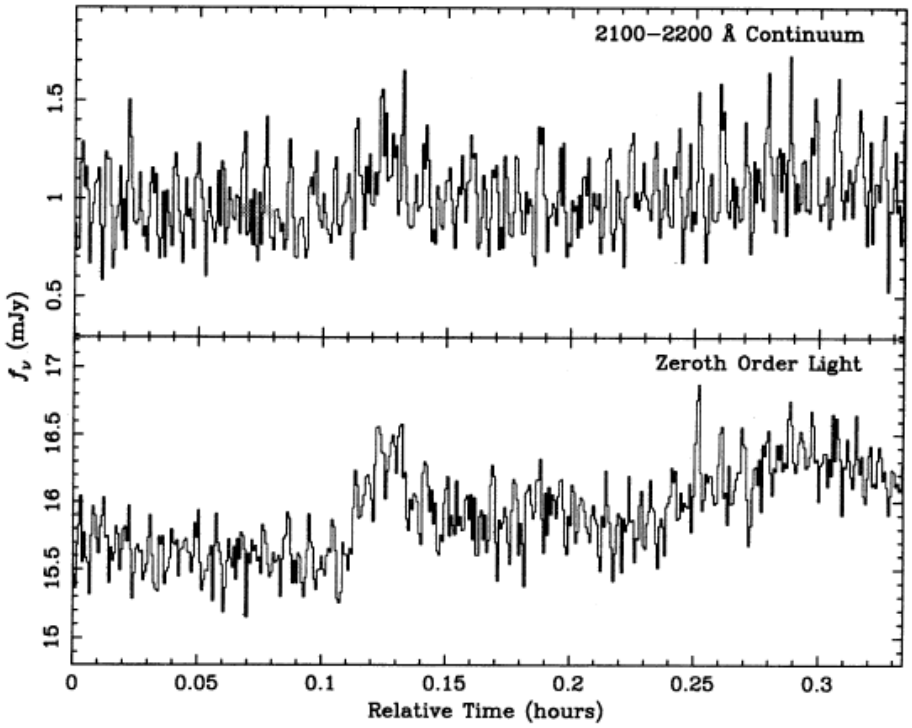

Figure 2.7: HST light curves, with the large amplitude of the 16.5 s pulses clearly visible (Adopted from Eracleous et al. (1994)).

Follow-up work on the spectroscopic nature of AE Aquarii was done by Welsh et al. (1995), using a second dataset from Mt Wilson obtained during July 1982. The analysis focused on the behaviour of the mass donor star, by analysing the observed weak absorption lines. Through modelling of the lines, the spectral type of the secondary star was found to be K2-K5. Parameter estimates put the orbital velocities at $K_1 \sim 138 \pm 6$ km s^{-1}, $K_2 \sim 157.9 \pm 0.8$ km s^{-1} and rotational veloc-

ity at $V_{rot} \sin i = 85 - 108$ km s^{-1}, and the total flux contribution to the system at $69 - 94\%$. A mass ratio range ($0.58 < q = (M_2/M_1) < 0.89$) was also derived, that proved to be dependent on the spectral type and limb darkening. Through the use of the amplitude of the pulse arrival-time delay curve (as estimated by Eracleous et al. (1994)) and the value for K_2, the mass ratio for the system was estimated as $q = 0.646 \pm 0.013$. An inclination of i=49°±15°was determined, based on the assumption that the absorption-line flux deficit variations were ellipsoidal variations. It was however noted that the deviations from the expected ellipsoidal strength were significant, suggesting a non-uniform distribution of absorption-line strength across the donor star. This result was interpreted as indicative of star-spot regions on the donor star. Finally using Monte Carlo simulations, where the mass of the primary star was limited to $M_{WD} < 1.4$ $M_\odot$ with no assumption on the mass of the donor star, realistic probability distributions for the inclination and system component masses were determined. This resulted in $M_{WD} = 0.89 \pm 0.23$ $M_\odot$, $M_K = 0.57 \pm 0.15$ $M_\odot$ and i=55°±7°.

The argument stated by Eracleous et al. (1994) that the flaring region was outside the WD magnetosphere, was strengthened by simultaneous time resolved polarimetric and photometric observations made by Beskrovnaya et al. (1996) at the Crimean Astrophysical Observatory. A nightly mean value of $0.06 \pm 0.01\%$ for the circular polarization was found. This correlates with the polarization found by Cropper (1986). This value, when interpreted in the context of a cyclotron mechanism, excludes an accreting WD model. It was also found that the lack of a noticeable change in the polarization between flaring and quiescent states and the intrinsic magnitudes and colours of the flaring component favoured a thermal model in the optical. The colour indices of the flares were found to be close to a blackbody with $T \sim 15000 - 20000$ K and an emitting area of $S \sim 10^{20}$ cm^2.

Patterson (1979) and later De Jager et al. (1994) stated that the secondary cool component of AE Aquarii is above the main sequence. This statement was investigated by Friedjung (1997) through parallax measurements with the *HIPPARCOS* satellite. A trigonometrical parallax value of 9.80 ± 2.84 milliarcseconds was obtained, resulting in a derived distance of $79 < D(\sim 102 \text{ pc}) < 144$ pc. These results

also implied that the radius of the cool component was significantly larger than that of a main sequence star of the same spectral type. Unfortunately the results were characterized by large errors and associated uncertainty.

The nature of the Hα emission from AE Aquarii was studied by Welsh et al. (1998) using the data presented in Welsh et al. (1995). The 10 000 plus spectra were obtained at a sampling rate of ~ 6 s. Although the known 16.5 and 33 s oscillations were not detected in either the continuum or line spectra, the Hα line did show remarkably complex behaviour, with flux variations of up to a factor 3 within a few hours. The behaviour of the instantaneous line profile could best be described by a complex system, and not a single entity because of the highly asymmetric nature of the line, as well as the superposition of emission components with different velocity components. It was also found that the Hα emission was delayed and decayed slower than the continuum during flares, and that the Hα variations were not linearly correlated with the continuum variations. These results, as well as an examination of the trailed spectrograms and Doppler tomograms, revealed no accretion disk signatures and strengthened the support of a propeller mechanism proposed by Wynn et al. (1997). These authors utilized the propeller model, wherein the flares observed in the system were driven by collisions between blobs that were ejected from the system by a magnetic propeller. In this framework the flares were the result of radiative cooling of shock-heated blobs during collisions.

The proposal that the cool component was a star above the main sequence, was explained by Echevarria et al. (2006) using high-dispersion time-resolved spectroscopy. From cross-correlation of the absorption-lines that showed an asymmetric profile, as expected from the heated side of the red star, the spectral type of the secondary star was shown to vary between K2 and K5, depending on the longitudinal position of the temperature measurement of the star surface (confirming the results obtained by Welsh et al. (1995) a decade earlier). A radial velocity for the secondary star was calculated as $K_{ad} = 165.2 \pm 0.6$ km s^{-1}. The rotational velocity of the red star showed ellipsoidal variations with a period at half the orbital period measured as a function of the orbital period. Rotational velocities showed variation between $V_{rot} \sin i = 105 \pm 3$ km s^{-1} and $V_{rot} \sin i = 130 \pm 3$ km s^{-1}, con-

straining the WD semi-amplitude to $K_{em} = 139 \pm 4$ km.s^{-1}. The inclination angle for the system was constrained to i = 58°±3° based on an absorption-line strength variation of 30%. The binary component masses were thus calculated as $M_{WD} = 1.07 \pm 0.07$ $M_\odot$ and $M_K = 0.90 \pm 0.05$ $M_\odot$. Based on these values the red star had to have a radius 40% larger than that expected for a main sequence star of the same mass (with an expected spectral type of G5), therefore resulting in a spectral type of K2-5. The presence of N and O lines in the UV spectra from both HST (Eracleous et al. (1994)) and IUE (Jameson et al. (1980)) studies also strengthened the case for an evolved secondary star, as these stars are in a CNO burning cycle.

The first Roche tomography reconstruction of the cool secondary star was done by Watson et al. (2006) using simultaneous spectroscopic (4.2 m William Herschel Telescope (WHT)) and photometric (1.0 m Jacobus Kapteyn Telescope (JKT)) observations from La Palma. The reconstructed tomogram revealed surface inhomogeneities that were explained due to the presence of large, cool star spots. The map not only showed a number of lower latitude spots, but also a large high latitude spot, and a relative paucity of spots at a latitude of 40°. The large high latitude spot was similar to that seen in Doppler images of rapidly rotating isolated stars. A total spot coverage of $\sim 18\%$ of the northern hemisphere was estimated. Additionally, the binary system parameters were calculated by applying the *entropy landscape* technique. Optimal masses for the system components were $M_{WD} = 0.74$ $M_\odot$ and $M_K = 0.50$ $M_\odot$ at an orbital inclination of i = 66° and a systemic velocity of $\gamma = -63$ km s^{-1}. The lack of correlation between these and earlier results could be based on the fact that this was the first study (tomography) of a secondary star within a CV. (Additional discussions of Roche tomography in general and of AE Aquarii can be found in Watson and Dhillon (2001); Watson et al. (2007)). The calculated mass and radius of the secondary, together with additional evidence of N and O lines in the observed spectra that infer CNO cycling in the envelope of the secondary, shows that the secondary star is an evolved star that has thrown off a large part of its envelope. The mass transfer of the envelope onto the primary WD resulted in the primary being spun up to its current spin period of ~ 33.08 s resulting in the propeller ejection of the mass transfer flow

from the secondary.

An in-depth analysis of the nature of the flickering variability of AE Aquarii was done by Zamanov et al. (2012) using simultaneous multicolour (UBVRI) photometry. The aim was to estimate the parameters (colours, temperature and size) of the fireballs that produce the optical flares. A rise time of 220-440 s was observed for the optical flares. The de-reddened colours of the fireballs were calculated at $(\mathrm{U}-\mathrm{B})_0 \sim 0.8-1.4, (\mathrm{B}-\mathrm{V})_0 \sim 0.03-0.24,$ and $(\mathrm{V}-\mathrm{I})_0 \sim 0.26-0.78$. Calculations based on the peak of the observed flares in the UBVRI bands resulted in temperatures for the fireballs between 10000 and 25000 K, masses of $(7-90)\times10^{19}$ g and sizes of $(3-7)\times10^{9}$ cm, based on a distance of 85 pc.

The most recent work was also Roche tomography of the cool K4V secondary star, by Hill et al. (2014). The datasets were acquired 9 days apart, with the aim of measuring the differential rotation of the stellar surface. As with Watson et al. (2006), many large cool star spots were observed, as well as a large high-latitude spot and a prominent limb down the trailing hemisphere. A spot coverage of $15.4-17\%$ on the northern hemisphere was estimated, with distinct spot bands around 22° and 43° latitude. See Figure 2.8 for a Roche tomogram of the second data block.

Two different techniques were used to measure the differential rotation (based on a solar-like differential rotation law), with the first giving an equator lap time of 269 d and the second a lap time of 262 d. Based on these values, it was shown by Hill et al. (2014), that the star was not fully tidally locked as previously assumed for CVs, but had a co-rotation latitude of 40°. The system parameters were again calculated based on the *entropy landscape* technique. For these datasets, mass values of $\mathrm{M_{WD}} = 1.20\ \mathrm{M_\odot}$ and $\mathrm{M_{WD}} = 1.17\ \mathrm{M_\odot}$, $\mathrm{M_K} = 0.81\ \mathrm{M_\odot}$ and $\mathrm{M_K} = 0.78\ \mathrm{M_\odot}$ at orbital inclinations of 50°and 51°with optimal systemic velocities of $\gamma = -64.7$ km s^{-1} and $\gamma = -62.9$ km s^{-1} were calculated, which was closer to previously calculated parameters. Finally it was proposed that the discovery of differential rotation has significant implications for stellar dynamo theory, and the cessation of mass transfer due to spot traversal of the $\mathrm{L_1}$ point. The highly

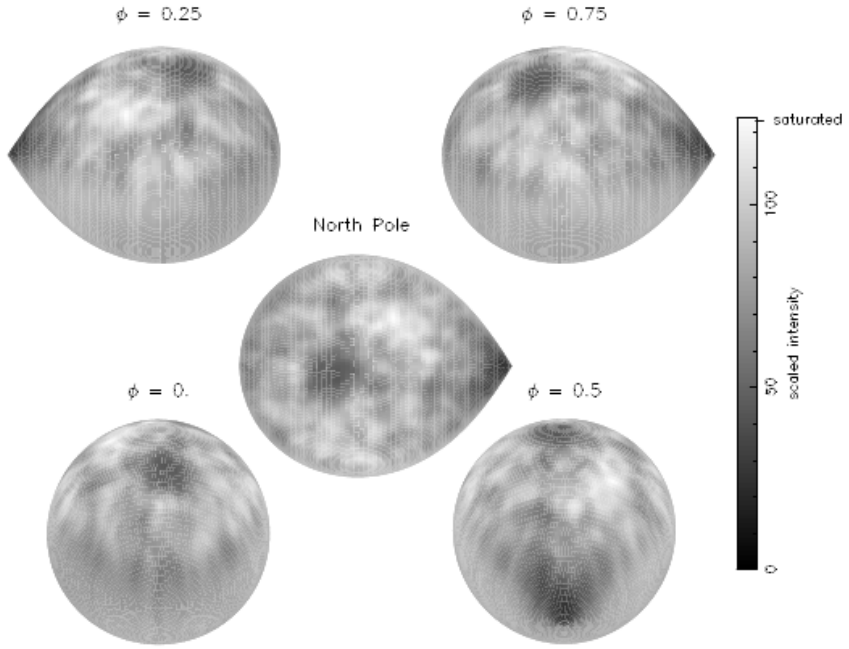

Figure 2.8: Roche Tomogram of AE Aquarii reconstructed using the data from the second observation block (Adopted from Hill et al. (2014)).

magnetized region around the L_1 point might create magnetized blobs of material, explaining the "blobby" accretion observed in CVs. This corresponded with the model proposed by Meintjes (2004) to explain the inferred blobby nature of the mass transfer in AE Aquarii which played a pivotal role in the propeller process from the source and possible non-thermal emission.

2.2.3 X-ray and γ-ray studies

The first scientifically significant work done on AE Aquarii in the very high energy (VHE) region was the discovery of 33 s coherent oscillations between $0.1 - 4.0$ keV presented by Patterson et al. (1980) using *Einstein Observatory* data. It was found that the period and phase of the oscillations correlated with those observed in optical wavelengths. These authors proposed that the origin of the oscillations was most probably an accretion induced hot spot on the rapidly rotating, magnetized WD. The possibility of transient pulsations (as observed in the optical) was also

mentioned.

Subsequent studies were made by Choi et al. (1999) using *Ginga* and *ASCA* data. Periods of 33.076 ± 0.001 s (*Ginga*) and 33.077 ± 0.003 s (*ASCA*) were detected between energies of $0.4 - 10$ keV. The time averaged spectrum was modelled for the first time using a thermal emission model with a combination of two different temperatures of $\mathrm{kT}_1 = 0.68^{+0.01}_{-0.02}$ keV and $\mathrm{kT}_2 = 2.9^{+0.03}_{-0.2}$ keV. Spectral analysis at these energies had no significant differences between quiescent and flare stages, although some hardening in the spectrum was recognized during the flaring stages.

Observations and analysis of the X-ray spectra of AE Aquarii were made by Itoh et al. (2006) using *XMM-Newton*. High resolution spectroscopy of the He-like triplet of N and O led to values $\sim 10^{11}$ cm^{-3} for the electron number density of the emitting plasma, with a value of $\mathrm{l_p} \simeq (2-3) \times 10^{10}$ cm for the geometrical scale of the plasma. These authors deduced that the plasma emission region was extended and not from accretion onto the WD as previously assumed. It was also found that the features of the X-ray spectra correlate with the optical, thus leading to the proposal that the broad emission lines from X-ray to optical wavelengths were from adiabatic cooling of plasma after initial heating to $\mathrm{T_{max}}$ in the deep gravitational well of the WD. It was also proposed that the absence of the high velocity component in the Hα emission line spectra was a result of ejected plasma from the propeller action being too hot to emit the Hα line within a region of $\mathrm{r} < \mathrm{l_p}$ ($\sim$ Roche lobe size) from the WD where the high velocity component was expected to originate.

The first possible non-thermal X-ray detection of AE Aquarii was made by Terada et al. (2007) using *Suzaku* data. AE Aquarii was chosen as a case study to test the sensitivity of the *Suzaku* space telescope. Observations in October 2005 in both soft (XIS at $0.2 - 12$ keV for 47.0 ks) and hard (HXD at $10 - 70$ keV for 52.7 ks) energy ranges were performed. Correlations were found between the XIS ($0.5 - 4$ keV and $4 - 10$ keV) and lower HXD ($10 - 25$ keV) folded light curves at a period of 33.07975 ± 0.00002 s, with slight modulations visible at higher HXD ($25 - 50$ keV). From the wide-band pulse component spectra both thermal and

non-thermal components could be identified with a simple power law fitting the $3 - 25$ keV region and the $10 - 100$ keV fitted with a photon index 2.29 ± 0.04 and a flux of $3.5 \pm 0.2 \times 10^{-12}$ erg cm^{-2} s^{-1}. The lower energy bands could be fitted with the following components: A stable 3.12 keV and a variable 0.84 ± 0.01 keV thermal component, and a variable non-thermal component with a $2.10^{+0.05}_{-0.20}$ index and a flux of $4.1 \pm 1.1 \times 10^{-12}$ erg cm^{-2} s^{-1}, which only appeared during maximum phase. A proposal was made that the flux from the non-thermal radiation from the WD consisted of no more than 0.1% of the spin-down energy.

A follow-up study by Terada et al. (2008) was also made using the 2005 data as well as data from October 2006 (42.2 ks). A refined period of 33.0769 ± 0.0001 s in the soft XIS data, as well as a statistically significant ($\chi^2_\nu = 2.6$ for $\nu = 6$) periodic signal at an energy of 10-30 keV in the second half of the 2005 HXD dataset, were observed. The thermal models for the $1.5 - 10$ keV phase averaged data were refined with two thermal components at temperatures of $2.9^{+0.20}_{-0.16}$ keV and $0.53^{+0.13}_{-0.14}$ keV. A significant excess above the extrapolated model for the HXD ($12 - 25$ keV) data was also observed. The proposed explanations for the excess were either a third thermal component of $54^{+0.26}_{-0.47}$ keV or a power law with a photon index of $1.12^{+0.63}_{-0.62}$. The thermal and additional component luminosities between $4 - 30$ keV for a inferred distance of 102 pc then became $1.7^{+1.3}_{-0.6} - 5.3^{+15.3}_{-0.3} \times 10^{29}$ erg cm^{-2} s^{-1} respectively. The latter luminosity corresponds to 0.09% of the spin-down luminosity of the WD. The non-thermal pulsed hard X-ray radiation was then also explained in terms of relativistic electrons from an acceleration mechanism in the strong magnetic fields of the fast rotating WD. See Figure 2.9 for the background subtracted X-ray spectra of AE Aquarii from *Suzaku* data for 2005 and 2006. The typical uncertainty in the PIN non X-ray background was indicated by the light green curves, while the expected cosmic X-ray background was indicated by the dark green curves.

An extensive ephemeris analysis on the nature of the 33 s X-ray pulsations using *ASCA, XMM-Newton* and *Chandra* data was performed by Mauche (2006). Using a ten year baseline of X-ray data and a 27 year cumulative baseline, the ephemeris was found to have an additional braking component compared to the very precise

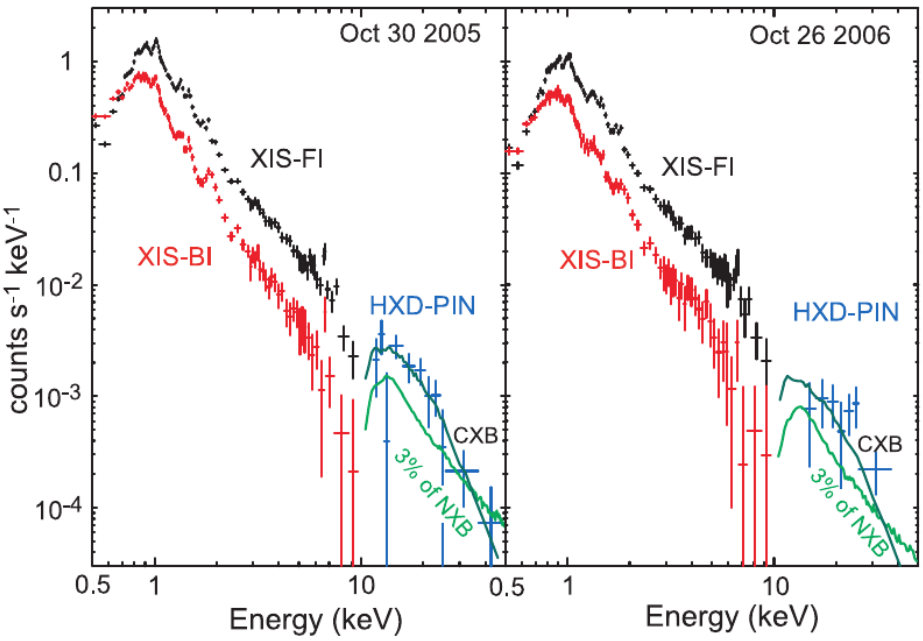

Figure 2.9: X-ray spectra of AE Aquarii from *Suzaku* data from 2005 and 2006 (Adopted from Terada et al. (2008)).

De Jager et al. (1994) ephemeris. The additional components were explained as either a cubic term of $\ddot{\mathrm{P}} = 3.46 \pm 56 \times 10^{-19}$ d^{-1}, which was inconsistent in both magnitude and sign with magnetic dipole radiation losses, or alternatively as an additional quadratic term with $\dot{\mathrm{P}} = 2.0 \pm 1.0 \times 10^{-15}$ d.d^{-1}, which was consistent with a modest increase in the accretion torques spinning down the WD.

More recent X-ray studies using datasets from *Swift* and *Chandra* were conducted by Oruru and Meintjes (2012) who modelled the hard and soft components. The emission below 10 keV was shown to be predominately thermal, characterised by flares and emission lines and dominated by the soft X-ray component. The multi-component thermal emission models proposed by Terada et al. (2007, 2008) were then also confirmed through modelling of the X-ray spectra. A time-averaged X-ray luminosity of $\mathrm{L_X} \sim 10^{31}$ erg s^{-1} was also determined. The pulsed 33 s X-ray emission below 10 keV was also confirmed in both the *Swift* and *Chandra* datasets, with the ephemeris parameters being consistent with the *Suzaku*-derived values. The X-ray emission below 10 keV was explained in terms of plasma heating at

the magnetospheric radius as a result of the dissipation of gravitational potential energy. The determined conversion efficiency of $\alpha \sim 0.01$ was also found to be sufficient to heat the plasma at the magnetospheric boundary to temperatures kT $\leq$ 10 keV, which was sufficient to drive the X-ray emission below 10 keV. With only a small fraction ($\beta \sim 0.3\%$) of the mass at the magnetospheric radius accreting onto the WD, the very effective nature of the magnetospheric propeller process was emphasized.

The possible non-thermal power-law hard X-ray component as measured by Terada et al. (2007, 2008) sparked renewed interest in AE Aquarii as a potential high energy source. Oruru and Meintjes (2012) showed that electrons could be accelerated to VHE energies ($\gamma \sim 10^7$) outside the light cylinder radius. The resultant proposed $\gamma-$ray emission might then be from up-scattering of soft photons from the K-type secondary star or propeller ejected outflow via inverse Compton processes.

A multi-wavelength campaign was conducted by Lopez-Coto et al. (2013); Aleksić et al. (2014) in 2012 using data from optical, UV, X-ray (*Swift*) and $\gamma-$ray (*MAGIC*) telescopes. The *Swift* data were used to determine the latest ephemeris for the pulsed emission from the WD to aid the search for steady pulsed TeV and variable TeV emission during high states. The X-ray data were fitted using the ephemeris calculated by Mauche (2006) with a resultant pulse amplitude of $A_1/A_0 = 16\% \pm 2\%$ which was higher than that determined for *ASCA* (13%), *XMM-Newton* (10%) and *Chandra* (15%). An offset to the fit of $\phi_{\rm off} = 0.15 \pm 0.02$ was observed, which might be an indication of inaccuracy in the ephemeris used or a drastic variation in $\dot{\rm P}$ or $\ddot{\rm P}$. See Figure 2.10 for the fitted *Swift* XRT spin-phase folded light curve for AE Aquarii.

Some of the earliest $\gamma-$ray studies of AE Aquarii were by Meintjes et al. (1992) (Potchefstroom group) using the Nooitgedacht Mk I Cherenkov telescope between June 1988 and August 1991 for a total of 93 observations. Coincidental and non-coincidental optical observations of AE Aquarii were also made using optical telescopes at SAAO. Evidence of strong coherent pulsed emission

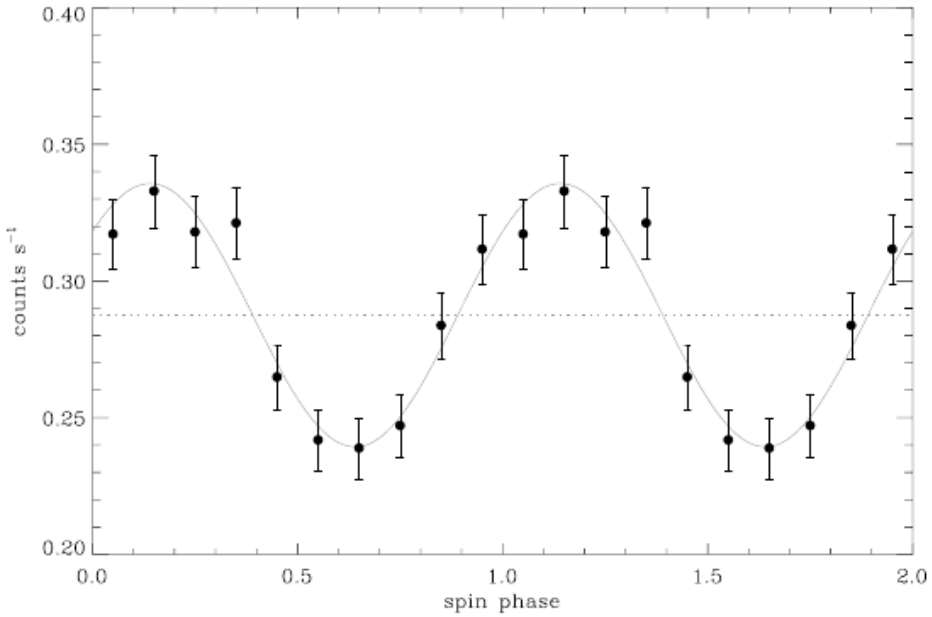

Figure 2.10: *Swift* XRT spin-phase folded light curve for AE Aquarii in the energy range 0.5-10 keV (Adopted from Aleksić et al. (2014)).

was found during optical flares at frequencies close to the spin frequency, i.e. $\sim 29.9 - 30$ mHz and a fundamental frequency $F_0 = 30.23$ mHz at the 4σ significance level. The total time-averaged luminosity at a threshold energy of ~ 2.4 TeV was $L_\gamma \sim 1.5 \pm 0.3 \times 10^{32}$ erg s^{-1}, corresponding with a conversion efficiency of 15% of the spin-down power. With the assumption that the source intensity remained constant during the observation period, a flat differential energy spectrum with a spectral index of 1 ± 1 could be fitted, compared to a cosmic-ray background spectrum of 2.6. A noteworthy result was the detection of pulsed emission during an optical flare at the same 30 mHz frequency (Figure 2.11). This observation also strengthened a hypothesis that indicated a correlation between the pulsed optical and VHE $\gamma -$ ray emission during optical flares. Also reported (Meintjes et al. (1992)) was a correlation between pulse profiles during near simultaneous observations in October 1990 between the Durham group in Australia and the Potchefstroom group in South Africa (Figure 2.12).

Follow-up work was done by Meintjes et al. (1994) between July 1992 and June

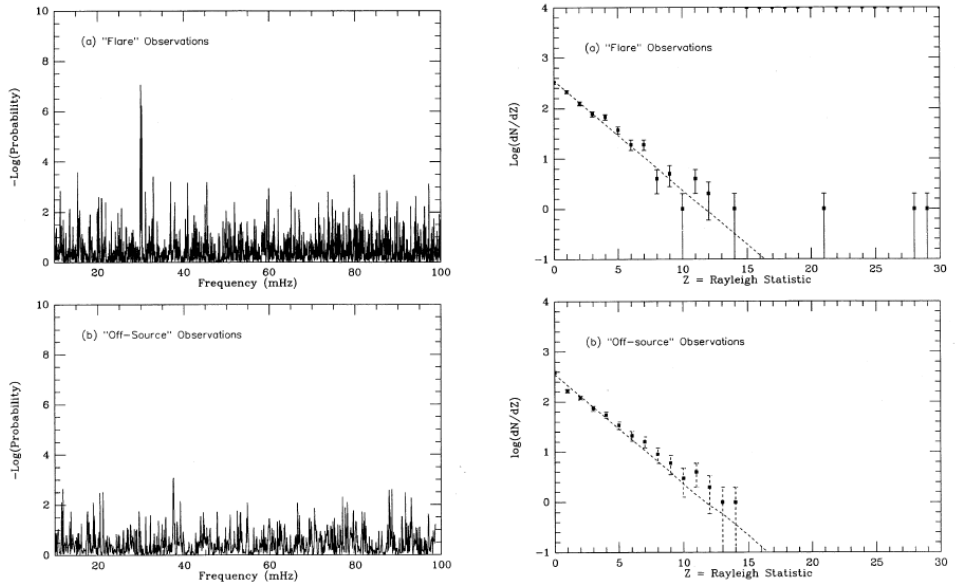

Figure 2.11: Comparison between Rayleigh power spectra and noise statistics for VHE Flare state and Off state of AE Aquarii (Adopted from Meintjes et al. (1992)).

1993, also using the Nooitgedacht Mk I Cherenkov telescope in combination with simultaneous optical observations on eight separate nights for a total of 32 h. Analysis of the combined TeV data independently confirmed previously identified optical and TeV $\gamma-$ray periodicities at a $-\log(\mathrm{Pr}) = 3$ level without any period searches, confirming an observed duty cycle of $\sim 10\%$. The strongest TeV signals were then also linked to optical flares, in the sense that the signals were confined to the time just before the onset of optical flares. The detection of two rapid bursts ($\sim$ 1-3 min duration within 25 min) with three independent telescopes, following an optical flare was significant. The strongest flare showed a significance of 4.6σ per min. The probability of the burst detections for the given trials was at 5.3×10^{-4}. It was suggested then that the full reservoir of the spin-down power ($-\mathrm{I}\dot{\Omega}\Omega \sim 6 \times 10^{33}$ erg s^{-1}) might account for the energy released by a TeV accelerator.

During the same time period as above, i.e. June 1992 and October 1993, 25 observations (a total of 78 h) were conducted by the Durham group using the VHE $\gamma-$ray telescopes at Narrabi, N.S.W. in Australia (Chadwick et al. (1995)). No

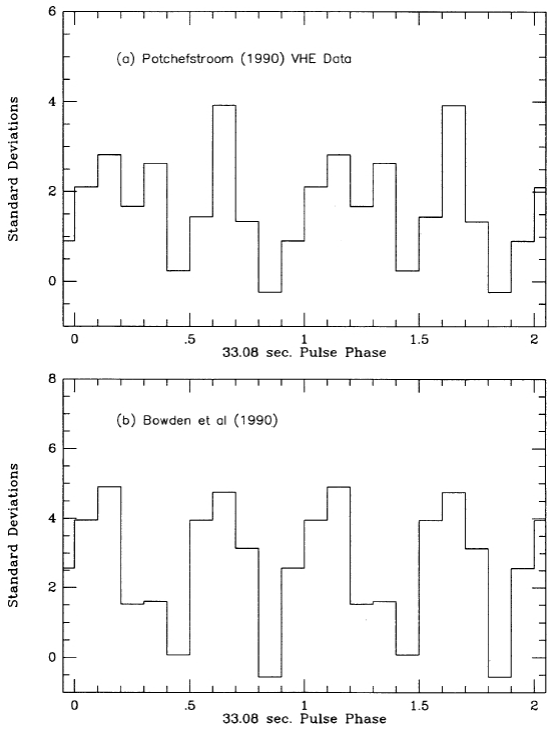

Figure 2.12: Comparison between light curves folded at the WD spin frequency F_0 for the Potchefstroom 2.4 TeV and the Durham 400 GeV data. (Adopted from Meintjes et al. (1992)).

persistent low-level pulsed emission was detected above an energy threshold of 350 GeV. An excess of pulsed VHE $\gamma-$ rays were however observed on 11 October 1993, lasting ~ 4200 s with a count rate excess of 4σ. The burst occurred at phase 0.62-0.74 of the 9.88 h orbital period, with a pulse periodicity at 16.5 s (first harmonic of the 33 s spin period) (Figure 2.13).

Through independent tests, a chance probability of 10^{-7} was determined for the significance of the emission of a burst of pulsed $\gamma-$ rays from AE Aquarii with a threshold energy above 350 GeV. Some evidence was presented for a hardening of the brightness spectrum of Cherenkov events during the burst as compared with the background sample. The flux during the burst was 4% of the total cosmic-ray background at E $>$ 350 GeV, which corresponds with a peak pulsed luminosity of 10^{32} erg.s^{-1}.

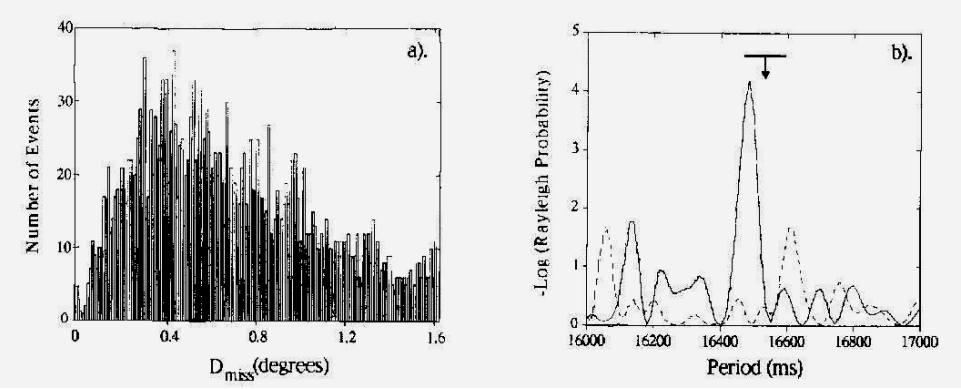

Figure 2.13: The distribution of events recorded during the burst of 11 October 1993 (left) and the -Log(Pr) spectrum with $\gamma-$ ray events represented by the solid line, and background events by the broken line (right) (Adopted from Chadwick et al. (1995)).

A search for TeV emission using the *Whipple* 10 m $\gamma-$ray telescope was done by Lang et al. (1998). AE Aquarii was observed for a total of 68.7 h between 1991 and 1995. No evidence of any steady, pulsed or episodic TeV emission was found. An upper limit value of 4.0×10^{-12} photons cm^{-2} s^{-1} at a threshold energy of 900 GeV for steady emission was determined. This upper limit for steady emission was three orders of magnitude lower than the flux levels during bursts as reported by Meintjes et al. (1994) and Chadwick et al. (1995). Upper-limits for coherent pulsed emission at the fundamental frequency and first harmonic were calculated at 1.5×10^{-12} photons cm^{-2} s^{-1}.

More recent (August 2005) studies were reported by Sidro et al. (2008) using the *MAGIC* telescope on four consecutive nights within a quasi-simultaneous multi-wavelength campaign covering radio, optical, UV, X-ray and $\gamma-$ ray wavelengths. No evidence of any steady or pulsed $\gamma-$ ray emission was found. Upper-limits for steady flux of $\sim 8.0 \times 10^{-12}$ cm^{-2} s^{-1} above 350 GeV and coherent pulsed flux of 4.0×10^{-12} cm^{-2} s^{-1} (at the first harmonic of WD spin) emission were determined.

During a multi-wavelength campaign conducted by Lopez-Coto et al. (2013) and Aleksić et al. (2014) in 2012 using data from optical, UV, X-ray (*Swift*) and $\gamma-$ ray

(*MAGIC*) telescopes, a search for steady TeV as well as variable TeV emission during high states and specifically pulsed emission at 33.08 and 16.54 s, did not result in any significant detections. From the campaign integral upper limit values at 95% confidence level for AE Aqr for steady emission of 6.4×10^{-12} cm^{-2} s^{-1} above 200 GeV and 7.4×10^{-13} cm^{-2} s^{-1} above 1 TeV for a Crab-like power-law photon spectral index of Γ=2.6 were determined. An upper limit for pulsed emission of 2.6×10^{-12} cm^{-2} s^{-1} for energies above 200 GeV was also determined. Aleksić et al. (2014) therefore concluded that AE Aquarii was not an emitter of VHE γ − rays at levels previously claimed (Figure 2.14).

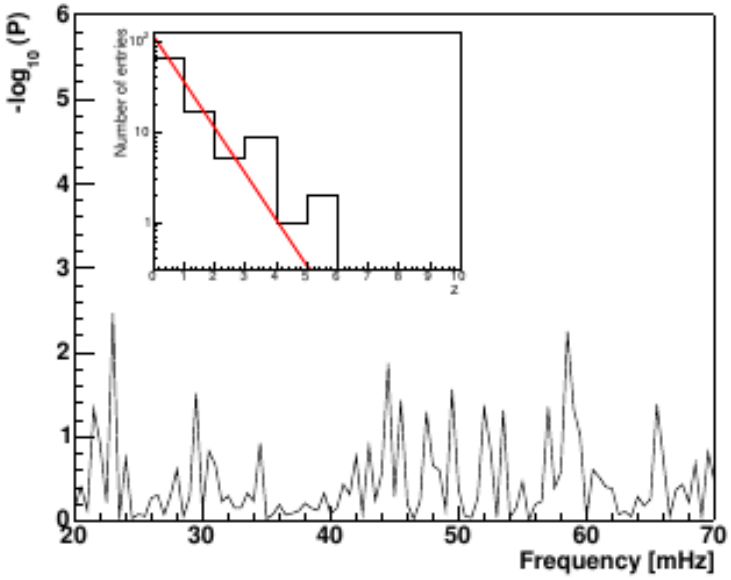

Figure 2.14: Rayleigh power spectrum and noise statistic for AE Aquarii (Adopted from Aleksić et al. (2014)).

All of the above-mentioned γ − ray work was done using Cherenkov radiation detection systems. With the relatively young space-based γ − ray telescopes (*Fermi* and *AGILE*) the amount of data available to analyse for possible steady, pulsed or episodic emission increased. This would require a discussion and comparison between spaced based γ − ray detection systems and ground-based Cherenkov telescopes that is unfortunately beyond the scope of this discussion, although Figure 2.15 could be used as a measure of the sensitivity ranges for different γ − ray

detection systems.

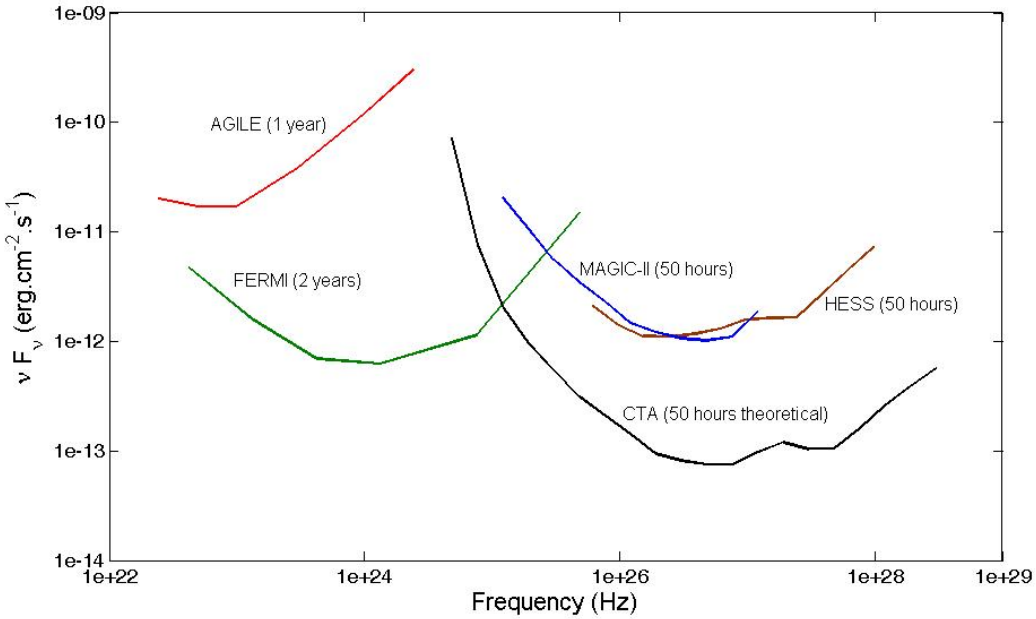

Figure 2.15: Sensitivity curves for selected $\gamma-$ray instruments. Instrumental sensitivity curve data acquired from the ASDC SED builder V3.1 available at http://tools.asdc.asi.it/SED. Fermi sensitivity curve is based on 2 year integration data from the 2FGL Catalogue. CTA theoretical curve is based on monte carlo design studies conducted by Bernlöhr et al. (2013)

As seen from Figure 2.15, the energy range for space based telescopes is lower than ground based telescopes, and therefore fills the gap between the energy range for X-ray telescopes and ground based Cherenkov detectors. Because AE Aquarii had been detected up to hard X-ray energies, with reports of possible VHE $\gamma-$ray emission, a search for pulsed/unpulsed emission signatures can be conducted utilizing data from the Fermi-LAT (20 MeV $-$ 300 GeV) and AGILE-GRID (30 MeV $-$ 50 GeV) instruments aboard the Fermi and AGILE space telescopes respectively.

It is evident from the above discussions that the enigmatic system AE Aquarii is a transient emitter over a very wide frequency range from radio to possible VHE

$\gamma-$ray energies. This multi-wavelength emission nature of AE Aquarii can be observed in the spectral energy distribution (SED) of the system (Figure 2.16).

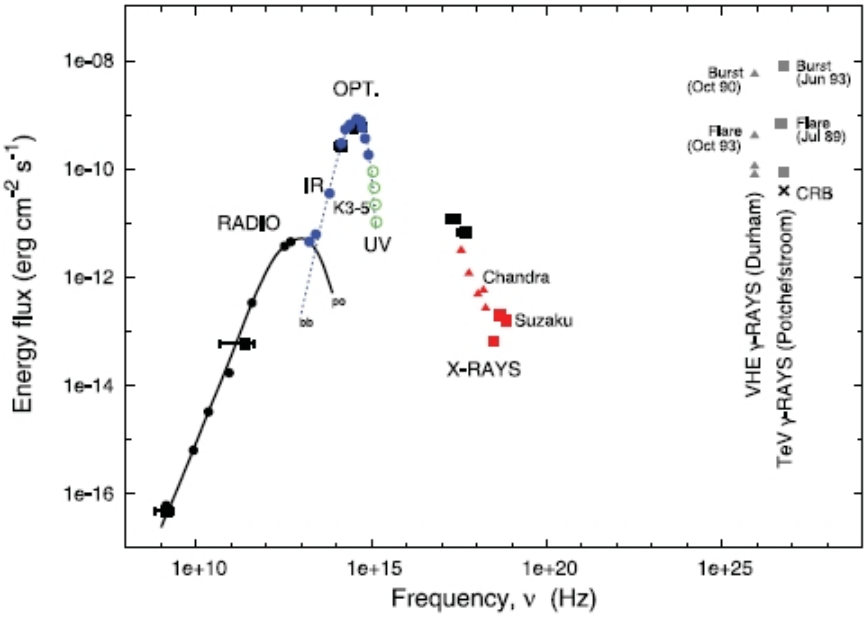

Figure 2.16: Spectral energy distribution of AE Aquarii (Adopted from Oruru and Meintjes (2012)).

Reports (Meintjes et al. (1992, 1994)) have also been made that the possible VHE emission is associated with optical flare activities. For this reason optical observations of AE Aquarii were performed on a continuous basis since 2010 in order to facilitate the search for possible VHE emission by identifying periods of enhanced optical activity, as well as pulsed optical signatures. These periods of enhanced optical activity, as well as identified pulsed optical signatures, can then be used to search for pulsed/unpulsed non-thermal $\gamma-$ray emission in Fermi-LAT and AGILE-GRID data. The analysis of the optical observations performed is presented in the following chapter.

"Part of this work is based on archival data, software or online services provided by the ASI SCIENCE DATA CENTER (ASDC)"

Chapter 3

Optical photometric observations of AE Aquarii

3.1 Introduction

Previous studies (Meintjes et al. (1992, 1994)) have shown correlations between optical flare events and burst-like VHE emission in that the burst-like VHE emission occurred just before optical flare events, as well as a correlation between pulsed optical and VHE emission. Thus to facilitate the search for VHE non-thermal emission from AE Aquarii using *Fermi*-LAT and AGILE-GRID data, we conducted an updated optical photometric study that coincided with the *Fermi*-LAT and AGILE-GRID observations. Fortunately both telescopes were launched (*Fermi* in 2008 and AGILE in 2007) before the onset of the optical studies, allowing for a long baseline of available data to analyse. The analysis of the optical photometric data was primarily to re-confirm the optical characteristics of the system and to identify features, such as strong optical flares, that could assist in the VHE non-thermal emission search. This chapter consists of the following: A discussion of the optical photometric observations conducted, a discussion of the photometry analysis technique used, results obtained and, finally, a discussion of the identification, selection and characterisation of flaring activity in the optical light-curves that coincides with *Fermi*-LAT and AGILE-GRID data.

3.2 Optical photometric observations

3.2.1 Observational systems

The experimental setup for the photometric observations conducted during this study was two-fold. The first and primary system was the Boyden 1.5 m reflector telescope and Apogee U55 CCD system, with datasets acquired primarily by the author during 2010 and 2011. During a combined effort in 2012, observational data were also acquired with the assistance of Mr. D. Wium and Dr. B. van Soelen during a special multi-wavelength campaign. A secondary dataset was acquired by Mrs. A. Odendaal using the SAAO 1.9 m reflector telescope and Sutherland High-speed Optical Camera (SHOC) system.

The Boyden 1.5 m telescope system consists of a 1.5 m Cassegrain optical system, with Bessel supplied UBVRI and Clear filters (see Figure 3.3 for the transmission curves), and an Apogee U55 CCD camera at the Cassegrain focus (Figure 3.1). The CCD is an E2V CCD55-20 back-illuminated mid-band system (see Figure 3.2 for the CCD response curves), with a pixel resolution of 770×1152 and digital resolution of 16 bits. The system has a plate-scale of 0.2 arcsec/pixel with a field of view (FOV) of $\sim 2'30''$ by $3'44''$.

The telescope control system and data-acquisition software used was the in-house developed Spica system (Refer to Appendix C for a concise discussion of the development and implementation of the software, as well as Van Heerden and Calitz (2010) for a detailed manual on the 1.5 m telescope system). The photometric analysis software used for the Boyden data sets was an in-house developed Boyden-IRAF package. For a detailed discussion of the development of the Boyden-IRAF package, as well as additional material relating to the 1.5 m telescope system, refer to Van Heerden (2008).

For the more recent observations, the Sutherland 1.9 m telescope was used with Bessel UBVRI filters and the SHOC2 camera system without a focal reducer. The SHOC instruments employed Andor iXon 888 EM CCD cameras. The cameras

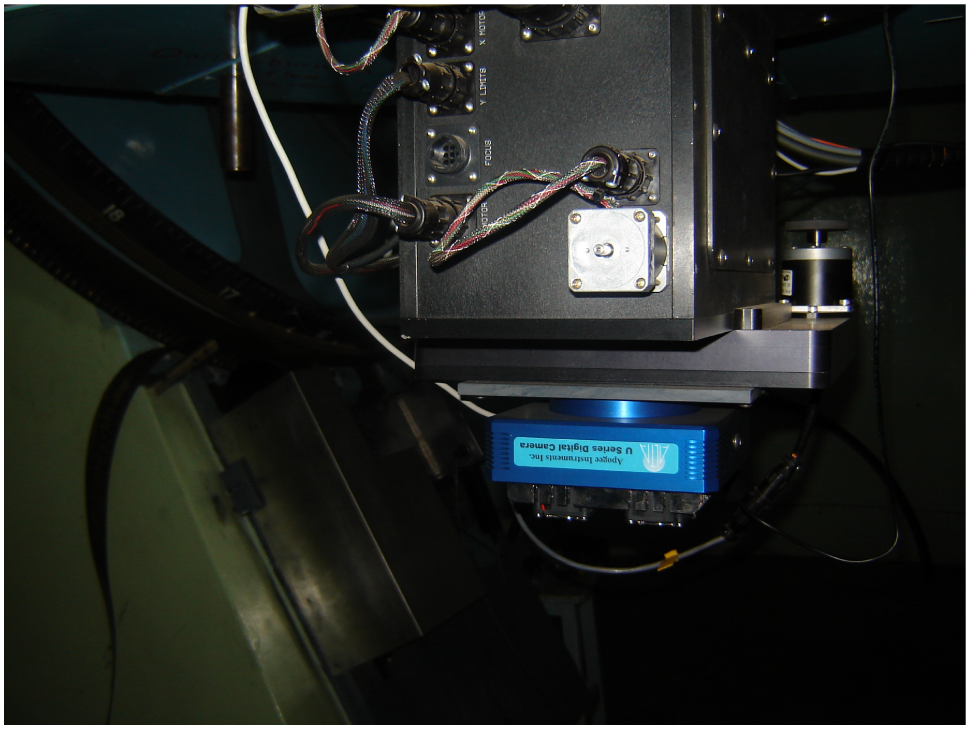

Figure 3.1: U55 CCD camera and filter-wheel assembly at Cassegrain focus of the Boyden 1.5 m telescope (Van Heerden (2008)).

have a pixel resolution of 2048×1024, that were operated in frame-transfer mode (allowing faster readout times), with resultant image resolution of 1024×1024. See Figure 3.5 for the quantum efficiency response curve for the CCD camera. The SHOC system also employed a GPS-triggering system for very accurate trigger-timing control at the microsecond scale.

Additional technical information relating to the 1.9 m telescope system can be found on the SAAO website at SAAO 1.9 m telescope (http://www.saao.ac.za/science/facilities/telescopes/1-9m/), with additional technical reference material of the 1.9 m telescope control system in Worters and Potter (2011). For the SHOC camera systems, additional information can be found in Coppejans and Gulbis (2014) and more information on the pipeline used during the photometry reductions and analysis in Kotze (2013).

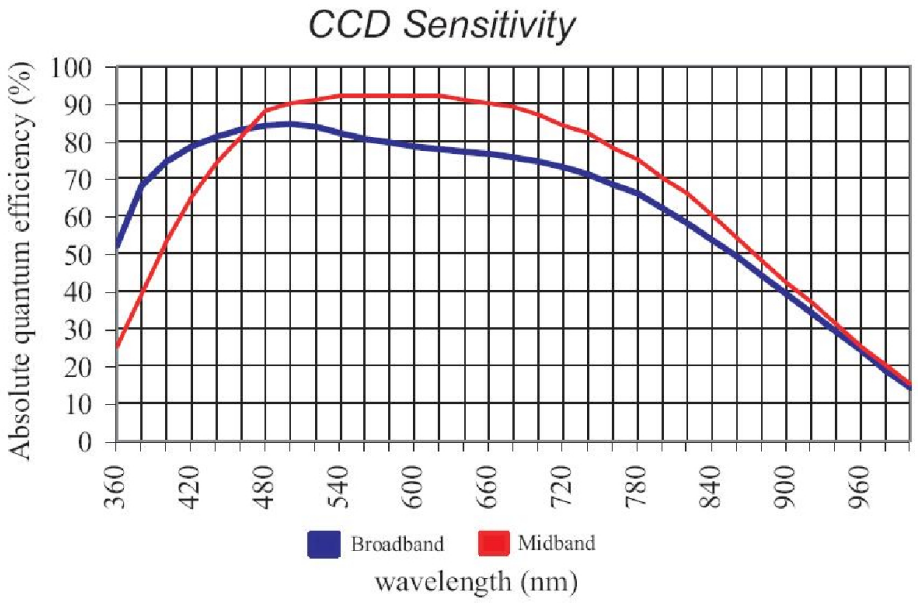

Figure 3.2: U55 CCD Camera response curve (Apogee Instruments Inc., http://www.ccd.com/).

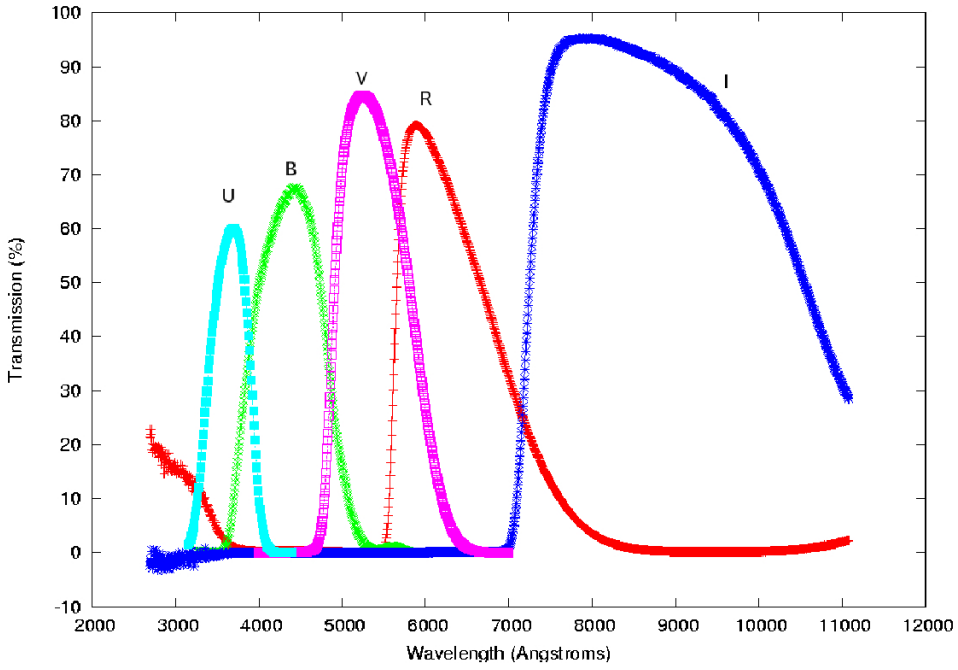

Figure 3.3: Transmission curves for the filters used on the Boyden 1.5 m telescope (Filter data from Kitt Peak Observatory).

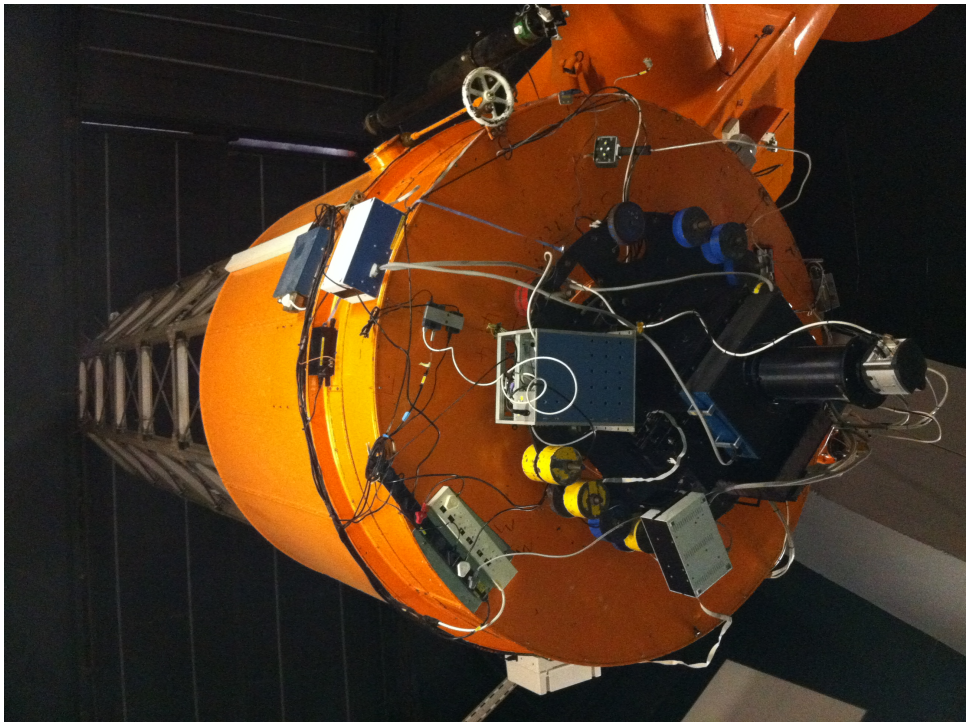

Figure 3.4: SAAO 1.9 m telescope with attached SHOC camera system at Cassegrain focus (SAAO 1.9 m telescope, http://www.saao.ac.za/science/facilities/ telescopes/1-9m/).

3.2.2 Photometric observations

The following observations (Table 3.1) were acquired at the Boyden observatory, in addition to relevant reduction frames, i.e. BIAS (ZERO) and FLAT. As there is no MASS-DIMM system available at Boyden yet, the logged seeing conditions were determined from the average point spread function (psf) radius of the project star for the relevant dataset from each night and the telescope system plate scale of 0.2 arcsec/pixel.

Observations of AE Aquarii were acquired at SAAO on the 12th, 13th and 14th of April 2013 (Table 3.2) in addition to relevant reduction frames, i.e. BIAS (ZERO) and FLAT. The logged seeing values were determined by the MASS-DIMM system available at SAAO.

Table 3.1: Observation log for Boyden Observatory for AE Aquarii using the 1.5 m telescope.

JD at start (2450000+)	Data length (s)	Exposure (s)	Filter	Binning	Seeing (“)	Notes
5350.4709	6105.469	1.000	C	4×4	2	Clear.
5355.4710	6845.903	1.000	C	4×4	3.6	Stop 00:56 UT Seeing
5365.4411	10422.200	1.000	C	4×4	3	Stop 01:46 UT Seeing
5373.4195	17167.282	1.000	C	4×4	2.4	Clear.
5394.3427	17888.016	1.000	C	4×4	3.6	Clear.
5406.3173	17523.110	1.000	C	4×4	3	Clear.
5429.2207	22874.343	1.000	C	4×4	3	Bright (Moon). Instr Errors.
5443.1979	19810.669	1.000	C	4×4	3	Clear.
5781.2175	25864.364	0.900	C	4×4	3	Moon First Q
5782.2204	24333.406	1.000	C	4×4	3	Moon First Q
5784.2100	24101.079	1.000	C	4×4	3	Bright (Moon).
5785.2050	23469.315	1.000	C	4×4	3	Thin, sparse UA clouds. Full Moon.
5793.2119	22610.234	1.000	C	4×4	3	Thin, sparse UA clouds. Moon 3rd Q
5798.1997	22604.576	1.000	C	4×4	3	Thin, sparse UA clouds.
5799.2027	22426.588	1.000	C	4×4	3	
5800.2070	20082.422	1.000	C	4×4	3	Clear.
6064.4982	14903.546	1.000	C	4×4	3	Clear. Instr Errors.
6066.6092	5783.172	1.000	C	4×4	3	
6068.6048	6319.063	1.000	C	4×4	3.6	
6069.5847	7193.328	1.000	C	4×4	3	Clouds. Stop. Bad seeing.
6070.5799	7513.546	1.000	C	4×4	3	Stop. Bad seeing.
6072.5890	6714.031	1.000	C	4×4	3.6	Instr Errors.
6074.5735	8056.516	1.000	C	4×4	3	Stop. Bad seeing.
6076.5714	8896.953	1.000	C	4×4	3.6	Hazy, Thin UA clouds.

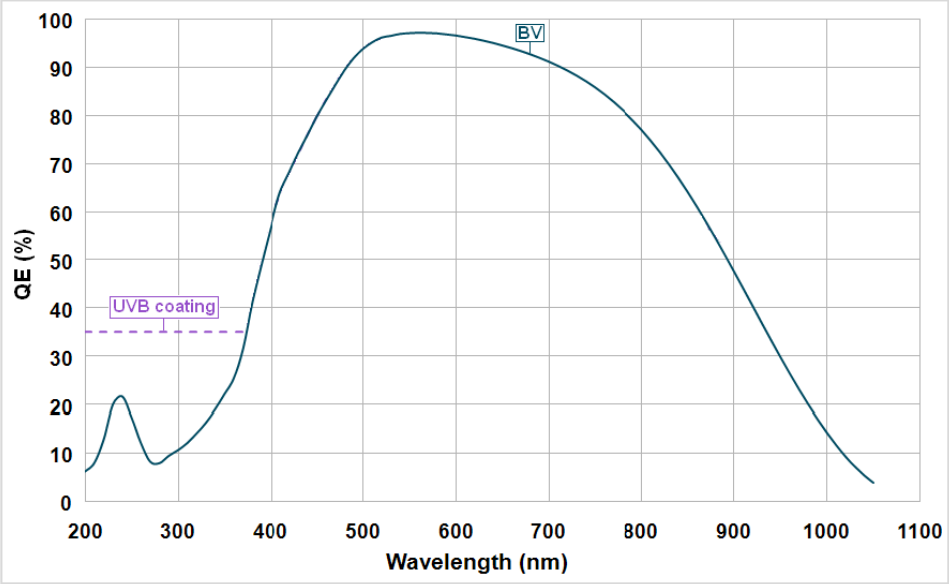

Figure 3.5: SHOC (Andor iXonÊM+888) Camera response curve (Andor (2009)).

Table 3.2: Observation log for SAAO for AE Aquarii using the 1.9 m telescope.

JD at start (2450000+)	Data length (s)	Exposure (s)	Filter	Binning	Seeing (“)	Notes
6394.6238	2342.165	0.0558	B	8×8	1.1	Abort at SAST=05:40
6395.6364	1375.6927	0.0558	B	8×8	1.7	
6396.6358	1469.4033	0.0558	B	8×8	1.7	

The acquired data frames from the different observational sites were analysed using relevant photometric software and analysis techniques.

3.3 Photometric analysis

The optical data were measured and analysed using IRAF and PyRAF reduction and photometry packages, as well as custom FORTRAN and MATLAB scripts written by the author. The Boyden data sets were photometrically reduced and measured using the Boyden-IRAF package developed *in situ* for the research telescopes at Boyden (Refer to Van Heerden (2008) for a detailed discussion of the

development and implementation). Basic aperture photometry was applied as the field of interest of AE Aquarii is sparsely populated by stars, therefore not requiring psf photometry (which is of greater importance for densely populated stellar fields). The SAAO data sets were analysed using the SHOC pipeline python/PyRAF scripts developed by Kotze (2013). Again, as with the Boyden data sets, the output was the aperture photometry values.

The measured output files were further analysed and managed using custom FORTRAN and MATLAB scripts. The first correction applied to the data was the re-binning of the SAAO data sets. This was done to reduce the amount of data points being used. This was possible because the required time resolution for analysis was between 0.5 and 1 s, while the data were acquired at a timing resolution of 0.0558 s. A mean binning technique was thus applied using a resolution width of 20 data points.

The re-binned SAAO data along with the Boyden data time stamps were corrected to barycentric, as well as AE Aquarii system values. This was accomplished using custom FORTRAN and/or MATLAB scripts that implements the SLALIB (Positional Astronomy Library) routines (Wallace (2003)). The script accuracy was tested by Professor Tom Marsh (Department of Physics, University of Warwick and Royal Observatory Edinburg. Tel: +44-24765-74739. Email: t.r.marsh@warwick.ac.uk), whose own barycentric correction code was tested against an independent pulsar code, which differs by only 0.002 s from the code used in this study. This difference could probably be attributed to the locality differences of the observatories. A more detailed discussion of timing corrections and analysis techniques, for instance barycentric time corrections, can be found in Appendix A.

Next the light-curves were examined and outliers, excessive noise and instrumental errors were removed using visual inspection methods. Also indicated in some of the light-curves is selected flare events that are to be used in additional analysis. Examples of RAW and cleaned instrumental light-curves for selected data sets are presented in Figures 3.6, 3.7 and Figures 3.8, 3.9.

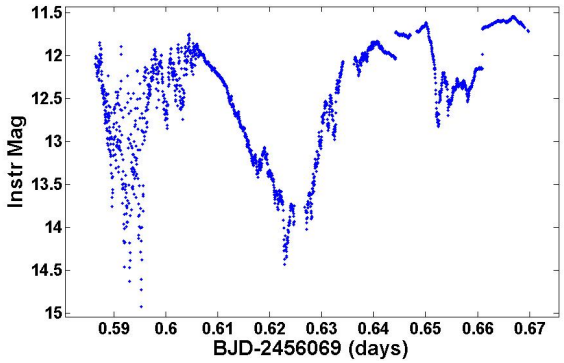

Figure 3.6: RAW Instrumental magnitude light-curve for AE Aquarii for 2456069.5865 with data S/N of 285.65 and data length of 7191.56 s.

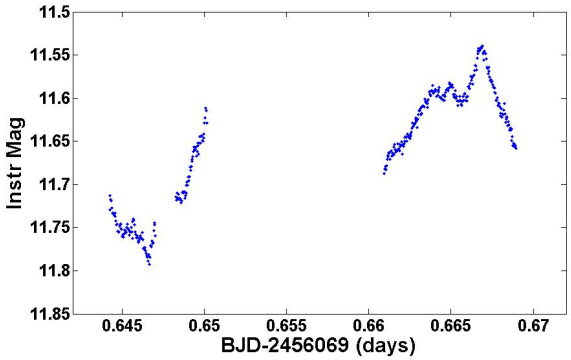

Figure 3.7: Cleaned Instrumental magnitude light-curve for AE Aquarii for 2456069.6442 with data S/N of 300 and data length of 2134.25 s.

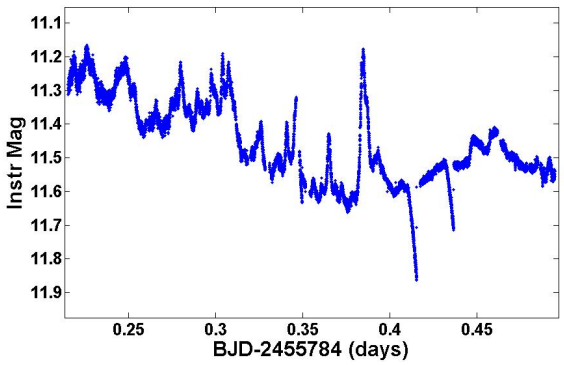

Figure 3.8: RAW Instrumental magnitude light-curve for AE Aquarii for 2455784.2156 with data S/N of 290.01 and data length of 24100.48 s.

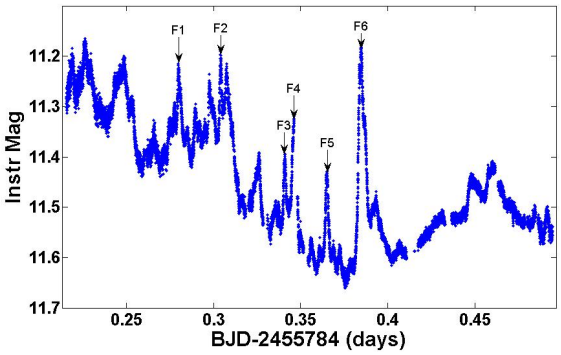

Figure 3.9: Cleaned Instrumental magnitude light-curve for AE Aquarii for 2455784.2156 with data S/N of 290.01 and data length of 24100.48 s.

From the figures, two important experimental influences on the data quality can be seen. Figures 3.6 and 3.7 display an extreme case of contamination by atmospheric conditions on data quality. During the night in question, some clouds and variable seeing conditions resulted in a large part of the light-curve being cut from the data. The secondary set (Figures 3.8 and 3.9) displays an example of instrumental errors that could contaminate the data. The night in question revealed

a sync problem between the 1.5 m telescope dome control and telescope slewing rates. This can happen sometimes when the telescope design requires variable tracking rates depending upon the telescope position (Note: Some of the data sets (notably 2455350 and 2455355) also contain gaps where additional experiments were conducted to test for possible UBVRI observational set ups and data sets. These data sets were beyond the scope of this study and are therefore not included).

The final light-curves used during flaring activity investigations and time series analysis include Figure 3.7 and Figure 3.9 and from Figure 3.10 until Figure 3.32. The light-curves also indicated which flares needed to be investigated in Section 3.4.

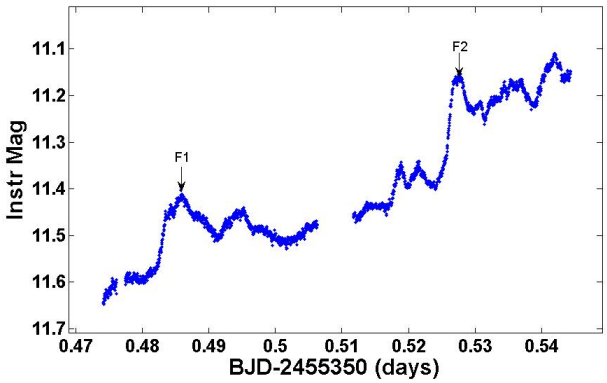

Figure 3.10: Instrumental magnitude light-curve for AE Aquarii for 2455350.4741 with data S/N of 310.27 and data length of 6067.61 s.

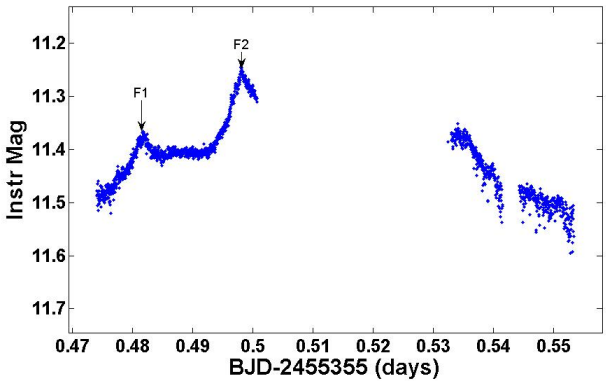

Figure 3.11: Instrumental magnitude light-curve for AE Aquarii for 2455355.4741 with data S/N of 282.59 and data length of 6845.90 s.

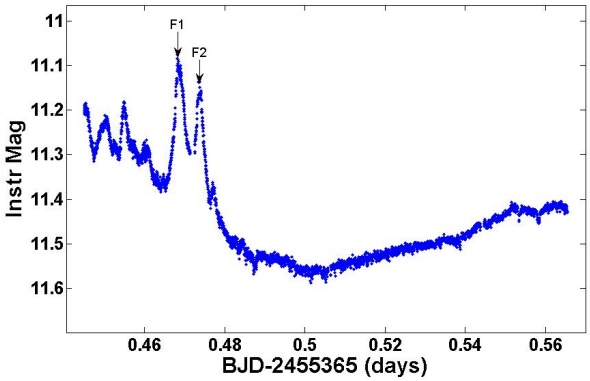

Figure 3.12: Instrumental magnitude light-curve for AE Aquarii for 2455365.4449 with data S/N of 312.87 and data length of 10422.20 s.

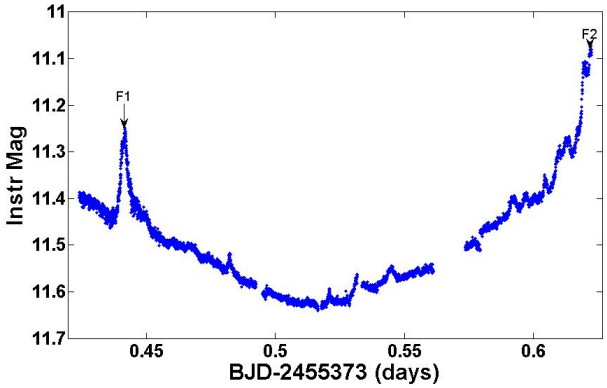

Figure 3.13: Instrumental magnitude light-curve for AE Aquarii for 2455373.4239 with data S/N of 318.30 and data length of 17167.28 s.

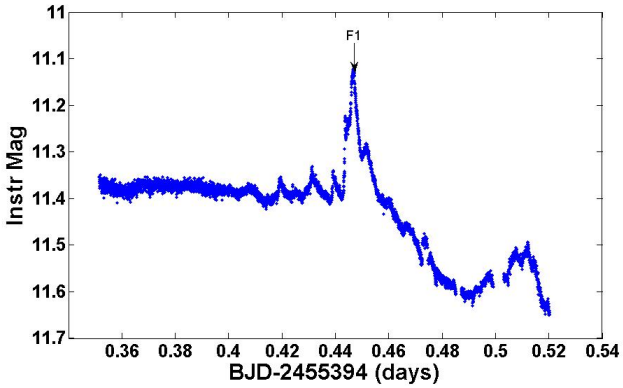

Figure 3.14: Instrumental magnitude light-curve for AE Aquarii for 2455394.3514 with data S/N of 274.85 and data length of 14594.34 s.

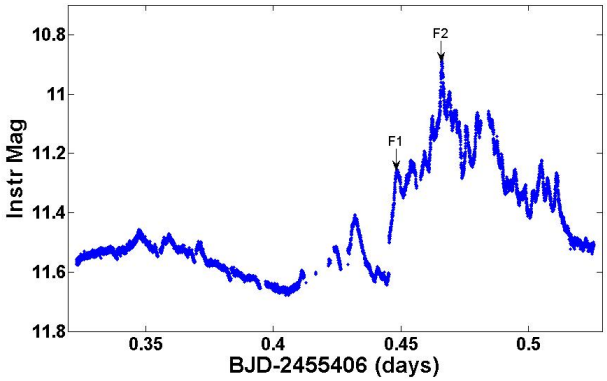

Figure 3.15: Instrumental magnitude light-curve for AE Aquarii for 2455406.3229 with data S/N of 293.50 and data length of 17522.81 s.

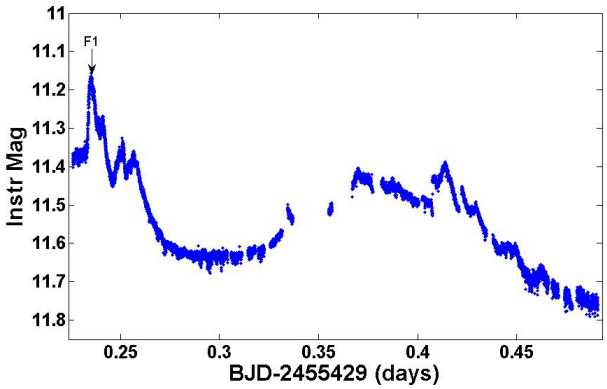

Figure 3.16: Instrumental magnitude light-curve for AE Aquarii for 2455429.2261 with data S/N of 278.18 and data length of 22874.81 s.

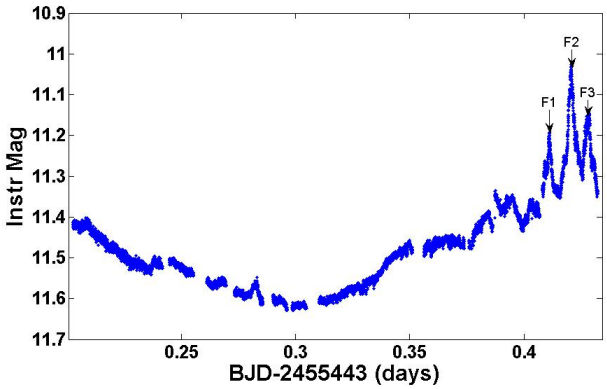

Figure 3.17: Instrumental magnitude light-curve for AE Aquarii for 2455443.2028 with data S/N of 293.31 and data length of 19810.67 s.

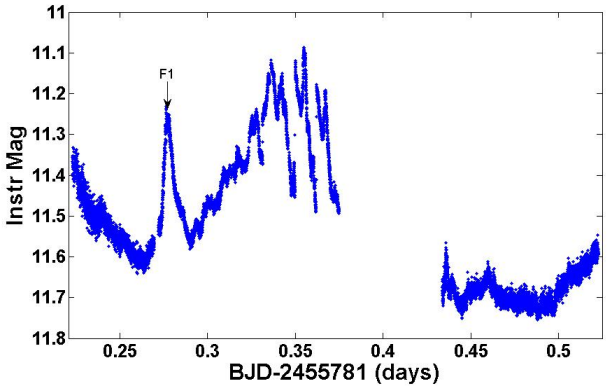

Figure 3.18: Instrumental magnitude light-curve for AE Aquarii for 2455781.2231 with data S/N of 242.05 and data length of 25864.36 s.

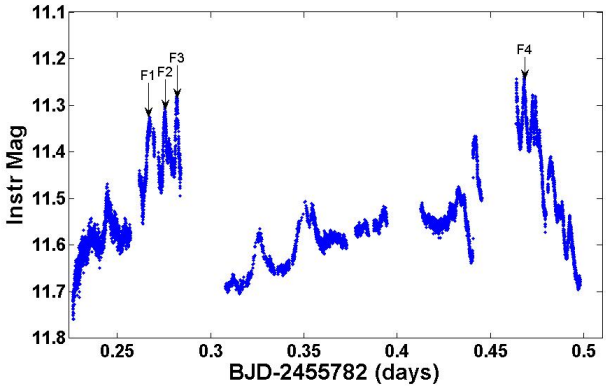

Figure 3.19: Instrumental magnitude light-curve for AE Aquarii for 2455782.226 with data S/N of 261.74 and data length of 23503.91 s.

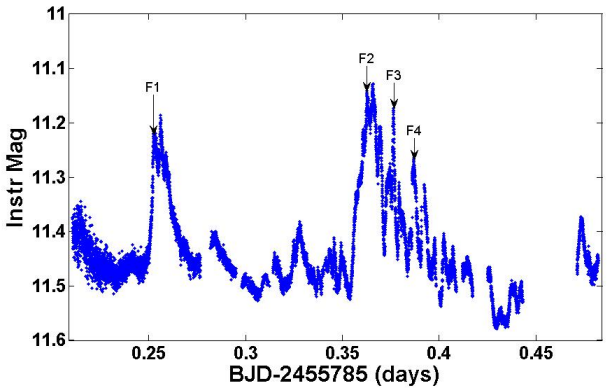

Figure 3.20: Instrumental magnitude light-curve for AE Aquarii for 2455785.2105 with data S/N of 282.03 and data length of 23469.32 s.

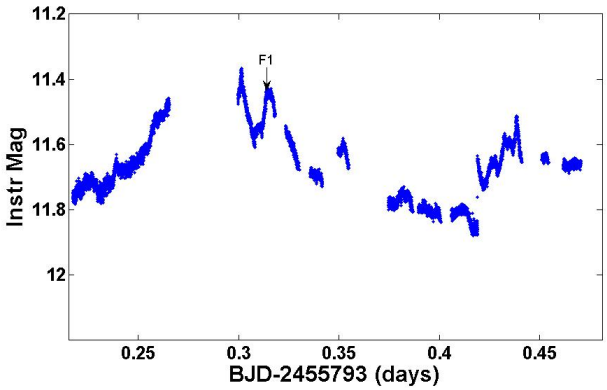

Figure 3.21: Instrumental magnitude light-curve for AE Aquarii for 2455793.2173 with data S/N of 245.27 and data length of 22609.28 s.

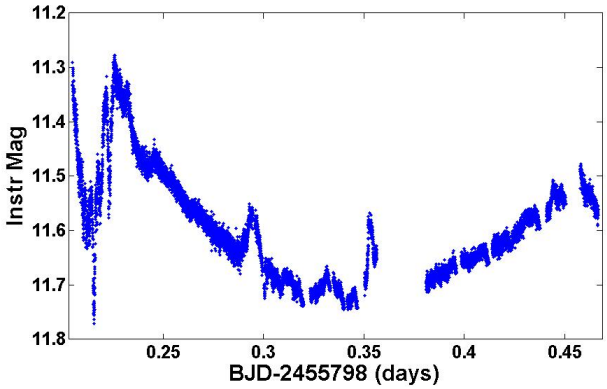

Figure 3.22: Instrumental magnitude light-curve for AE Aquarii for 2455798.205 with data S/N of 300 and data length of 22604.58 s.

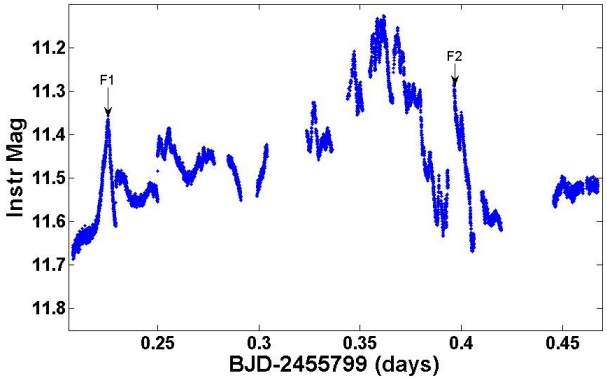

Figure 3.23: Instrumental magnitude light-curve for AE Aquarii for 2455799.208 with data S/N of 250 and data length of 22426.59 s.

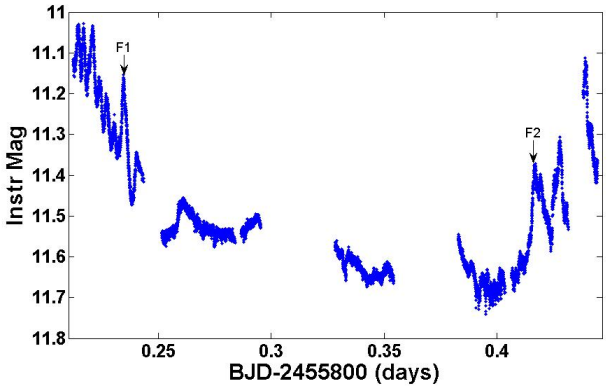

Figure 3.24: Instrumental magnitude light-curve for AE Aquarii for 2455800.2122 with data S/N of 250 and data length of 20082.14 s.

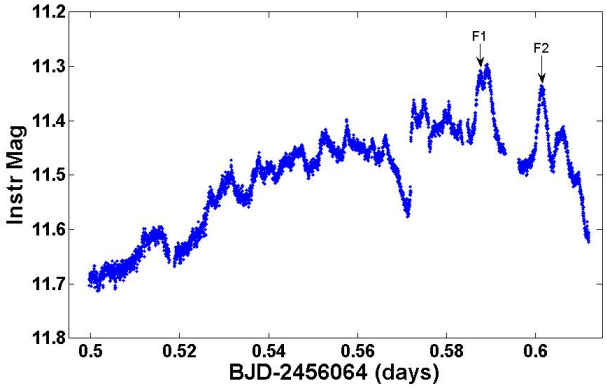

Figure 3.25: Instrumental magnitude light-curve for AE Aquarii for 2456064.4996 with data S/N of 272.72 and data length of 9712.22 s.

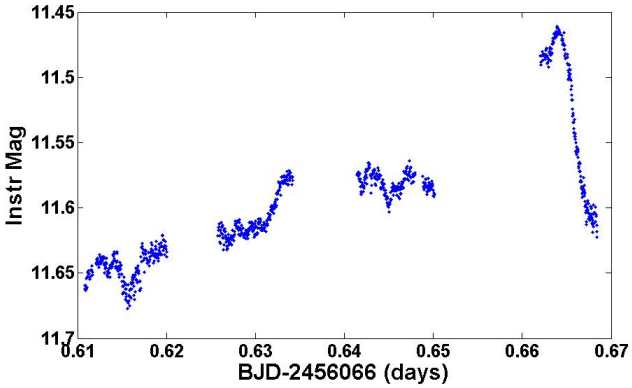

Figure 3.26: Instrumental magnitude light-curve for AE Aquarii for 2456066.6108 with data S/N of 250 and data length of 975.60 s.

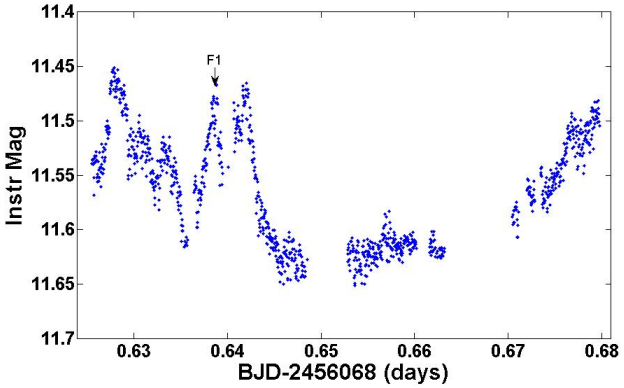

Figure 3.27: Instrumental magnitude light-curve for AE Aquarii for 2456068.6066 with data S/N of 200 and data length of 681.41 s.

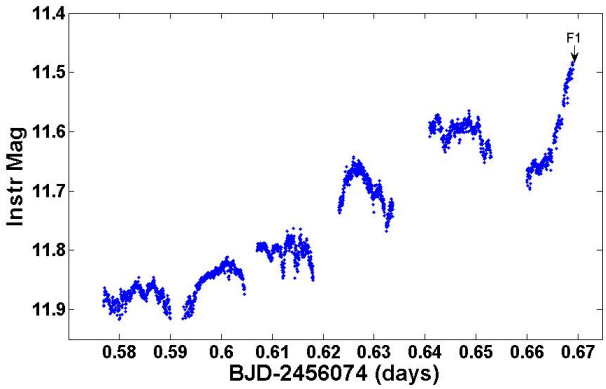

Figure 3.28: Instrumental magnitude light-curve for AE Aquarii for 2456074.5769 with data S/N of 250 and data length of 7957.35 s.

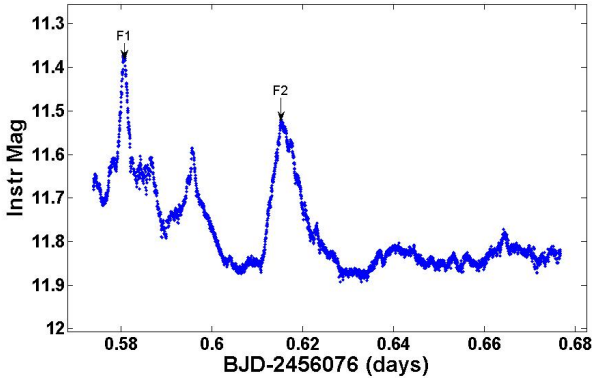

Figure 3.29: Instrumental magnitude light-curve for AE Aquarii for 2456076.5739 with data S/N of 266.99 and data length of 8894.84 s.

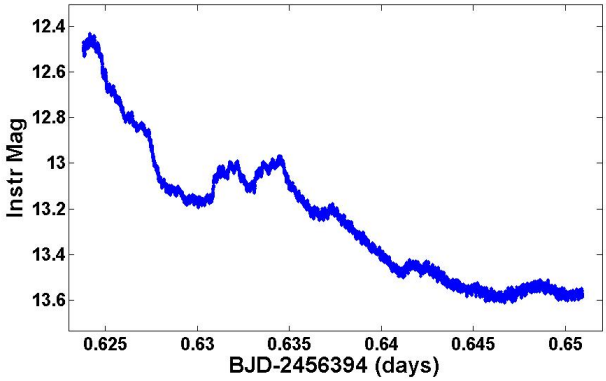

Figure 3.30: Instrumental magnitude light-curve for AE Aquarii for 2456394.6238 with data S/N of 300 and data length of 2342.17 s.

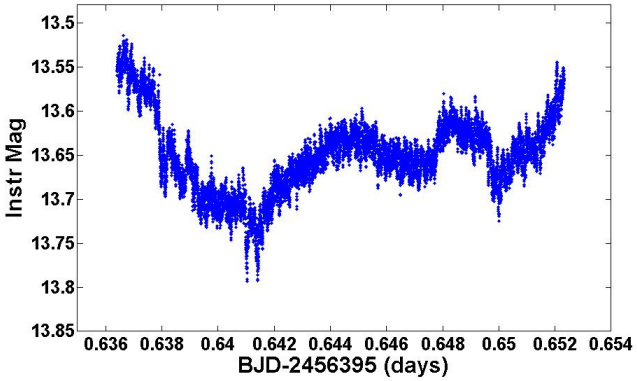

Figure 3.31: Instrumental magnitude light-curve for AE Aquarii for 2456395.6364 with data S/N of 300 and data length of 1374.69 s.

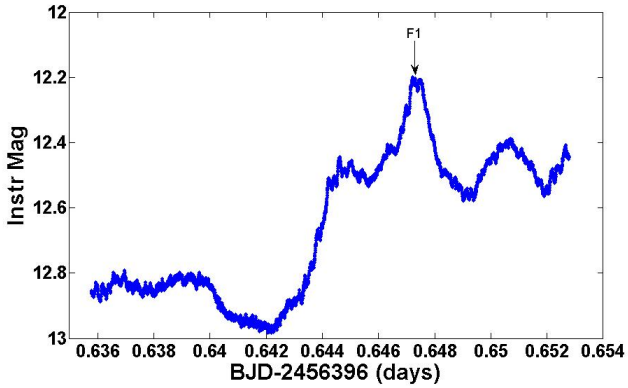

Figure 3.32: Instrumental magnitude light-curve for AE Aquarii for 2456396.6358 with data S/N of 300 and data length of 1469.40 s.

3.4 Flaring activity

The highly variable nature of AE Aquarii can clearly be discerned from the light-curves, for instance on 2455365 and 2455373 after strong singular flares, it became fairly quiescent, while on 2455781 and 2455785 it showed strong and rapid flaring activity. There is also a large scale sinusoidal structure visible in the data that corresponds to the ellipsoidal variation of the secondary star due to its orbital motion, as well as smaller scale variability that corresponds to the rotational period of the primary star seen as a low amplitude variation.

From previous studies (Meintjes (2004); Hill et al. (2014)), the flaring variability in AE Aquarii can be identified as the result of: Clumpy mass transfer from the secondary star that interacts with the WD magnetosphere upon closest approach after which the interacting blobs or fireballs are ejected from the system through the propeller effect. The physics involved in these mechanisms can thus be characterised through measurement and analysis of these flares. Also, with the primary component of this study being the search for VHE non-thermal pulsed emission from AE Aquarii, together with the case made by Meintjes et al. (1994) that the strongest possibility for detection of VHE $\gamma-$ray emission occurs just before the onset of strong optical flares, the strongest flares were characterised for the purpose of searching for possible VHE emission in the *Fermi*-LAT and AGILE-GRID data.

The selection of suitable flares was performed as follows: First a visual inspection was made of the optical light-curves, with possible candidate flares identified and marked in sequence from left to right as F1, F2, F3 etc. (refer to light-curves in the previous section). The properties such as rise times and magnitude variation of the selected flares were then measured, with the rise time and Δmag defined from the start of the flare up to the flare peak. Secondly, the selected flares were reduced through further selection criteria by calculating the ratio between the flare peak strength and the flare rise time, and is represented by equation 3.1:

$$\text{Flare Strength Ratio} = \frac{\Delta\text{mag}}{\text{Rise Time(s)}}(\times 1000). \tag{3.1}$$

Where the value of 1000 is simply a scaling factor. The FS Ratio defines a potency of the flare in terms of the production of possible non-thermal emission, i.e. the higher the ratio, the more rapid the flare event and the higher the possibility of rapid impulsive particle acceleration of non-thermal VHE emission (De Jager and Meintjes (1993); Meintjes et al. (1994)). A ratio limit of 0.5 was set based upon measured flare properties based on visual inspection (Refer to Figure 3.33 for a graphical representation of the selection criteria based upon the flare-strength (FS) ratio). Based upon the selection criteria, flares that are below the cut-off line are "Fast", while flares that are above the cut-off line are "Slow". And it is these "Fast" rapid flare events that could possibly be the result of a more energetic interaction. In addition, for clarity, a histogram form of the selection criteria is also included, displayed in Figure 3.34.

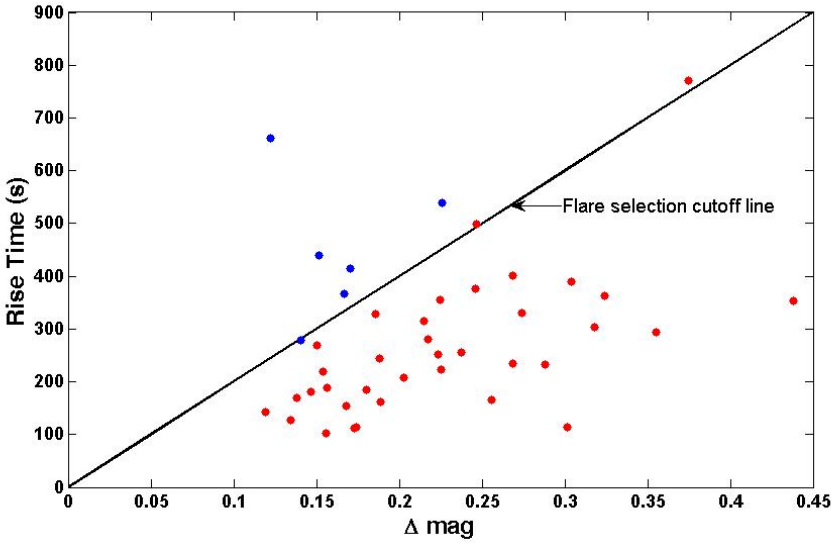

Figure 3.33: Graph of selection criteria for flares based on a FS-Ratio level of 0.5 for Rise time vs Δmag.

Finally the selected flares were inspected with the fringe candidates included or excluded based upon the shape of the flare. Upon inspection, two flares above the flare selection cut-off line were included while a single flare below the cut-off line was excluded. This selection criteria resulted in 36 flares selected for further

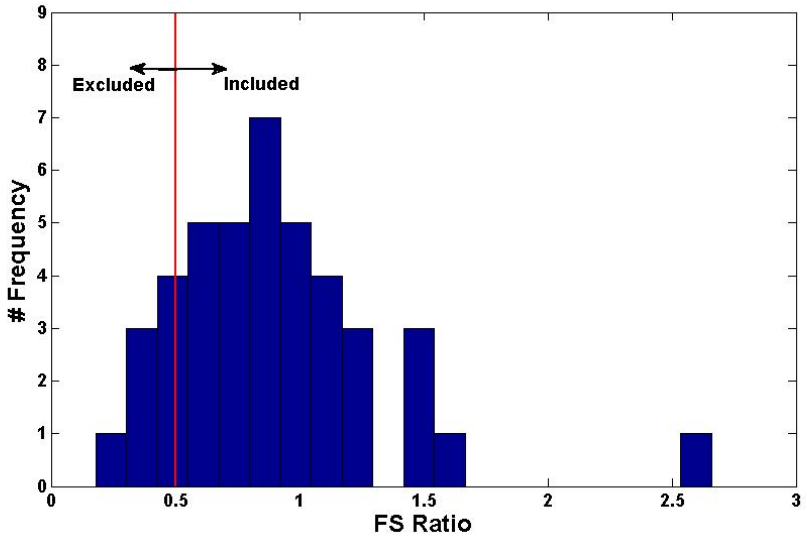

Figure 3.34: Histogram of FS Ratio used in selection criteria for flares based on a FS-Ratio level of 0.5 for Rise time vs Δmag.

analysis procedures. The measurements and properties of the 36 selected flares are tabulated in Table 3.3.

The duty cycle for the 36 selected flares from the observed datasets was calculated based upon the total rise time for all the selected flares within each dataset versus the dataset length, and is represented by equation 3.2:

$$\text{Duty Cycle}_{\text{dataset}} = \frac{\text{Total rise time (s)}}{\text{Dataset length (s)}}(\times 100\%). \tag{3.2}$$

The calculated duty cycle of the 36 selected flares is presented in Table 3.4.

The maximum duty cycle was for dataset 2456396 (MJD) at 7.7%, although considering the very short (1469.4 s) duration of the observation run it is not very significant. Considering however dataset 2455785 (MJD) which had a duty cycle of 7.1% for an observation run duration of 23469.32 s, it shows that instances of strong and continuous flaring of the kind identified for this study occurs within the system. On the other hand, some light-curves had a total lack of required flare events. The averaged flare distribution duty cycle for flares identified for this

Table 3.3: Measured properties, including rise times, magnitude variation and FS Ratio of the 36 selected flares. Table sorted on FS Ratio value.

JD-Dataset	Flare ID	Peak (day)	Rise Time (s)	M_{peak}	Δm	FS Ratio
2456396	F1	0.647212	113.53	12.20	0.30	2.66
2455782	F3	0.281804	111.46	11.28	0.17	1.55
2456076	F1	0.580829	165.97	11.37	0.26	1.54
2455784	F2	0.304019	113.10	11.19	0.17	1.54
2455365	F2	0.473791	102.73	11.14	0.16	1.52
2455365	F1	0.468217	231.81	11.07	0.29	1.24
2455784	F6	0.384687	353.72	11.18	0.44	1.24
2455406	F1	0.448542	294.88	11.25	0.36	1.20
2455800	F1	0.234524	161.22	11.15	0.19	1.17
2455406	F2	0.466053	235.35	10.88	0.27	1.14
2455784	F5	0.365026	155.00	11.43	0.17	1.09
2455784	F1	0.279786	126.92	11.21	0.13	1.06
2455781	F1	0.276521	304.30	11.23	0.32	1.04
2455785	F1	0.252483	223.08	11.22	0.23	1.01
2455782	F2	0.275488	183.86	11.30	0.18	0.98
2455429	F1	0.235275	206.84	11.16	0.20	0.98
2455799	F2	0.396405	255.57	11.28	0.24	0.93
2456076	F2	0.615170	362.71	11.52	0.32	0.89
2455350	F2	0.527510	251.60	11.16	0.22	0.89
2456064	F1	0.587499	143.16	11.31	0.12	0.83
2455782	F4	0.468104	187.92	11.23	0.16	0.83
2455394	F1	0.446755	330.65	11.12	0.27	0.83
2456064	F2	0.601277	169.52	11.34	0.14	0.82
2455784	F3	0.340876	181.09	11.39	0.15	0.81
2455443	F2	0.420561	390.01	11.03	0.30	0.78
2455785	F4	0.386897	280.63	11.26	0.22	0.77
2455784	F4	0.346125	244.51	11.32	0.19	0.77
2455793	F1	0.314039	218.42	11.42	0.15	0.71
2455443	F1	0.410994	314.15	11.19	0.21	0.68
2455785	F3	0.376436	401.41	11.17	0.27	0.67
2455800	F2	0.417150	377.14	11.37	0.25	0.65
2455782	F1	0.267651	355.62	11.33	0.22	0.63
2455373	F1	0.441553	328.92	11.25	0.19	0.56
2455443	F3	0.428415	268.53	11.15	0.15	0.56
2455799	F1	0.225298	499.05	11.36	0.25	0.49
2455785	F2	0.362763	770.60	11.14	0.37	0.49

Table 3.4: Duty cycle for the 36 selected flare events in the corresponding light-curve datasets based upon total rise-time versus dataset length.

Dataset (MJD)	Length (s)	Flares	Total Risetime (s)	Duty Cycle (%)
2455350	6067.61	1	251.60	4.1
2455355	6845.9	0	0.00	0.0
2455365	10422.2	2	334.54	3.2
2455373	17167.28	1	328.92	1.9
2455394	14594.34	1	330.65	2.3
2455406	17522.81	2	530.24	3.0
2455429	22871.81	1	206.84	0.9
2455443	19810.67	3	972.69	4.9
2455781	25864.36	1	304.30	1.2
2455782	23503.91	4	838.86	3.6
2455784	24100.48	6	1174.35	4.9
2455785	23469.32	4	1675.73	7.1
2455793	22609.28	1	218.42	1.0
2455798	22604.58	0	0.00	0.0
2455799	22426.59	2	754.62	3.4
2455800	20082.14	2	538.36	2.7
2456064	9712.22	2	312.68	3.2
2456066	975.6	0	0.00	0.0
2456068	681.41	0	0.00	0.0
2456069	2134.25	0	0.00	0.0
2456074	7957.35	0	0.00	0.0
2456076	8894.84	2	528.68	5.9
2456394	2342.17	0	0.00	0.0
2456395	1374.69	0	0.00	0.0
2456396	1469.4	1	113.53	7.7

study for the total observed time of all the light-curves was also calculated, i.e.:

$$\begin{aligned}\text{Duty Cycle}_{\text{total}} &= \frac{\text{Total Flare Rise Time}}{\text{Total Observed Time}}(\times 100\%) \\ &= \frac{9415.008 \text{ seconds}}{335505.21 \text{ seconds}}(\times 100\%) \\ &= 2.81\%\end{aligned}$$

The duty cycle per orbit (how many flares per orbit) was also calculated as follows. The average length for the 25 observation runs considered during the analysis was 13420.21 seconds, which was ~ 0.377 P_{orbit}. For the 36 flares selected for analysis, with an average flare rise time of 376.6 seconds, the flare duty cycle per orbit was then calculated as:

$$\begin{aligned}\text{Duty Cycle}_{\text{orbit}} &= \frac{\text{Average Flare Rise Time}}{\text{Average Observed Time} \times 2.65}(\times 100\%) \\ &= \frac{376.6 \text{ seconds}}{13420.21 \text{ seconds} \times 2.65}(\times 100\%) \\ &= 1.06\%\end{aligned}$$

The 36 selected flares were thereafter used as reference points in searching for *Fermi* photon events for possible detection of pulsed/unpulsed VHE $\gamma-$ ray emission. Refer to Section 5.4 for a detailed discussion. The selected flares are also included for visual reference in the same sequence as in Table 3.3. See Figures 3.35 to Figures 3.70. Additional optical analysis and characterisation of the flares is possible, but lies beyond the scope of this study and is therefore reserved for future studies.

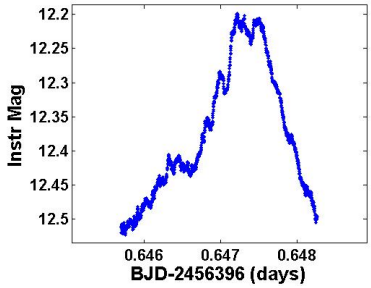

Figure 3.35: Flare 1 for 2456396 with rise-time of 113.53 s and Δmag of 0.302.

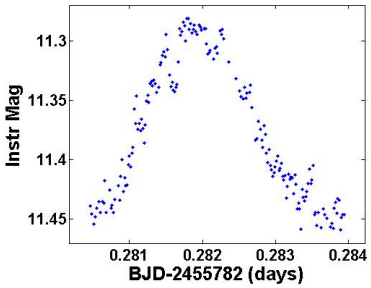

Figure 3.36: Flare 3 for 2455782 with rise-time of 111.46 s and Δmag of 0.173.

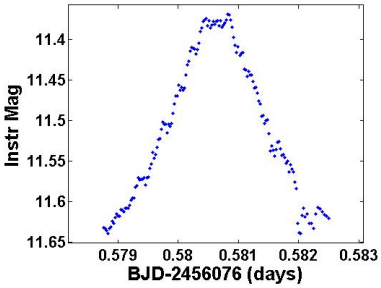

Figure 3.37: Flare 1 for 2456076 with rise-time of 165.97 s and Δmag of 0.256.

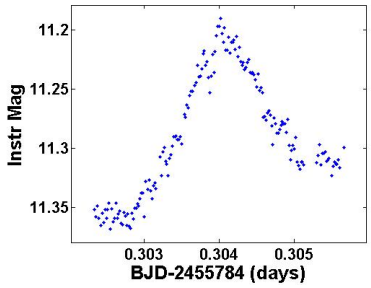

Figure 3.38: Flare 2 for 2455784 with rise-time of 113.10 s and Δmag of 0.174.

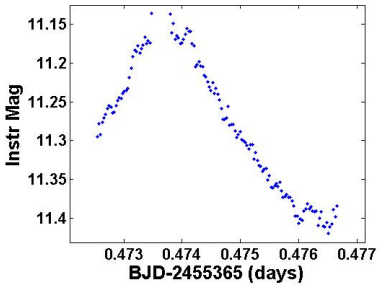

Figure 3.39: Flare 2 for 2455365 with rise-time of 102.730 s and Δmag of 0.156.

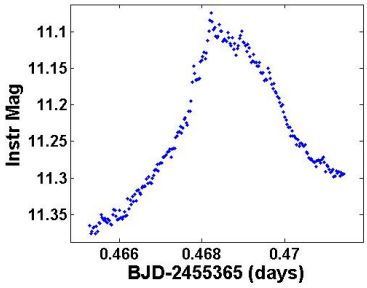

Figure 3.40: Flare 1 for 2455365 with rise-time of 231.811 s and Δmag of 0.288.

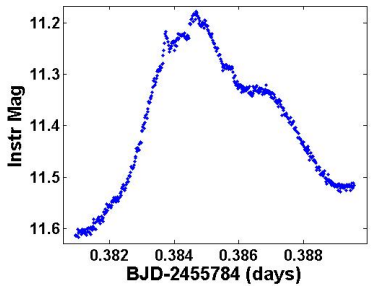

Figure 3.41: Flare 6 for 2455784 with rise-time of 353.722 s and Δmag of 0.438.

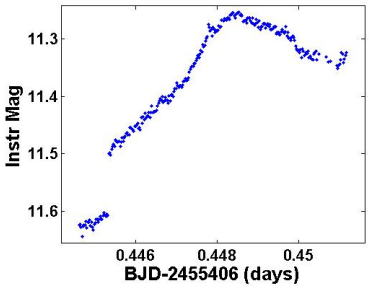

Figure 3.42: Flare 1 for 2455406 with rise-time of 294.883 s and Δmag of 0.355.

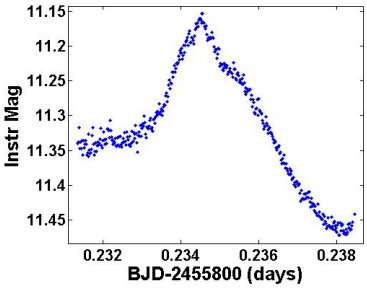

Figure 3.43: Flare 1 for 2455800 with rise-time of 161.222 s and Δmag of 0.189.

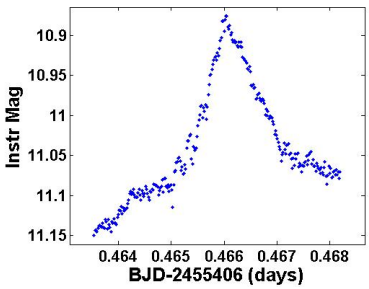

Figure 3.44: Flare 2 for 2455406 with rise-time of 235.354 s and Δmag of 0.269.

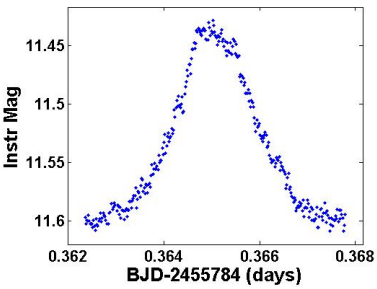

Figure 3.45: Flare 5 for 2455784 with rise-time of 155.002 s and Δmag of 0.168.

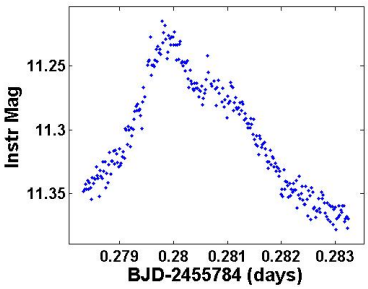

Figure 3.46: Flare 1 for 2455784 with rise-time of 126.922 s and Δmag of 0.135.

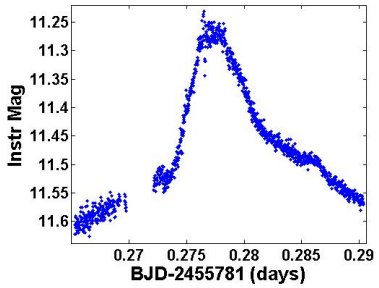

Figure 3.47: Flare 1 for 2455781 with rise-time of 304.301 s and Δmag of 0.318.

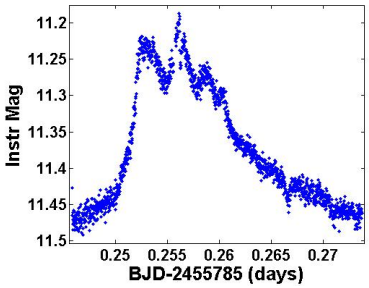

Figure 3.48: Flare 1 for 2455785 with rise-time of 223.085 s and Δmag of 0.225.

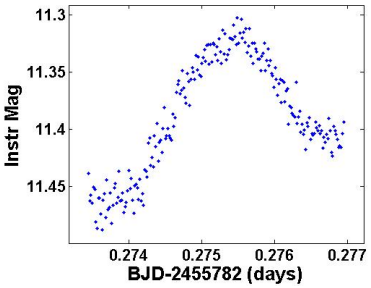

Figure 3.49: Flare 2 for 2455782 with rise-time of 183.859 s and Δmag of 0.180.

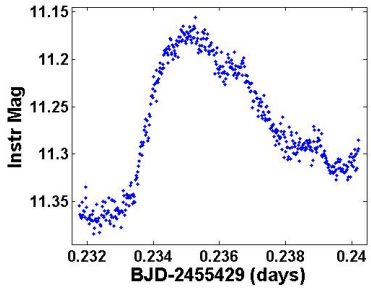

Figure 3.50: Flare 1 for 2455429 with rise-time of 206.842 s and Δmag of 0.203.

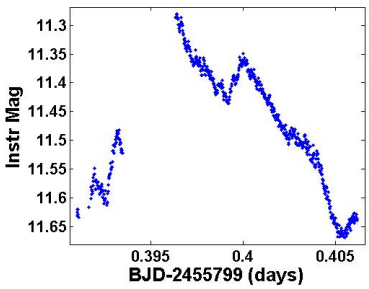

Figure 3.51: Flare 2 for 2455799 with rise-time of 255.571 s and Δmag of 0.238.

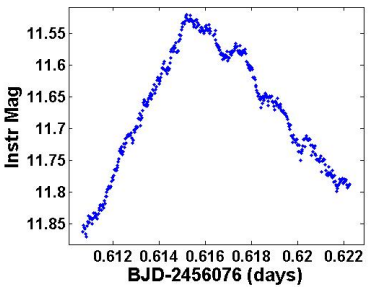

Figure 3.52: Flare 2 for 2456076 with rise-time of 362.707 s and Δmag of 0.324.

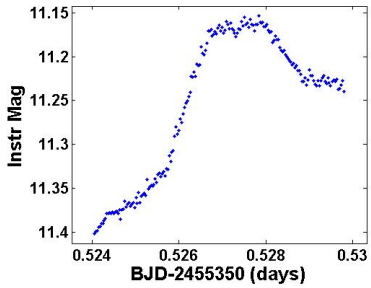

Figure 3.53: Flare 2 for 2455350 with rise-time of 251.597 s and Δmag of 0.224.

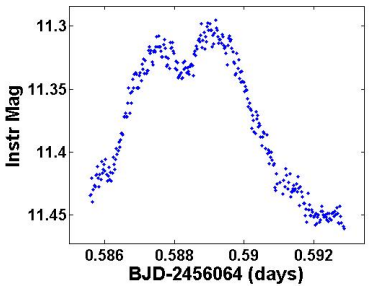

Figure 3.54: Flare 1 for 2456064 with rise-time of 143.165 s and Δmag of 0.119.

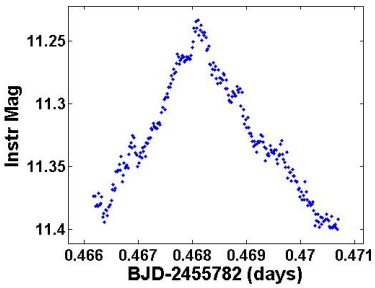

Figure 3.55: Flare 4 for 2455782 with rise-time of 187.920 s and Δmag of 0.156.

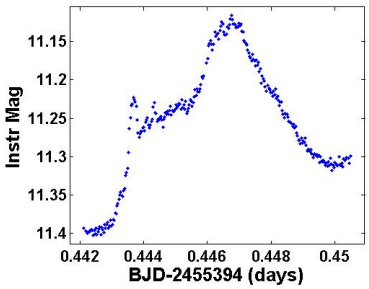

Figure 3.56: Flare 1 for 2455394 with rise-time of 330.653 s and Δmag of 0.274.

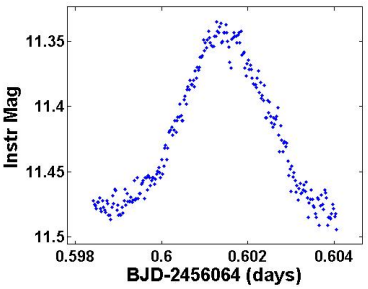

Figure 3.57: Flare 2 for 2456064 with rise-time of 169.517 s and Δmag of 0.138.

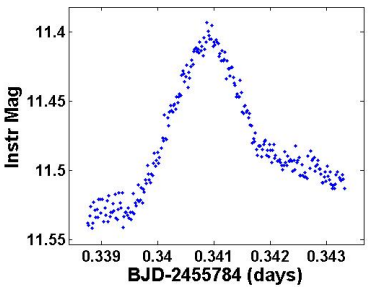

Figure 3.58: Flare 3 for 2455784 with rise-time of 181.094 s and Δmag of 0.146.

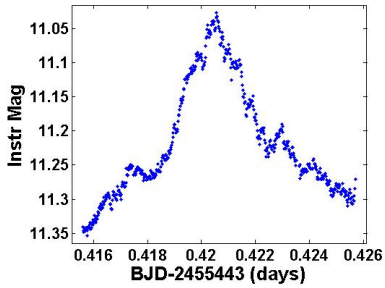

Figure 3.59: Flare 2 for 2455443 with rise-time of 390.010 s and Δmag of 0.304.

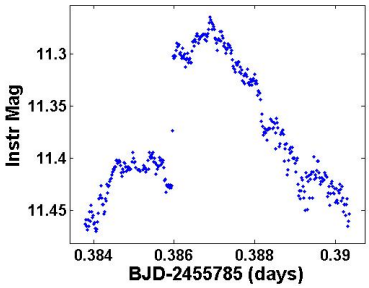

Figure 3.60: Flare 4 for 2455785 with rise-time of 280.627 s and Δmag of 0.217.

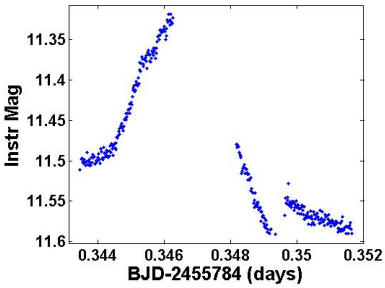

Figure 3.61: Flare 4 for 2455784 with rise-time of 244.512 s and Δmag of 0.188.

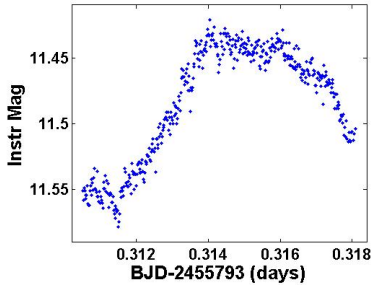

Figure 3.62: Flare 1 for 2455793 with rise-time of 218.419 s and Δmag of 0.154.

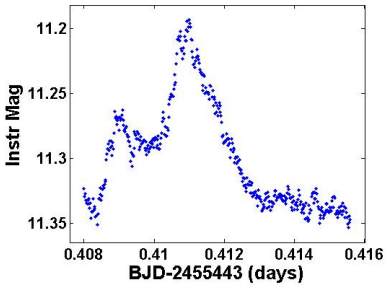

Figure 3.63: Flare 1 for 2455443 with rise-time of 314.150 s and Δmag of 0.215.

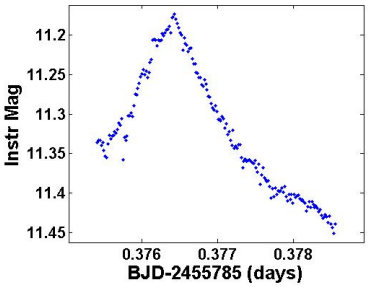

Figure 3.64: Flare 3 for 2455785 with rise-time of 401.414 s and Δmag of 0.269.

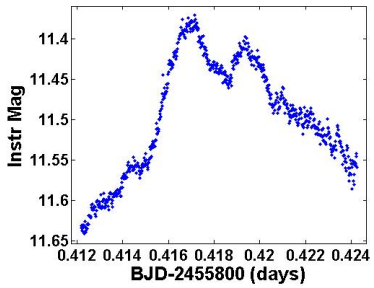

Figure 3.65: Flare 2 for 2455800 with rise-time of 377.136 s and Δmag of 0.246.

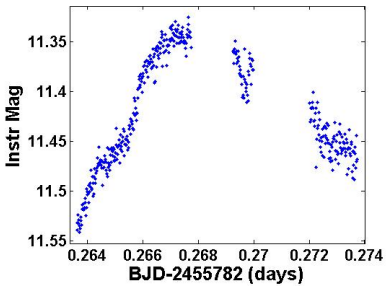

Figure 3.66: Flare 1 for 2455782 with rise-time of 355.622 s and Δmag of 0.225.

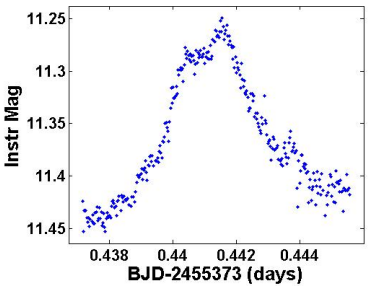

Figure 3.67: Flare 1 for 2455373 with rise-time of 328.925 s and Δmag of 0.185.

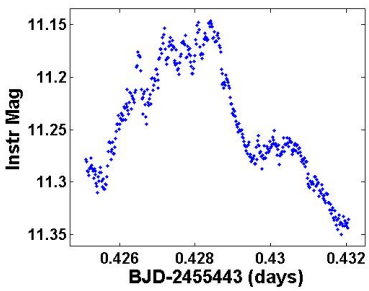

Figure 3.68: Flare 3 for 2455443 with rise-time of 268.531 s and Δmag of 0.150.

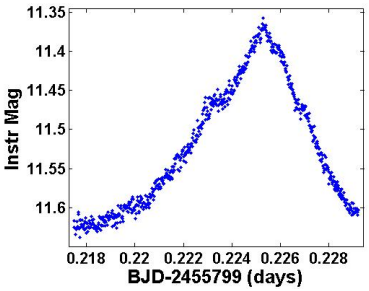

Figure 3.69: Flare 1 for 2455799 with rise-time of 499.046 s and Δmag of 0.247.

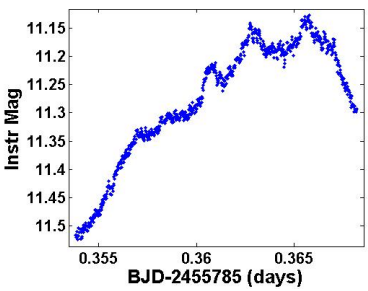

Figure 3.70: Flare 2 for 2455785 with rise-time of 770.602 s and Δmag of 0.375.

3.5 Time series analysis

Timing analysis in terms of the WD spin period was performed on the time-corrected optical light-curve data for each observation set respectively. The timing analysis of the light-curves was performed using an independent package "Period" (Version 5.0-2) available in the Starlink (Version star-hawaiki) astronomy software tools. A Lomb-Scargle analysis was performed using a minimum frequency = 0.01 Hz, maximum frequency = 0.1 Hz and a frequency interval = 5×10^{-6} Hz. The frequency interval was chosen because of the variable nature of the lengths of the observations, with the software defined standard frequency interval nominally determined as $f_{int} = 1/(4 \times$ Data set lenght (s)). The maximum frequency is as a standard defined by the Nyquist critical frequency, which is nominally defined as $f_{Ny} = 1/(2 \times$ Smallest sampling interval (s)), but with the medium sampling interval for the data-sets varying between $2 - 2.5$ s for the Boyden data and 1.25 s for the re-sampled SAAO data, the Nyquist frequency range is $f_{Ny} = 0.25 - 0.2$ Hz for the Boyden data and 0.4 Hz for the SAAO data. This is beyond the required range for the frequencies of interest, as the fundamental frequency (F_0) and first harmonic ($2F_0$) is within the frequency range $0.01 - 0.1$ Hz. The output from these analyses were subsequently plotted, with the fundamental frequency (F_0) and first harmonic ($2F_0$) of the current WD spin ephemeris model indicated in red, and 4σ in terms of the Lomb-Scargle peak power, for the selected frequency range, indicated by a black line. These periodograms (in frequency space) are presented in Figures 3.71 to 3.95.

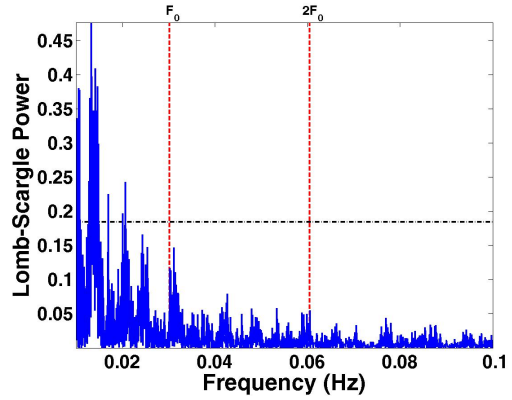

Figure 3.71: Lomb-Scargle power spectrum for AE Aquarii for 2455350.4741 at frequency resolution of 5×10^{-6} Hz.

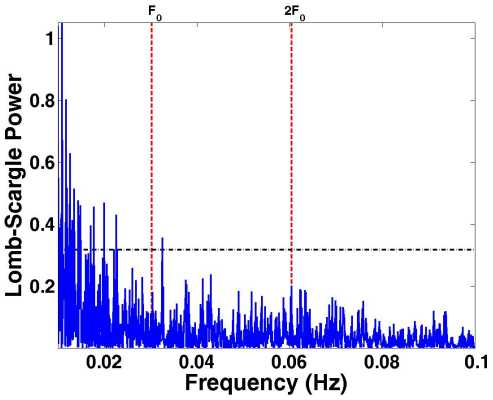

Figure 3.72: Lomb-Scargle power spectrum for AE Aquarii for 2455355.4710 at frequency resolution of 5×10^{-6} Hz.

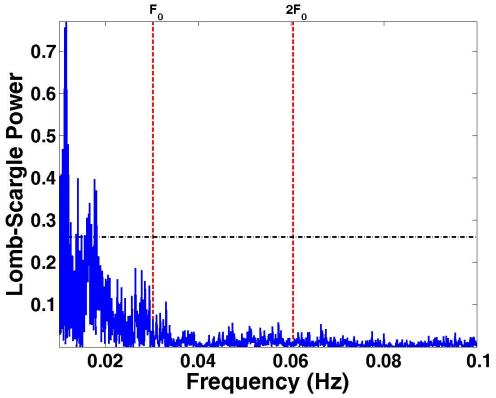

Figure 3.73: Lomb-Scargle power spectrum for AE Aquarii for 2455365.4411 at frequency resolution of 5×10^{-6} Hz.

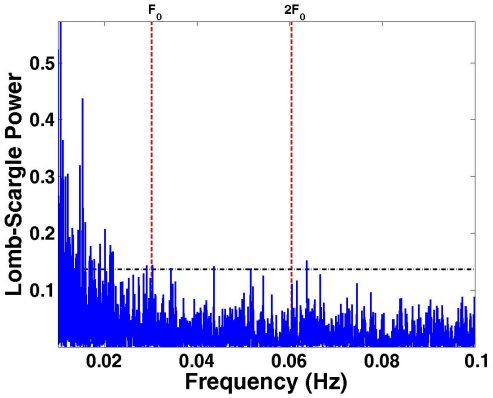

Figure 3.74: Lomb-Scargle power spectrum for AE Aquarii for 2455373.4195 at frequency resolution of 5×10^{-6} Hz.

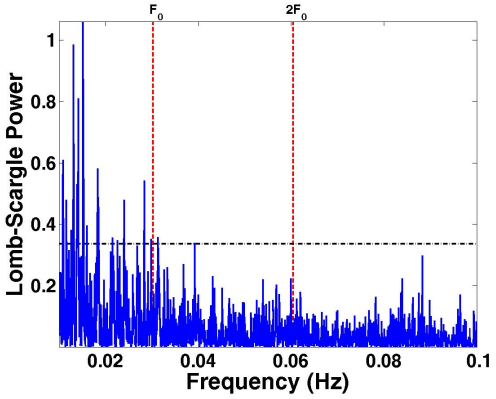

Figure 3.75: Lomb-Scargle power spectrum for AE Aquarii for 2455394.3427 at frequency resolution of 5×10^{-6} Hz.

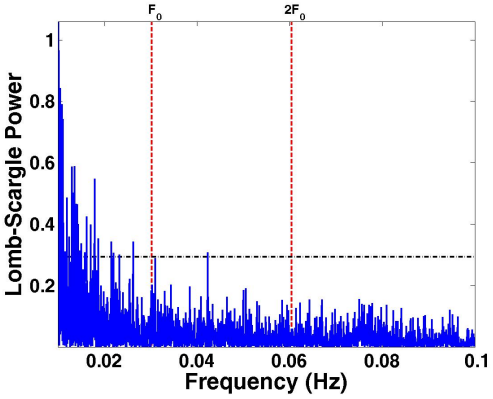

Figure 3.76: Lomb-Scargle power spectrum for AE Aquarii for 2455406.3229 at frequency resolution of 5×10^{-6} Hz.

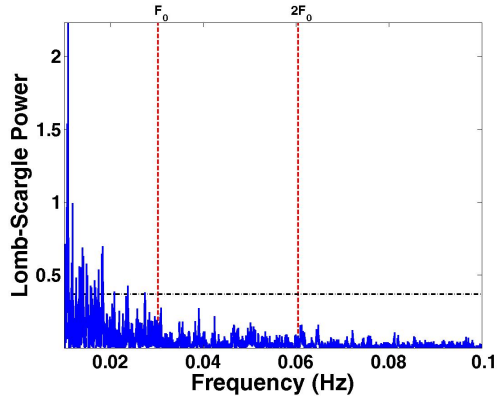

Figure 3.77: Lomb-Scargle power spectrum for AE Aquarii for 2455429.2207 at frequency resolution of 5×10^{-6} Hz.

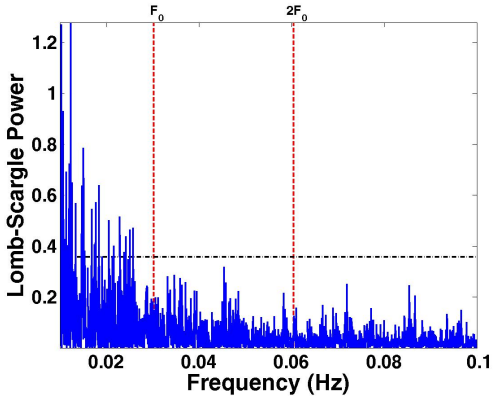

Figure 3.78: Lomb-Scargle power spectrum for AE Aquarii for 2455443.1979 at frequency resolution of 5×10^{-6} Hz.

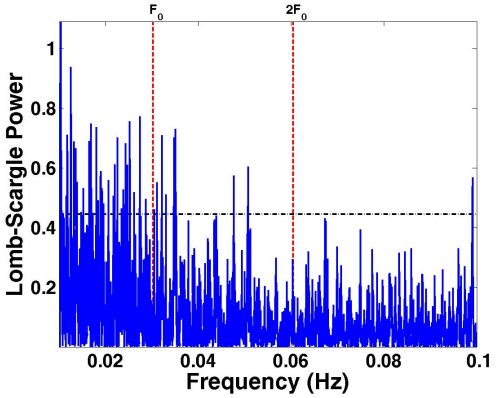

Figure 3.79: Lomb-Scargle power spectrum for AE Aquarii for 2455781.2175 at frequency resolution of 5×10^{-6} Hz.

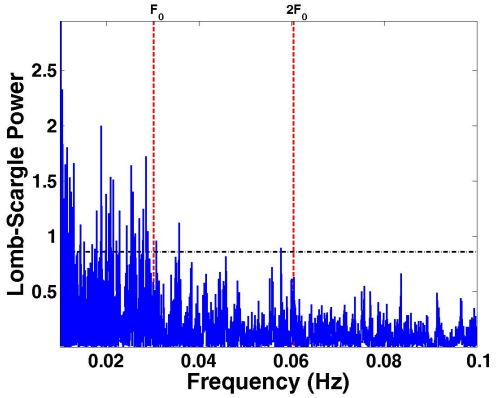

Figure 3.80: Lomb-Scargle power spectrum for AE Aquarii for 2455782.2204 at frequency resolution of 5×10^{-6} Hz.

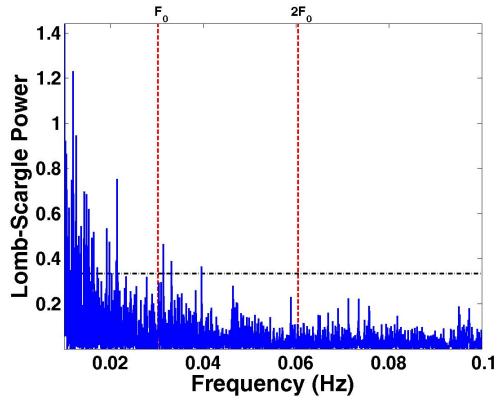

Figure 3.81: Lomb-Scargle power spectrum for AE Aquarii for 2455784.2105 at frequency resolution of 5×10^{-6} Hz.

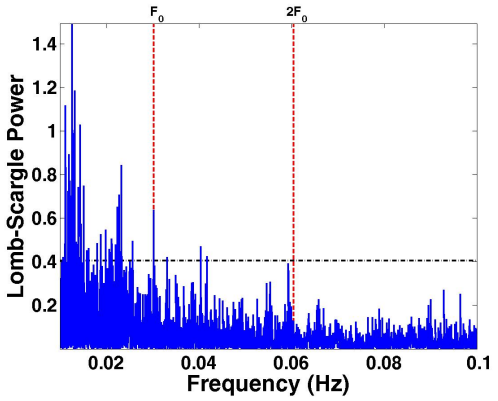

Figure 3.82: Lomb-Scargle power spectrum for AE Aquarii for 2455785.2050 at frequency resolution of 5×10^{-6} Hz.

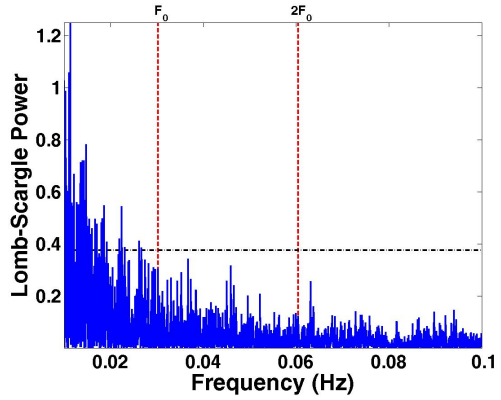

Figure 3.83: Lomb-Scargle power spectrum for AE Aquarii for 2455793.2119 at frequency resolution of 5×10^{-6} Hz.

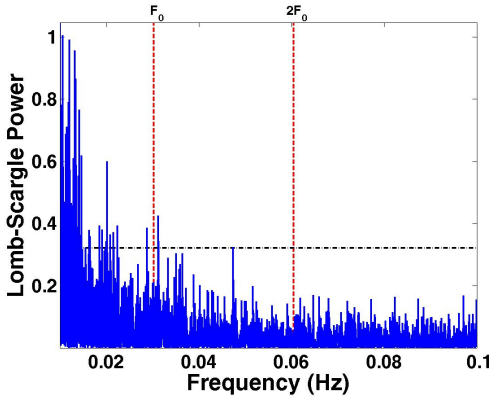

Figure 3.84: Lomb-Scargle power spectrum for AE Aquarii for 2455798.1997 at frequency resolution of 5×10^{-6} Hz.

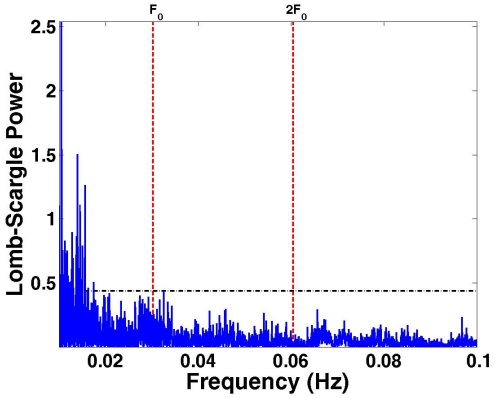

Figure 3.85: Lomb-Scargle power spectrum for AE Aquarii for 2455799.2027 at frequency resolution of 5×10^{-6} Hz.

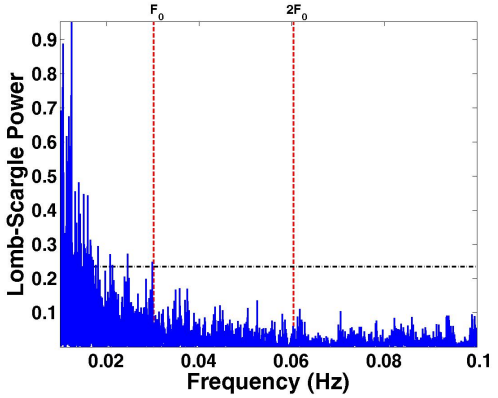

Figure 3.86: Lomb-Scargle power spectrum for AE Aquarii for 2455800.2070 at frequency resolution of 5×10^{-6} Hz.

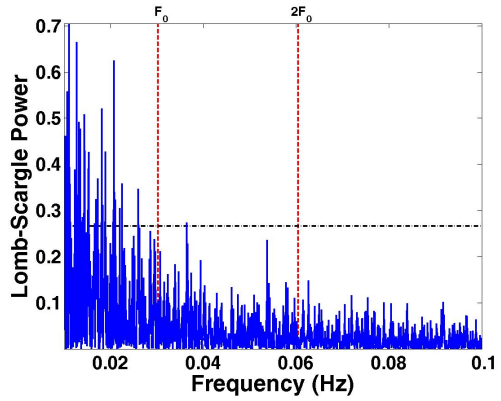

Figure 3.87: Lomb-Scargle power spectrum for AE Aquarii for 2456064.4982 at frequency resolution of 5×10^{-6} Hz.

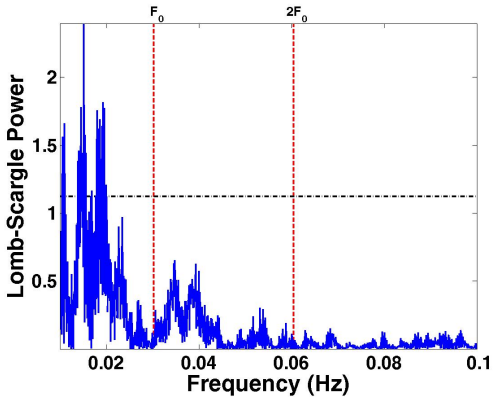

Figure 3.88: Lomb-Scargle power spectrum for AE Aquarii for 2456066.6092 at frequency resolution of 5×10^{-6} Hz.

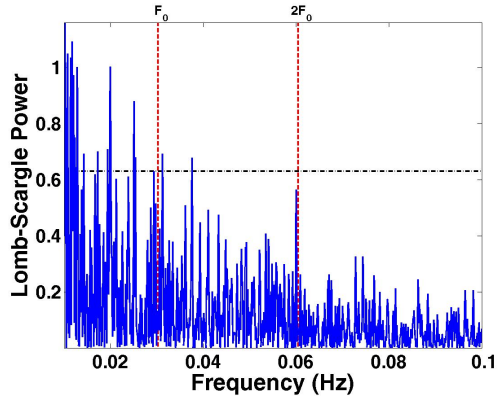

Figure 3.89: Lomb-Scargle power spectrum for AE Aquarii for 2456068.6048 at frequency resolution of 5×10^{-6} Hz.

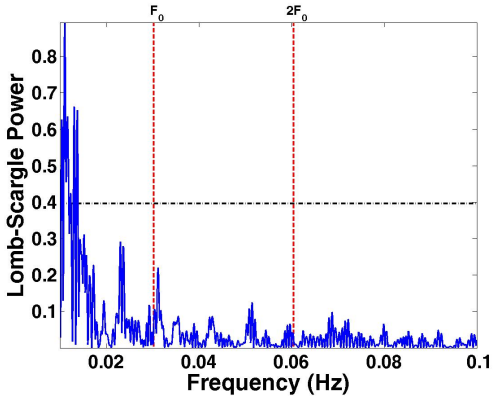

Figure 3.90: Lomb-Scargle power spectrum for AE Aquarii for 2456069.5846 at frequency resolution of 5×10^{-6} Hz.

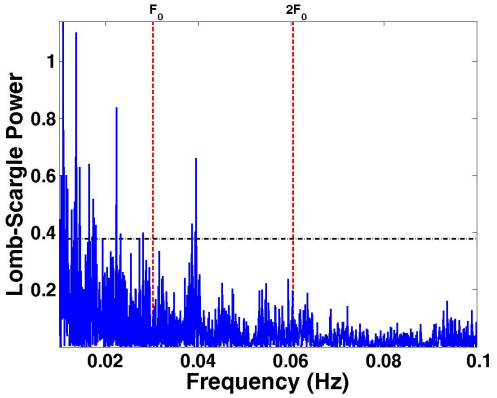

Figure 3.91: Lomb-Scargle power spectrum for AE Aquarii for 2456074.5735 at frequency resolution of 5×10^{-6} Hz.

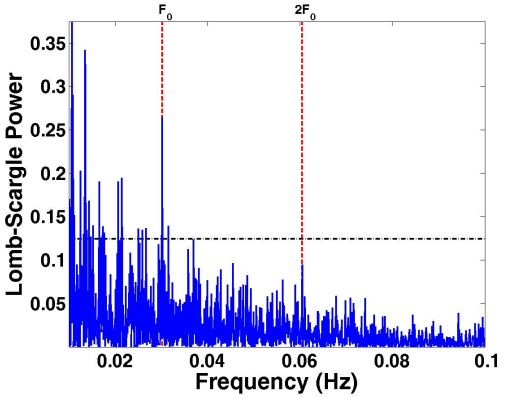

Figure 3.92: Lomb-Scargle power spectrum for AE Aquarii for 2456076.5714 at frequency resolution of 5×10^{-6} Hz.

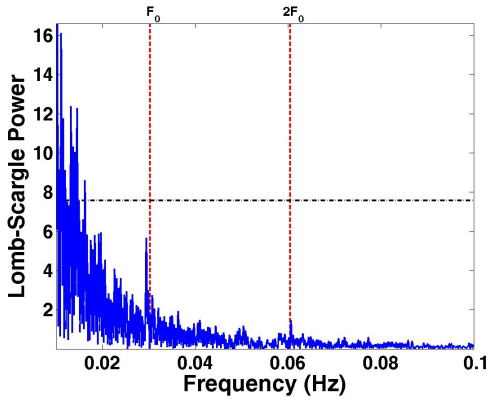

Figure 3.93: Lomb-Scargle power spectrum for AE Aquarii for 2456394.6238 at frequency resolution of 5×10^{-6} Hz.

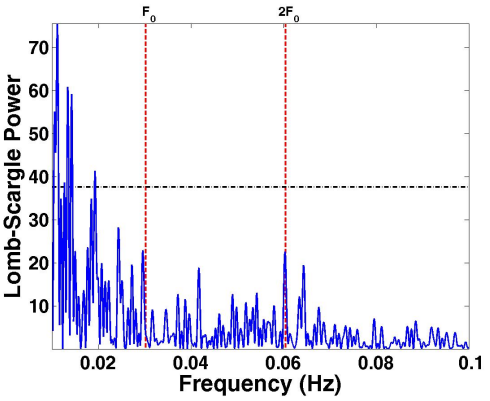

Figure 3.94: Lomb-Scargle power spectrum for AE Aquarii for 2456395.6364 at frequency resolution of 5×10^{-6} Hz.

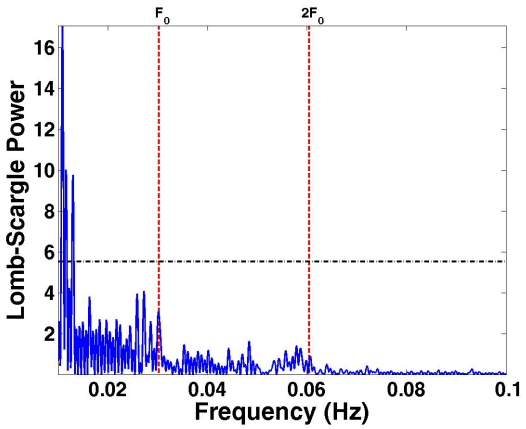

Figure 3.95: Lomb-Scargle power spectrum for AE Aquarii for 2456396.6358 at frequency resolution of 5×10^{-6} Hz.

The Lomb-Scargle periodograms shows an almost complete lack of spin power at F_0 and $2F_0$ above 4σ in the different data-sets. Even though the pulsed amplitude of the spin period varies between 0.2-0.3%, and up to 1% during optical flaring (Patterson (1979)), a greater number of periodograms were expected to show spin power. The presence of spin power is expected considering the origin of the 33 s pulsed emission is due to the interaction of the magneto-spheric propeller with the in-falling mass from the donor star at the magnetosphere radius. The contributions from the "front" facing hot polar region as well as the propeller ejected gas illuminated by the second pole should not only result in an observable F_0 spin power, but in an even stronger $2F_0$ spin power.

The lack of power could possibly be explained as follows: The presence of stronger power peaks towards the shorter frequencies is indicative of the large amount of flickering and flaring present in the light-curves. Therefore, the lack of power for F_0 and $2F_0$ in specifically the Boyden data is possibly because of the nature of the observations, in that the observations were made using a C-filter (i.e. white light), that covers a broad wavelength regime, which would lead to dilation of the signal due to the emission at longer optical wavelengths. This is also displayed by the difference in the power scales between the Boyden data and the SAAO data, which was observed using a B-filter, in that the Lomb-Scargle power between $0.01 - 0.1$ Hz for the SAAO data is significantly higher than for the Boyden

data. Or, alternatively, there is significantly less large scale structures, that could lead to "noise" at lower frequencies, present in the single filter SAAO data, than in the white-light C-filter Boyden data.

Analysis was performed on the power spectra that display power at F_0 and $2F_0$ above the 4σ line, or singular peaks without strong QPO-like features at F_0 and $2F_0$ (Figures 3.82, 3.92). The spin periods were measured at the peak centre, with the error in the period measured as $0.5 \times$ (FWHM) of the peak. The measured values were then tabulated in Table 3.5.

Table 3.5: Measured WD spin periods for selected optical data.

Dataset (JD)	P_0 (s)	P_0 Error (s)	$2P_0$ (s)	$2P_0$ Error (s)
2455785.2105	33.113	0.022	-	-
2456076.5739	33.124	0.055	-	-

The results of the optical observations presented have shown that AE Aquarii displays low to medium-level flaring activity during some observations that were made in the period it has been observed with *Fermi* and *AGILE*. Although there was a lack of power at the WD spin period and first harmonic in the timing analysis, some pulsed emission signatures, such as a possible increase in emission around the WD spin frequencies during stronger periods of flaring, was identified that can be searched for in *Suzaku*, *Fermi* and *AGILE* data. A discussion of *Suzaku* observations and analysis is presented in the following chapter.

Chapter 4

Analysis of *Suzaku* data to characterise X-ray emission from AE Aquarii

4.1 Introduction

The studies of the non-thermal hard X-ray component presented by Terada et al. (2007, 2008) and explored by Oruru and Meintjes (2012) sparked a renewed interest in the non-thermal emission at higher energies in AE Aquarii. The system shows strong features in the soft X-ray part of the EM spectrum, with models proposing multi-thermal emission mechanisms. The hard X-ray component however still has to be conclusively modelled. How the X-ray components (hard and soft) correlate with other wavelengths, specifically in relation to possible VHE $\gamma-$ray emission had to be investigated. To this end, an analysis of the X-ray emission that corresponds to the available data coverage time for the *Fermi* and *AGILE* telescopes was conducted. A search in the HEASARC data archive was performed for X-ray data that was available during the time in question. Usable data was available for *Swift* and *Suzaku*. The *Suzaku* data-set (ID 404001010) was chosen, as the *Swift* data had already been examined by Oruru and Meintjes (2012). Following is a detailed discussion of the analysis of the chosen data-set, for both the soft X-ray imaging spectrometer (XIS) data and the Hard X-ray detector (HXD) data. Both

data-sets were analysed for timing as well as spectral properties.

The Japanese *Suzaku* X-ray telescope was launched on 10 July 2005 into a low earth orbit (LEO) at an altitude of 550 km. The telescope has two active instruments, the "primary" XIS which has a high X-ray spectral resolution between 0.2-12 keV, and the HXD that has a energy range between 10-600 keV. General information, data archive access and detailed analysis guidelines can be accessed through *Suzaku* at HEASARC (http://heasarc.gsfc.nasa.gov/docs/suzaku/).

The XIS consists of four CCD sensors, and has a field of view (FOV) of $19' \times 19'$. The data from the XIS that are available for scientific purposes are from only three of the sensors (one CCD (XIS2) is unavailable), and are made available as **xis0**, **xis1** and **xis3** datasets in two editing modes of 3×3 pixels and 5×5 pixels. The sensors are also different in that xis0 and xis3 are front illuminated (FI) and xis1 is a back illuminated (BI) CCD sensor. Refer to Figure 4.1 for a graphical representation of the XIS CCD sensors. As can be seen, the sensors are orientated perpendicular to one another, and have to be considered together with the CCD type (FI or BI) when conducting analysis. The timing resolution of the XIS in timing mode is 7.8125 ms.

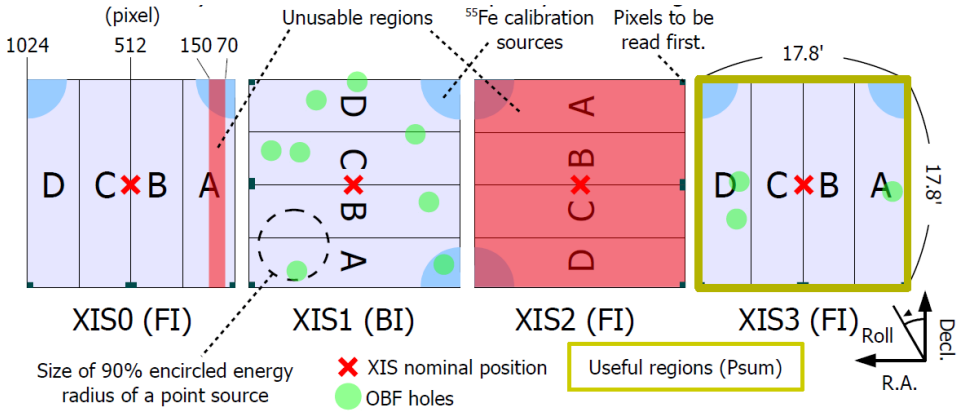

Figure 4.1: XIS sensors, with available sensor areas and calibration sections indicated (Adopted from http://heasarc.gsfc.nasa.gov/docs/suzaku/).

The HXD is a non-imaging instrument and consists of two independent sensor

components, the GSO (Gadolinium Silicate) phoswich counters (sensitive to energies above ~ 30 keV at an energy resolution of $7.6\sqrt{\mathrm{E}}\%$(FWHM) with E the photon energy in MeV) and the PIN silicon diode detectors (sensitive to energies below ~ 60 keV at a resolution of ~ 3.0 keV), that are configured in a "well" detector configuration (Figure 4.2). The FOV for the HXD is 0.65 deg $\times$ 0.56 deg ($\mathrm{E} < 100$ keV). The available scientific data are made available as **gso** and **pin** data-sets. The timing resolution of the HXD is a nominal 61 μs.

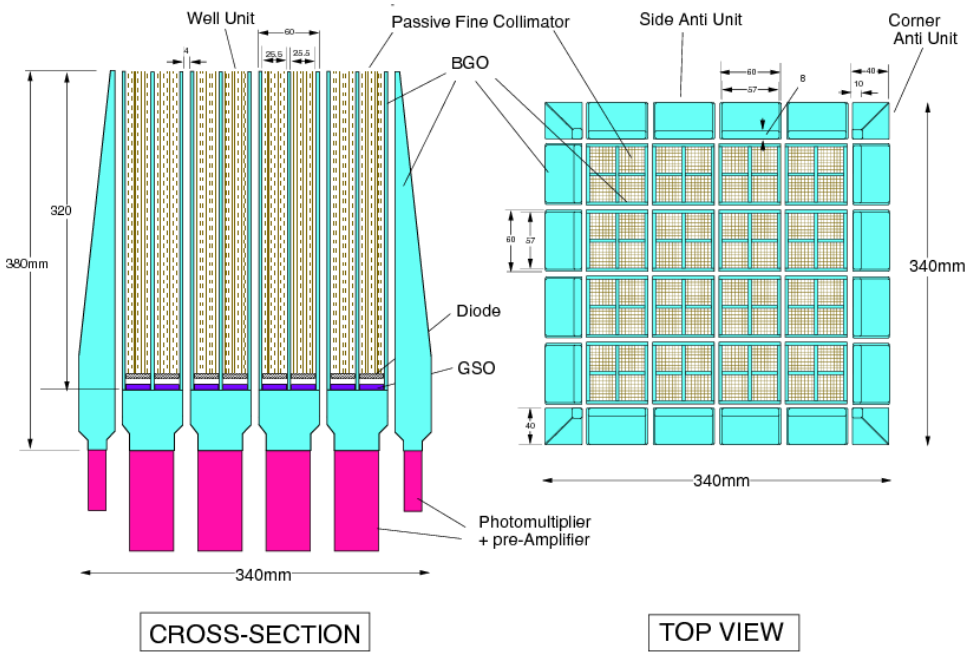

Figure 4.2: Graphical representation of the *Suzaku* HXD (Adopted from http://heasarc.gsfc.nasa.gov/docs/suzaku/).

4.2 XIS data analysis

Suzaku observed AE Aquarii between 2009-10-16 T18:17:04 and 2009-10-20 T05:26:13 for a total of 294159 s. The XIS preprocessed data were used for the analysis. Six data files were downloaded from the data archive site consisting of a 3×3 and 5×5 editing mode file for each of the XIS sensors (Table 4.1). A Fedora 20 (x86_64) Linux system was used for the data analysis utilizing the general and *Suzaku* specific tools available in the Heasoft v6.15.1 software package. These software packages and instruction manuals are freely available from the HEASARC website.

Table 4.1: List of XIS cleaned data files downloaded for analysis.

Filename
ae404001010xi0_0_3x3n112l_cl.evt.gz
ae404001010xi0_0_5x5n112l_cl.evt.gz
ae404001010xi1_0_3x3n112l_cl.evt.gz
ae404001010xi1_0_5x5n112l_cl.evt.gz
ae404001010xi3_0_3x3n112l_cl.evt.gz
ae404001010xi3_0_5x5n112l_cl.evt.gz

The data files were analysed as follows. The xis0 files are considered for the discussion. Using "XSELECT" (Version 2.4c) the events for each of the xis0 detector editing modes were read. An image was extracted for the combined data for visual inspection and selection of analysis regions of interest. The extraction of data for combined analysis, even though the two data files have different editing modes, is possible since only the central 3×3 pixel information is used during conventional extraction and analysis procedures. Figure 4.3 displays the extracted image for xis0 at a default binning value of 16 s. From the image, a region for the source (AE Aquarii) as well as a background region were selected for "filter region" selection in "XSELECT" for more specific analyses. Refer to Figure 4.4 for the selected source (AE Aquarii) region.

A spectrum, light-curve and image were extracted for each filtered region using

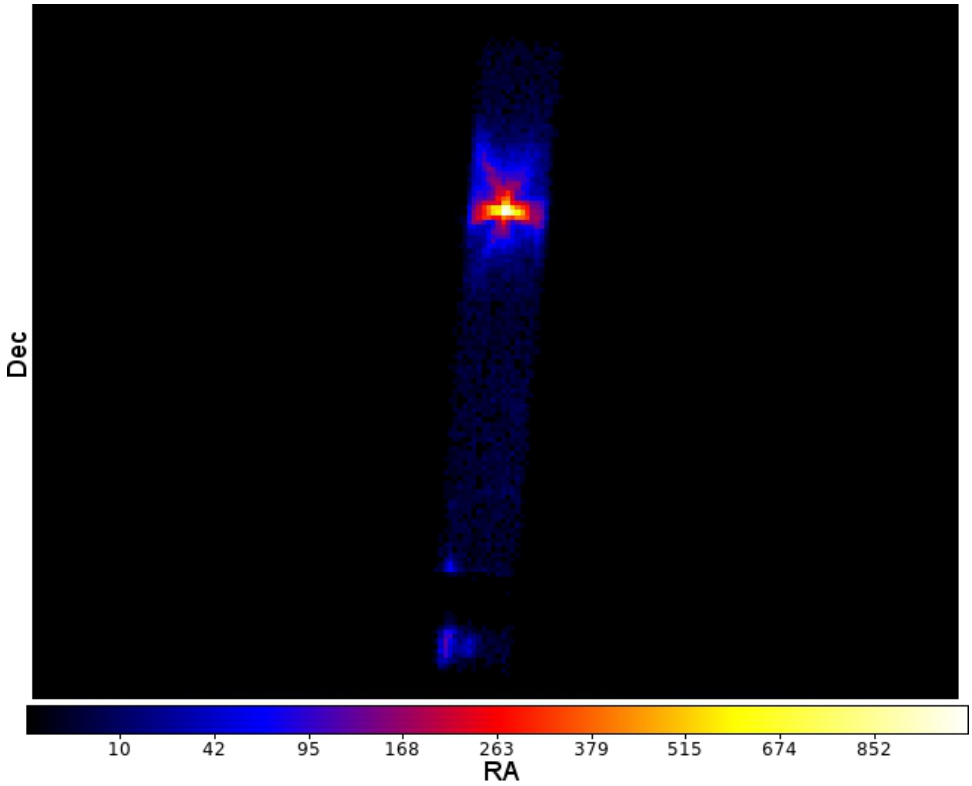

Figure 4.3: Extracted image for xis0 data at a default binned value of 16 s for AE Aquarii. The colour bar indicates the normalised counts levels.

the command "extract all". Two different binning values were used during the extraction of the light-curves for analysis purposes, i.e. 1 s and 168.06 s. The former was chosen for very accurate timing analysis of the WD spin period, and is the nominal smallest time resolution available from the data. The latter was chosen not only for a check of the extracted light-curve against the quick look curves (Figure 4.5) available in the data archives, but also for additional examination of the flaring activities in the X-ray emission. The same procedure and binning values were also used to extract background spectra, curves and images. The source light-curves were background corrected by subtracting the manually-scaled background light-curves specific to each data-set. The background light-curves had to be scaled, since for *Suzaku* the total area of the coordinate space is different between sky and detector coordinates, with the region files used during the filtering process having sky coordinates. This means the regions for source and

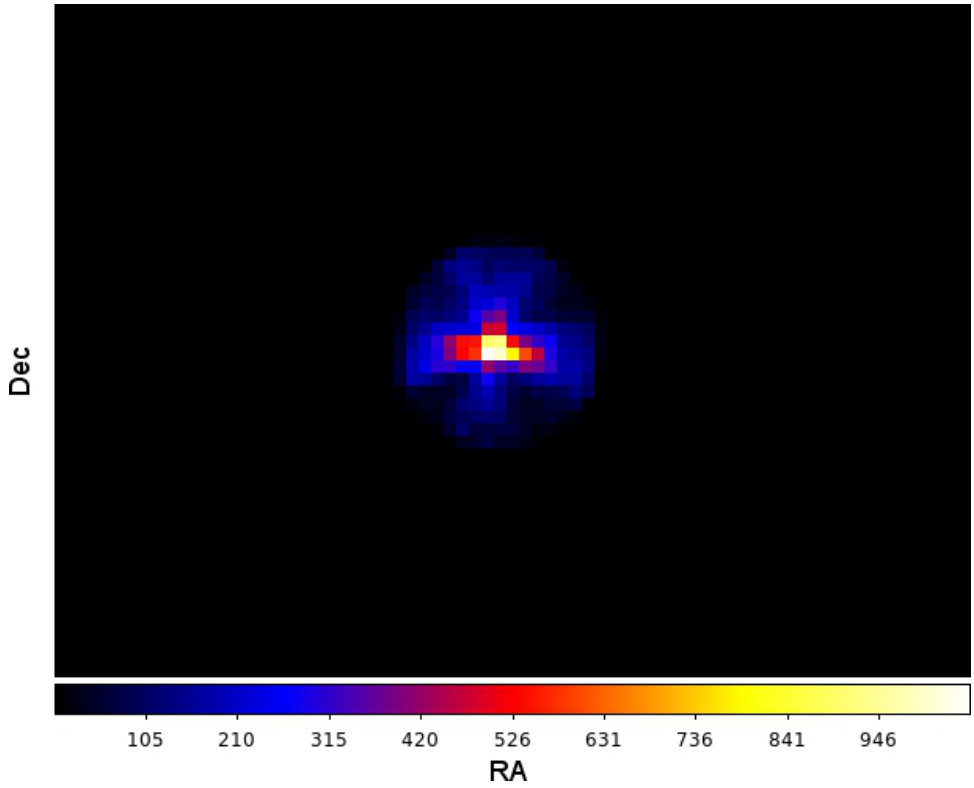

Figure 4.4: Selected source region for XIS timing and spectral analysis of AE Aquarii. The colour bar indicates the normalised counts levels.

background will have different total areas for the same size region, with the size of the area recorded in the fits header keyword "BACKSCAL". The ratio between the source and the background "BACKSCAL" values determines the scaling factor for the background light-curve. Although the same scaling correction has to be performed for spectral analysis, it is done automatically during the spectral analysis process. The background subtracted 168.06 s extracted light-curves are represented by Figures 4.6, 4.7 and 4.8. The light-curves were also added incoherently and are presented in Figure 4.9. The x-axis is scaled to modified Julian day, i.e. MJD = JD - 2400000. Thus the axis values are presented as, for example, $\mathrm{MJD(JD} - 2400000) = 55121 = 5.5121 \times 10^4$.

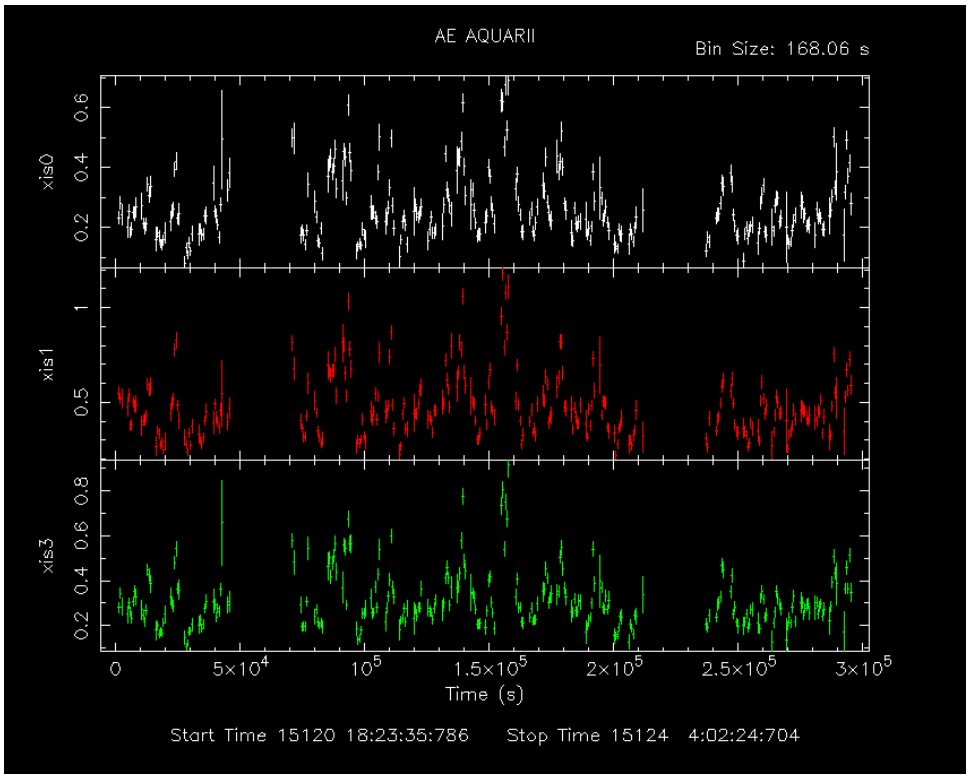

Figure 4.5: Available quick look count rate (counts s^{-1}) light-curves for XIS for 3×3 editing modes (Adopted from http://www.darts.isas.jaxa.jp/pub/suzaku/ver2/404001010/xis/products/).

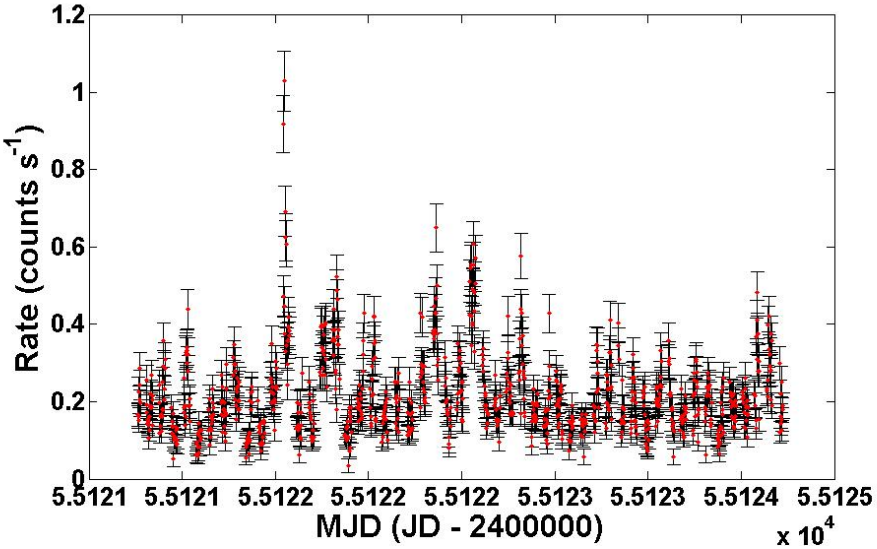

Figure 4.6: Background-subtracted 168.06 s light-curve for xis0 3×3 and 5×5 data.

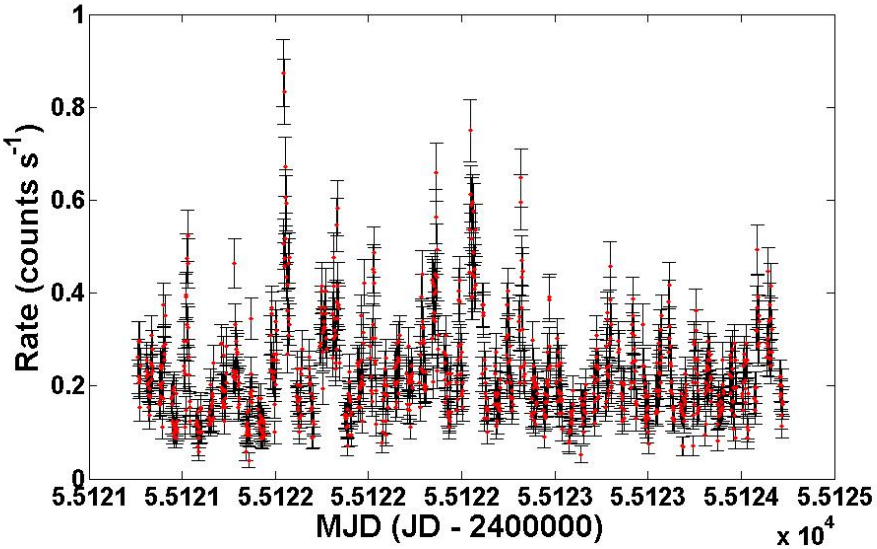

Figure 4.7: Background-subtracted 168.06 s light-curve for xis1 3×3 and 5×5 data.

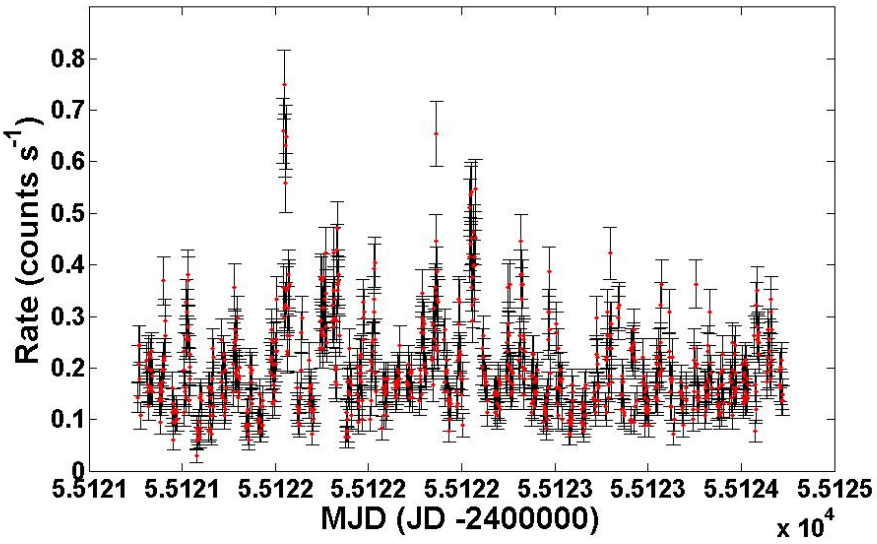

Figure 4.8: Background-subtracted 168.06 s light-curve for xis3 3×3 and 5×5 data.

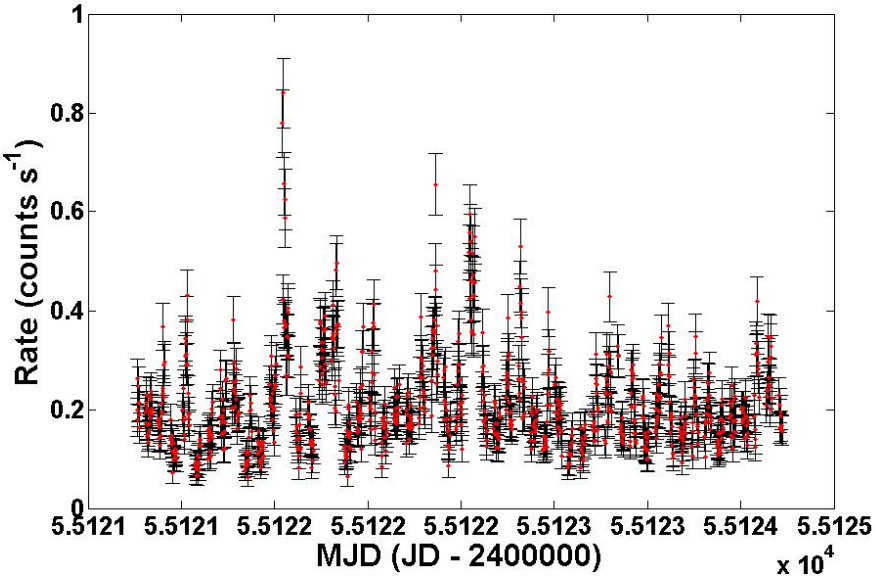

Figure 4.9: In-coherently added background-subtracted 168.06 s light-curve for all XIS data.

4.2.1 Timing analysis

Timing analysis was performed on the background subtracted 1 s count rate light-curve data for each detector respectively. The time-stamp for the data was corrected from terrestrial time (TT) to barycentric dynamical time (TDB) using the *Suzaku* specific tool "Aebarycen". See Appendix A for a detailed discussion of TT and TDB and timing analysis techniques. The timing analysis of the light-curves was performed using an independent package "Period" (Version 5.0-2) available in the Starlink (Version star-hawaiki) astronomy software tools. A Lomb-Scargle analysis was performed using a minimum frequency = 0.01 Hz, maximum frequency = 0.1 Hz and a software defined standard frequency interval = $1/(4 * \text{Overall time interval})$. The resultant power spectra from these analyses were subsequently plotted, with the fundamental frequency (F_0) and first harmonic ($2F_0$) of the current WD spin ephemeris model indicated in red, and 4σ in terms of the power indicated by a black line. This is illustrated in Figures 4.10, 4.11 and 4.12.

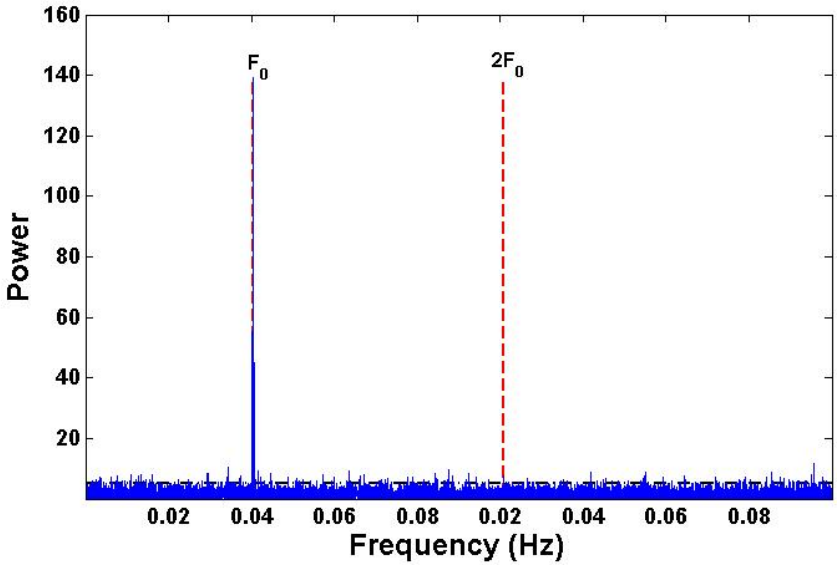

Figure 4.10: Lomb-Scargle power spectrum for xis0 ($0.4 - 5.0$ keV) data between 0.01-0.1 Hz, with the fundamental frequency (F_0) and first harmonic ($2F_0$) of the current WD spin ephemeris model indicated in red.

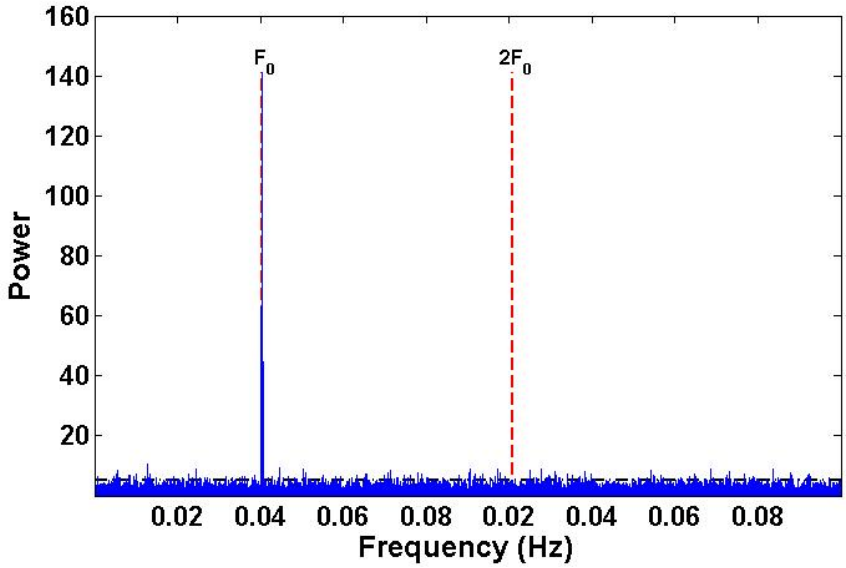

Figure 4.11: Lomb-Scargle power spectrum for xis1 ($0.4 - 5.0$ keV) data between 0.01-0.1 Hz, with the fundamental frequency (F_0) and first harmonic ($2F_0$) of the current WD spin ephemeris model indicated in red.

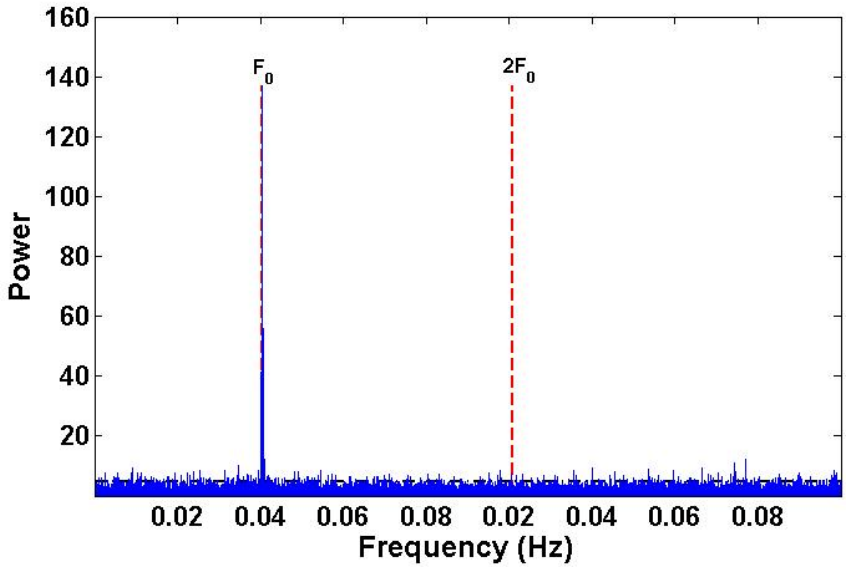

Figure 4.12: Lomb-Scargle power spectrum for xis3 ($0.4 - 5.0$ keV) data between 0.01-0.1 Hz, with the fundamental frequency (F_0) and first harmonic ($2F_0$) of the current WD spin ephemeris model indicated in red.

For all these power spectra it is clear that the dominant contribution occurs at F_0. The reason for the strong singular peak at F_0 and a total lack of a peak at $2F_0$ is due to the slight difference in the origins between the soft X-ray emission and the optical emission. The magneto-spheric propeller interacts with the in-falling mass from the secondary at the magnetosphere radius. The interaction causes thermal emission from optical to soft X-ray. This means that from the perspective of an observer, at the inclination of the system, the "front" heated hot spot (to use a term relating to accretion disks) is observed, together with the propeller ejected gas illuminated by the second pole. This double feature results in the (sometimes) strong first harmonic $2F_0$ together with the fundamental F_0 peak in the optical and UV wavelengths. In comparison, the gas is optically thin for the soft X-rays, which means that only the "front" part of the heated emission region is observed in the soft X-ray spectrum. For greater clarity and visual inspection the areas around the WD spin ephemeris model locations in the power spectra were enhanced. These enhanced sections that showed clear power at the WD spin period (F_0) were subsequently plotted and are represented by Figures 4.13, 4.14 and 4.15.

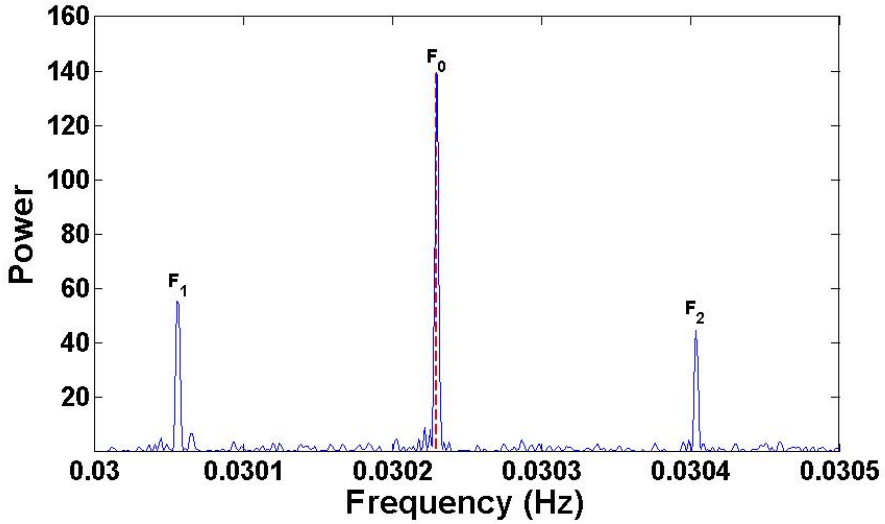

Figure 4.13: Lomb-Scargle power spectrum for xis0 data centred around the fundamental frequency (F_0) of the WD spin indicated in red. Two additional beat period peaks (F_1 and F_2) are also indicated.

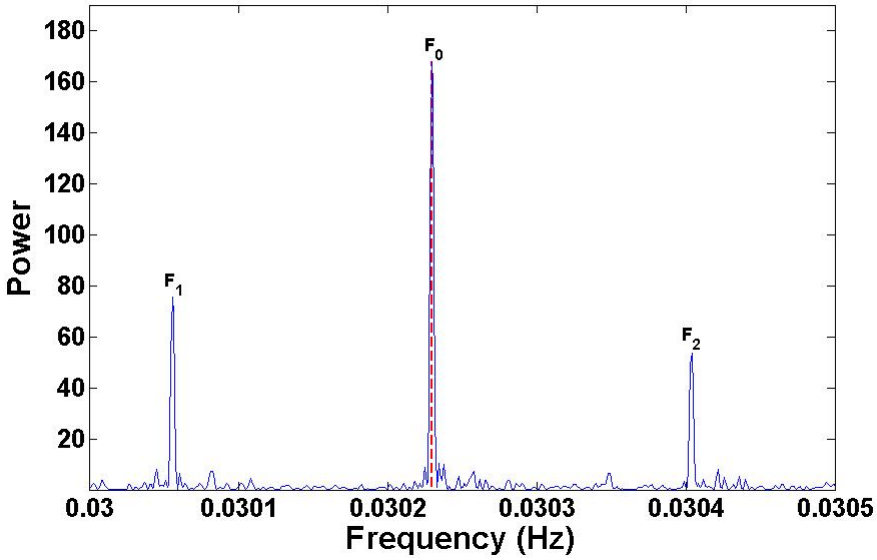

Figure 4.14: Lomb-Scargle power spectrum for xis1 data centred around the fundamental frequency (F_0) of the WD spin indicated in red. Two additional beat period peaks (F_1 and F_2) are also indicated.

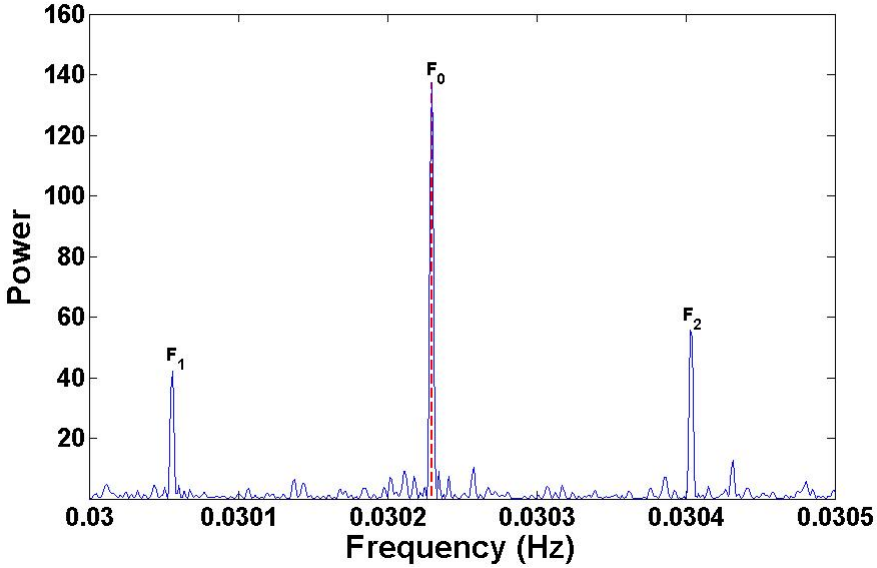

Figure 4.15: Lomb-Scargle power spectrum for xis3 data centred around the fundamental frequency (F_0) of the WD spin indicated in red. Two additional beat period peaks (F_1 and F_2) are also indicated.

For measurement and analysis of the detected peaks, the central region around each peak was plotted. The detected fundamental frequency peaks for xis0, xis1 and xis3 are represented by Figures 4.16, 4.17 and 4.18.

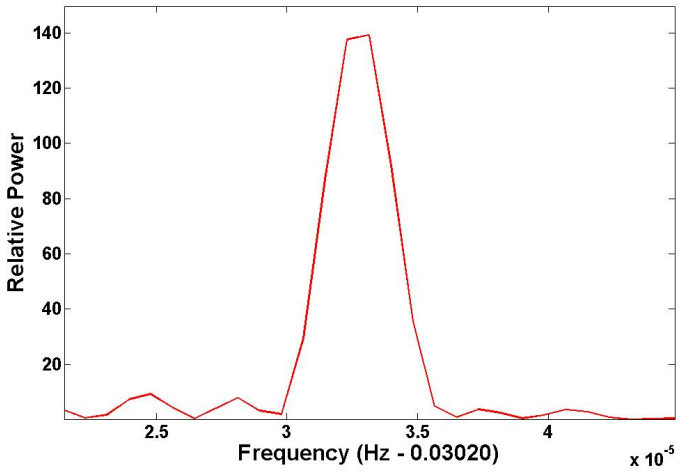

Figure 4.16: Central region around the detected fundamental frequency WD spin peak in xis0 data.

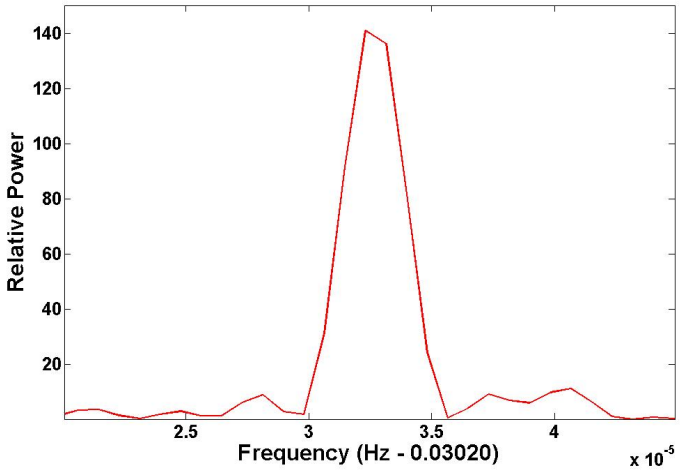

Figure 4.17: Central region around the detected fundamental frequency WD spin peak in xis1 data.

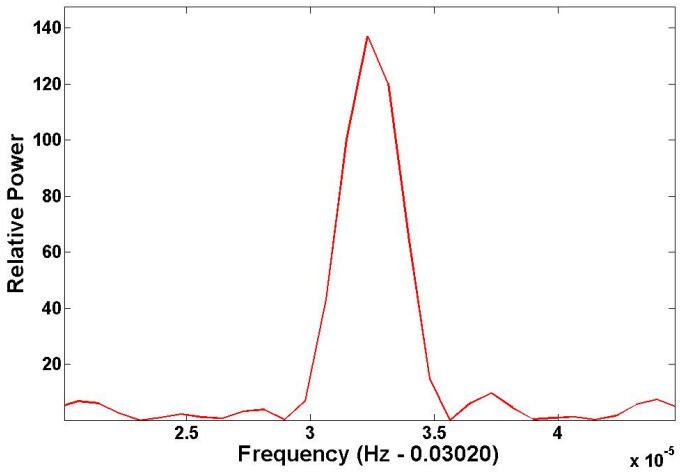

Figure 4.18: Central region around the detected fundamental frequency WD spin peak in xis3 data.

The spin periods were measured at the peak centre, with the error in the period measured as $0.5 \times$ (FWHM) of the peak. The average peak values were also determined for use in further analyses, with the average error for the three measured data-sets determined as (F_0 Avg Error)/$\sqrt{3}$. The measured values were then listed in Table 4.2. The beat periods were also measured, with additional values determined and listed in Table 4.3.

Table 4.2: Measured WD spin periods for xis0, xis1 and xis3 data.

Dataset	F_0 (Hz)	F_0 Error (Hz)
xis0	3.02327×10^{-2}	1.5×10^{-6}
xis1	3.02327×10^{-2}	1.5×10^{-6}
xis3	3.02325×10^{-2}	1.5×10^{-6}
Average F (Hz)	3.023265×10^{-2}	8.66×10^{-7}
Average P (s)	33.076823	9.475×10^{-4}

An analysis of the beat periods was conducted to determine their origin. The dif-

Table 4.3: Measured beat periods for xis0, xis1 and xis3 data.

Dataset	F_1 (Hz)	F_1 Error (Hz)	F_2 (Hz)	F_2 Error (Hz)
xis0	3.0059×10^{-2}	1.5×10^{-6}	3.0407×10^{-2}	1.5×10^{-6}
xis1	3.0059×10^{-2}	1.5×10^{-6}	3.0407×10^{-2}	1.5×10^{-6}
xis3	3.0059×10^{-2}	1.5×10^{-6}	3.0407×10^{-2}	1.5×10^{-6}
Average F (Hz)	3.0059×10^{-2}	8.66×10^{-7}	3.0407×10^{-2}	8.66×10^{-7}
Average P (s)	33.2679	9.5846×10^{-4}	32.8872	9.3666×10^{-4}

ference in frequency between the fundamental F_0 and the measured beat periods was $\sim 1.74 \times 10^{-4}$ Hz, which corresponds to a time period of ~ 95.8 min. Based on this result, the origin of the beat periods was identified as amplitude modulation (AM) modes of the spin period signal due to the orbital motion of the *Suzaku* space telescope, which has an orbital period of ~ 96 min. The "Aebarycen" tool therefore did not fully remove the orbital motion of the telescope, even though it did correct the data time-stamps to TDB time.

The very strong and clear WD spin period was then compared against previously measured spin periods to determine the properties of the WD spin. The values for the 33.08 s (fundamental frequency) spin period were extracted from selected references for a balanced spread of data-points over as long a baseline as possible. Refer to Table 4.4 for a list of the selected values. The listed values were plotted, after which regression analysis was performed to determine a likely first approximation ephemeris for the WD spin period, with regression models chosen based upon previous studies by De Jager et al. (1994) and Mauche (2006). The data and results from the regression analysis is illustrated in Figure 4.19.

Figure 4.19 indicates the fit of the selected linear and quadratic models to the data, although, considering the size of the error bars for the data, a flat line model fit would also be a possibility. A flat line fit, which would indicate no change in the spin period of the WD, was however excluded due to the previously mentioned

Table 4.4: Measured WD spin periods from selected datasets.

Reference	WD Spin (s)	Error (s)	T_{max} (JD)
Patterson (1979)	33.0767	0.001	2443707.3800000
De Jager et al. (1994)	33.0767	0.0001	2445172.0000420
Mauche (2006) - ASCA	33.0767	0.0001	2450004.7037529
Mauche (2006) - XMM	33.0767	0.0001	2452221.5720142
Mauche (2006) - Chandra	33.0767	0.0001	2453613.2767058
Suzaku_2009 XIS	33.0768	0.0009	2455121.6968135

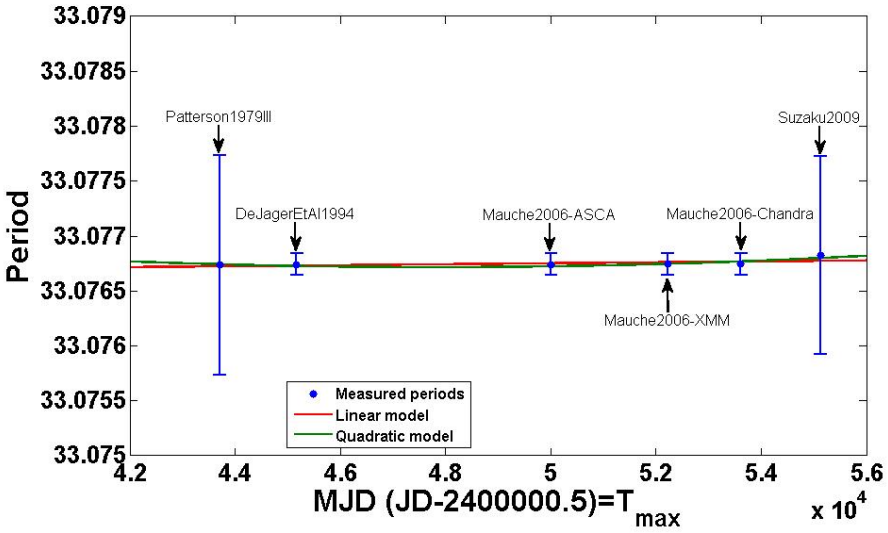

Figure 4.19: Selected WD spin periods of AE Aquarii, with linear and quadratic regression lines indicated.

studies that found that the spin period of the WD changes over time, thus necessitating the choice for more complex regression models. The parameters of the fitted regression models are listed in Table 4.5, with P_{33} the 33 s WD spin period model, and the norm of the residuals the goodness of fit for the regression analysis, with a smaller value indicating a better fit. It is related to the inverse of the R^2 value. From the data, that spans a total of 31.25 years, and fitted models, a possible spin-down trend in the WD spin period can be observed, confirming the current model of a torque-induced spin-down due to the magnetic propeller effect. The preliminary results also seem to indicate an increase in the spin-down of the WD.

The increased spin-down will result in an increased spin-down luminosity and resulting spin-down power that is available for particle acceleration and non-thermal emission.

Table 4.5: Fitted models and parameters for WD spin ephemeris.

Regression model	Norm of residuals
Linear	
$P_{33} = 5.0762 \times 10^{-14}\ T + 0.00038271$	6.896×10^{-10}
Quadratic	
$P_{33} = 1.7915 \times 10^{-17}\ T^2 - 8.7703 \times 10^{-11}\ T + 0.00049017$	4.598×10^{-10}

The implications of the proposed models are as follows: The parameters of the quadratic model, which has a slightly better fit, does not fit in with the known physics of the system. The $\dot{\mathrm{P}} = -8.7703 \times 10^{-11}$ d d^{-1} which would be expected to be due to the torque moments spinning the WD down, in this case would result in a spin-up of the WD. While the $\ddot{\mathrm{P}} = 1.7915 \times 10^{-17}$ d^{-1} term could be explained as magnetic dipole radiation losses, but is inconsistent in sign and magnitude with the expected value of $\ddot{\mathrm{P}} = -8.4 \times 10^{-24}$ d^{-1} as calculated by Mauche (2006). The $\mathrm{P}_0 = 0.00049017$ d $= 42.350688$ s value for the WD spin period is also $\sim 128\%$ larger than expected. The parameters in the linear model however is more realistic, in the sense that the $\dot{\mathrm{P}} = 5.0762 \times 10^{-14}$d d^{-1} is comparable to the $\dot{\mathrm{P}} = 5.64 \times 10^{-14}$ d d^{-1} value determined by De Jager et al. (1994). The $\mathrm{P}_0 = 0.00038271$ d $= 33.066144$ s is also realistic and in line with the expected trend for the WD spin period, in that the WD spin period is slowing down due to spin-down torque moments.

The newly calculated values for the WD spin ephemeris can be used to determine some additional system parameters. The characteristic time for the WD spin-down is then $\mathrm{P}_{33}/\dot{\mathrm{P}} \approx 2 \times 10^7$ yr with $\mathrm{P}_{33} = 0.00038283$ d $= 33.076823$ s. The spin-down luminosity $\mathrm{L_{sd}} = -\mathrm{I}\Omega\dot{\Omega}$ can also be determined as follows: The white dwarf moment of inertia $\mathrm{I} \approx 0.2\ \mathrm{M_{WD}R_{WD}^2} \approx 2 \times 10^{50}$ g cm^2 with $\mathrm{M_{WD}}$ the WD mass and $\mathrm{R_{WD}}$ the WD radius, with the 0.2 factor extrapolated from Andronov

and Yavorskij (1990) for a WD mass of ~ 0.48 $M_{\odot}$ (Welsh et al. (1993)). $\Omega = 2\pi/P_{33} = 0.19$ s^{-1} and $\dot{\Omega} = -2\pi\dot{P}/P^2 = -3.24 \times 10^{-16}$ s^{-2}. This gives a spin-down luminosity $L_{sd} \approx 1.23 \times 10^{34}$ erg s^{-1}, which is twice the spin-down luminosity determined by De Jager et al. (1994). For a WD mass of ~ 0.95 $M_{\odot}$ (De Jager et al. (1994)) the moments of inertia becomes $I \approx 1.13 \times 10^{50}$ g cm^2, resulting in a spin-down luminosity of $L_{sd} \approx 6.95 \times 10^{33}$ erg s^{-1}, which is ~ 1.1 times larger than the spin-down luminosity determined by De Jager et al. (1994). This means that there is possibly a greater amount of power available for particle acceleration and production of non-thermal emission. The large uncertainty in the mass of the WD (0.48 $M_{\odot} < M_{WD} < 1.2$ $M_{\odot}$) however also results in a large uncertainty in the spin-down luminosity, and until the mass of the WD can be constrained better, the amount of spin-down luminosity that is available for particle acceleration and production of non-thermal emission cannot be constrained.

4.2.2 Spectral analysis

A first approximation spectral analysis of the XIS data was performed as follows. The extracted source spectra for the different XIS detectors were saved using the "save spectrum response=yes" option for a point source in "Xselect". With this option the response files for each specific sensor data-set are determined using the latest calibration database (CALDB) response and model files for the *Suzaku* telescope and XIS intrument and data. These calibration files are available from the online CALDB at HEASARC. The same was also done for the background spectra. The output files were then combined sensor type specific, i.e., xis0 and xis3 source spectra (*.pha files), response (*.rsp files) and background (*bg.pha) files for a total FI spectrum, and xis1 source spectra (*.pha file), response (*.rsp file) and background (*bg.pha) file for a total BI spectrum, using the "addascaspec" tool. These xis03 and xis1 spectrum-related files were then used to conduct spectral analysis using XSpec (Version 12.8.2). The spectrum.pha files for xis03 were read into "XSpec" with the relating response and background files linked to the source or data spectrum. This spectrum was analysed first as it was of a higher quality due to the multiplicative effect of adding the spectra for xis0 and xis3.

A RAW normalised counts versus channels spectrum was plotted for inspection (Figure 4.20).

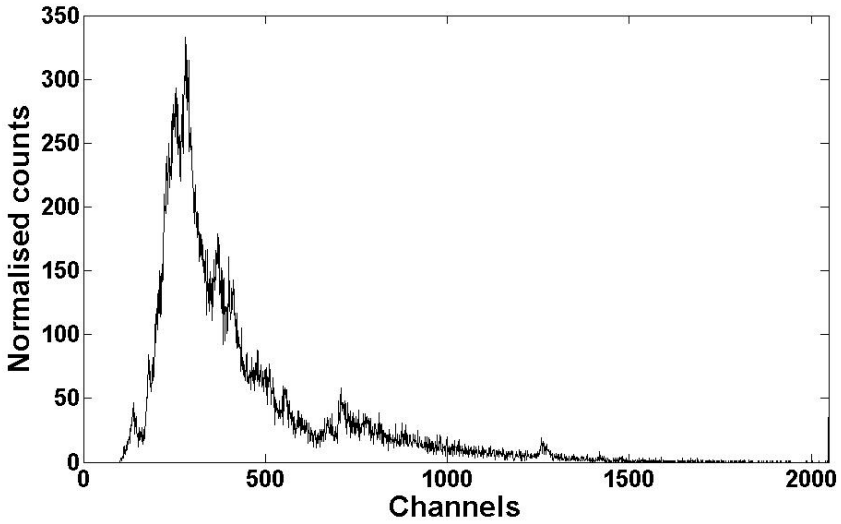

Figure 4.20: Raw spectrum for xis03 data.

A can be seen there are sections at low and high channels that contain no variance data (i.e. values = 0). These sections were removed from the analysis process by first using the "ignore bad" command that uses the data quality included values in the spectrum.pha files to ignore the specified "bad" quality channels for spectral analysis. A new log-log spectrum was plotted with the x-axis set to energy (keV) and the y-axis set to normalised counts $s^{-1}keV^{-1}$. Upon inspection null variance points were still present at low and high energies. A new ignore section was therefore specified in terms of energy channels, i.e., "ignore **-0.4 5.0-**", which ignores all data below 0.4 keV and all data above 5.0 keV. The cleaned spectrum was now ready for model fitting processes. The model fitting consists of two primary components: The **additive** component, which represents different kinds of X-ray sources (this component, after being convolved with the instrument response, prescribes the number of counts per energy bin) and the **multiplicative** components, which represent phenomena (e.g., reddening or an absorption edge) that modify the observed X-ray emission. This latter component applies an energy dependant multiplicative factor to the source

radiation. The result is then convolved with the instrument response. For a complete list of available models and model descriptions refer to the XSpec user manual (https://heasarc.gsfc.nasa.gov/xanadu/xspec/manual/manual.html). Refer to Section 4.4 for a brief description of additive models considered during the analysis of both XIS and HXD *Suzaku* spectra.

The choice of models was based upon previous analysis (Terada et al. (2008)) and the XspecWalkthrough manual (https://heasarc.gsfc.nasa.gov/xanadu/xspec/manual/XspecWalkthrough.html). A simple case was chosen initially, with an absorbed two Mekal model specified, i.e., "model phabs(mekal + mekal)". The fit was conducted on the spectrum using χ^2 statistics, with the reduced χ^2 value used in conjunction with the null hypothesis probability value to determine the goodness of the fit. The model fit improved with a decrease in the reduced χ^2 value, and an increase in the null hypothesis value. The first initial fit resulted in a very small null hypothesis value of $\sim 1.8 \times 10^{-41}$ and a reduced χ^2 value of ~ 1.76. The models were thus reconsidered.

Terada et al. (2008) proposed either a two component Mekal with a power law, or a triple Mekal model. Considering that the spectra under investigation has an upper energy limit of 5.0 keV, a power law component was excluded, and the triple Mekal model chosen, i.e., "phabs(mekal + mekal + mekal)". The fit was reapplied and showed a noticeable improvement, with the null hypothesis value improving to $\sim 6.8 \times 10^{-22}$ with a reduced χ^2 value of ~ 1.5. The fit however showed large residuals below 1.5 keV. There was thus a component missing. With the proposed VHE $\gamma -$ ray emission requiring a large amount of free charged particles, a Bremsstrahlung component was considered, i.e. "phabs(mekal + mekal + mekal + bremss)". The fit was reapplied, with an improved null hypothesis value of $\sim 4.7 \times 10^{-13}$ and reduced χ^2 value of ~ 1.37. Multiple iterations of the fit were applied, with a final best null hypothesis value of $\sim 3.17 \times 10^{-7}$ and reduced χ^2 value of ~ 1.25. The same model was then also applied to the spectrum for xis1. The fit had a null hypothesis value of $\sim 1.9 \times 10^{-7}$ and a reduced χ^2 value of ~ 1.3. The spectra and accepted fitted models were then plotted on the same graph for clarity (Figure 4.21). From the figure the slight difference between the

detector sensitivities for the FI and BI sensors can be seen, in that the BI sensors is more sensitive for higher energy photons than the FI sensor. This is because the FI sensor detects the photons in the front of the sensor, while and the BI detects the photons in the back of the sensor. Additionally, the "phabs(mekal + mekal + mekal + bremss)" model was used to determine a preliminary uncorrected flux value for the XIS spectrum between 0.4 and 5.0 keV. The "flux" command was used to calculate the flux of the current model over the selected energies. The determined photon flux was $\sim 4.7 \times 10^{-3}$ photons s^{-1} keV^{-1} with an energy flux of $\sim 8 \times 10^{-12}$ erg cm^{-2} s^{-1}.

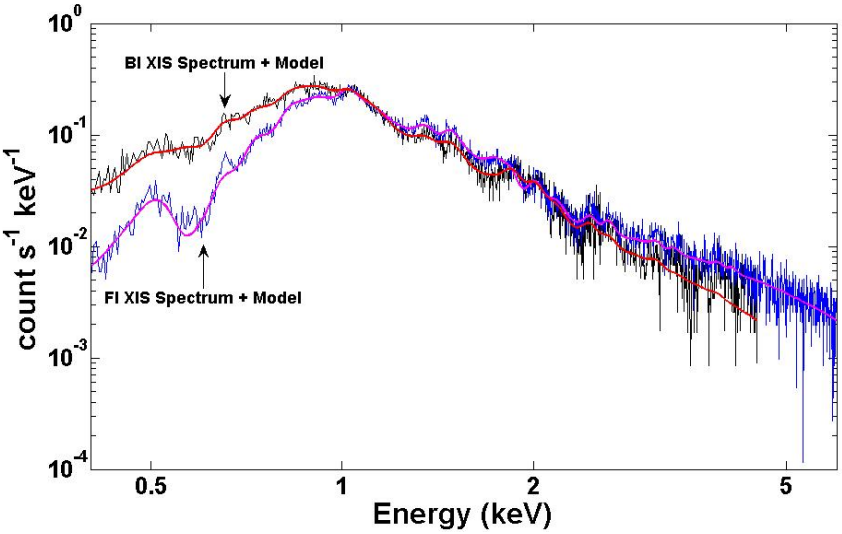

Figure 4.21: XIS Spectra for FI and BI sensors, with best fit models.

4.3 HXD data analysis

The analysis procedures for HXD data is slightly different from those used for XIS data, primarily because the HXD device is a non-imaging instrument. Processing and screening of measured photon events follow more closely the procedures applied to other similar collimated instruments, such as *Ginga-LAC*. Because the HXD is not an imaging device, the non-X-ray background (NXB) for the PIN is derived

from a model. Additionally the cosmic X-ray background (CXB), which consists of $\sim 5\%$ of the background of the PIN, should also be considered. These components are constantly studied, with the latest models available from the HEASARC CALDB. Also, the gain on the GSO changes with time, with the latest gain parameter table (GPT) made available for HXD data processing. These, in addition to other smaller instrument response variables, determine the calibration values used during the calculation of the photon intensity (PI) column values. Taking these varying calibration values, and specifically considering the possibility of a discrepancy between the HXD GSO preprocessed data gain values, and the calibration data gain values, it was decided that the unfiltered WELL data files that contain PIN and GSO data would be used. These data files together with the required background models for the epoch of the observation in question and the available auxiliary and housekeeping files were thus downloaded from the archive site (Table 4.6).

Table 4.6: List of HXD unfiltered and calibration data files downloaded for analysis.

Filename
ae404001010hxd_1_wel_uf.evt.gz
ae404001010hxd_2_wel_uf.evt.gz
ae404001010hxd_3_wel_uf.evt.gz
ae404001010hxd_4_wel_uf.evt.gz
ae404001010_hxd$_g$sobgd.evt.gz
ae404001010_hxd_pinbgd.evt.gz
ae404001010hxd_0_pse_cl.evt.gz
ae404001010hxd_0.hk

The processing and screening of the unfiltered data were as follows. First the HXD event arrival time correction had to be calculated and applied. This was achieved through the use of the "hxdtime" procedure. The (time) invariant pulse height (PI) values were then determined using "hxdpi". The procedure also corrects for the gain drift values by using the latest gain-history file (GHF) for the PIN and GPT for the GSO available from the CALDB. The final step in the preprocessing

was the grading of the events using "hxdgrade". The procedure not only determines the data quality of the measured events, but also lists the origin of the events. This process was applied to each WELL data file respectively. At this stage the PIN and GSO data were still combined in the four WELL data files. The next step was therefore additional screening and separating of the PIN and GSO data. This was done as follows. The four processed WELL files were read simultaneously into "xselect". The combined events data were then screened using the *Suzaku* recommended filter:

"SAA_HXD == 0 && T_SAA_HXD > 500 && ELV > 5 && ANG_DIST < 1.5 && HXD_DTRATE < 3 && AOCU_HK_CNT3_NML_P == 1 && COR > 6 && HXD_HV_W0_CAL > 700 && HXD_HV_W1_CAL > 700 && HXD_HV_W2_CAL > 700 && HXD_HV_W3_CAL > 700 && HXD_HV_T0_CAL > 700 && HXD_HV_T1_CAL > 700 && HXD_HV_T2_CAL > 700 && HXD_HV_T3_CAL > 700″.

This filter was applied using the "filter mkf" command in "xselect". The final filtered and screened data were split into two cleaned event files, for both the PIN and GSO data by extracting events based on a filter applied to the "DET_TYPE" column, i.e. "filter column DET_TYPE == 0" for GSO data and "filter column DET_TYPE == 1" for PIN data. The respectively extracted events were thus saved to be used for timing and spectral analysis.

4.3.1 Timing analysis

The extraction of light-curves for the PIN and GSO data was accomplished using the automated scripts "hxdpinxblc" and "hxdgsoxblc". The "hxdpinxblc" script produces the dead-time corrected PIN source with background, the PIN background (NXB + constant CXB) and the background-subtracted source light-curves. The "hxdgsoxblc" script produces the dead-time-corrected GSO source with background, the GSO background (NXB) and the background-subtracted source light-curves. The quick look light-curves for HXD (PIN and GSO) data were then used as reference to check the data processing and quality. Although

the GSO quick look light-curve could be reproduced, it was characterized as purely the result of the local background, with a 24 h cycle clearly visible. No further analysis on the GSO light-curve was therefore considered.

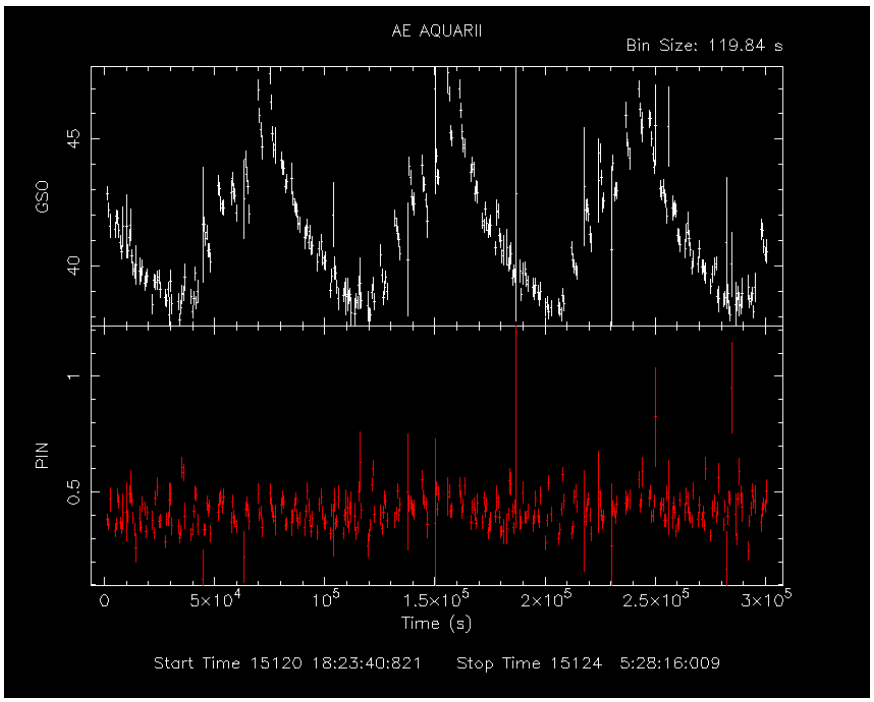

Figure 4.22: Available quick look count rate (counts s^{-1}) light-curves for HXD (PIN and GSO) data (Adopted from http://www.darts.isas.jaxa.jp/pub/suzaku/ver2/404001010/hxd/products/).

PIN timing analysis

The PIN dead-time-corrected and background-subtracted source light-curve (Figure 4.23) was used for timing analysis. A large binning size (128 s) in terms of time resolution was recommended for best accuracy in terms of data quality for the PIN light-curves. Because of this low time resolution, standard FFT techniques, like Lomb-Scargle, as used for the XIS data, could not be used for analysis of the WD spin period. Therefore the data were folded on the WD spin (33.08 s) and AE Aquarii orbital (35568 s) periods, with the pulse phase diagrams represented by Figures 4.24 and 4.25 respectively. The pulse phase diagrams were plotted over

two phases for clarity. The blue curves represent the best non-linear regression fit for the test periods in question. As can be seen the spread in terms of the calculated pulse phase values provided some difficulty for the fitting process. The fit for the orbital period for instance had to be recalculated by excluding the outliers above 0.02 and below -0.025. This recalculation produced a better fit (red curve) upon visual inspection. The results from the pulse-phase diagrams might indicate that any hard X-ray emission around the WD spin period would be at a very low level, while the possibility exist for hard X-ray emission sourced around the system orbital period diameter.

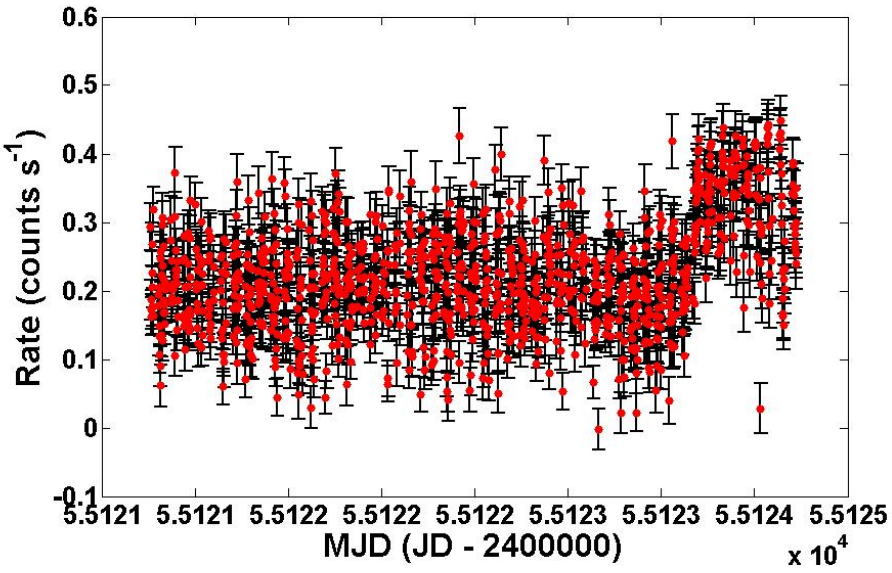

Figure 4.23: Background subtracted 128 s light-curve for PIN data.

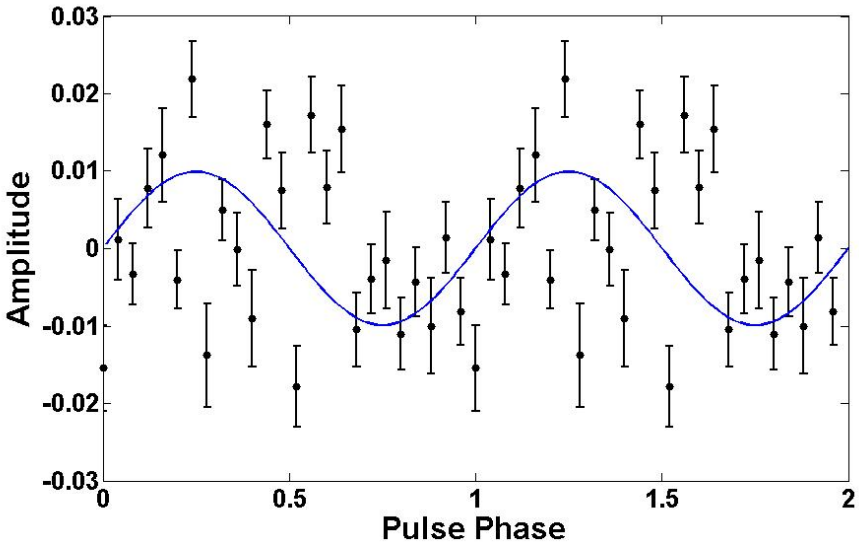

Figure 4.24: Pulse phase diagram for the WD spin (F_0) period using PIN data. The blue curve indicates best fit analysis.

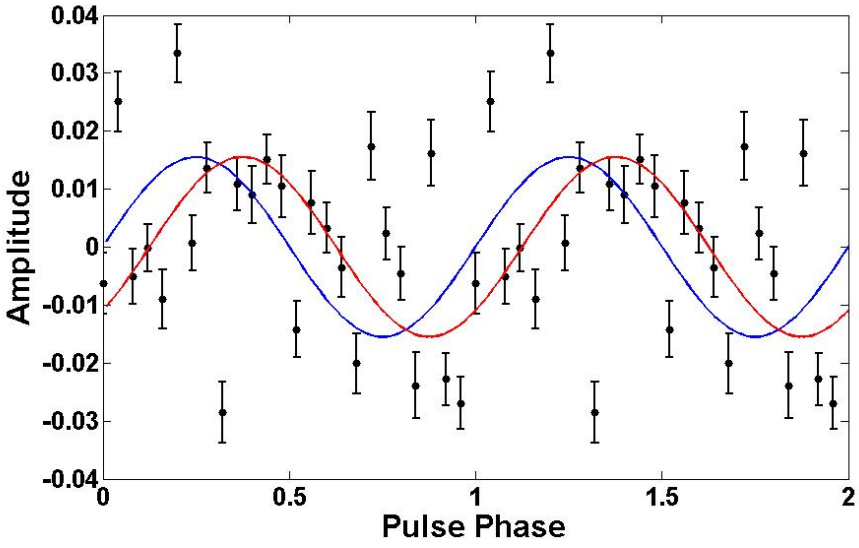

Figure 4.25: Pulse phase diagram for the orbital period of AE Aquarii using PIN data. The blue curve indicates best fit analysis, while the red curve indicates the recalculated fit, after removal of selected outliers.

4.3.2 Spectral analysis

A first approximation spectral analysis was performed on the HXD data in the following way. The extraction of spectra for the PIN and GSO data was accomplished using the automated scripts "hxdpinxbpi" and "hxdgsoxbpi". The "hxdpinxbpi" script produces the dead-time corrected PIN source as well as the PIN background (NXB + CXB) spectra in addition to the required response file. The "hxdgsoxbpi" script produces the dead-time corrected GSO source as well as the GSO background (NXB) spectra in addition to the required response file. It is important to take note of the requirement of an additional auxiliary response file (ARF) that is required to correct the GSO data. This new arf file is required due to the currently remaining issues in the uncertainty of the linearity above the Gd-K edge (mainly 50-70 keV) as well as a cross normalisation between HXD-PIN and HXD-GSO on the HXD-GSO responses. Figure 4.26 displays the effect that the incorporation of the new ARF response model has on the data quality of the GSO spectrum. Unfortunately no events were detected within the GSO spectrum, and no further analysis could therefore be performed.

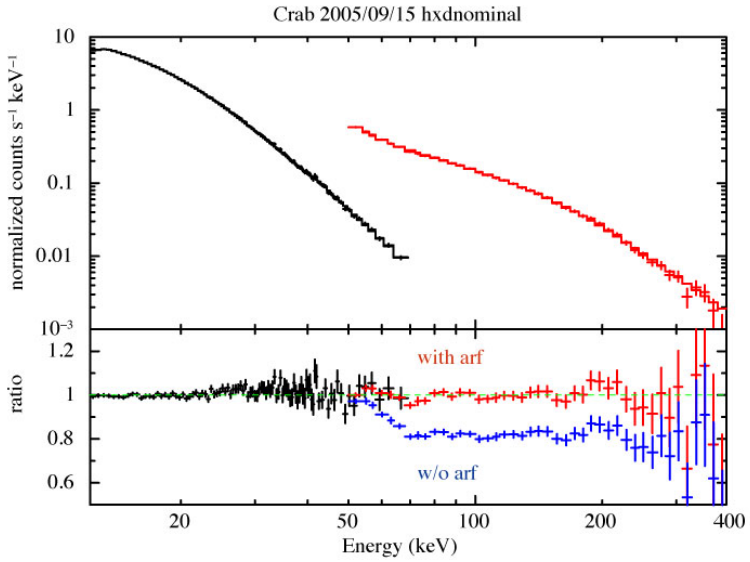

Figure 4.26: Effect of the inclusion of the new arf on *Suzaku* HXD data of the CRAB Nebula observed in 2005 (Adopted from http://heasarc.gsfc.nasa.gov/docs/suzaku/analysis/gso_newarf.html).

PIN spectral analysis

The PIN spectrum related files were used to conduct spectral analysis using XSpec (Version 12.8.2). The "hxdpinxbpi" script produced grouped spectrum.pi file for the PIN data, was read into "XSpec", with the relating response and background files linked to the source or data spectrum. A RAW normalised counts versus channels spectrum was first plotted for inspection (Figure 4.27).

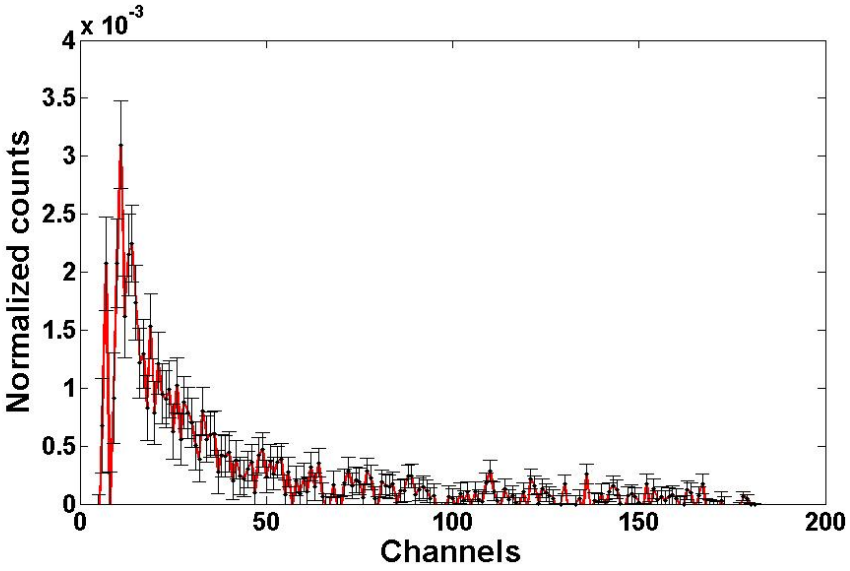

Figure 4.27: Raw spectrum for PIN data.

Similarly to the XIS spectra, there are sections at low and high channels that possibly contain no variance data (i.e., values = 0). These sections were removed from the analysis process by first using the "ignore bad" command that uses the data quality included values in the spectrum.pi files to ignore the specified "bad" quality channels for spectrum analysis. A new log-log spectrum was plotted with the x-axis set to energy (keV) and the y-axis set to normalised counts $s^{-1}keV^{-1}$. Upon inspection, null variance points were still present at low energies. A new ignore section was therefore specified in terms of energy channels, i.e., "ignore **-14.0", which ignores all data below 14.0 keV. The cleaned spectrum was now ready for model fitting procedures.

The choice of models was based upon previous analysis (Terada et al. (2008)) and the XspecWalkthrough manual (https://heasarc.gsfc.nasa.gov/xanadu/xspec/manual/XspecWalkthrough.html). A simple case was chosen initially, with a power-law model specified, i.e., "model phabs(pow)". The fit was conducted on the spectrum using χ^2 statistics, with the reduced χ^2 value used in conjunction with the null hypothesis probability value to determine the goodness of the fit. The first initial fit resulted in a null hypothesis value of $\sim 2.2 \times 10^{-6}$ and a reduced χ^2 value of ~ 1.58. The proposed model fit was further tested.

From the results of the XIS spectral analysis two additional components were tested in an attempt to improve the fit. A thermal component in the form of a Mekal or Bremsstrahlung was considered, with the Bremsstrahlung component relying on the presence of a large amount of free charged particles that can be accelerated to high energies (Oruru and Meintjes (2012)). The first consideration in terms of a Mekal component fortunately resulted in such a bad fit that it does not warrant further mentioning. The fit for the Bremsstrahlung component, i.e. "phabs(pow + bremss)", had a null hypothesis value of $\sim 1.59 \times 10^{-6}$ with a reduced χ^2 value of $\sim$ 1.59. An alternative for the power-law component was also considered in the form of a Bremsstrahlung sourced self-Compton (compLS) component, i.e. "phabs(compls + bremss)". The reapplied fit had a null hypothesis value of $\sim 1.82 \times 10^{-5}$ and a reduced χ^2 value of $\sim$ 1.51. The spectra and fitted models were then plotted on the same graph for clarity (Figure 4.28). The "phabs(pow + bremss)" model was used to determine a preliminary uncorrected flux value for the PIN spectrum for two different energy ranges, $14 - 40$ keV and $40 - 96$ keV. The "flux" command was then used to calculate the flux of the current model over the selected energies ranges. The determined photon flux between $14 - 40$ keV was $\sim 2.7 \times 10^{-4}$ photons s^{-1} keV^{-1} with an energy flux of $\sim 1.6 \times 10^{-11}$ erg cm^{-2} s^{-1}, with the determined photon flux between $40 - 96$ keV, $\sim 3.7 \times 10^{-4}$ photons s^{-1} keV^{-1} with an energy flux of $\sim 2.1 \times 10^{-11}$ erg cm^{-2} s^{-1}.

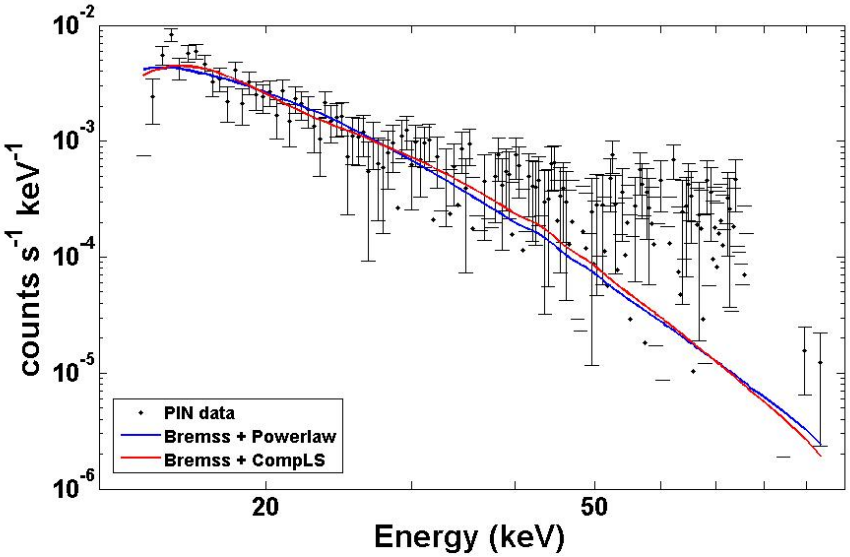

Figure 4.28: Background and CXB corrected PIN spectrum, with best fit models.

4.4 Description of selected spectral analysis models

Mekal and VMekal model

The Mekal model is for an emission spectrum from a hot diffuse gas. The model is based on model calculations published by Mewe and Kaastra, with Fe L calculations by Liedahl. The model also include line emissions for several elements. The difference between the Mekal and VMekal variants is that for the VMekal the user can set the relative individual element abundances for the model. (References for the model include: Mewe et al. (1985, 1986) and Liedahl et al. (1995))

Bremsstrahlung model

The bremss model, and vbremss and zbremss variants, is for a thermal Bremsstrahlung spectrum based on the Kellogg et al. (1975) polynomial fit to the Karzas and Latter (1961) numerical values. The abundance of He is assumed at 8.5% of H by number.

CompLS

The CompLS model is for a self-Comptonization of a Bremsstrahlung emission from a optically thick spherical plasma cloud with a given optical depth and temperature. The Comptonization spectrum is based after Lamb and Sanford (1979).

Powerlaw model

The powerlaw model is for a simple photon power law, with the zpowerlaw variant used in computing a redshifted spectrum. For the powerlaw the equation used is,

$$\mathrm{A(E)} = \mathrm{KE}^{-\alpha} \tag{4.1}$$

and for the red-shifted power law,

$$\mathrm{A(E)} = (\mathrm{K}/(1+\mathrm{z}))(\mathrm{E}(1+\mathrm{z}))^{-\alpha}/(1+\mathrm{z}) \tag{4.2}$$

with K = photons keV^{-1} cm^{-2} s$-$1 at 1 keV, α = photon index and z = redshift.

Based on the spectral analysis of the high energy component of the X-ray spectra, a thermal component in conjunction with a power-law, which implies the presence of a non-thermal population of particles, cannot be excluded. This may be an indication that AE Aquarii may contain a particle accelerator that may accelerate a small population of particles to VHE energies, resulting in $\gamma-$ray emission above a few hundred MeV. This will be investigated in the following chapter.

"This research has made use of data obtained from the Suzaku satellite, a collaborative mission between the space agencies of Japan (JAXA) and the USA (NASA)."

Chapter 5

Analysis of *Fermi* and *AGILE* data in the search for pulsed high-energy non-thermal γ – ray emission from AE Aquarii

5.1 Introduction

The possible pulsed non-thermal hard X-ray emission reported from the *Suzaku* data (Terada et al. (2007, 2008) and Oruru and Meintjes (2012)), combined with earlier reports of possible pulsed and burst-like TeV emission (Meintjes et al. (1992, 1994) and Chadwick et al. (1995)), stimulated an extensive search for similar features utilizing the data archives of the *Fermi*-LAT and *AGILE*-GRID datasets. The availability of contemporaneous optical observations allow the selection of VHE data sets that correspond to periods when the source showed enhanced activity, such as flaring, in optical wavelengths. Additionally, a study of the optical data over a wide range of frequencies around the fundamental and first harmonic spin periods, allows the possible characterization of similar periodic signatures that could possibly be searched for in the VHE data. This chapter consists of the following:

i) a concise discussion of the *Fermi* and *AGILE* space telescopes,

ii) a full discussion of the primary analysis method used and results obtained using recommended *Fermi* science-support methods, as well as a test for validity of the analysis process for the *Fermi*-LAT data analysis,

iii) a discussion of a multi-wavelength analysis to search for possible correlations between optical, *Suzaku* X-ray and *Fermi*-LAT data,

iv) a discussion of analysis conducted and results obtained using *AGILE*-GRID data, and

v) the calculation of upper limits for AE Aquarii using *Fermi*-LAT data analysis techniques and its inclusion in an updated SED diagram for AE Aquarii.

5.2 *Fermi* and *AGILE* space telescopes

The *Fermi* $\gamma-$ ray Space Telescope was launched by NASA on 11 June 2008 into a low earth orbit (LEO) at an altitude of 550 km. The primary instrument on *Fermi* is the Large Area Telescope (LAT), with a field of view (FOV) that covers about 20% of the sky. *Fermi* is predominantly operated in survey mode and covers the whole $\gamma-$ ray sky every 3 hours. The LAT has a very large energy sensitivity range, from 20 MeV - 300 GeV. Refer to Atwood et al. (2009) for a more detailed discussion related to the *Fermi*-LAT instrumentation and extended technical specifications. General information, data archive access and software tools, as well as support in the form of tutorials and the *Fermi* "Cicerone" can by accessed through *Fermi* at ASDC (Fermi at ASDC, http://fermi.asdc.asi.it/) and *Fermi* Science Support Center at HEASARC (from here-on Fermi_HEASARC, (Fermi Science Support Center at HEASARC, http://fermi.gsfc.nasa.gov/ssc/)).

AGILE was launched by the Italian Space Agency from the Shriarikota ISRO Base in India on 23 April 2007 into a LEO at an altitude of 540 km. The two main instruments available are the Gamma Ray Imaging Detector (GRID) that covers an energy range of 30 MeV $-$ 50 GeV with a FOV of 3 sr, and the Super *AGILE* (SA) X-ray detector that covers an energy range of $20-60$ keV with a FOV of 1 sr. Refer to Angelini (2007); Chen et al. (2013) for more detailed discussions re-

lated to *AGILE* and extended technical specifications. General information, data archive access and software tools, as well as support in the form of tutorials can by accessed through *AGILE* at ASDC (AGILE at ASDC, http://agile.asdc.asi.it/) and the *AGILE* Home Page (AGILE at Astro-rivelatore Gamma a Immagini Leggero, http://agile.rm.iasf.cnr.it/).

Compared to Imaging Atmospheric Cherenkov (IAC) Telescope systems, space-based telescope systems detect lower energy $\gamma-$ ray photons (50 MeV to 300 GeV) using particle detection methods, i.e. production of electron-positron pairs through interaction with a metal. This technique is employed in both *Fermi* (Figure 5.1) and *AGILE* (Figure 5.2). The main $\gamma-$ ray detector structure on both telescopes consists of a detector-cube constructed as follows: The structure is surrounded by an anti-coincidence detector that is used to identify and eliminate background cosmic rays. The cube consists of an array of modular "towers" made of thin layers of tungsten foil (that produce the electron-positron pair when an incoming $\gamma-$ ray interacts with one of the atoms) and silicon strip detectors that track the progress of the charged particles through alternating X and Y directions. The total energy of the charged particle pair is then measured by a caesium iodide calorimeter or scintillator. The combined information from the anti-coincidence detector, silicon tracker and calorimeter is used to determine the energy and direction of the detected $\gamma-$ ray.

The timing resolution for *Fermi*-LAT events is ~ 10 μs with a readout cycle dead-time for triggered events of ~ 27 μs. The time and telescope position for the *Fermi* telescope are provided by an onboard GPS system. Initial event filtering and identification are performed on the spacecraft, after which the data are downloaded $\sim 10-11$ times per day. The downloaded data then undergo additional filtering and characterization. The filtered and cleaned data are then made available for public access. The timing resolution for *AGILE*-GRID events is ~ 20 μs for Level-1 triggering, while readout cycle dead-time (including Level-2 trigger stages) is ~ 100 μs and is dominated by the Tracker readout. The time and telescope position for the *AGILE* telescope are provided by an onboard GPS system. Initial filtering is done on the telescope, with additional filtering and characterization

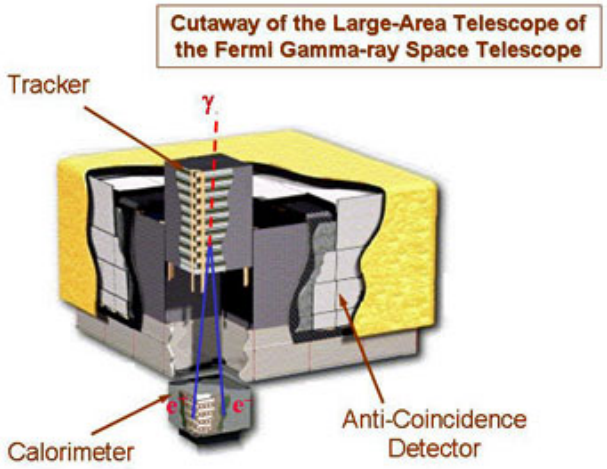

Figure 5.1: Diagram showing the *Fermi* $\gamma-$ray detector (Fermi at ASDC, http://fermi.asdc.asi.it/).

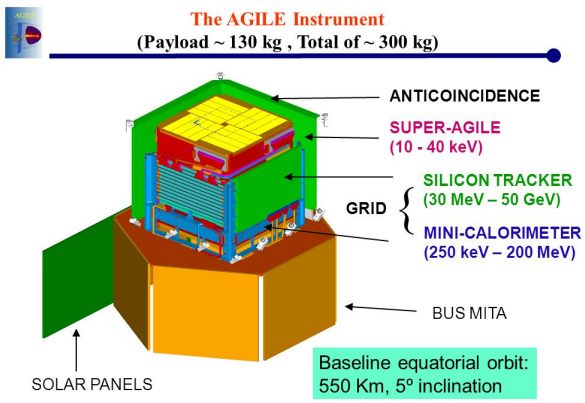

Figure 5.2: Diagram showing the *AGILE* $\gamma-$ray detector (AGILE at Astro-rivelatore Gamma a Immagini Leggero, http://agile.rm.iasf.cnr.it/).

performed on the downloaded data before release for public access.

5.3 *Fermi*-LAT analysis

The following procedure was applied during the search for possible detection of $\gamma-$ray emission from AE Aquarii using *Fermi* data. First a search through *Fermi*-LAT data was conducted by scanning the *Fermi*-LAT catalogues for any possible source detections in the region of AE Aquarii (20 40 09, -00 52 15, J2000, Sexagesimal Equatorial). *Fermi* had a few notable source detections within the region, as listed in Table 5.1.

The *Fermi* data archive was the next point of interest. A "LAT Data Query" on the Fermi_HEASARC site was completed. The search criteria for extraction from the *Fermi*-LAT database was set to a region centred on AE Aquarii (310.04, -0.87, J2000, Decimal Equatorial). A whole range of different datasets were extracted

Table 5.1: List of objects from the 2nd *Fermi* Catalogue.

Number	Source Name	Counterpart	RA (J2000)	Dec (J2000)	Optical
1	2FGLJ2014.0-0046	PMNJ2014-0047	20 14 04.0	-00 46 17.1	BL Lac
2	2FGLJ2015.1-0137	PKS2012-017	20 15 06.7	-01 37 11.1	BL Lac
3	2FGLJ2017.3+0603	PSRJ2017+0603	20 17 23.8	+06 03 14.1	Pulsar
4	2FGLJ2021.5+0632		20 21 33.7	+06 32 31.0	Unassociated
5	2FGLJ2025.6-0736	PKS2023-07	20 25 39.7	-07 36 18.6	FSRQ
6	2FGLJ2030.3-0622	TXS2027-065	20 30 22.3	-06 22 21.6	FSRQ
7	2FGLJ2031.7+1223	PKS2029+121	20 31 45.6	+12 23 21.5	BL Lac
8	2FGLJ2035.4+1058	PKS2032+107	20 35 24.1	+10 8 18.0	FSRQ
9	2FGLJ2039.1-1046	TXS2036-109	20 39 08.7	-10 46 44.1	BL Lac
10	2FGLJ2049.8+1001	PKS2047+098	20 49 48.7	+10 01 16.2	AGU
11	2FGLJ2050.0+0408	PKS2047+039	20 50 00.7	+04 08 59.3	BL Lac
12	2FGLJ2053.2+1212c		20 53 17.4	+12 12 43.0	Unassociated
13	2FGLJ2055.4-0023	1RXSJ205528.2 -002123	20 55 26.5	-00 23 52.8	BL Lac
14	2FGLJ2108.7-0246	TXS2106-030	21 08 43.1	-02 46 48.2	BL Lac

using region of interest (ROI) sizes of 15 and 30 degrees, with energy ranges set between 100 MeV − 300 GeV and in subsets for analysis of different energy bins. The time frame of the data query was set to the maximum time available at the time of extraction, e.g. 239557417 - END (MET) or 2008-08-04 - END, with MET standing for Mission Elapsed Time.

A Fedora 20 (x86_64) Linux system was used for time series analysis of the datasets, after installation of the Fermi Science Tools v9r32p5 in conjunction with the python LATAnalysisScripts v0.2.0 and Heasoft v6.15.1. These software packages and instruction manuals are freely available from the Fermi_HEASARC site. The likelihood analysis and upper limit calculation were done by the author using the University of the Free State (UFS) High Performance Computing (HPC) facility.

The files extracted from the LAT database were in the form of spacecraft files L..._SC00.fits and photon or event files L..._PH0(i).fits (where i varied according to the amount of files required to split the extracted photon events based upon

the parameters of the extracted datasets).

5.3.1 Binned likelihood analysis

The analysis and search for $\gamma -$ ray emission from AE Aquarii were initiated by doing a binned likelihood analysis, to search for possible long term continuous VHE emission from AE Aquarii that might be revealed through the cumulative effect of the binning process. The events files were filtered as follows: The energy range under consideration was set between 100-300 000 MeV for evclass = 2. The value for the evclass was based on the fact that for LAT Pass 7 data the source events were specified as event class 2. The ROI radius was set to 15 degrees at a zenith angle of 100 degrees with a pixel scale defined as 0.1 degrees/pixel resulting in a resolution of 150 x 150 pixels.

The value for the ROI was chosen based on the criterion that the area in question must just be large enough to include enough of the already identified sources to strengthen the models used during the analysis process for a search of a specific source within the ROI. An additional criterion for the size of the ROI was such that the boundary of the 3D counts map should define the ROI used during binned likelihood analysis. To include the full square 3D counts map spatial boundary, the ROI must be larger because the region selected during the data extraction step was conical.

Because the Earth limb was a strong source of background photons, the value for the zenith angle was chosen in such a way that this effect was minimized. By setting the zenith at 100 degrees (the value most commonly used), a buffer of 13 degrees between the Earth limb and the ROI was established. The resolution was chosen such that a strong enough probability map could be generated with enough fine detail to identify features, while at the same time setting the resolution low enough to limit computer processing. These criteria were set after careful study of the Web based tutorials and *Fermi* "Cicerone" (See Figure 5.3 for an example of a raw and filtered photon/events file).

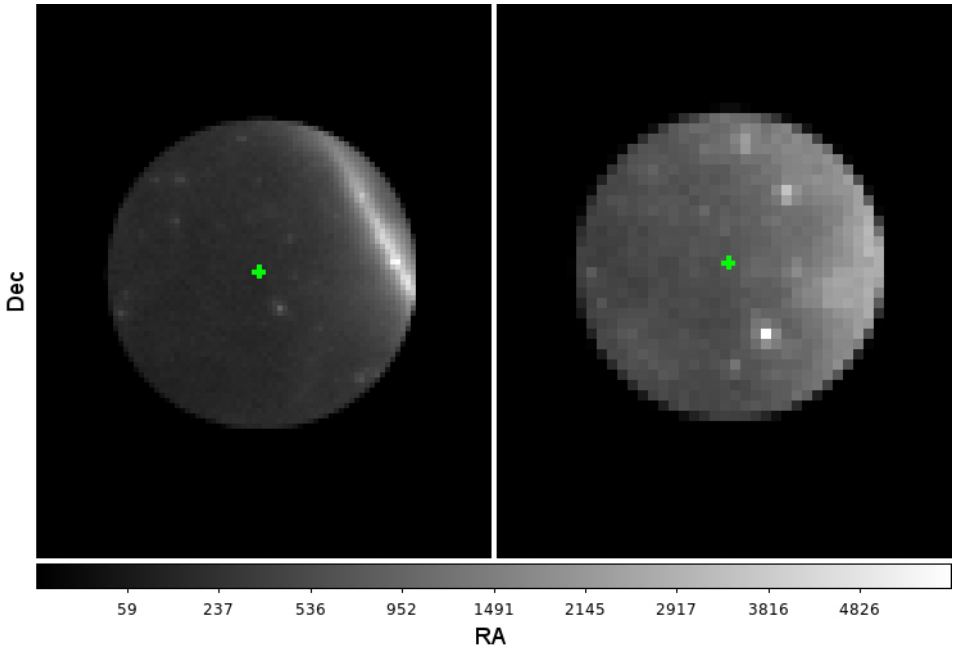

Figure 5.3: Raw ($60° \times 60°$) and filtered ($30° \times 30°$) photon/events file. The coordinates for AE Aquarii are indicated by a green cross. The colour bar indicates the normalised counts levels.

Binned likelihood analysis was performed on the filtered events files using the prescribed methods from the Web-based tutorials and the Cicerone (See Figure 5.4 for a counts map generated using the above-mentioned values).

The latest background models available at the time of analysis were used along with a source model file created using the available tools and resources (See Figure 5.5 for the completed binned likelihood analysis image or TS map for the total time).

The region encircled in green is centred on AE Aquarii, while the known sources from the 2nd *Fermi* Catalogue are encircled in yellow and numbered according to Table 5.1. The sizes of the circles are inversely proportional to the probability of the likelihood analysis model, i.e., the smaller the circle the better the model fitted for the detected source, or in other words the stronger the $\gamma -$ ray emission from

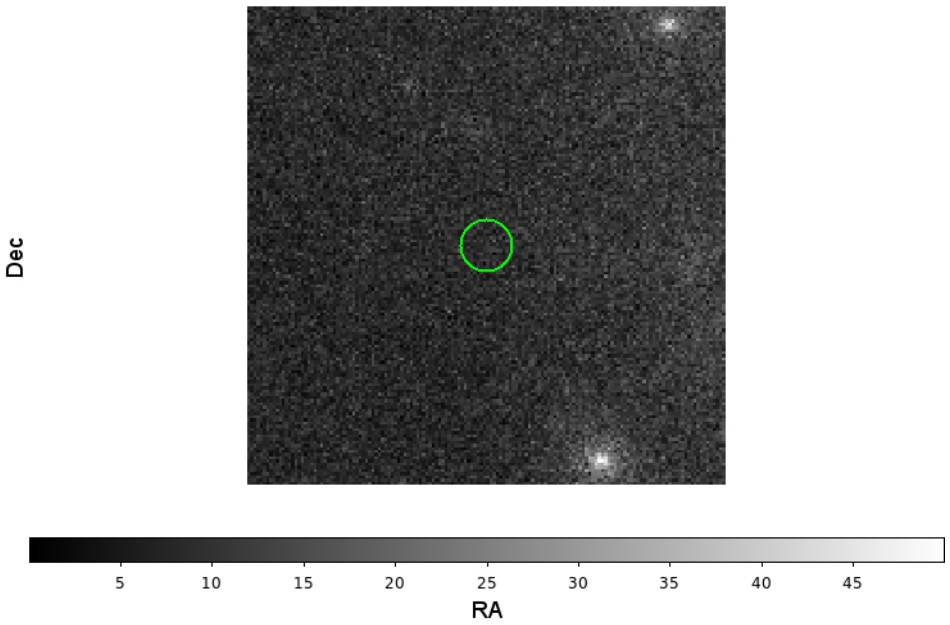

Figure 5.4: Counts map centered around AE Aquarii (150×150 pixels). The colour bar indicates the normalised counts levels.

the source. As seen in Figure 5.5, no statistically significant source (actually no source) was detected at the target coordinates for AE Aquarii. For this reason the size of the circle was set to 2 degrees (which is the size of the error box for *Fermi*-LAT sources as listed in the *Fermi*-LAT source catalogue). Based on the visual results obtained, no conclusive argument could be made for a positive detection of any steady continuous $\gamma-$ray emission from AE Aquarii. Therefore additional source detection methods were used.

5.3.2 Unbinned likelihood analysis

An unbinned likelihood analysis was also performed on the central 80x80 pixel area of the filtered events file, with the ROI set to 10 degrees based on the fact that with unbinned likelihood analysis the ROI is not defined by a 3D counts map boundary. This helped to facilitate the search and analysis of possible variable VHE emission from AE Aquarii, since it is recommended to use the unbinned likelihood

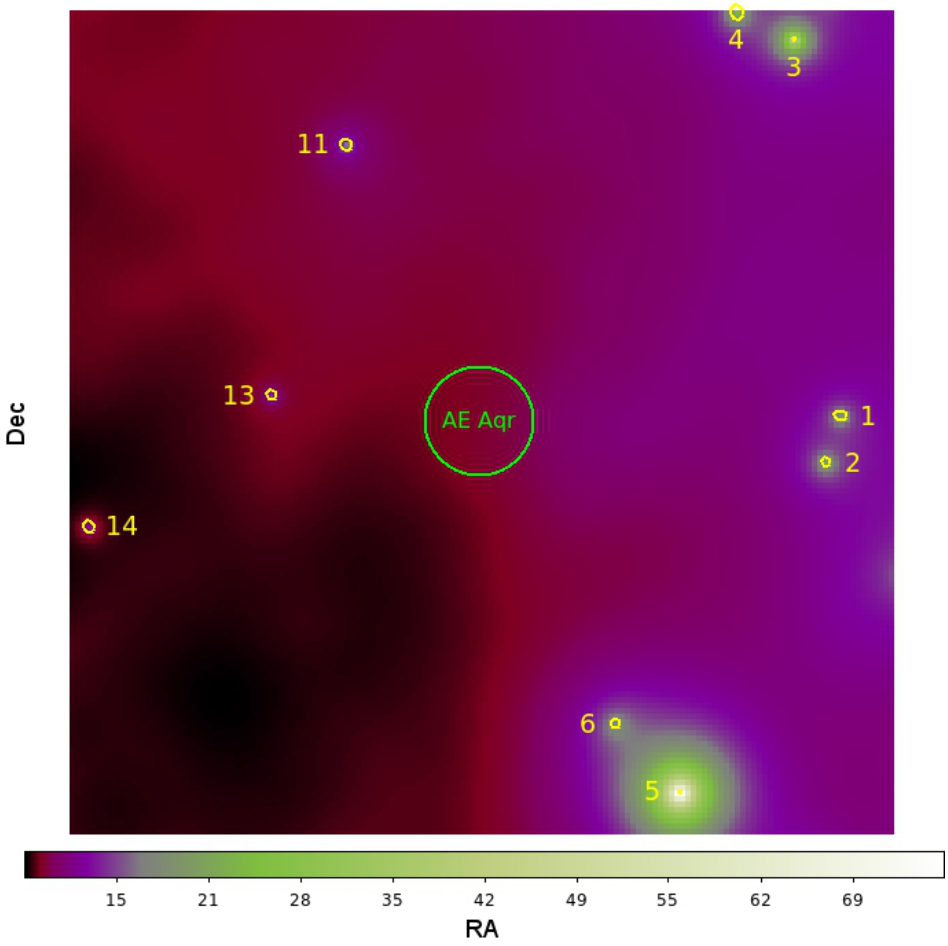

Figure 5.5: Binned likelihood analysis map indicating fitted sources. The colour bar indicates the normalised counts levels.

analysis when considering data over short time periods with few events. This was also the preferred method for time series analysis of low event probability *Fermi* data. Thus if any $\gamma-$ ray emission mechanism exists close to the WD, the emission could inherently have event arrival times at frequencies centred close to the WD spin period of 33.08 s (fundamental frequency) and 16.54 s (first harmonic) (as reported by Meintjes et al. (1992, 1994) and Chadwick et al. (1995)). Therefore with event times being relatively short compared to total available region coverage time, unbinned likelihood analysis was explored.

As with the binned likelihood analysis, the unbinned likelihood analysis method was performed as prescribed by the Web based tutorials and *Fermi* "Cicerone" (See Figure 5.6 for the final residual TS map for the unbinned likelihood analysis).

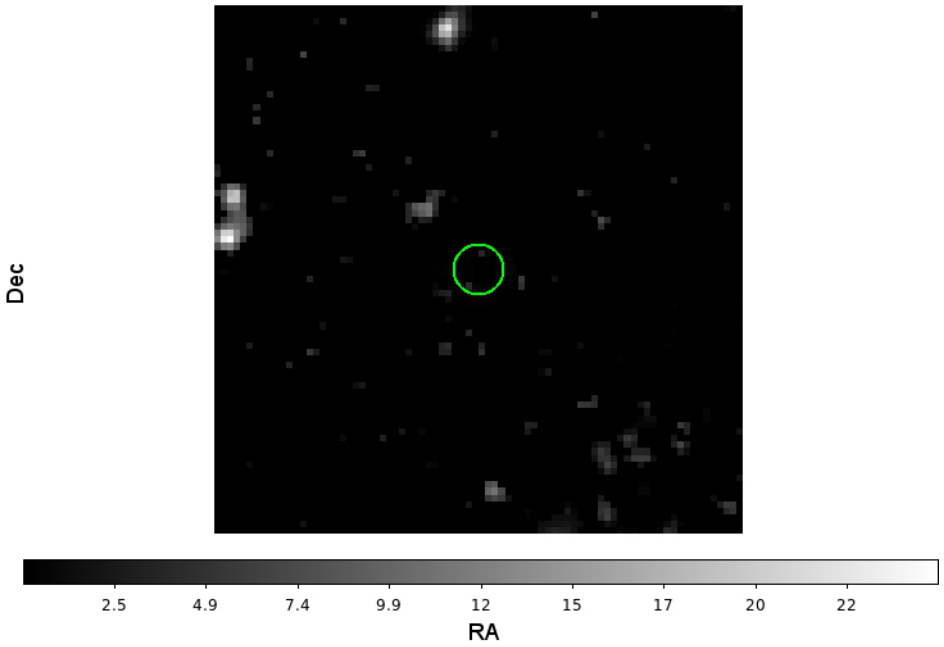

Figure 5.6: Unbinned 80×80 pixel likelihood analysis map. The colour bar indicates the normalised counts levels.

The region encircled in green is centred on AE Aquarii. Comparing this map to the full binned TS map is represented by Figure 5.7.

Based on the results obtained, again no conclusive argument could be made for a positive detection of any $\gamma-$ray excess from AE Aquarii as with the binned likelihood analysis results. Therefore additional source detection methods were used.

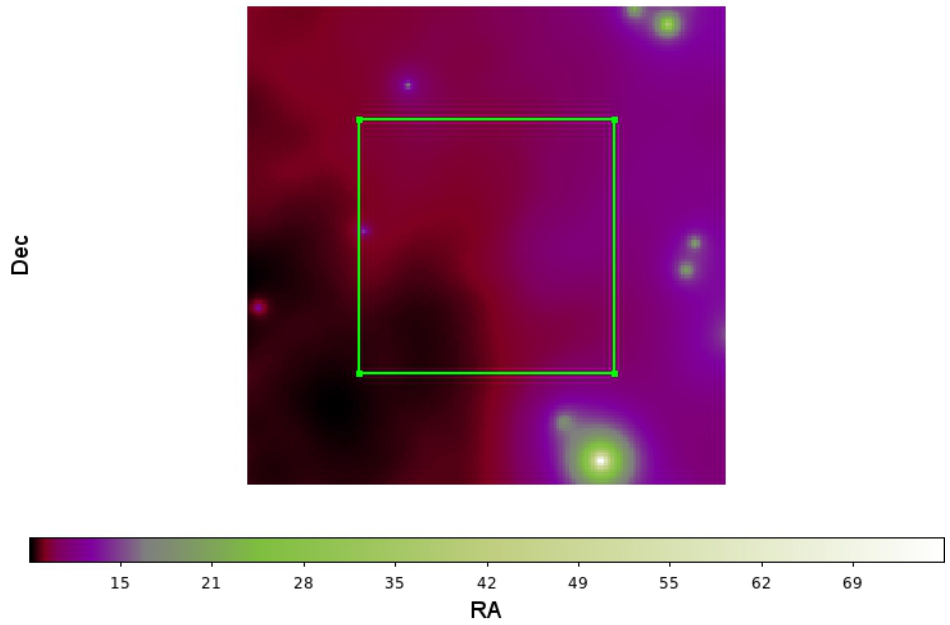

Figure 5.7: Smaller 80×80 pixel region compared to full binned TS map. The colour bar indicates the normalised counts levels.

5.3.3 Periodogram analysis

Considering the results from the likelihood analysis indicating no statistically significant detection, the assumption can safely be made that if there is any $\gamma-$ray emission from AE Aquarii, it will be at the noise level. Therefore an analysis of the noise profile and structures of the photon events data were considered.

Because of the known fundamental frequency and first harmonic periodicity of 33.08 s (30.23 mHz) and 16.54 s (60.459 mHz) for the rapidly spinning WD (detectable from Optical to X-ray), and the argument that the WD in AE Aquarii could possibly behave like a spun-up pulsar (Oruru and Meintjes (2012)), a search for periodicities conducted around these two periods was justified. However, earlier reports of pulsed VHE emission involve QPO-like features close to the spin period. Therefore, as a first step, a search over a wide frequency range has been conducted within a preselected energy range of the *Fermi*-LAT.

The following technique was used. A *Fermi* dataset covering an energy range of 250 MeV-300 GeV was downloaded from the Fermi_HEASARC site as well as the latest spacecraft file. The use of the latest spacecraft file is important as it contains the telescope telemetry data and good time interval values, which has to cover the whole photon events dataset in question. The specified energy range was chosen in such a way as to exclude galactic background noise contamination at lower energies, and also compensate for lack of counts at high energies due to the rapid fall-off of detected events at higher energies. The selected dataset was used to construct a power spectrum using the "gtpsearch" tool available in the Fermi Science tools package. A Rayleigh analysis was done, centred on the coordinates of AE Aquarii, with the step size (2.97×10^{-5} Hz) at 5000 times the Fourier resolution (5.94×10^{-9} Hz), considering the very long time baseline of the datasets, and the number of trials set at 2000, centred on 40 mHz to cover the frequencies from 10-70 mHz. The "gtpsearch" tool automatically corrects the event times to barycentric time. The barycentric time corrections are for a space based detector and therefore require the latest spacecraft file for the most complete telescope telemetry and time information values. A concise discussion of barycentric corrections and timing analysis techniques such as Rayleigh analysis is included in Appendix A.

An analysis of the Rayleigh statistic Z peak distribution from the Rayleigh analysis for the selected energy range was done to determine the signal/noise significance. The spread of the power was determined through the calculation of the standard deviation (σ) of the power for an expected normal distribution. For additional discussions of different distributions, refer to Appendix A.

For the power spectrum the assumption was made that the peaks with a power distribution level below 4σ could be considered as either not significant or noise. This assumption was made based on the fact that a 5σ level is recommended in the *Fermi* "Cicerone" for a first time detection of a source using *Fermi* data. Therefore any source or signal detections below 5σ has to be tested for significance through additional independent tests, while anything below 4σ could in theory be considered as noise. The Rayleigh power spectrum was plotted with lines indi-

cating the 4σ level in terms of the power values. Additionally, lines indicating the current model for the fundamental frequency (F_0) and first harmonic ($2F_0$) of the WD spin for AE Aquarii were also indicated. The Rayleigh power spectrum was graphed in terms of the Rayleigh probability value, i.e. $-\text{Log}_{10}(\text{Pr})$ (See Appendix A for a discussion of Rayleigh time series analysis). The spectra were also used to evaluate the noise structure. Based on accepted white noise models a $-\text{Log}_{10}(\text{Pr})$ spectrum graph for a dataset will have a horizontal base with the noise at a $-\text{Log}_{10}(\text{Pr}) \leq 3$ level. Another way to consider the noise structure of the power spectra is by plotting a histogram of $\log_{10}(\text{dN/dZ})$ versus the Rayleigh statistic Z. The $\log_{10}(\text{dN/dZ})$ graph for white noise will have an inverse linear trend (i.e. $\log_{10}(\text{x})$ becomes $\frac{1}{\text{xln10}}$) in the peak power distribution, with any strong deviations from the trend considered as possible signatures for a departure from the white noise or possible signals within the data. Figures 5.8 and 5.9 represent the results for the analysis.

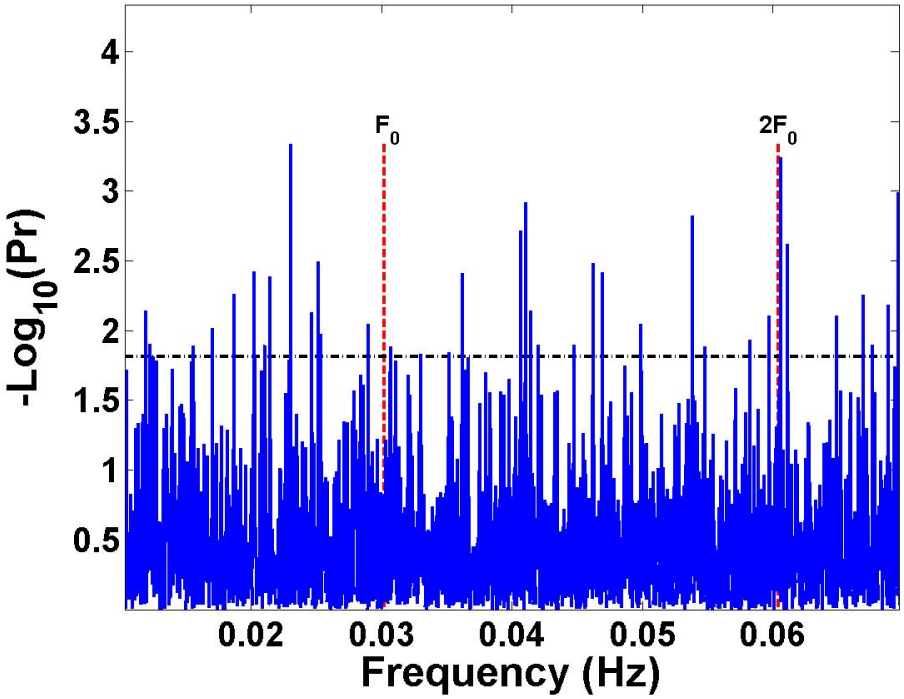

Figure 5.8: Rayleigh $-\text{Log}_{10}(\text{Pr})$ spectrum for 250 MeV-300 GeV for AE Aquarii.

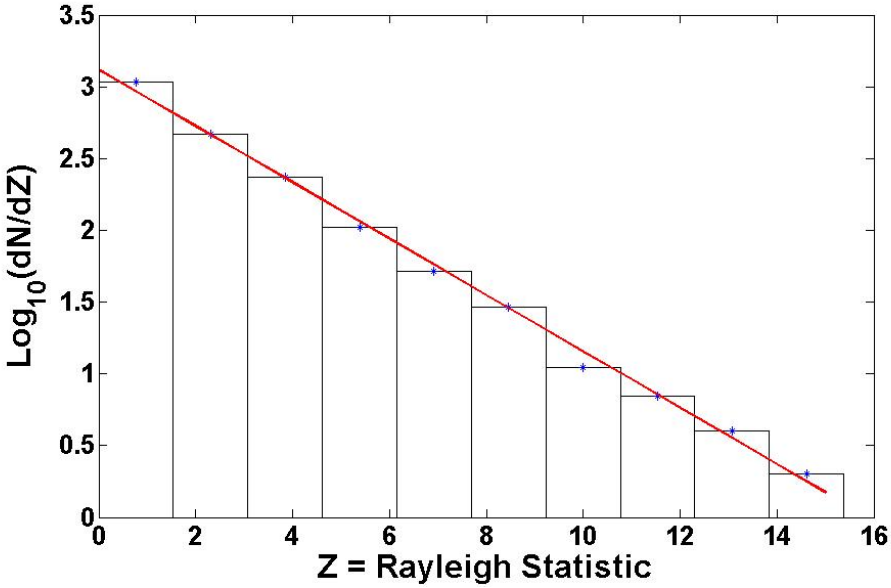

Figure 5.9: Histogram of the Rayleigh Z distribution for 250 MeV-300 GeV for AE Aquarii.

As can be seen, a peak at the first harmonic of the WD spin period is observable, but below the 4σ level, i.e., within the noise. The 4σ level is indicated with a black line. As shown in Figure 5.9 the Rayleigh power peaks has a white noise distribution. Figure 5.10 represents a closer view of the peaks centred around the first harmonic of the WD spin, with lines indicating the $3\sigma, 4\sigma$ and 5σ levels for the frequency range considered. As can be seen there is a strong peak close to the first harmonic of the WD spin resembling strong QPO features absent during periods of enhanced activity (Patterson (1979) and Meintjes et al. (1992, 1994)). These QPO features are not unique, and are observable in multiple wavelengths from optical to VHE power spectra, with examples seen in Figures 2.4 and 5.11.

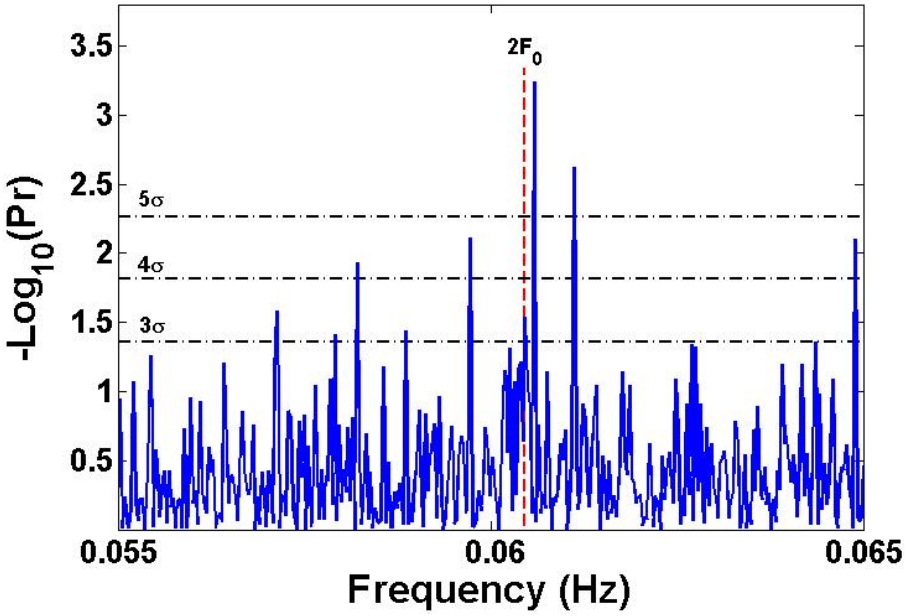

Figure 5.10: Rayleigh $-\mathrm{Log}_{10}(\mathrm{Pr})$ spectrum centred on the first harmonic for the WD spin ephemeris for 250 MeV-300 GeV for AE Aquarii.

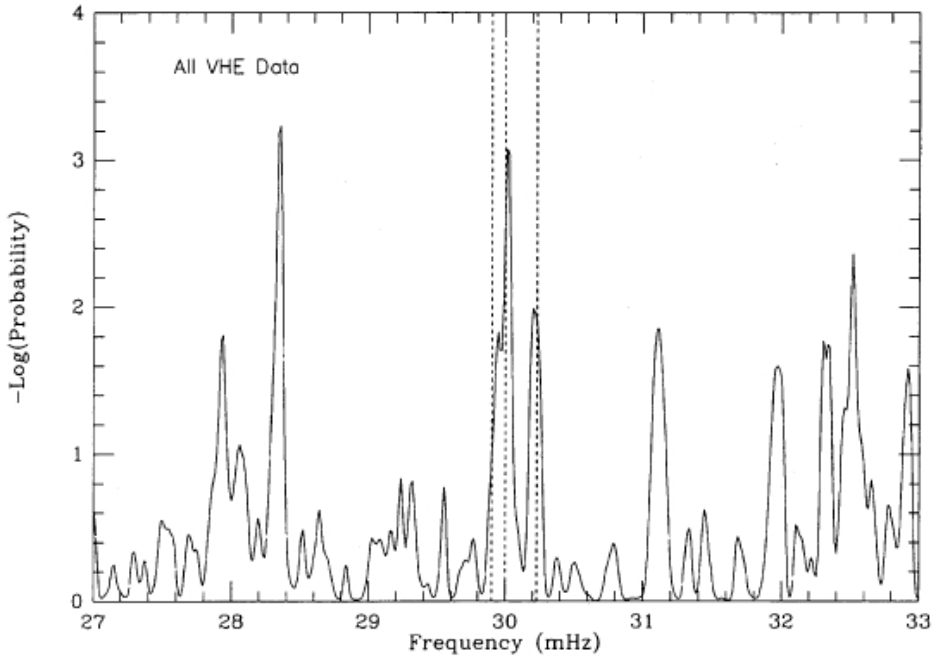

Figure 5.11: Example of QPO frequencies observable in VHE data resembling optical QPOs observed during optical bursts (Adopted from Meintjes et al. (1992)).

The peak observed (16.5398 s) at the first harmonic of the WD spin period as well as the QPO peak (16.507 s) were subsequently tested through pulse phase analysis. The "gtpphase" tool was used to assign pulse phases to each record in the event files, with barycentric corrections automatically applied by the algorithm using the coordinates for AE Aquarii and the relevant spacecraft file. The determined pulse phases over the energy range considered (250 MeV − 300 GeV) for the two test periods were plotted as folded light curves with best-fit sinusoidal waves indicated. The pulse phase diagrams were plotted over two phases for clarity. As can be seen there appears to be a better fit for a double peak structure to the pulse phase diagram for the QPO peak observed, than for the peak observed at the first harmonic of the WD spin period. This is consistent with the corresponding peak power strengths in the Rayleigh spectrum. Although it has to be mentioned that the error bars within the pulse phase diagrams is also consistent with a constant signal, which is consistent with the shown white noise for the Rayleigh power peak distribution.

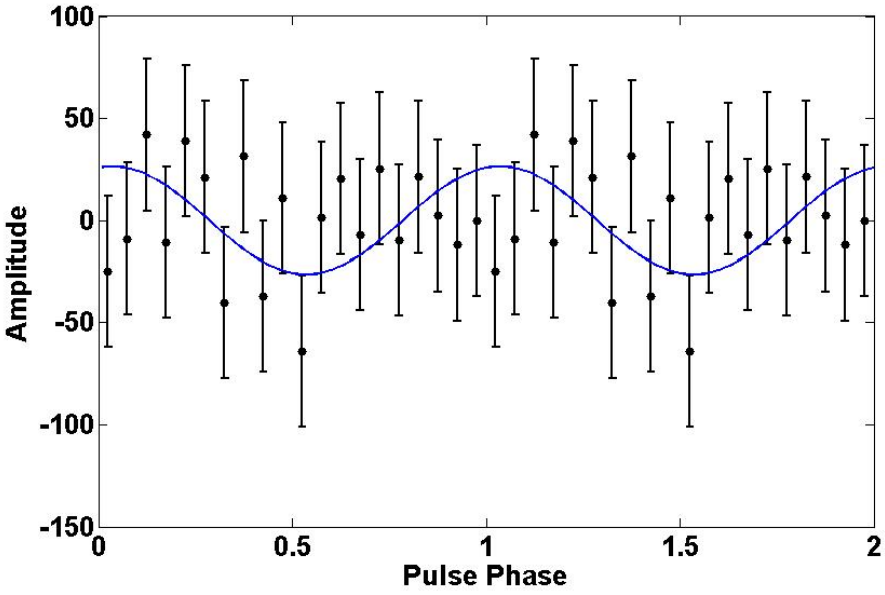

Figure 5.12: Pulse phase diagram for the peak at the first harmonic of the WD spin period. Best-fit sine wave is shown, with two phases shown for clarity.

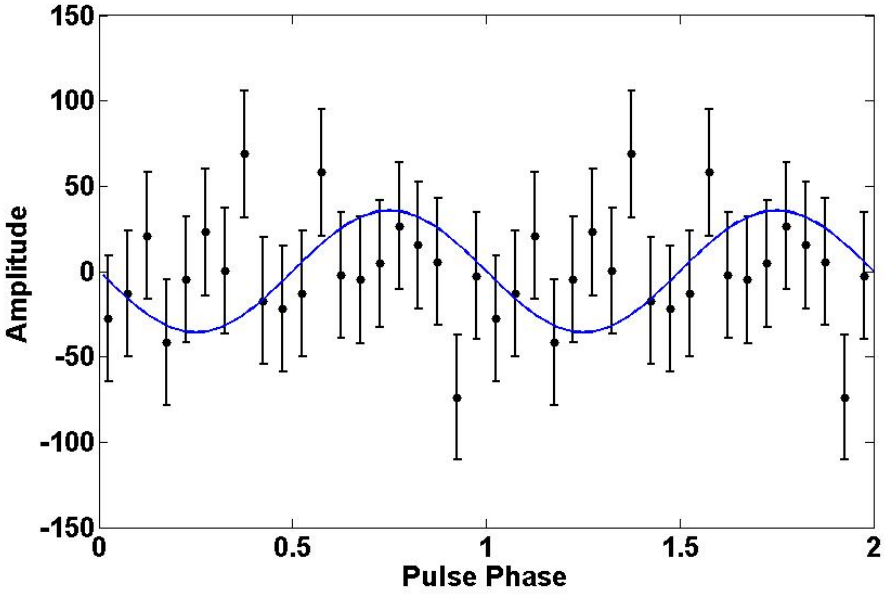

Figure 5.13: Pulse phase diagram for the peak at the strong QPO-like peak close to the WD spin period. Best-fit sine wave is shown, with two phases shown for clarity.

5.3.4 Test of periodogram analysis results

To check the periodogram analysis results for AE Aquarii, where there might be a possible low level peak at the first harmonic $2F_0$, the occurrence of this peak through different energy ranges was tested. This consisted of the following technique: A series of *Fermi* energy bins were downloaded from the Fermi_HEASARC site as well as the latest spacecraft file. The bins were 250-500 MeV, 500-750 MeV, 750-1000 MeV, 1-10 GeV, 1-100 GeV and 1-300 GeV. The bins were chosen in such a way as to make modular analysis possible. The bins had to exclude galactic background noise contamination at lower energies, and also compensate for lack of counts at high energies due to the rapid fall-off of detected events at higher energies.

Each energy bin was used to construct power spectra using the "gtpsearch" tool available in the Fermi Science tools package. A Rayleigh analysis was done, centred on the coordinates of AE Aquarii, with the step size (2.97×10^{-5} Hz) at 5000 times the Fourier resolution (5.94×10^{-9} Hz), considering the very long time

baseline of the datasets, and the number of trials set at 2000, centred on 40 mHz to cover the frequencies from 10-70 mHz.

As with the previous analysis, an analysis of the Rayleigh statistic Z peak distribution in each energy bin was done to determine the signal/noise significance. For the power spectra the assumption was again made that the peaks with a power distribution level below 4σ could be considered as either not significant or noise, with the σ value determined using the same method as with the previous analysis. The Rayleigh power spectra for the different energy bins were plotted with lines indicating the 4σ level in terms of the peak values. Additionally, lines indicating the current model for the fundamental frequency (F_0) and first harmonic ($2F_0$) of the WD spin for AE Aquarii were also indicated.

The Rayleigh power spectra were graphed in terms of the Rayleigh probability value, i.e. $-\mathrm{Log}_{10}(\mathrm{Pr})$. The spectra were also used to evaluate the noise structure. As mentioned previously, a $-\mathrm{Log}_{10}(\mathrm{Pr})$ spectrum graph for a dataset will have a horizontal base with the noise at a $-\mathrm{Log}_{10}(\mathrm{Pr}) \leq 3$ level, similarly a histogram of $\log_{10}(\mathrm{dN/dZ})$ versus the Rayleigh statistic Z will have an inverse linear trend (i.e., $\log_{10}(\mathrm{x})$ becomes $\frac{1}{\mathrm{xln10}}$) in the peak power distribution for white noise data. Any strong deviations from the white noise trend in the histogram can be considered as possible signatures for a departure from the white noise or possible signals within the data. Refer to Figures 5.14 and 5.20 for energy bin 250-500 MeV, Figures 5.15 and 5.21 for energy bin 500-750 MeV, Figures 5.16 and 5.22 for energy bin 750-1000 MeV, Figures 5.17 and 5.23 for energy bin 1-10 GeV, Figures 5.18 and 5.24 for energy bin 1-100 GeV and Figures 5.19 and 5.25 for energy bin 1-300 GeV.

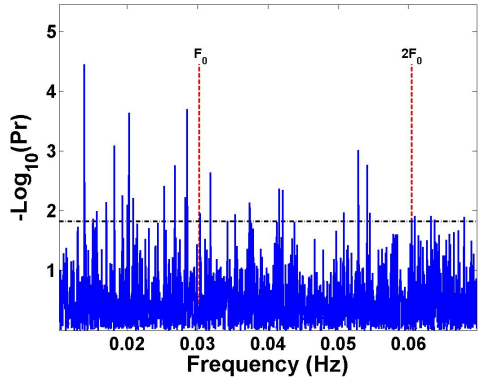

Figure 5.14: Rayleigh $-\mathrm{Log}_{10}(\mathrm{Pr})$ spectrum for 250-500 MeV for AE Aquarii.

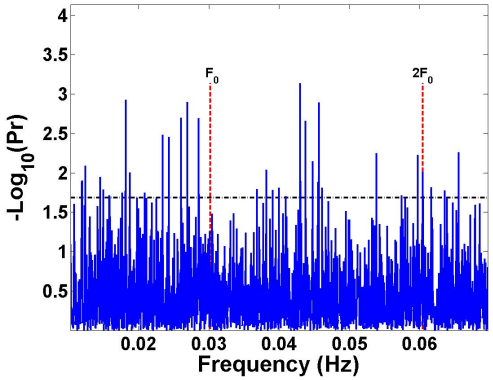

Figure 5.15: Rayleigh $-\mathrm{Log}_{10}(\mathrm{Pr})$ spectrum for 500-750 MeV for AE Aquarii.

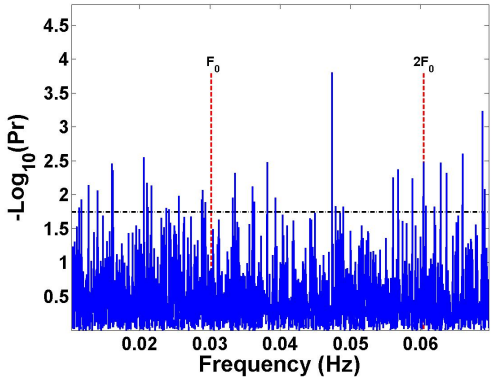

Figure 5.16: Rayleigh $-\mathrm{Log}_{10}(\mathrm{Pr})$ spectrum for 750-1000 MeV for AE Aquarii.

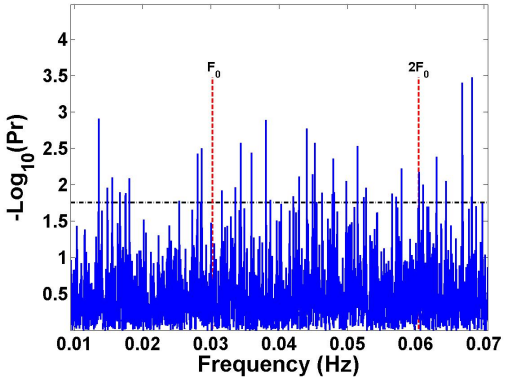

Figure 5.17: Rayleigh $-\mathrm{Log}_{10}(\mathrm{Pr})$ spectrum for 1-10 GeV for AE Aquarii.

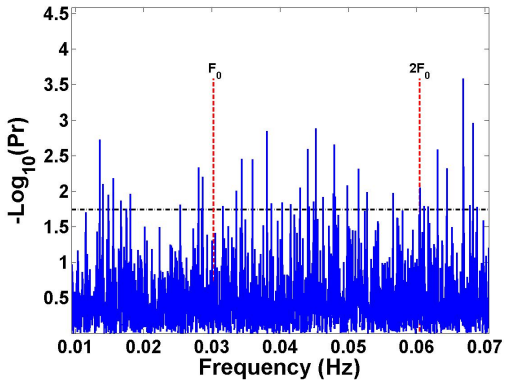

Figure 5.18: Rayleigh $-\mathrm{Log}_{10}(\mathrm{Pr})$ spectrum for 1-100 GeV for AE Aquarii.

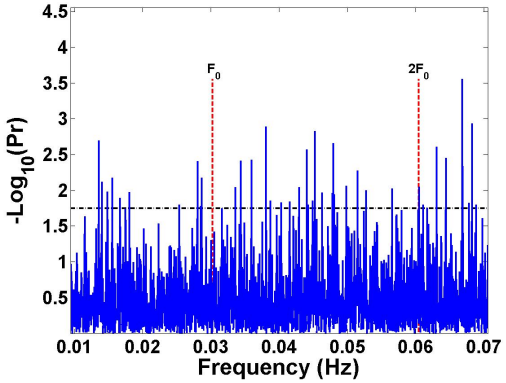

Figure 5.19: Rayleigh $-\mathrm{Log}_{10}(\mathrm{Pr})$ spectrum for 1-300 GeV for AE Aquarii.

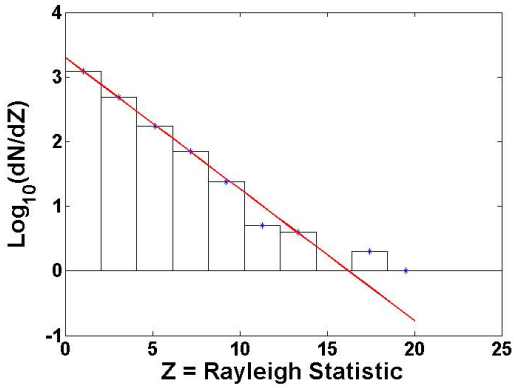

Figure 5.20: Histogram of the Rayleigh Z distribution for 250-500 MeV for AE Aquarii.

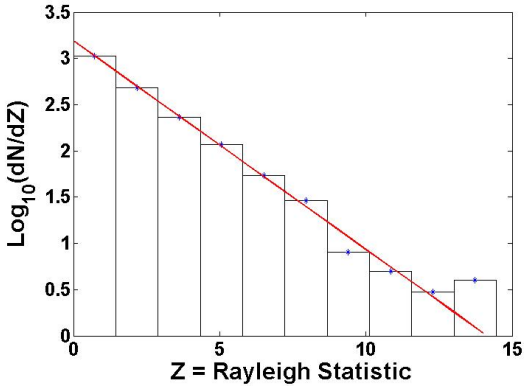

Figure 5.21: Histogram of the Rayleigh Z distribution for 500-750 MeV for AE Aquarii.

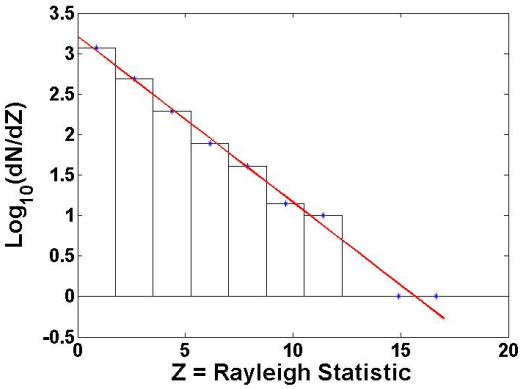

Figure 5.22: Histogram of the Rayleigh Z distribution for 750-1000 MeV for AE Aquarii.

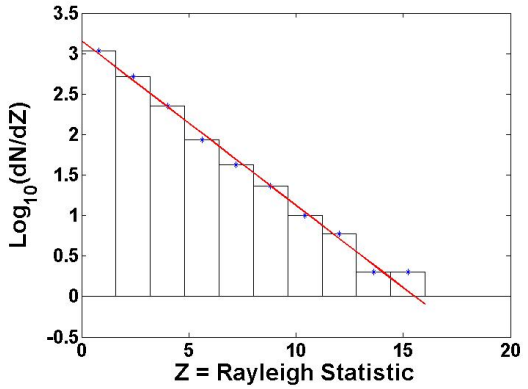

Figure 5.23: Histogram of the Rayleigh Z distribution for 1-10 GeV for AE Aquarii.

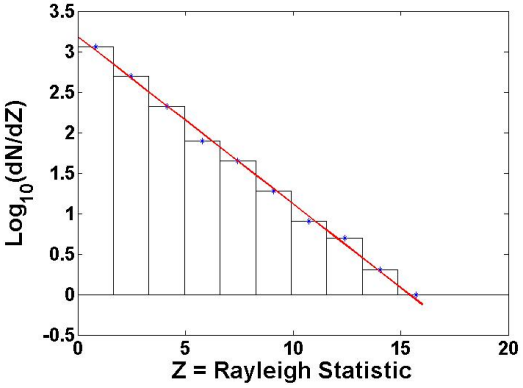

Figure 5.24: Histogram of the Rayleigh Z distribution for 1-100 GeV for AE Aquarii.

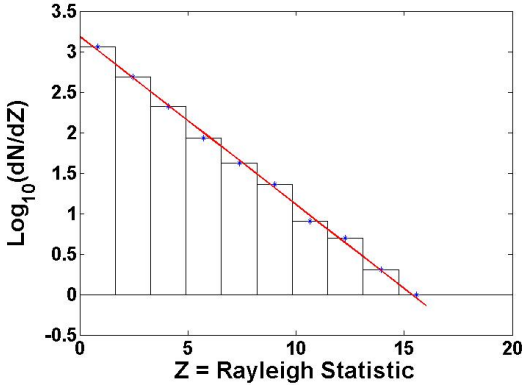

Figure 5.25: Histogram of the Rayleigh Z distribution for 1-300 GeV for AE Aquarii.

The Rayleigh power spectra were analysed for signal/noise level. With the data structure of the power spectra shown as predominantly white noise, and based upon above mentioned assumptions that the power spectrum peak power distribution levels below 4σ could be considered as white noise, the peaks with power greater than 4σ were sampled and analysed for signal/noise significance. Figures 5.26 and 5.27 show the sampled peaks with power above 4σ for the relevant energy bins.

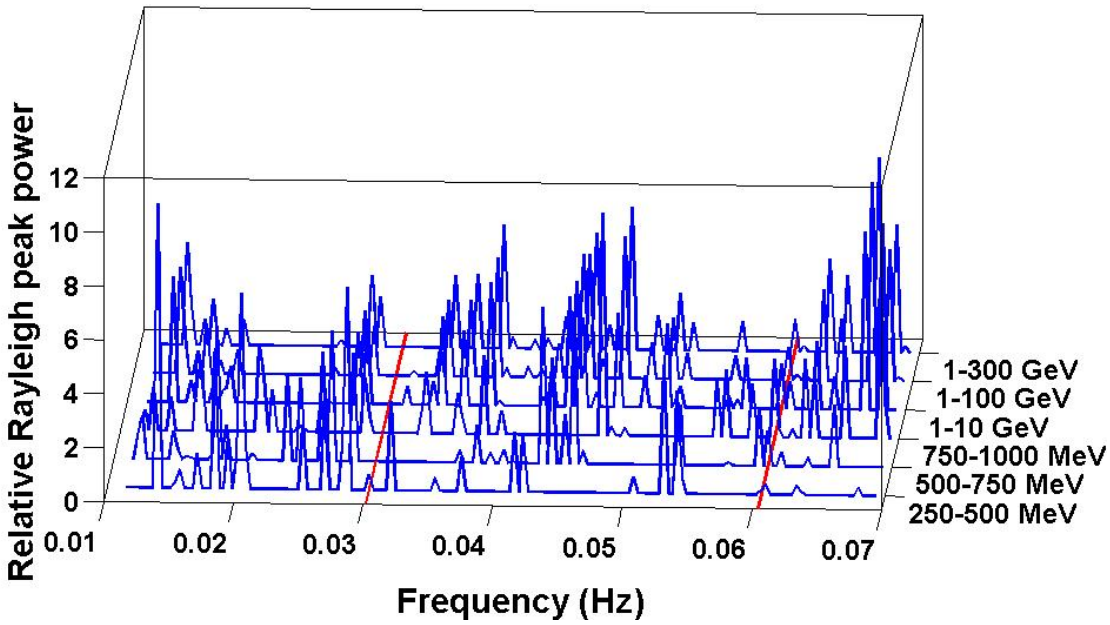

Figure 5.26: 3D view of sampled Rayleigh peaks with power above 4σ for examined energy bins for AE Aquarii. The fundamental frequency and first harmonic of the current model ephemeris for the WD spin is shown in red.

The sampled power peaks greater than 4σ from the different energy bins were then stacked incoherently. This was based upon the assumption that possible signal peaks within the noise structure would have components in a greater number of bins, while noise patterns would have a more random distribution. This summation of the sampled power peaks would lead to a boost in signal peak power, and a drop in noise peak power. The final resultant power spectrum (Figure 5.28) were then considered for signal detection tests.

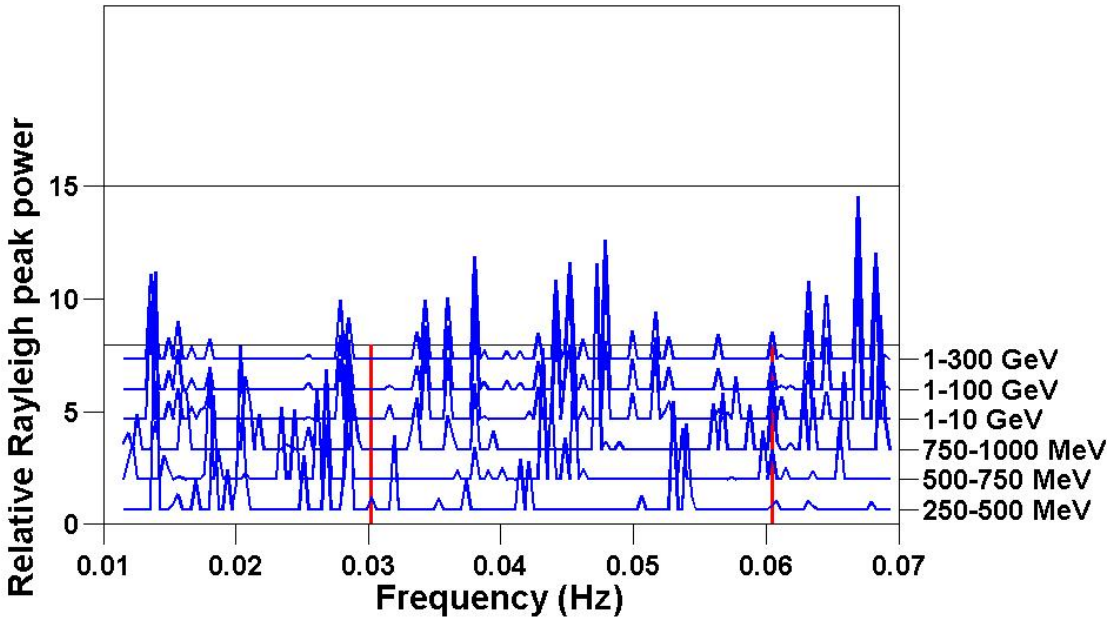

Figure 5.27: Front view of sampled Rayleigh peaks with power above 4σ for examined energy bins for AE Aquarii. The fundamental frequency and first harmonic of the current model ephemeris for the WD spin is shown in red.

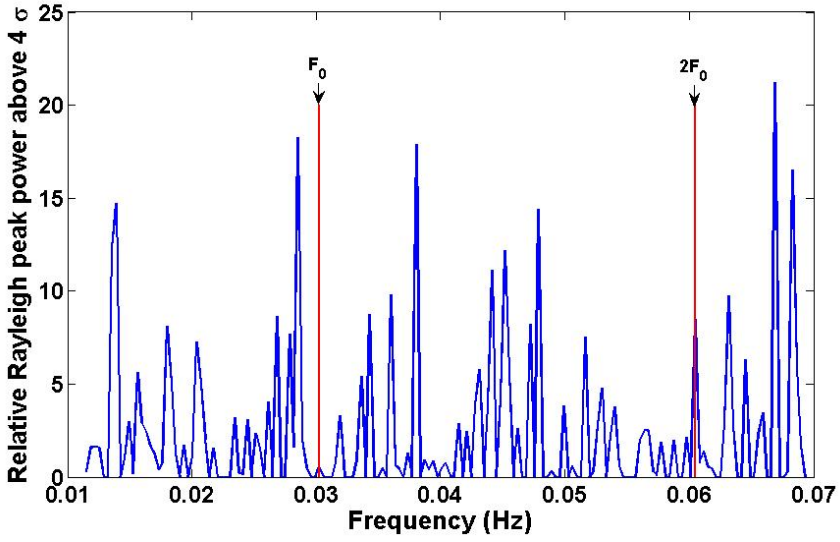

Figure 5.28: Combined power peaks from the separate energy bins for AE Aquarii.

As seen from Figure 5.28, there appears to be a power peak at the current ephemeris model position for the first harmonic at 60.46 mHz, with the fundamental frequency and first harmonic indicated in red. Whether this peak is a possible signal peak (although there are stronger peaks) can only be considered with further analysis of the nature of the different peaks surrounding it. With a histogram of the peak distribution in terms of the Rayleigh power Z, a noise profile versus peak power can be examined. A combined histogram for all datasets considered in the above analysis was therefore plotted (Figure 5.29), with a white noise profile trend indicated.

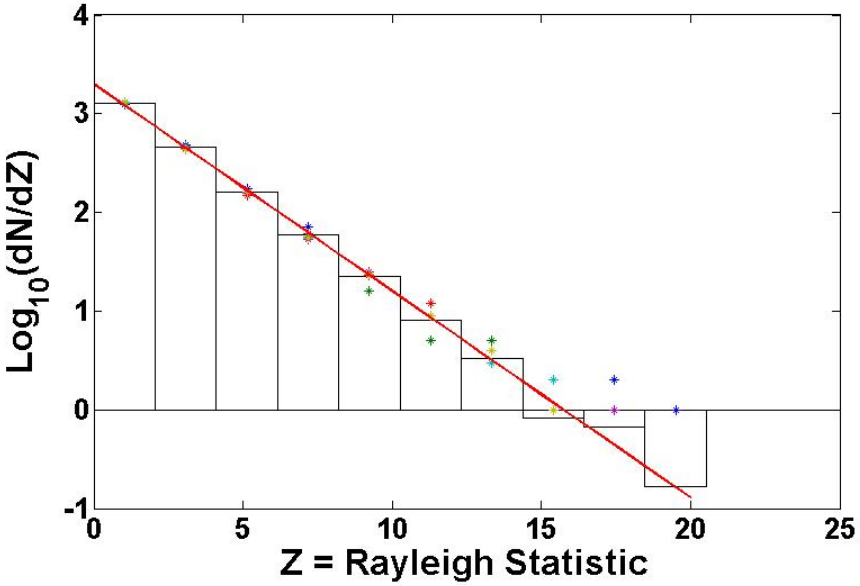

Figure 5.29: Histogram of the combined relative Rayleigh power Z for the separate energy bins for AE Aquarii, with the histogram values for the separate energy bins indicated. A white noise trend is also shown in red.

The occurrence of power above the 4σ level at $2F_0$ is a positive development although the total power at all frequencies conform to white noise. To test the hypothesis that AE Aquarii may exhibit low level power at $2F_0$ the frequency of occurrence of the pulse at $2F_0$ in the power spectra related to the different energy bins is compared to the power in all the other test frequencies above the 4σ significance level. It can be seen (Figures 5.26 and 5.27) that the pulse at $2F_0$ is

the only pulse with frequency of occurrence at the 100% ($> 3\sigma$) level in all energy levels (e.g. Figure 5.30).

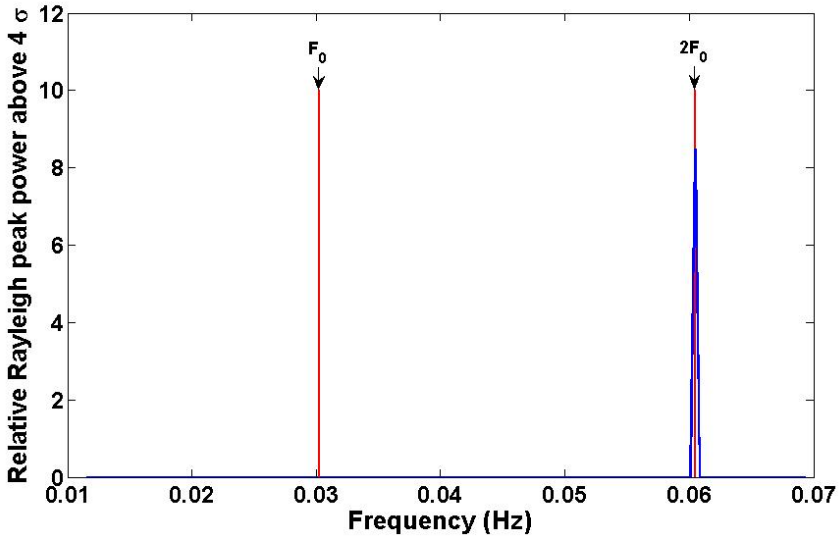

Figure 5.30: Rayleigh power peaks above the 4σ level with frequency of distribution at $> 3\sigma$ level between investigated energy bins for AE Aquarii.

It can be interpreted as an indication of a possible signal within the noise structure. Although Chadwick et al. (1995) also found pulsed emission centred on the first harmonic of the WD spin period, the nature and significance of the possible signal detected in this analysis can only be considered through further examination. The peak observed (16.5386 ± 0.02323 s) at the first harmonic of the WD spin period in the different energy bins was subsequently tested through pulse phase analysis. The "gtpphase" tool was used to assign pulse phases to each record in the event files, with barycentric corrections automatically applied by the algorithm using the coordinates for AE Aquarii and the relevant spacecraft file. The determined pulse phases over the different energy bins considered for the test period were plotted as folded light curves with best fit sinusoidal waves indicated. The pulse phase diagrams were plotted over two phases for clarity.

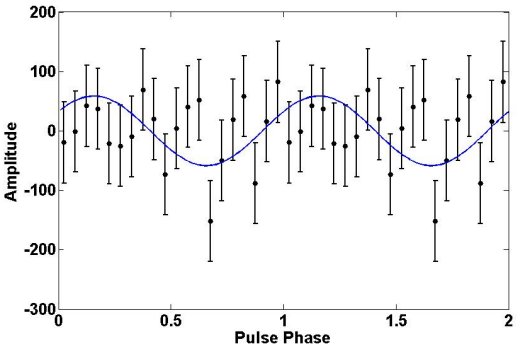

Figure 5.31: Pulse profile of the detected power peak at the first harmonic $2F_0$ for the 250-500 MeV energy bin for AE Aquarii.

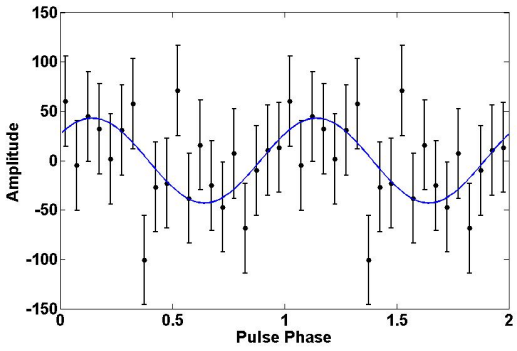

Figure 5.32: Pulse profile of the detected power peak at the first harmonic $2F_0$ for the 500-750 MeV energy bin for AE Aquarii.

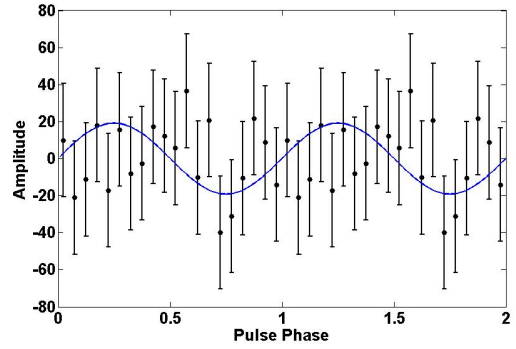

Figure 5.33: Pulse profile of the detected power peak at the first harmonic $2F_0$ for the 750-1000 MeV energy bin for AE Aquarii.

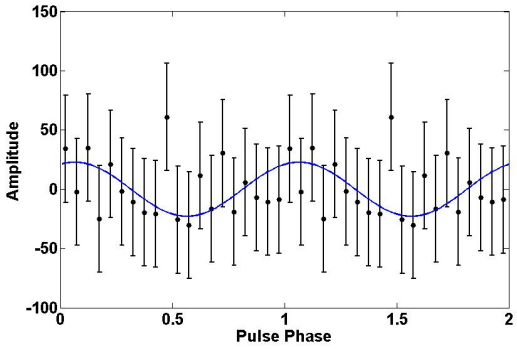

Figure 5.34: Pulse profile of the detected power peak at the first harmonic $2F_0$ for the 1-10 GeV energy bin for AE Aquarii.

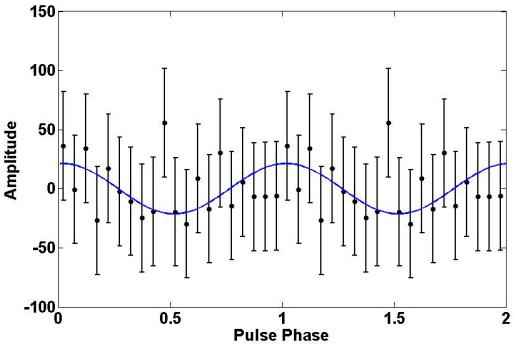

Figure 5.35: Pulse profile of the detected power peak at the first harmonic $2F_0$ for the 1-100 GeV energy bin for AE Aquarii.

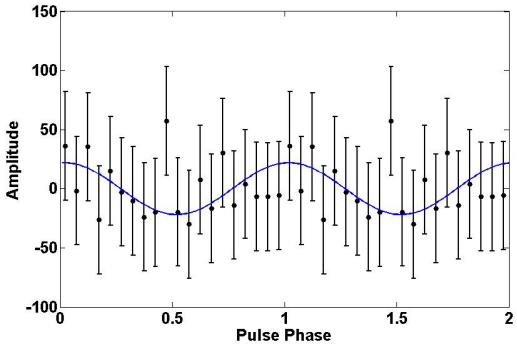

Figure 5.36: Pulse profile of the detected power peak at the first harmonic $2F_0$ for the 1-300 GeV energy bin for AE Aquarii.

5.3.5 Test for validity of analysis technique

The validity of the analysis technique was tested by doing a search for a similar signal within the *Fermi* data at two different locations not containing any known detected source within the ROI used during the analysis process. If a signal was detected at an independent location at the same frequency with the same properties, then the proposed signal detected for AE Aquarii could possibly be an inherent structure of the data or analysis technique. But if no signals were detected at locations with no suspected $\gamma-$ ray sources and only white noise structures were detected within the data, then it strengthens the case for the possible validity of the analysis technique and the results obtained.

This test was applied on two independent locations within the ROI, i.e. Zone-1 (306.0, 3.0, J2000, Decimal Equatorial) and Zone-2 (314.0, -5.0, J2000, Decimal Equatorial). Refer to Figure 5.37 for a graphical representation of the location of the two test zones in relation to AE Aquarii.

The same analysis technique was applied on these two test zones as described for the region centred on AE Aquarii. Following is the Rayleigh power spectra graphed in terms of the Rayleigh probability $-\mathrm{Log}_{10}(\mathrm{Pr})$ and the Rayleigh statistic Z distribution histograms for the different energy bins used during the analysis for Zone-1 and Zone-2 respectively.

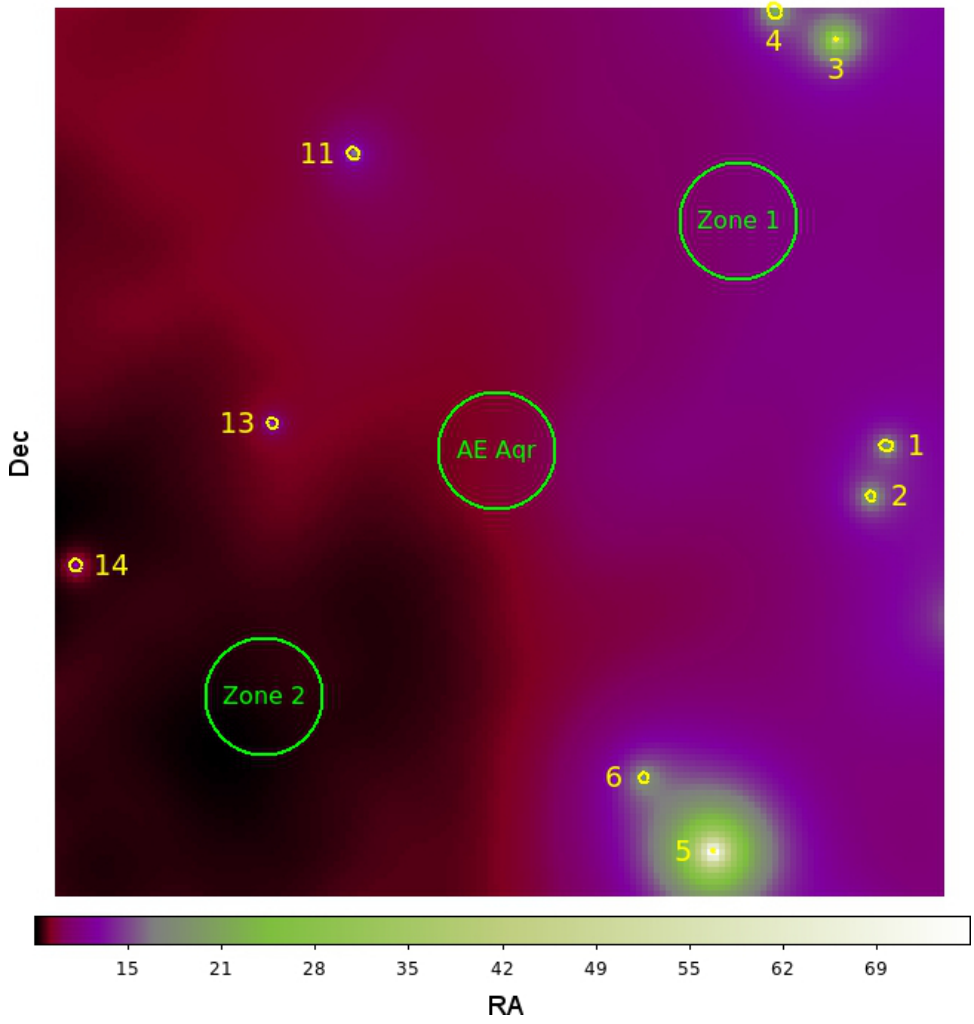

Figure 5.37: Binned TS map for the ROI centred on AE Aquarii, indicating the additional test zones. The colour bar indicates the normalised counts levels.

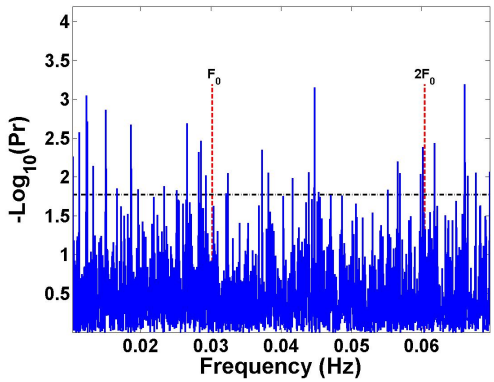

Figure 5.38: Rayleigh $-\mathrm{Log}_{10}(\mathrm{Pr})$ spectrum for 250-500 MeV for Zone 1.

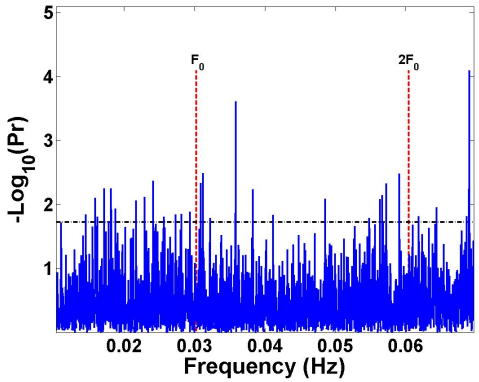

Figure 5.39: Rayleigh $-\mathrm{Log}_{10}(\mathrm{Pr})$ spectrum for 500-750 MeV for Zone 1.

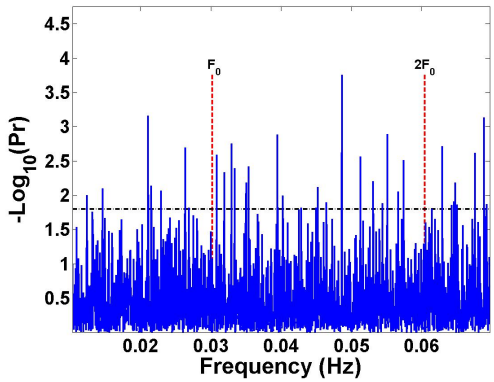

Figure 5.40: Rayleigh $-\mathrm{Log}_{10}(\mathrm{Pr})$ spectrum for 750-1000 MeV for Zone 1.

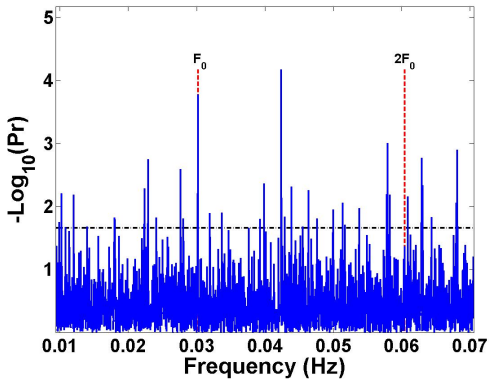

Figure 5.41: Rayleigh $-\mathrm{Log}_{10}(\mathrm{Pr})$ spectrum for 1-10 GeV for Zone 1.

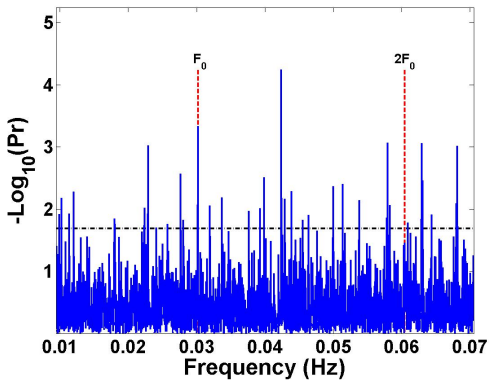

Figure 5.42: Rayleigh $-\mathrm{Log}_{10}(\mathrm{Pr})$ spectrum for 1-100 GeV for Zone 1.

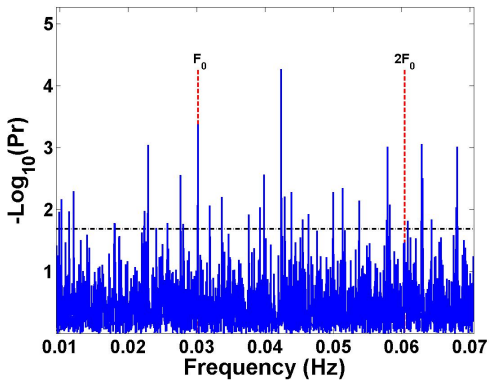

Figure 5.43: Rayleigh $-\mathrm{Log}_{10}(\mathrm{Pr})$ spectrum for 1-300 GeV for Zone 1.

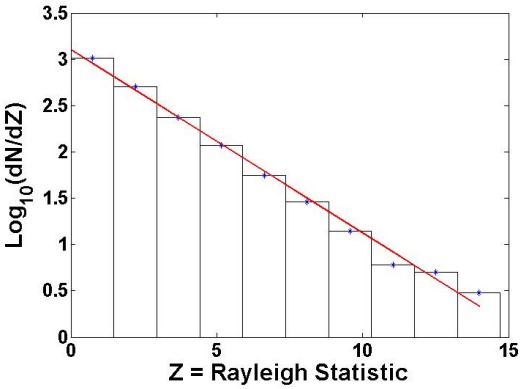

Figure 5.44: Histogram of the Rayleigh Z distribution for 250-500 MeV for Zone 1.

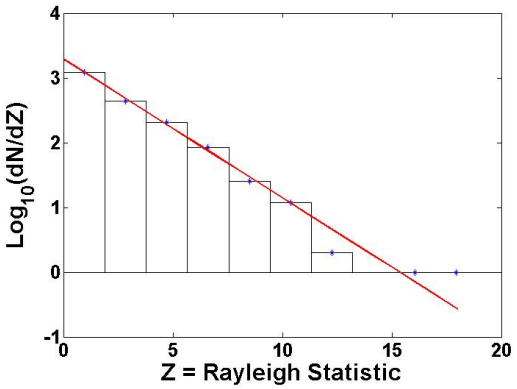

Figure 5.45: Histogram of the Rayleigh Z distribution for 500-750 MeV for Zone 1.

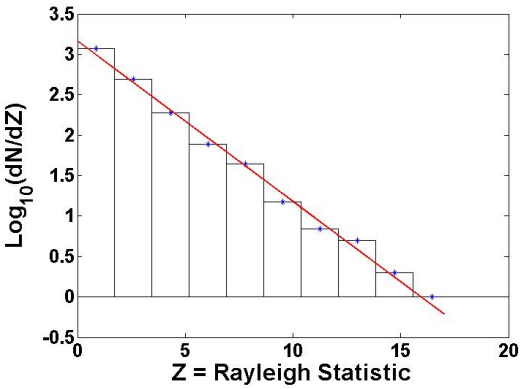

Figure 5.46: Histogram of the Rayleigh Z distribution for 750-1000 MeV for Zone 1.

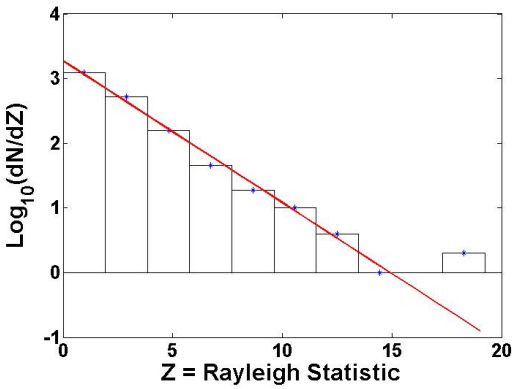

Figure 5.47: Histogram of the Rayleigh Z distribution for 1-10 GeV for Zone 1.

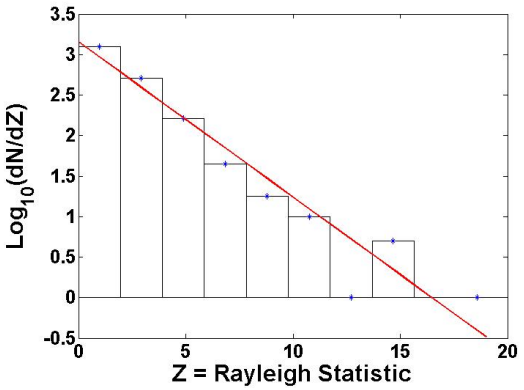

Figure 5.48: Histogram of the Rayleigh Z distribution for 1-100 GeV for Zone 1.

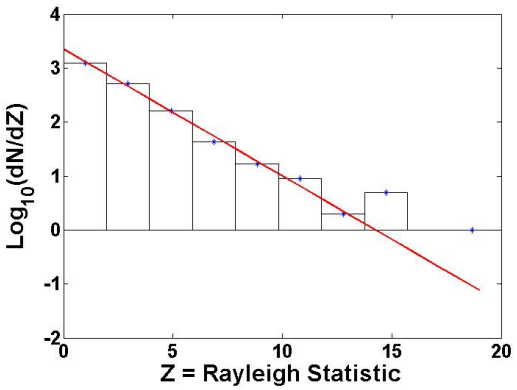

Figure 5.49: Histogram of the Rayleigh Z distribution for 1-300 GeV for Zone 1.

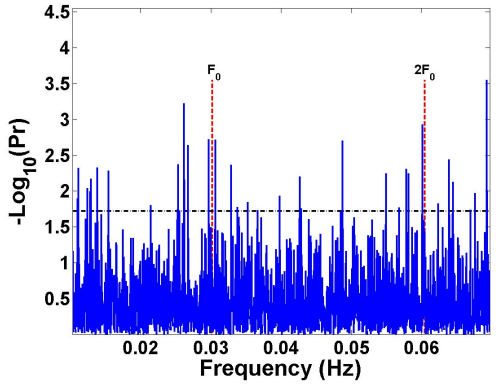

Figure 5.50: Rayleigh $-\mathrm{Log}_{10}(\mathrm{Pr})$ spectrum for 250-500 MeV for Zone 2.

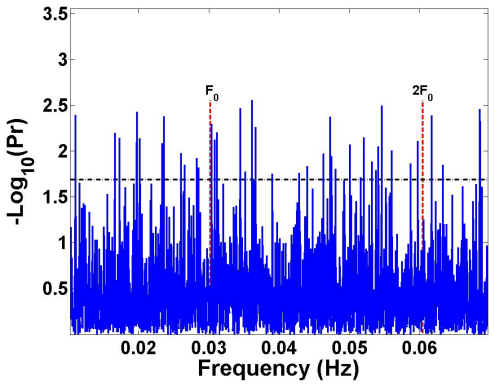

Figure 5.51: Rayleigh $-\mathrm{Log}_{10}(\mathrm{Pr})$ spectrum for 500-750 MeV for Zone 2.

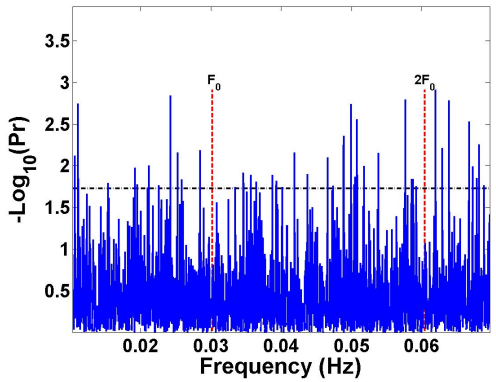

Figure 5.52: Rayleigh $-\mathrm{Log}_{10}(\mathrm{Pr})$ spectrum for 750-1000 MeV for Zone 2.

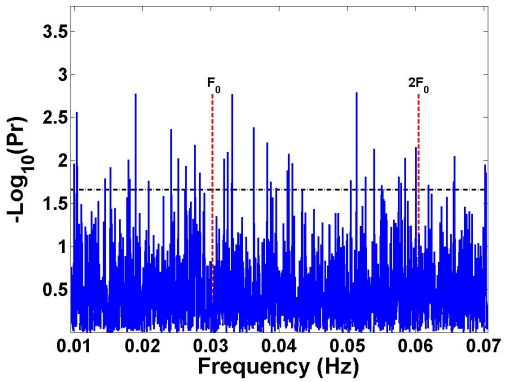

Figure 5.53: Rayleigh $-\mathrm{Log}_{10}(\mathrm{Pr})$ spectrum for 1-10 GeV for Zone 2.

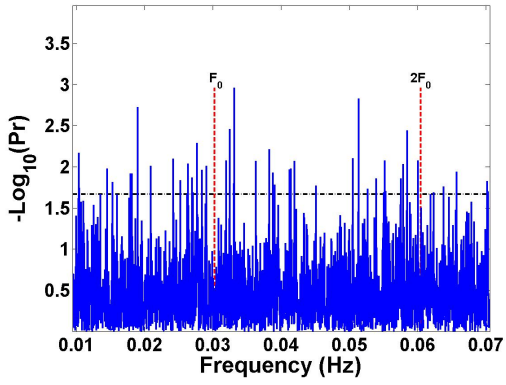

Figure 5.54: Rayleigh $-\mathrm{Log}_{10}(\mathrm{Pr})$ spectrum for 1-100 GeV for Zone 2.

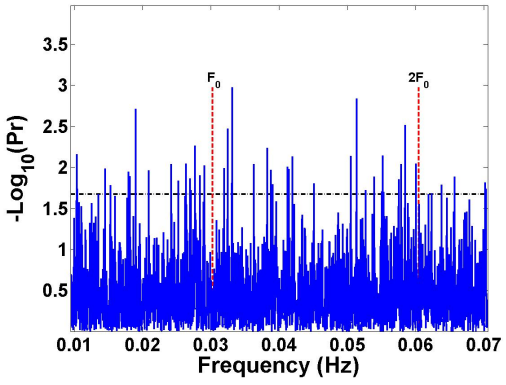

Figure 5.55: Rayleigh $-\mathrm{Log}_{10}(\mathrm{Pr})$ spectrum for 1-300 GeV for Zone 2.

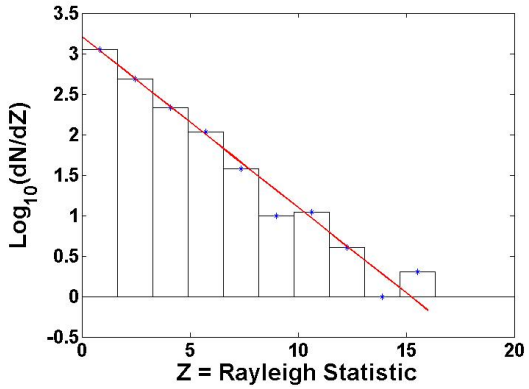

Figure 5.56: Histogram of the Rayleigh Z distribution for 250-500 MeV for Zone 2.

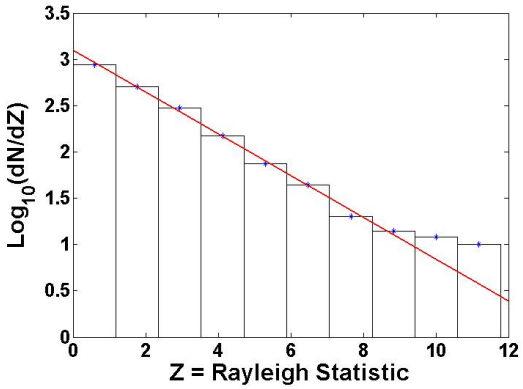

Figure 5.57: Histogram of the Rayleigh Z distribution for 500-750 MeV for Zone 2.

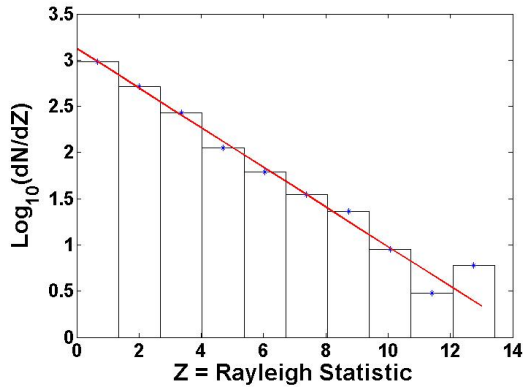

Figure 5.58: Histogram of the Rayleigh Z distribution for 750-1000 MeV for Zone 2.

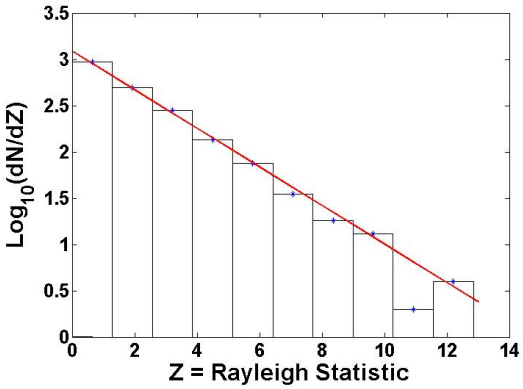

Figure 5.59: Histogram of the Rayleigh Z distribution for 1-10 GeV for Zone 2.

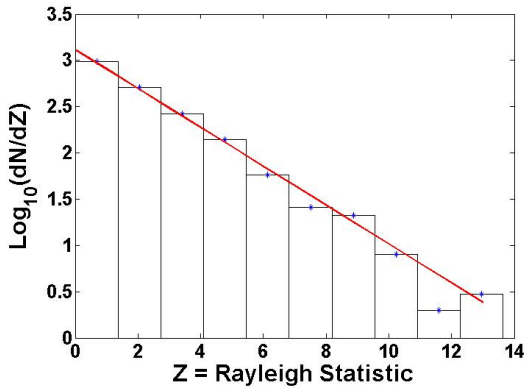

Figure 5.60: Histogram of the Rayleigh Z distribution for 1-100 GeV for Zone 2.

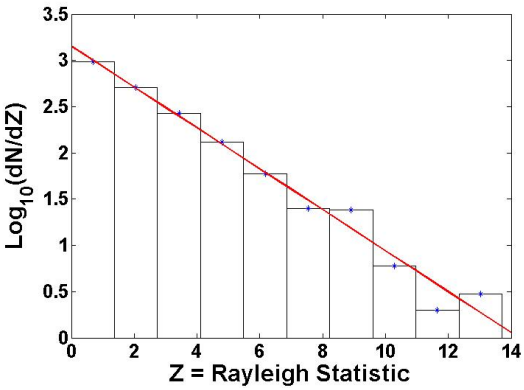

Figure 5.61: Histogram of the Rayleigh Z distribution for 1-300 GeV for Zone 2.

As with the datasets centred on AE Aquarii, the Rayleigh power spectra were analysed for signal/noise ratio. With the data structure of the power spectra shown as predominantly white noise and based upon the previously stated assumption that the power spectrum peak power distribution levels below 4σ can be considered as white noise, the peaks with power greater than 4σ were sampled and analysed for signal/noise significance.

Figures 5.62,5.63,5.64 and 5.65 represent the sampled peaks with power above 4σ for the relevant energy bins for Zone-1 and Zone-2 respectively.

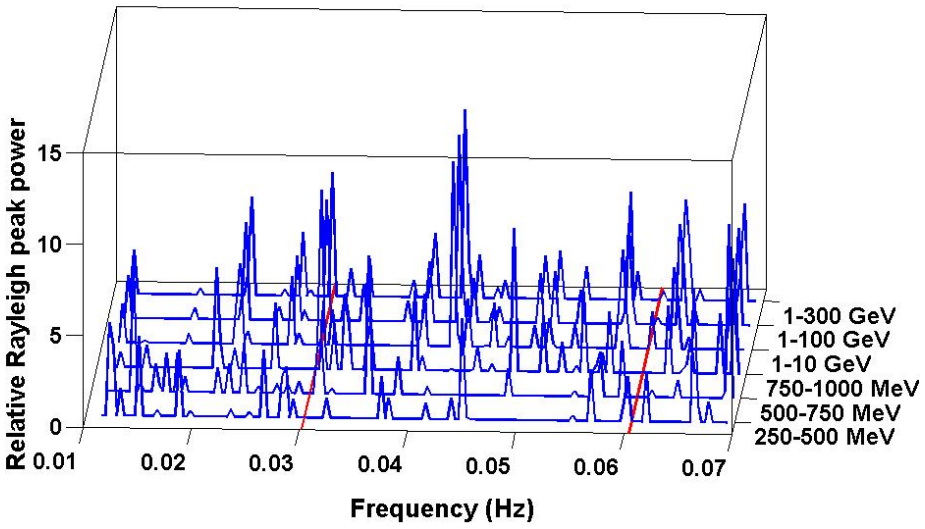

Figure 5.62: 3D view of sampled peaks with power above 4σ for examined energy bins for Zone 1. The fundamental frequency and first harmonic of the current model ephemeris for the WD spin is shown in red.

The sampled power peaks greater than 4σ from the separate energy bins were then combined for Zone 1 and Zone 2. (Figures 5.66 and 5.67.) This was done to check for possible signal peaks, as with the sampled data for AE Aquarii.

Also by plotting a histogram of the peak distribution in terms of the Rayleigh power Z, a noise profile versus peak power could be produced for the two test zones. A combined histogram for all datasets considered in the analysis of the

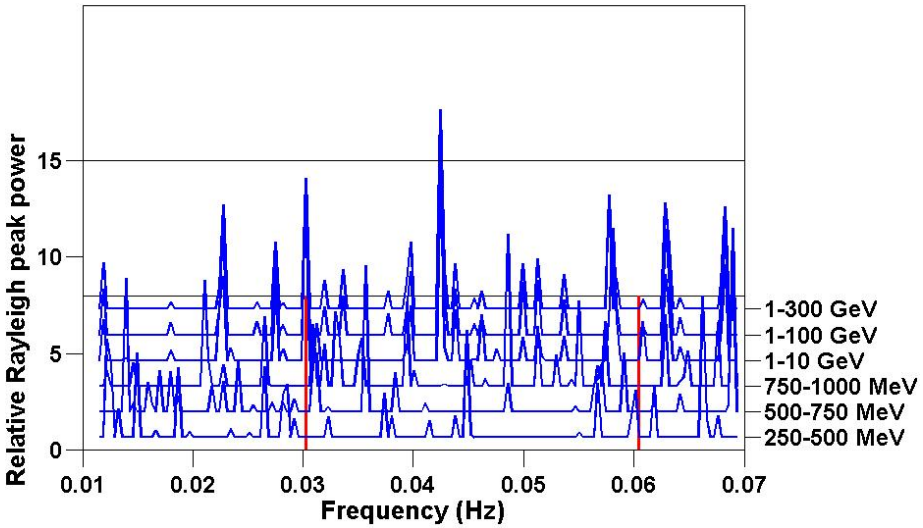

Figure 5.63: Front view of sampled peaks with power above 4σ for examined energy bins for Zone 1. The fundamental frequency and first harmonic of the current model ephemeris for the WD spin is shown in red.

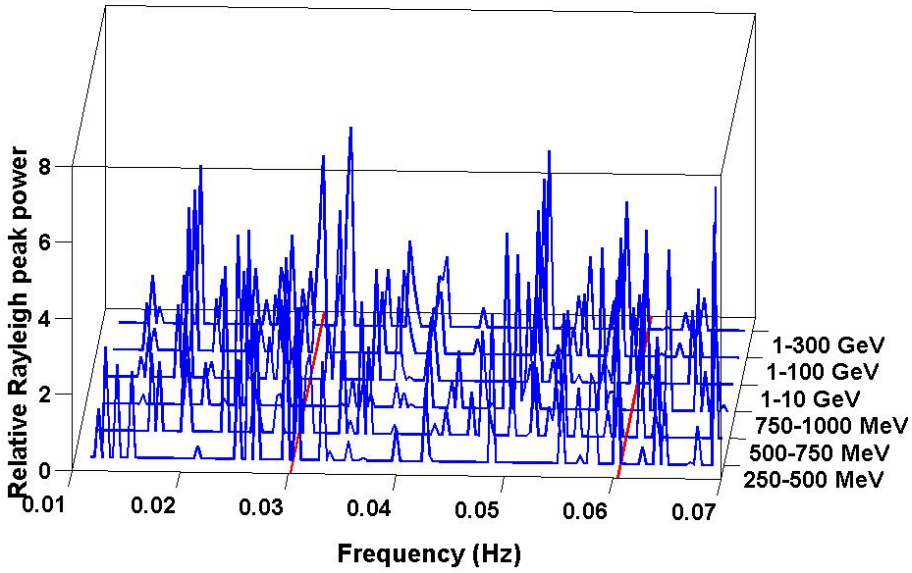

Figure 5.64: 3D view of sampled peaks with power above 4σ for examined energy bins for Zone 2. The fundamental frequency and first harmonic of the current model ephemeris for the WD spin is shown in red.

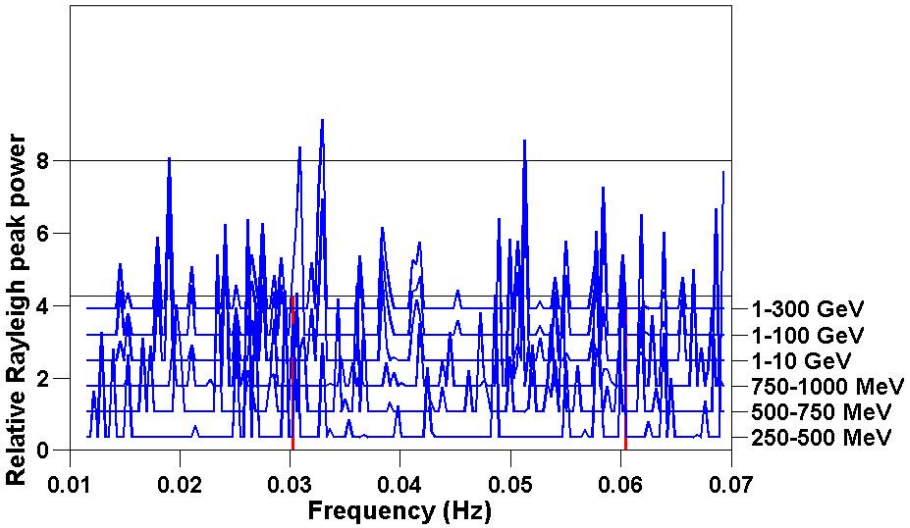

Figure 5.65: Front view of sampled peaks with power above 4σ for examined energy bins for Zone 2. The fundamental frequency and first harmonic of the current model ephemeris for the WD spin is shown in red.

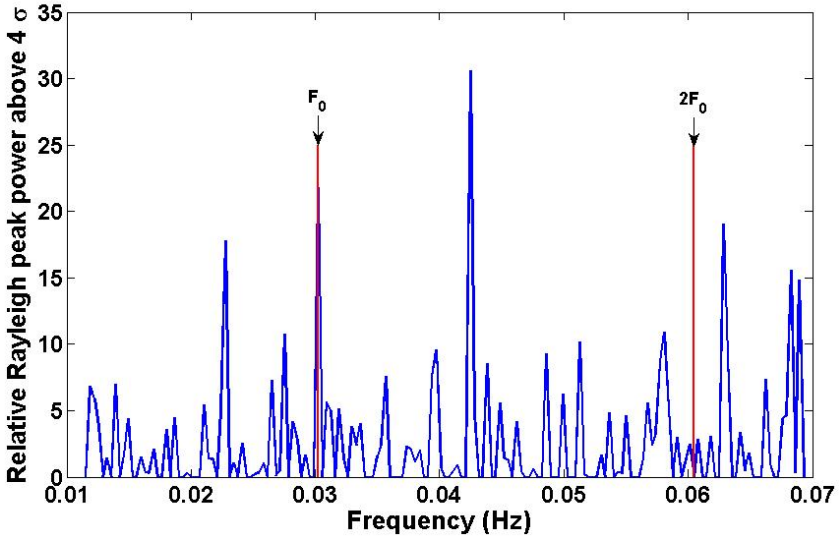

Figure 5.66: Combined power peaks from the separate energy bins for Zone 1. The fundamental frequency and first harmonic of the current model ephemeris for the WD spin is shown in red.

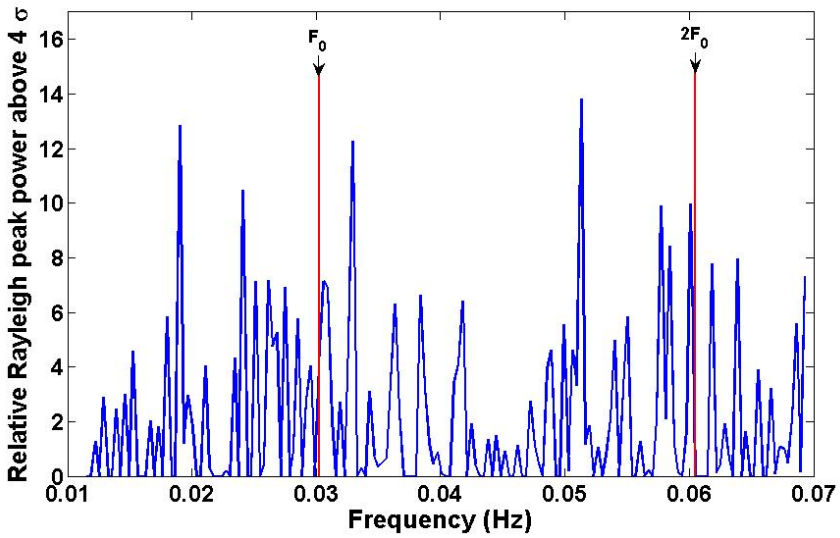

Figure 5.67: Combined power peaks from the separate energy bins for Zone 2. The fundamental frequency and first harmonic of the current model ephemeris for the WD spin is shown in red.

two test zones were therefore plotted, with a white noise profile trend fitted (Figures 5.68 and 5.69).

From the histograms of the Rayleigh power distribution Z, a white noise profile trend can be seen at lower powers, with slight deviations at higher power values. Thus with the power peaks above 4σ distributed as white noise through the different energy bins, the assumption can be made that peaks distributed through the different energy bins under consideration at a level occurrence greater than 3σ (see discussion related to Figure 5.28), would inherently be a signature of a hidden signal within the noise structures. Analysis of the peak distributions were performed. No peaks were found at a distribution occurrence level through the energy bins of $> 3\sigma$, therefore no possible signal peak was found similar to the one found in the AE Aquarii data analysis section, i.e., displayed in Figure 5.30.

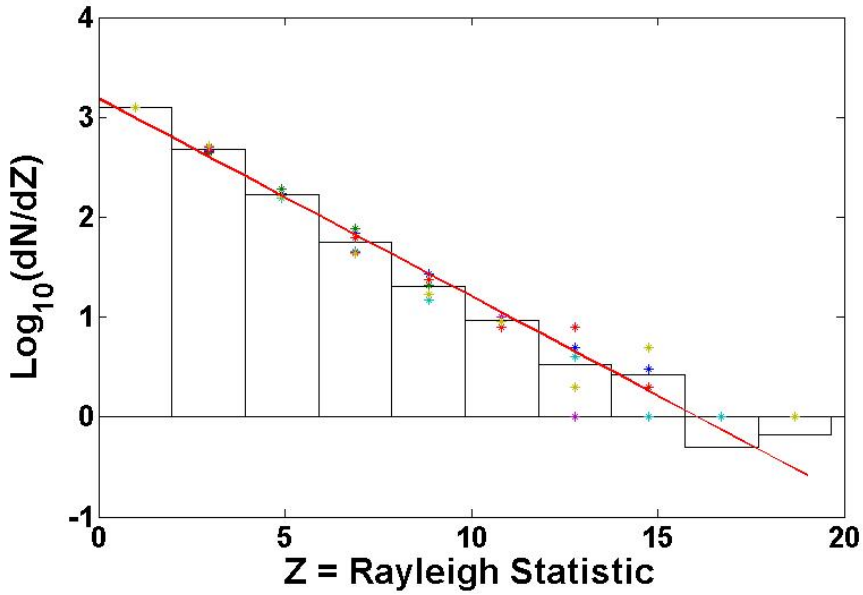

Figure 5.68: Histogram of the combined relative Rayleigh power Z for the separate energy bins for Zone 1, with the histogram values for the separate energy bins indicated. A white noise trend is also shown in red.

5.4 Multi-wavelength analysis - A search for correlations between optical, *Suzaku* X-ray and *Fermi*-LAT γ − ray emission

Aperture photometry of photon events for the regions of interest was used as basis for a multi-wavelength correlation analysis technique. Previous studies by Meintjes et al. (1992, 1994) found a correlation between optical flares and VHE burst-like emission. An analysis using reference parameters from optical photometric data as time constraints (refer to section 3.4) could therefore be conducted to search for possible correlations between the available optical data and *Fermi*-LAT data. These constrained time windows were used as part of the aperture photometry data analysis of *Fermi*-LAT data. Analysis for correlation between *Suzaku* X-ray data and *Fermi*-LAT aperture photometry data was also conducted. This was based on previous studies that showed that the hard X-ray emission possibly constrain a non-thermal component (Terada et al. (2008)), and in addition with the

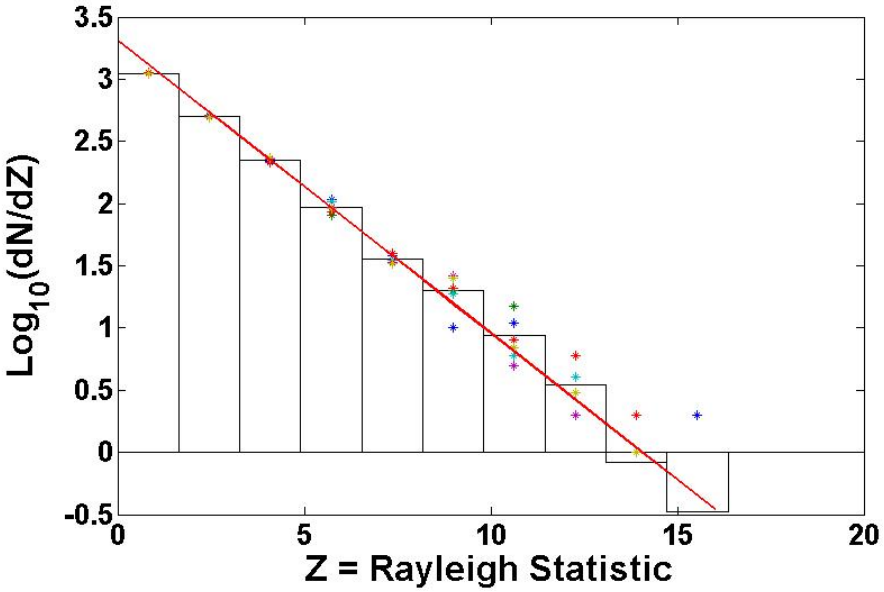

Figure 5.69: Histogram of the combined relative Rayleigh power Z for the separate energy bins for Zone 2, with the histogram values for the separate energy bins indicated. A white noise trend is also shown in red.

WD spin period being a very strong feature of the soft X-ray component (Refer to chapter 4 for a discussion on the analysis of *Suzaku* data for the current study).

Aperture photometry for energies between 250 MeV-300 GeV for a FOV radius of 1 degree of the full time window available for the *Fermi*-LAT datasets was performed using the *Fermi* recommended analysis method. The extracted photon event data was then analysed for possible correlation signatures with optical flares as well as features with strengthened emission (flaring or bursts) in X-ray data. As with the noise structure distribution analysis technique, if enough photon events could be correlated with strong optical flares or X-ray data features and there is a definable structure to the correlation, then its significance could be estimated. *Fermi*-LAT data light curves were therefore produced for inspection and analysis. The light curves for the three regions of interest were produced to check for consistency and correlation between photon events and regions (Figures 5.70 and 5.71).

As can be seen from the light curves for the three regions of interest, no strong

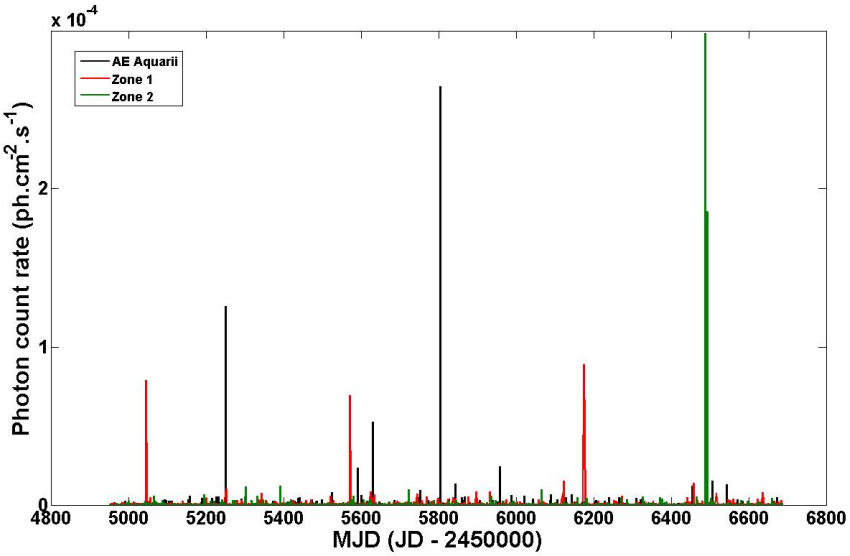

Figure 5.70: Combined photon count rate light curves for all three regions in question using *Fermi*-LAT aperture photometry data.

correlation exists between the measured photon events for the three regions. A light curve was thus produced that includes the available optical coverage and X-ray data, with the photon count rate displayed as the black lines, and the available optical coverage displayed as red blocks and the 2009 *Suzaku* data coverage displayed as a blue block. The width of the different blocks then represents the dataset lengths (Figure 5.72).

5.4.1 Optical versus *Fermi*-LAT correlation analysis

A closer inspection was performed on the available optical data coverage compared to the *Fermi*-LAT data. Enlarged views were therefore plotted of the optical data coverage areas for greater detail and visual inspection to facilitate the search for corresponding optical data coverage and *Fermi*-LAT photon events (Figures 5.73, 5.74, 5.75 and 5.76).

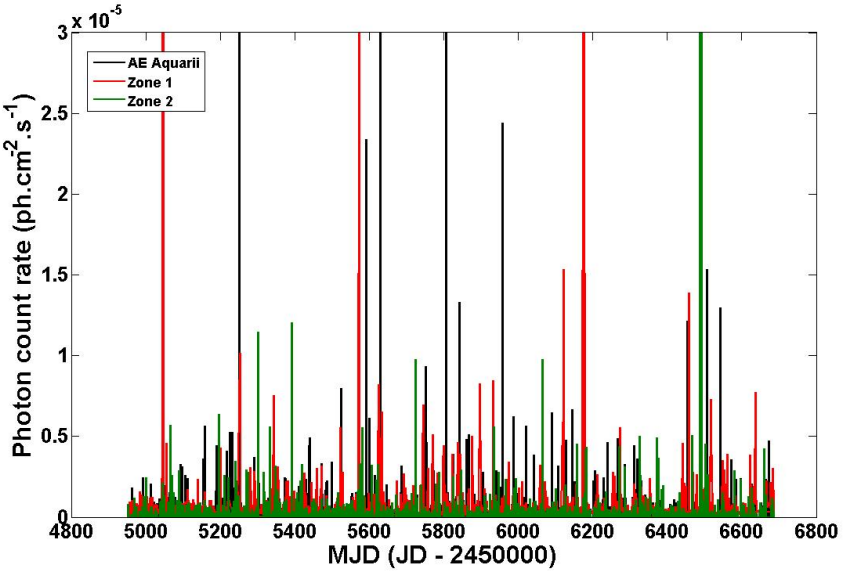

Figure 5.71: Rescaled combined photon count rate light curves for all three regions in question using *Fermi*-LAT aperture photometry data. The photon count rate axis is rescaled to 10% of the maximum count level for clarity of the distribution of photon events at this level.

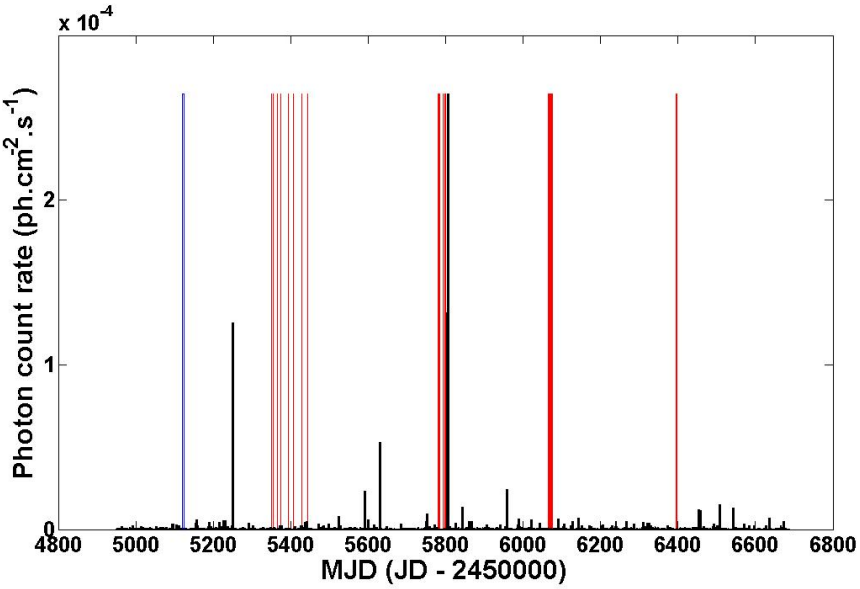

Figure 5.72: Photon count rate light curve for AE Aquarii using *Fermi*-LAT aperture photometry data (black lines). Also displayed are the available optical coverage (red blocks) and 2009 *Suzaku* data coverage (blue blocks).

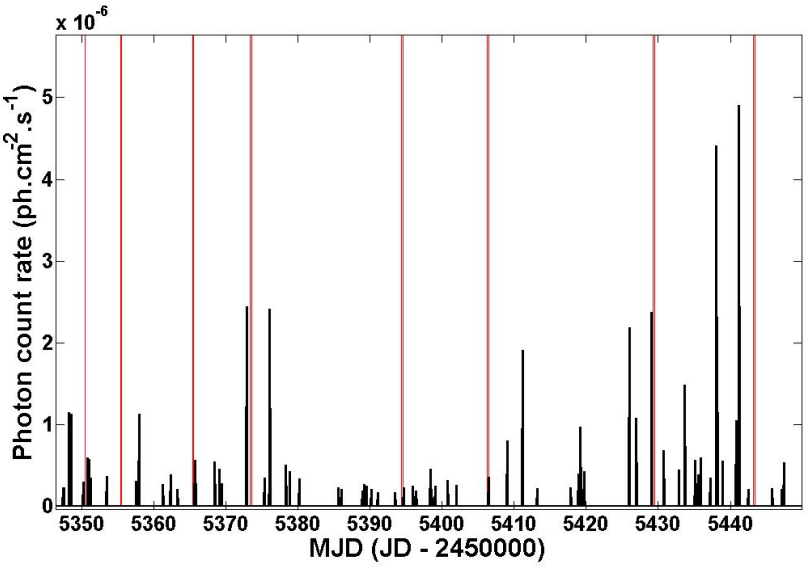

Figure 5.73: Enlarged view of *Fermi*-LAT photon count rate light curve (Black) for AE Aquarii displaying the available optical coverage (Red) during 2010. The width of the blocks correspond to the optical data set lengths.

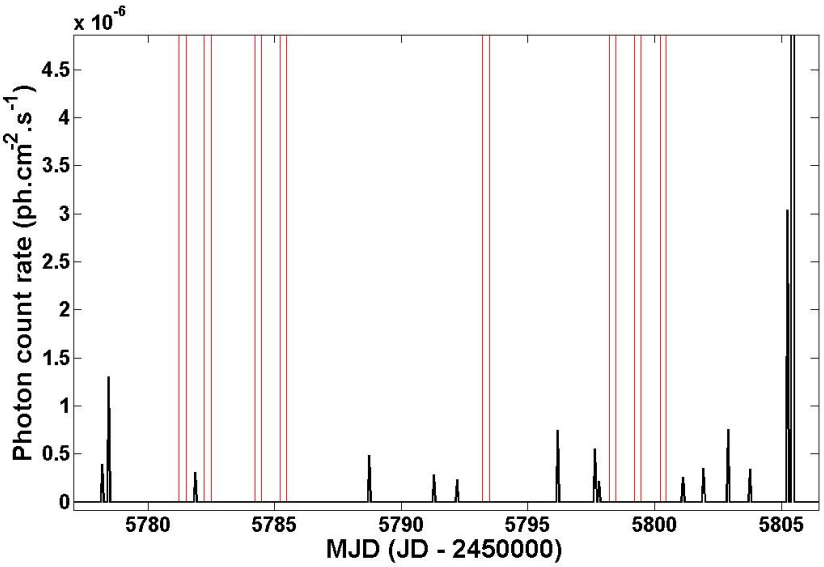

Figure 5.74: Enlarged view of *Fermi*-LAT photon count rate light curve (Black) for AE Aquarii displaying the available optical coverage (Red) during 2011. The width of the blocks correspond to the optical data set lengths.

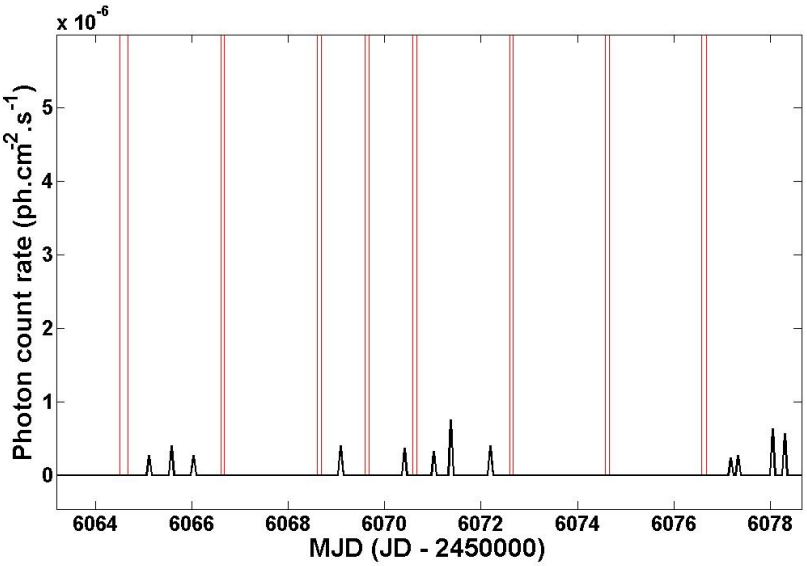

Figure 5.75: Enlarged view of *Fermi*-LAT photon count rate light curve (Black) for AE Aquarii displaying the available optical coverage (Red) during 2012. The width of the blocks correspond to the optical data set lengths.

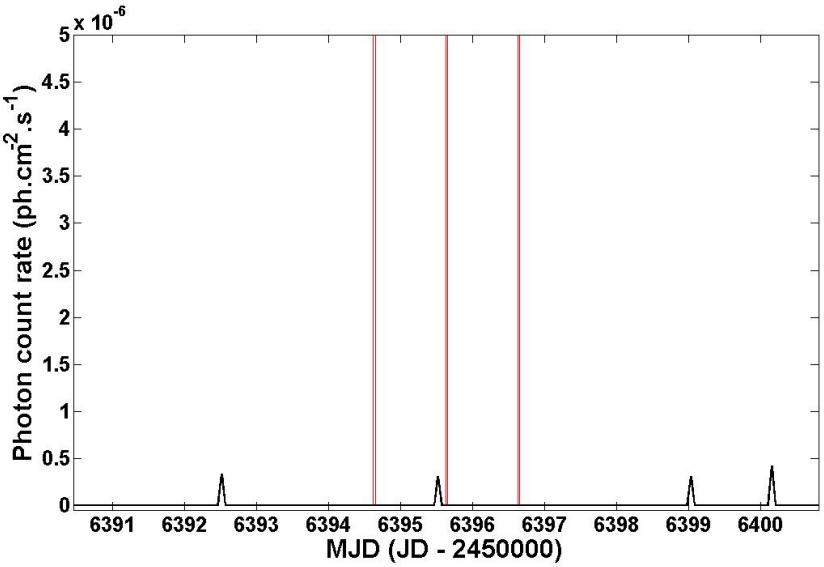

Figure 5.76: Enlarged view of *Fermi*-LAT photon count rate light curve (Black) for AE Aquarii displaying the available optical coverage (Red) during 2013. The width of the blocks correspond to the optical data set lengths.

In Figure 5.73 a photon event that corresponds to an available optical data coverage period can be observed. This region was therefore also enlarged for better visualization (Figure 5.77).

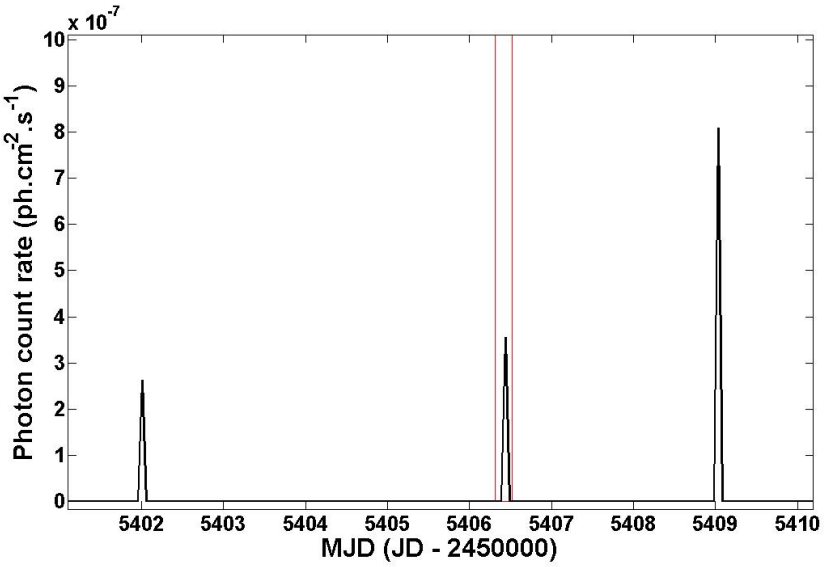

Figure 5.77: Enlarged view of *Fermi*-LAT photon count rate light curve (Black) for AE Aquarii displaying a photon event that fell within the available optical coverage (Red) during 2010.

Additional analysis of the detected photon event in question that fell within the region of the optical data set (2455406 (JD) or 2010-07-28) was conducted for greater accuracy and characterisation of the time and energy of the detected photon event. The search resulted in the detected photon event corresponding to an optical flare time and window size. The detected photon event was plotted on the optical light curve for the time in question (See Figure 5.78).

The detection of only a single photon event, even though it was featured just before a large optical flare, could unfortunately not be used for correlation testing, as it could not be tested for significance and therefore not excluded as a singular event, or conversely interpreted as a meaningful signature for $\gamma-$ray emission. This could only have been achieved if a number of photon events were detected

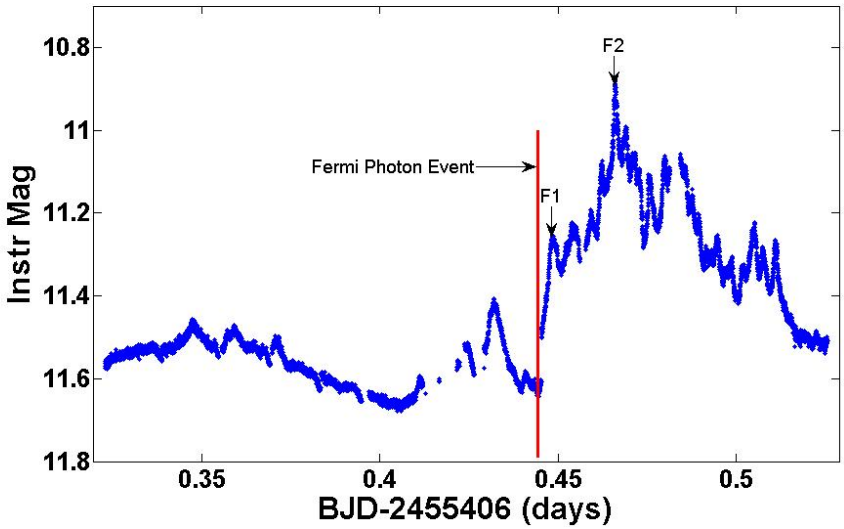

Figure 5.78: Detected *Fermi*-LAT photon event plotted on the optical light curve in question.

within the available optical data, and if there was a definable correlation between optical flares and *Fermi* photon events. The photon event was however characterised as follows: The event time window was used to do a search for the event in different energy bins to determine the exact energy flux of the event. The event was found in the energy range between 250-500 MeV. There is however a visual correlation with similar results obtained by Meintjes et al. (1994) as represented by Figure 5.79. As can be seen in the figure, an VHE event (upper panel) occurred before the onset of an optical flare (bottem panel) after a period of quiescence.

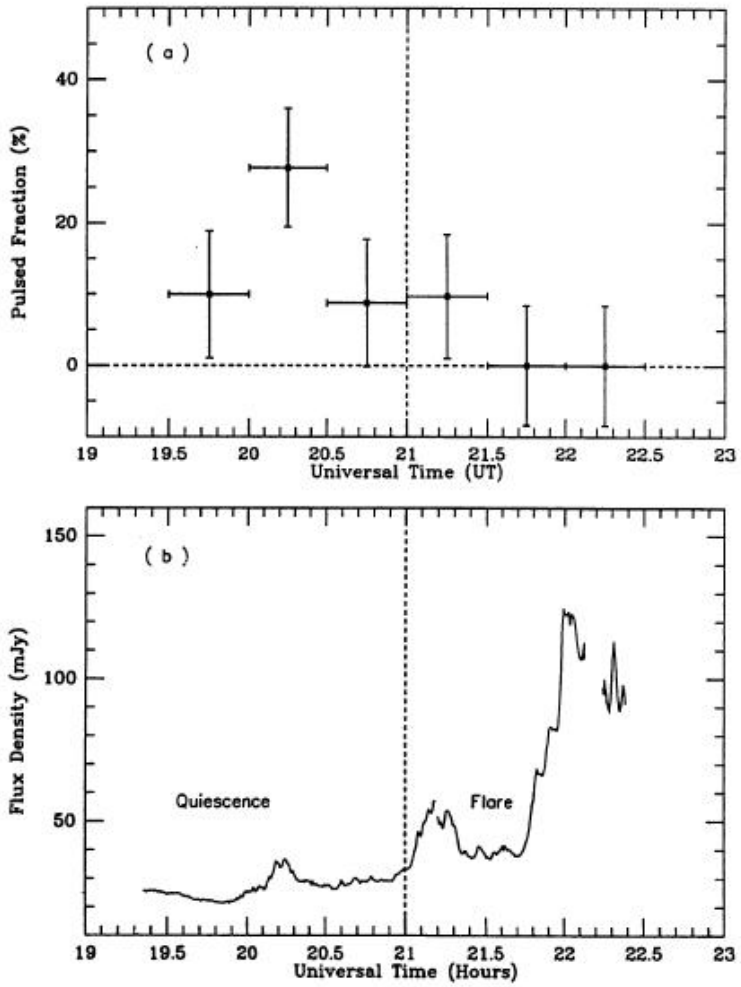

Figure 5.79: Comparison between VHE and optical data (Adopted from Meintjes et al. (1994)).

5.4.2 *Suzaku* X-ray data versus *Fermi*-LAT correlation analysis

As with the optical data, a closer inspection was also performed on the *Suzaku* X-ray data coverage compared to the *Fermi*-LAT data. An enlarged view of the X-ray data area was plotted for greater detail and visual inspection to facilitate the search for corresponding X-ray data coverage and *Fermi*-LAT photon events (Figure 5.80).

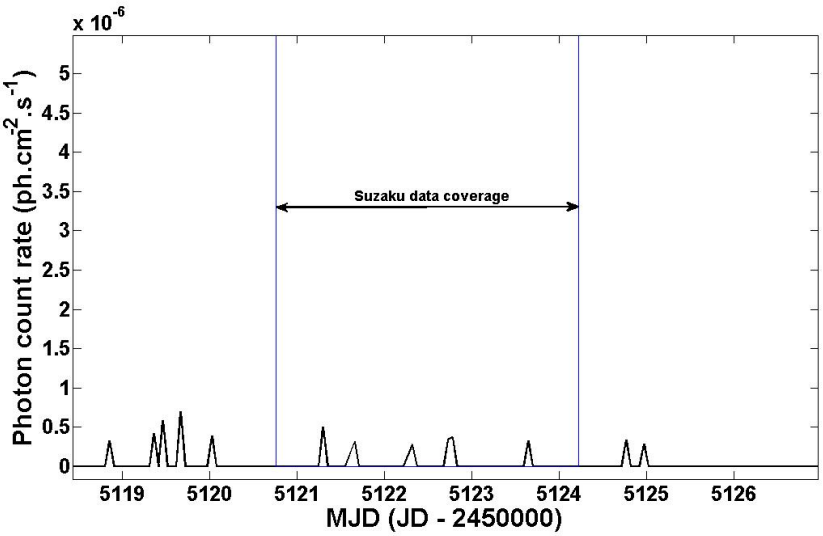

Figure 5.80: Enlarged view of *Fermi*-LAT photon count rate light curve (Black) for AE Aquarii displaying the X-ray data coverage (Blue) during 2009. The width of the block corresponds to the X-ray data-set length.

In Figure 5.80, six photon events that correspond to the available X-ray data coverage can be observed. Additional analysis of the detected photon events that fell within the region of the 2009 X-ray data-set was conducted. A similar aperture photometry method was applied as with the optical data analyses. The only difference was the time window that was set to the width of the X-ray coverage, with the time resolution initially set to a bin value of 84.03 s. This was because the first search was aimed at finding possible correlation between the soft X-ray (XIS) data, at X-ray energies between 0.4 and 6 keV, and the detected *Fermi*-LAT photon events. The detected photon events (annotated as E1 to E6 on the graph)

were plotted on the XIS light curve (Figure 5.81).

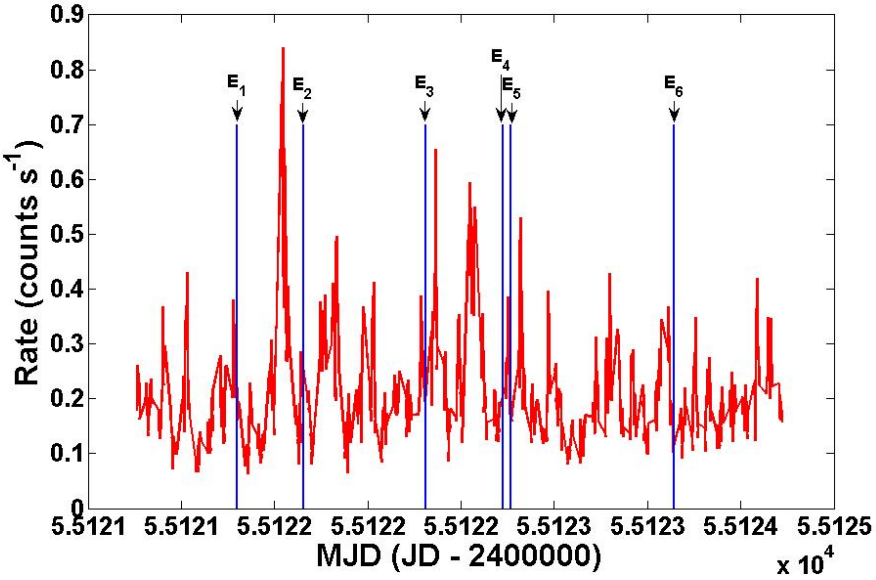

Figure 5.81: Detected *Fermi* photon events plotted on the *Suzaku* XIS light curve in the energy range 0.4 - 6.0 keV.

The detected photon events (except for E4), seemed to correlate to times just following increased soft X-ray emission (i.e. flaring). The detected photon events were then also checked for correlation with detected hard X-ray data. The detected photon events, annotated in the same way as Figure 5.81, were thus plotted on the light curve for the harder X-ray (PIN) data (Figure 5.82), at X-ray energies between 14 and 100 keV.

The detected photon events seemed to correlate to times just following increased harder X-ray emission in the form of short clusters of detected X-ray activity. The time and energy of the detected photon events were also determined (Table 5.2).

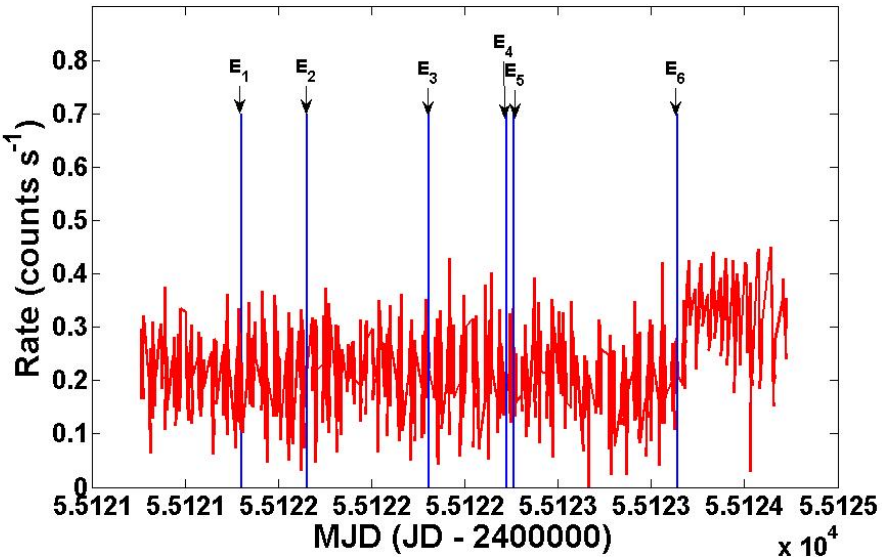

Figure 5.82: Detected *Fermi* photon events plotted on the *Suzaku* PIN light curve in the energy range 14 - 100 keV.

Table 5.2: Table of detected *Fermi*-LAT events in *Suzaku* XIS observational window.

Fermi-LAT Event	JD (days)	Energy Range (MeV)
E1	2455121.30192858	500-750
E2	2455121.65691642	500-750
E3	2455122.30951052	1000-10000
E4	2455122.72285253	1000-10000
E5	2455122.76564559	250-500
E6	2455123.64387580	500-750

5.5 *AGILE*-GRID analysis

Analysis was performed using *AGILE* data-sets centred on AE Aquarii (20 40 09, -00 52 15, J2000, Sexagesimal Equatorial). For the first few years of operation (2007/07/09-2009/10/15) *AGILE* operated in pointing mode, and therefore searching within these pointed regions, an increased sensitivity could be achieved.

A similar procedure was followed during the search for possible detection of $\gamma-$ ray emission from AE Aquarii using *AGILE* data as with *Fermi* data. First a search through *AGILE*-GRID data was conducted by scanning the 1$^{\text{st}}$ *AGILE*-GRID catalogue for any possible source detections in and around the region centred on AE Aquarii. *AGILE* has a few notable source detections within the region, as listed in Table 5.3.

Table 5.3: List of objects from the 1^{st} *AGILE* catalogue.

Number	*AGILE* Name	RA (J2000)	Dec (J2000)	Classification	Possible Counterparts(positional association)
1	1AGL J1922+1403	19 22 53.6	+14 03 45.2	Unclassified	PSRJ1921+1419
2	1AGL J1908+0614	19 08 08.4	+06 14 34.4	Unclassified	PSRJ1905+0616
3	1AGL J1901+0429	19 01 20.8	+04 29 38.3	Unclassified	PSRJ1901+0435
4	1AGL J2026-0732	20 26 30.7	-07 32 45.3	Blazar-FSRQ	PKS2023-07
5	1AGL J1855+0122	18 55 57.7	+01 22 24.4	Unclassified	PSRJ1856+0113

The *AGILE* public data archive was the next point of interest. Observation Blocks (OB) within a box of 30 square degrees of the coordinates of AE Aquarii were chosen for analysis, because noisy residual artefacts at off-axis angles $> 40°$ may be present at the border of the FOV. The data retrieved was summarized in Table 5.4.

The retrieved data for each OB consisted of two series of file sets: The standard "RAW" photon events files ag..._FM.EVT.gz or ag..._FT3AB.EVT.gz and spacecraft pointing log files ag..._STD0P.LOG.gz and the "CLEANED" photon events files ag..._GO_FM.EVT.gz or ag..._GO_FT3AB.EVT.gz and corresponding spacecraft pointing log files ag..._STD0P_GO.LOG.gz. Additionally three Aitoff maps for COUNTS, EXPOSURE and GAS were included, which were automatically generated for each data set, that could be used further analysis. It was however recommended that the cleaned data files be used along with the publicly available software AGILE_SW_5.0 (BUILD_GRID_5.0) to generate new target and analysis-specific COUNTS, EXPOSURE and GAS maps for use during likelihood analysis

Table 5.4: *AGILE*-GRID Observation Blocks retrieved for data analysis.

♯	OB ♯	RA_{PNT} (J2000)	DEC_{PNT} (J2000)	OB start date	OB end date	Mean OB Exposure (cm^2s)
1	5600	19 36 00.0	+20 30 00.0	2008-04-10	2008-04-30	33769890
2	6200	18 08 47.9	-28 36 00.0	2008-09-10	2008-10-10	50466571
3	6310	19 48 24.0	+10 00 00.0	2008-10-17	2008-10-31	20191330
4	6400	20 07 12.0	+34 00 00.0	2008-10-31	2008-11-30	45884068
5	6500	22 02 48.0	+35 12 00.0	2008-11-30	2008-12-20	29918380
6	6810	18 37 59.9	-29 18 00.0	2009-03-25	2009-03-31	10656097
7	7010	19 33 59.9	-19 18 00.0	2009-04-07	2009-04-15	14089878
8	7100	19 48 47.9	+16 00 00.0	2009-04-15	2009-04-30	22197061
9	7200	20 21 12.0	+29 23 59.9	2009-04-30	2009-05-15	25864056
10	7310	22 03 35.9	+10 48 00.0	2009-05-25	2009-05-29	5459572
11	8300	19 05 11.9	-23 11 59.9	2009-09-30	2009-10-15	24411329
12	8400	19 08 24.0	+28 48 00.0	2009-10-15	2009-10-31	4099810

processes. The software was installed and used on the same Fedora 20 (x86_64) Linux system as the *Fermi* analysis, with the analysis technique based on procedures as described in Chen et al. (2011). The software was then used to extract a region centred on AE Aquarii from the events files. Figure 5.83 represents the selected region compared to the events file region. The emission from the galactic plane can clearly be discerned to the right of the selected region.

Based on this extracted region COUNTS, EXPOSURE, GAS and INTENSITY maps were generated. Refer to Figures 5.84, 5.85, 5.86 and 5.87. The region encircled in green is centred on the location of AE Aquarii, while the known *AGILE* sources, as listed in Table 5.3, are encircled in yellow. The sizes of the circled regions are not scaled to a specific value, and is only relative. As seen only a single detected *AGILE* source is within the direct analysis region.

The generated files, along with a source list file for the region under consideration, were used to do likelihood analysis using the AG_multi4 task for source detection and location using the maximum likelihood method. The output for all the OB

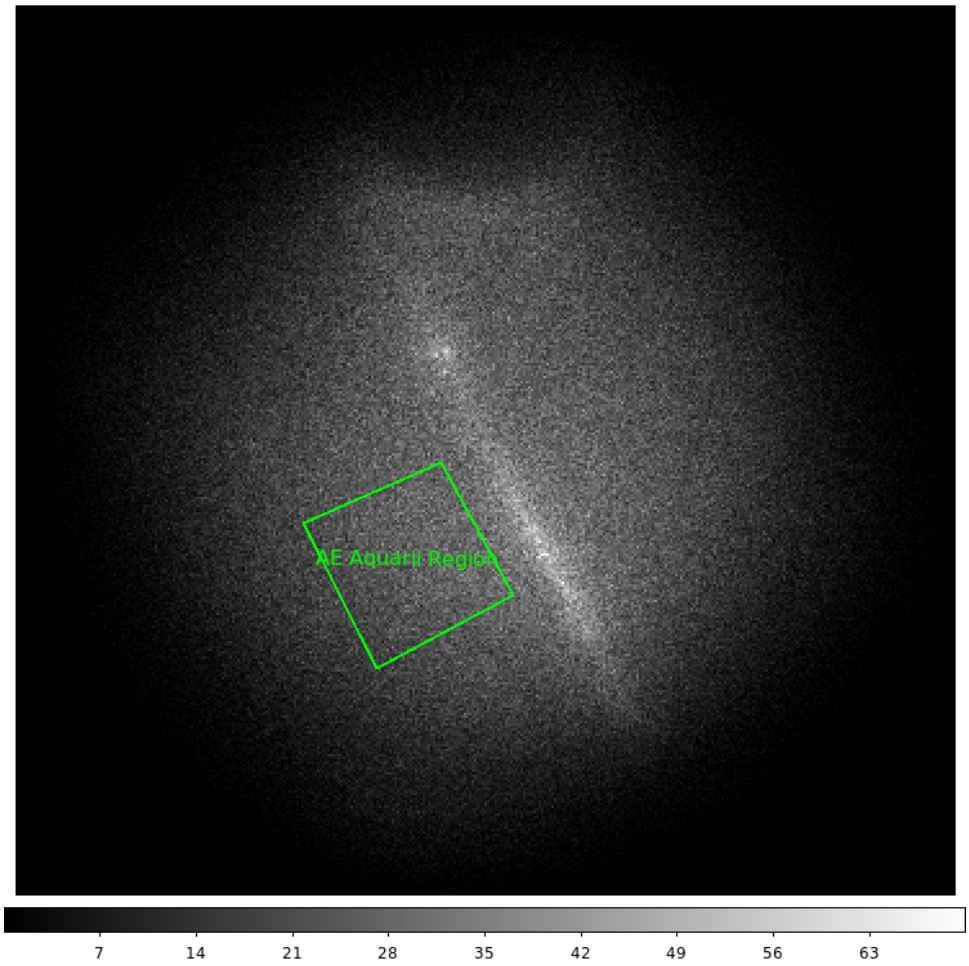

Figure 5.83: Selected AE Aquarii region displayed in green compared to the events file.

regions did not result in any converged maximum likelihood values for AE Aquarii. This was expected, as the sensitivity range for *AGILE* is lower than for *Fermi*, and as the results from the previous sections indicated, any possible detection of $\gamma-$ray emission from AE Aquarii would be at the noise level of *Fermi*, which means that probably no detection in the OB data from *AGILE* would be possible.

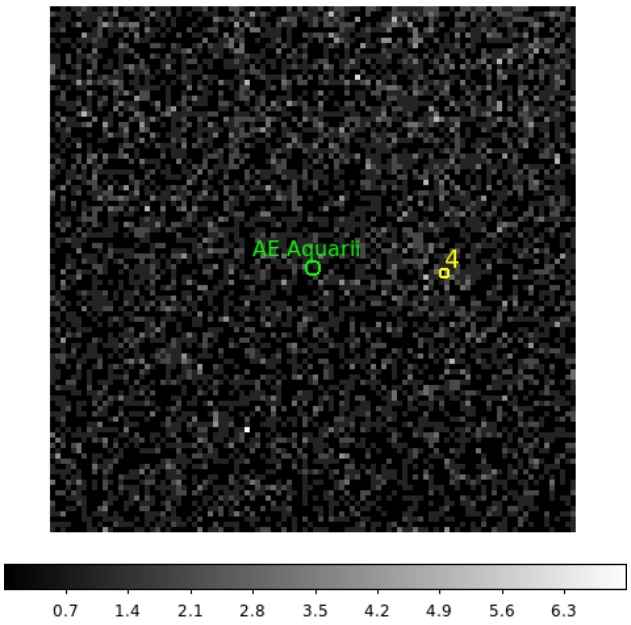

Figure 5.84: Generated COUNTS map for the AE Aquarii region analysed.

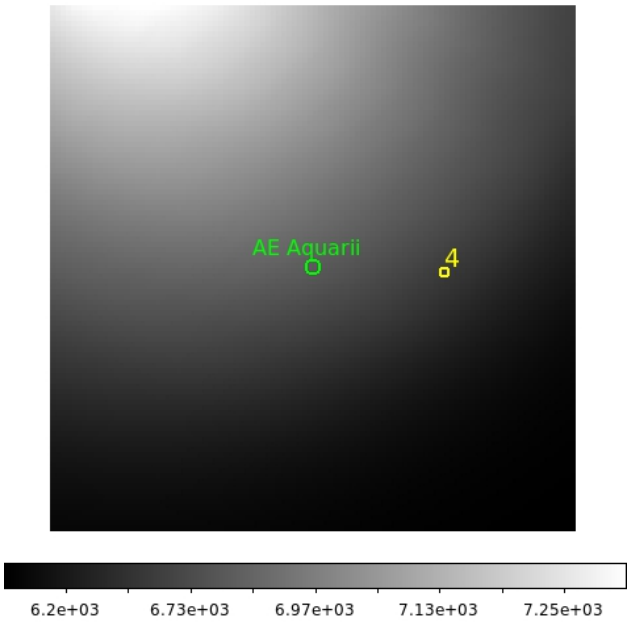

Figure 5.85: Generated EXPOSURE map (rescaled) for the AE Aquarii region analysed.

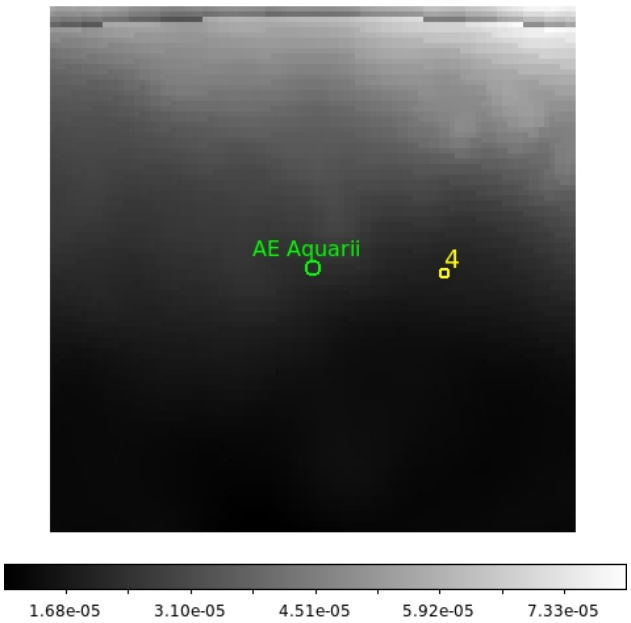

Figure 5.86: Generated GAS map for the AE Aquarii region analysed.

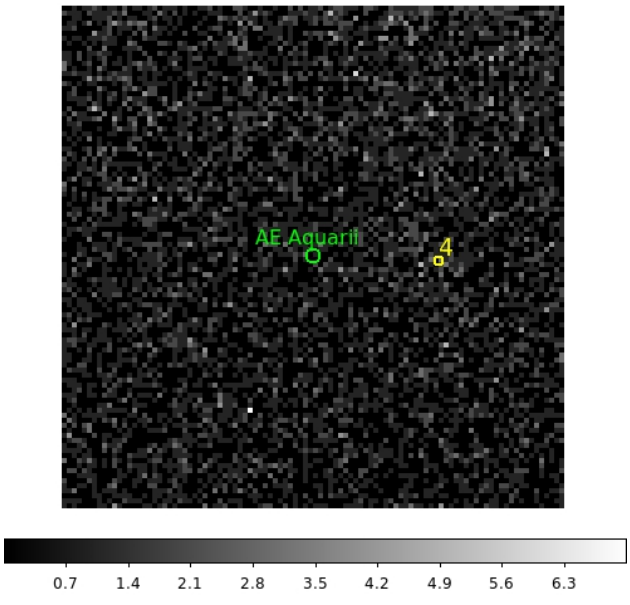

Figure 5.87: Generated INTENSITY map for the AE Aquarii region analysed.

5.6 Upper-limit calculations and SED

Considering the results obtained from the sections above as well as previous studies, an updated SED can serve as an investigative tool to constrain model parameters for non-thermal emission from AE Aquarii. Therefore an updated SED was determined for AE Aquarii that included the earlier reported pulsed emission as well as the more recent upper limits calculated by Lopez-Coto et al. (2013); Aleksić et al. (2014). Upper limits were also calculated for the *Fermi* data for AE Aquarii at different energies. The upper limit calculations were completed using the *Fermi* python based LATAnalysisScripts on the UFS HPC cluster. The upper limits are determined from the fit to the proposed model for the object of interest. With a power law the most likely model for AE Aquarii at higher energies (Terada et al. (2007, 2008); Oruru and Meintjes (2012)), a "PowerLaw2" model was selected. This is the same model as used during the likelihood analysis procedures, and was chosen for the fact that the integrated flux is used as a free parameter, rather than the pre-factor. The model is then given by the following equation

$$\frac{\mathrm{dN}}{\mathrm{dE}} = \frac{\mathrm{N}(\gamma+1)\mathrm{E}^{\gamma}}{\mathrm{E}_{\mathrm{max}}^{\gamma+1} - \mathrm{E}_{\mathrm{min}}^{\gamma+1}}, \tag{5.1}$$

where N is the integral or normalisation factor, γ is the index and $\mathrm{E}_{\mathrm{max}}$ and $\mathrm{E}_{\mathrm{min}}$ are the upper and lower limit values respectively. Using the likelihood analysis results, this equation is then fitted for a specific upper limit energy range. With the upper limits given in terms of photon count rate (ph cm^{-2} s^{-1}) at a fitted index value, given an expected model response, the values had to be converted to an energy flux density ($\nu\mathrm{F}_{\nu}$) value. This was achieved through the following equation

$$\nu\mathrm{F}_{\nu} = \nu(\mathrm{E}\frac{\mathrm{dN}}{\mathrm{dE}}\frac{1.6\times10^{-6}\ \mathrm{erg/MeV}}{2.42\times10^{20}\ \mathrm{Hz/Mev}})\ (\mathrm{erg\ cm}^{-2}\ \mathrm{s}^{-1}). \tag{5.2}$$

Here $\mathrm{E}\frac{\mathrm{dN}}{\mathrm{dE}}$ is the photon count rate or flux density at a particular energy E (MeV). With the values 1.6×10^{-6} erg/MeV and 2.42×10^{20} Hz/Mev the conversion factors to convert to cgs units. The converted upper limit values calculated using Equation 5.2 and parameters used were summarized in Table 5.5.

Table 5.5: *Fermi* upper limits at different energies for AE Aquarii as calculated using the LATAnalysisScripts.

Number	Energy (E_{max})	Frequency (Hz)	Photon count rate (ph $cm^{-2}s^{-1}$)	Index (loglike)	Energy flux density (erg $cm^{-2}s^{-1}$)
1	250 MeV	6.05×10^{22}	2.65×10^{-7}	1.35	1.06×10^{-10}
2	500 MeV	1.21×10^{23}	2.67×10^{-7}	1.35	2.14×10^{-10}
3	750 MeV	1.815×10^{23}	2.72×10^{-7}	1.35	3.26×10^{-10}
4	1 GeV	2.42×10^{23}	2.68×10^{-7}	1.35	4.29×10^{-10}
5	5 GeV	1.21×10^{24}	2.68×10^{-7}	1.35	2.14×10^{-9}
6	10 GeV	2.42×10^{24}	2.72×10^{-7}	1.35	4.35×10^{-9}
7	50 GeV	1.21×10^{25}	2.73×10^{-7}	1.35	2.18×10^{-8}
8	100 GeV	2.42×10^{25}	2.73×10^{-7}	1.35	4.37×10^{-8}
9	300 GeV	7.26×10^{25}	2.74×10^{-7}	1.35	1.32×10^{-7}

The calculated values were included into the SED (indicated in red). The values as determined by Lopez-Coto et al. (2013); Aleksić et al. (2014) also had to be converted, with the values and parameters used indicated in Table 5.6.

Table 5.6: *MAGIC* upper limits at different energies for AE Aquarii.

Number	Energy (E_{max})	Frequency (Hz)	Photon count rate (ph $cm^{-2}s^{-1}$)	Index (Crab-like)	Energy flux density (erg $cm^{-2}s^{-1}$)
1	250 GeV	6.05×10^{25}	6.4×10^{-12}	-2.6	2.56×10^{-12}
2	1 TeV	2.42×10^{26}	7.4×10^{-13}	-2.6	1.18×10^{-12}

These converted values were also included in the SED (indicated in blue). The preliminary determined flux values for the 2009 *Suzaku* data were also included (dark green crosses), which can be compared to the published Terada et al. (2007, 2008) flux values (dark green pentagrams). See Figure 5.88 for the most recent SED for AE Aquarii, with sensitivity curves for selected instruments included. The sensitivity curves included were the 2-year sensitivity curve for *Fermi*, the

1-year sensitivity curve for *AGILE* and 50-hours sensitivity curves for *HESS* and *MAGIC II*. The sensitivity curve for the CTA was a theoretically predicted 50-hours. The instrumental sensitivity curve data were acquired from the ASDC SED builder V3.1 available at http://tools.asdc.asi.it/SED. The Fermi sensitivity curve is based on 2 year integration data from the 2FGL Catalogue. The 50-hours CTA theoretical curve is based on monte carlo design studies conducted by Bernlöhr et al. (2013)

From the SED, the upper limits of the *Fermi* data for AE Aquarii are just above the sensitivity curve for *AGILE*, which then also supports the results obtained from the previous sections, i.e., no detection of any $\gamma-$ray emission from any of the OB datasets of *AGILE*, but a slight possibility of perhaps a very weak spin modulated ($2F_0$) $\gamma-$ray modulation hidden in the noise level of the *Fermi*-LAT data. The preliminary uncorrected flux values for the 2009 *Suzaku* spectra show an upward turn to the higher energies which would be indicative of a possible power law component. Although it has to be noted that a more in-depth analysis and comparison of the spectra with the results from Terada et al. (2008) might change the level of the flux values. Whether the possible $\gamma-$ray emission in the *Fermi* data is a signature of a continuous emission mechanism, or more likely a signature of a cumulative effect from burst-like $\gamma-$ray emissions as reported by Meintjes et al. (1992, 1994) and Chadwick et al. (1995), can only be answered through additional analysis of VHE data in conjunction with simultaneous optical and X-ray data to search for possible burst events. The indication of a power law component in the X-ray data however strengthens the case for an acceleration mechanism that can potentially accelerate particles to VHE energies.

"This research has made use of data, software and/or web tools obtained from NASA's High Energy Astrophysics Science Archive Research Centre (HEASARC), a service of the Goddard Space Flight Centre and the Smithsonian Astrophysical Observatory."

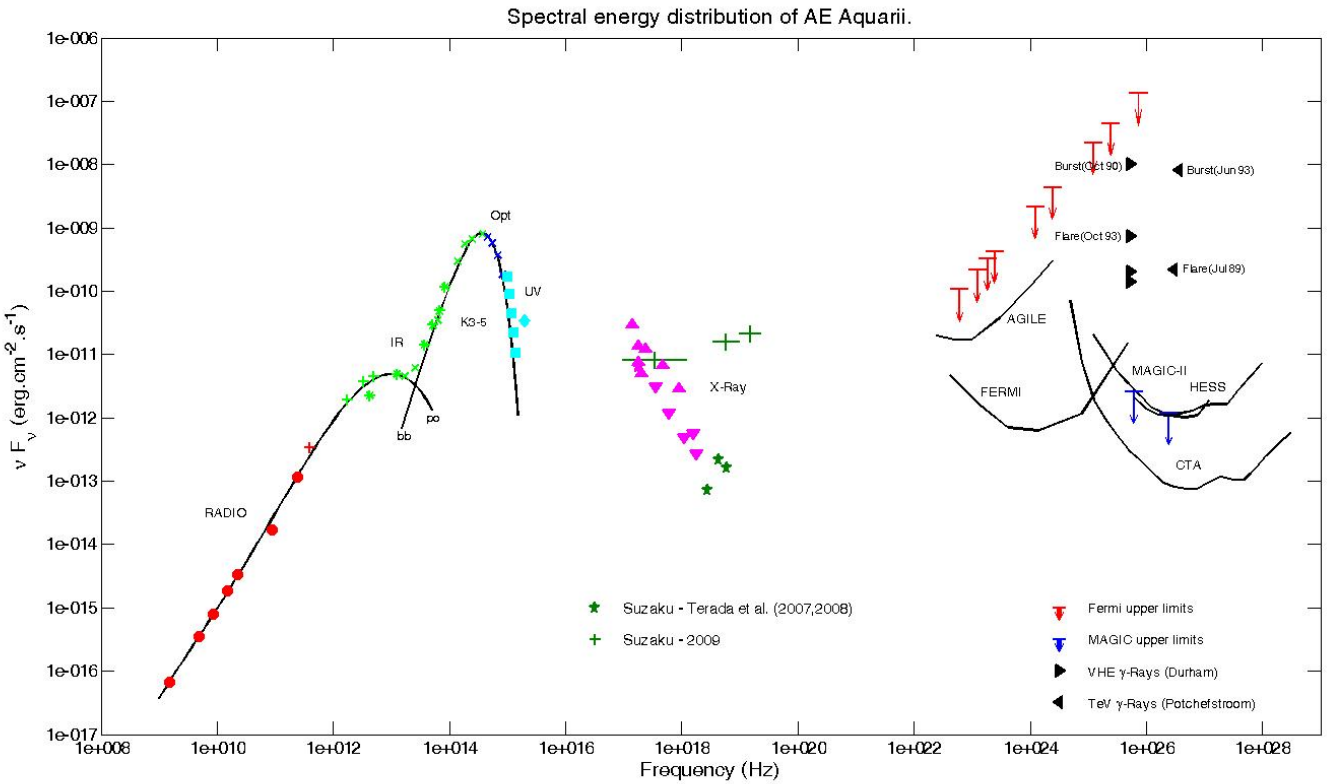

Figure 5.88: SED of AE Aquarii including recent calculated upper limits.

Chapter 6

Final discussions and conclusion

The aim of this study was the search for non-thermal high-energy emission from AE Aquarii. A historical overview of the main properties of AE Aquarii was given to identify signatures that could be used in the search for high energy pulsed non-thermal emission. From previous studies, non-thermal synchrotron emission at radio wavelengths (Bastian et al. (1988)) as well as possible non-thermal (based on a power-law fit with a photon index of 1.12) emission from hard X-rays (Terada et al. (2007, 2008)) using *Suzaku* data were found. In addition, studies conducted by Meintjes et al. (1992, 1994) and Chadwick et al. (1995) found possible pulsed emission at VHE ($\epsilon_\nu \leq 1$ TeV) and TeV ($\epsilon_\nu \geq 1$ TeV) energies, with a possible correlation between the pulsed optical and VHE $\gamma-$ray emission during optical flares. Therefore, archival data from the *Suzaku*, *Fermi* and *AGILE* space telescope systems, together with contemporaneous optical data acquired using the Boyden 1.5 m and SAAO 1.9 m telescope systems were used in the search for high energy non-thermal emission.

The analysis of the optical data clearly illustrated the variable and flaring nature of the system which can be seen from the instrumental light curves. A selection criterion for the potency of optical flares was also presented, with selected flares analysed for use in the search for high energy non-thermal emission. The flares were selected based on a flare-strength ratio FS $= \frac{\Delta \text{mag}}{\text{Rise Time}} \geq 0.5$. This selection criterion were used to characterise the flares as "Slow" or "Fast", with the "Fast"

flare events being possible indicators of enhanced production of energetic emission. What this means is that a greater amount of energy would have to be released at a faster rate to facilitate the rapid flaring events, i.e. the interactions at the flaring mechanisms is more energetic. This could then also help facilitate the emission of high energy non-thermal emission. The duty cycle for the flares was also calculated to determine the frequency of these strong and rapid flaring events. The duty cycle per orbital period was calculated at $\sim 1.06\%$.

Timing analysis of the optical data resulted in a almost complete lack of power at the know first and second harmonics of the WD spin. A large amount of flickering and flaring present in the light curves can also be seen in the power spectra at shorter frequencies. The lack of power is mostly due to the contamination of noise because of the flaring and flickering, as well as the broad band filter used during the Boyden observations. The comparative analysis between the current ephemeris model and the two selected power peaks around F_0 unfortunately resulted in peak position errors too large for accurate timing analysis for a possible update of the WD spin ephemeris. A more in-depth analysis process that involves different time series analysis techniques, as well as more selective light curve analysis, could possibly reduce the noise levels, as well as strengthen the WD spin signal. Certain pulsed emission signatures were however identified that were searched for in *Suzaku*, *Fermi* and *AGILE* data.

The *Suzaku* archival data were primarily analysed in the search for a non-thermal emission signature, and in a secondary capacity to confirm and possibly update the current system parameters. The timing analysis of the soft X-ray component resulted in a very strong and clear power peak at the fundamental frequency F_0. This singular component means that the WD spin period observable in the soft X-rays is a lot more stable at a higher resolution. This is because the emission is observed from only one location, the "front" heated emission region, and not a double location separated with a distance equal to twice the magneto-spheric radius, as observed in optical and UV, due to the "front" heated region as well as the propeller ejected gas illuminated by the second pole. The accurate F_0 soft X-ray signal was used to update the WD spin ephemeris. A WD spin period of

$P = (382.83 \pm 0.01097) \times 10^{-6}$ d $= 33.076823 \pm 0.0009475$ s was determined. This was used along with selected spin periods from literature to re-analyse the WD spin ephemeris over a total baseline of 31.25 yrs. The analysis resulted in an updated $\dot{P} = 5.0762 \times 10^{-14}$d d^{-1} term, which is larger than the $\dot{P}$ value determined by De Jager et al. (1994). This means that the white dwarf is spinning down faster, resulting in a stronger spin-down luminosity of either $L_{sd} \approx 1.23 \times 10^{34}$ erg s^{-1} for a WD mass of ~ 0.48 M$_\odot$ (Welsh et al. (1993)) or $L_{sd} \approx 6.95 \times 10^{33}$ erg s^{-1} for a WD mass of ~ 0.95 M$_\odot$ (De Jager et al. (1994)). This means that there is possibly a greater amount of power available for particle acceleration and production of non-thermal emission. A O-C pulse phase analysis would be required for greater clarity of the exact nature of the spin-down rate of the WD, i.e., is it spinning down faster, or is the spin down rate cyclic, and to what extend is it linked to the mass transfer rate from the secondary.

A first approximation spectral analysis of the soft X-ray data resulted in a fit of a three-Mekal thermal model as well as a possible Bremsstrahlung component. The fitted model was used to determine an energy flux of $\sim 8 \times 10^{-12}$ erg cm^{-2} s^{-1} for the soft X-ray component between energies of 0.4-5.0 keV. Conversely, the first approximation spectral analysis of the hard X-ray data resulted in a power-law fit. An additional Bremsstrahlung component to the fit was also investigated. The presence of a thermal Bremsstrahlung component above 14 keV is possible if an optically thin plasma is present at a high enough temperature. The presence of an increased emission towards higher energies increases the probability for non-thermal emission. The fitted power-law model was used to determine energy flux values of $\sim 1.6 \times 10^{-11}$ erg cm^{-2} s^{-1} between energies of $14 - 40$ keV and $\sim 2.1 \times 10^{-11}$ erg cm^{-2} s^{-1} between energies of $40 - 96$ keV. This result suggest the possibility of a non-thermal contribution at the high energy end of the *Suzaku* spectrum. However, pulse phase timing analysis of the hard X-ray data did not result in strong pulsed emission close to the WD spin period, although the pulse phase analysis of the hard X-ray component in terms of the orbital period did show some correlation, indicating that there possibly exists a source of high energy non-thermal emission within the binary.

If there is a hard X-ray component at the orbital radius, it would most likely be due to interactions between the ejected gas surrounding the system, which can act as a target material, and any form of accelerated particles that sweeps across this surrounding gas. A more in-depth spectral analysis, using different spectral analysis packages, could improve the parameters for the proposed models, which could result in a tighter constrain on the model for the locations of and components involved in the production of X-rays in the system.

If there is thermal Bremsstrahlung, it requires a population of free electrons, which cannot be excluded due to the presence of a thermal component in conjunction with a power-law. A small population of these particles could then be accelerated to VHE energies, resulting in $\gamma-$ ray emission above a few hundred MeV, if AE Aquarii contains one of many possible kinds of particle accelerators, which is possible given the results obtained, in conjunction to the inferred spin-down power which can be channelled to particle acceleration and non-thermal emission.

Given the probability of non-thermal pulsed emission from AE Aquarii found in the *Suzaku* data, an extensive search at higher energies was performed using *Fermi*-LAT and *AGILE*-GRID archival data. Binned as well as unbinned likelihood analyses did not result in any significant detections for both *Fermi*-LAT and AGILE-GRID, but did result in upper-limit values for VHE emission between 250 MeV-300 GeV from AE Aquarii being determined for *Fermi*-LAT. Based on the probable non-thermal hard X-ray emission from *Suzaku* as well as the upper-limits for *Fermi*-LAT, the possibility for VHE $\gamma-$ ray emission in the *Fermi*-LAT data could not be excluded.

An in-depth timing analysis was therefore performed on the *Fermi*-LAT data covering energies between 250 MeV-300 GeV. The minimum energy of 250 MeV was chosen to exclude possible contamination of the galactic background between 100 MeV-250 MeV. From Rayleigh power spectra, as well as pulse phase folding analysis a possible low-level peak at $2F_0$ as well as a stronger QPO-like feature were found. To test whether these features are bound to a specific energy range, or spread throughout the energies considered, a peak distribution anal-

ysis test was presented. The analysis showed a possible low level peak at $2F_0$ at 16.5386 $\pm$ 0.02323 s that was distributed throughout the different energy bins analysed, at an occurrence level $> 3\sigma$. No other comparative feature was found in data analysed for the coordinates of AE Aquarii, or two selected test regions on either side of the region centred on AE Aquarii. This result therefore indicates a possible low level signal at $2F_0$ in the noise structure of the *Fermi*-LAT data.

The detected photon events in the region centred on AE Aquarii were tested for correlation with optical as well as *Suzaku* data. Comparison with optical data found a visual correlation between a *Fermi* photon event and an optical observation dataset. Upon closer inspection the photon event in the energy range 250-500 MeV was found to occur just before an optical flare. This result showed a possible correlation with similar results obtained by Meintjes et al. (1994). Comparative analysis between *Fermi* photon events and *Suzaku* X-ray light-curves, found visual correlations of five out of six photon events that occurred just after instances of (hard and soft) X-ray emission. This suggests the possibility that just after an X-ray burst, the resultant population of higher energy particles could also be involved in the production of low-level VHE $\gamma-$ rays. This hypothesis however needs further analysis, modelling and testing to determine the exact parameters involved.

The results obtained in this study for the *Suzaku* energy flux as well as Fermi-LAT upper limits, were included in an updated SED, along with recent upper-limit values calculated for GeV and TeV emission using *MAGIC*. The SED shows that a strong emphasis needs to be placed on additional analysis of the hard X-ray component, to place tighter constraints on the possible non-thermal emission, and to identify a possible particle accelerator. One possible particle accelerator is the strong magnetic fields of the WD, that can drive synchrotron emission not just at the radio end of the spectrum, but also towards higher energies, as proposed by Terada et al. (2008). The constraints of the non-thermal hard X-ray component will help to constrain the parameters for a possible VHE $\gamma-$ ray accelerator and associated emission process.

On the other side of the spectrum, the increased sensitivity of HESS-II as well as the future CTA system could dramatically increase the probability for the detection of the possible low-level pulsed non-thermal VHE emission indicated in this and previous studies. Studies using these systems however will need to be conducted on a multi-wavelength platform, i.e. contemporaneous long term - long observation time studies in Radio (KAT-7, meerKAT, SKA), Optical, X-ray and $\gamma-$ ray energies to find possible correlations, that could once and for all constrain the origin and parameters of the possible high energy non-thermal emission from this enigmatic source.

Bibliography

M. Abada-Simon, A. Lecacheux, T.S. Bastian, J.A. Bookbinder, and G.A. Dulk. The spectrum and variability of radio emission from AE Aquarii. *ApJ*, 406: 692–700, 1993.

M. Abada-Simon, M. Mouchet, J. Casares, I. G. Martinez-Pais, A. Evans, S. P. S. Eyres, R. P. Fender, S. T. Garrington, O. de Jager, N. Kuno, H. Matsuo, D. de Martino, G. Pooley, G. Ramsay, A. Salama, and B. Schulz. First detection of the cataclysmic variable AE Aquarii in Near and Far Infra-Red with ISO. In F. Combes and D. Barret, editors, *SF2A-2002: Semaine de l'Astrophysique Francaise*, page 497, June 2002. URL `http://adsabs.harvard.edu/abs/2002sf2a.conf..497A`. Provided by the SAO/NASA Astrophysics Data System.

M. Abada-Simon, J. Casares, A. Evans, S. Eyres, R. Fender, S. Garrington, O. de Jager, N. Kuno, I.G. Martínez-Pais, D. de Martino, H. Matsuo, M. Mouchet, G. Pooley, G. Ramsay, A. Salama, and B. Schulz. First detections of the cataclysmic variable AE Aquarii in the near to far infrared with ISO and IRAS: Investigating the various possible thermal and non-thermal contributions. *A&A*, 433:1063–1077, 2005.

AGILE at ASDC. `http://agile.asdc.asi.it/`.

AGILE at Astro-rivelatore Gamma a Immagini Leggero. `http://agile.rm.iasf.cnr.it/`.

J. Aleksić et al. MAGIC search for VHE γ-ray emission from AE Aquarii in a multiwavelength context. *ArXiv:1407.3707v1 [astro-ph.HE]*, July 2014.

Andor. *iXon EM 888 Back-Illuminated Digital Microscope Camera*. Andor, November 2009. URL `http://www.andor.com/scientific_cameras/ixon/`.

I. L. Andronov and Y. B. Yavorskij. On the moments of inertia and radii of the white dwarfs and polytropic stars. *Contributions of the Astronomical Observatory Skalnate Pleso*, 20:155, 1990.

L. Angelini. Agile. HEASARC Research Group (HUG) meeting, October 2007.

Apogee Instruments Inc. `http://www.ccd.com/`.

Apogee Instruments Inc. *Apogee Alta COM (ActiveX) API Specification*. Apogee Alta Software Reference, Apogee Instruments Inc., Specification Version 1.3 edition, August 2006.

W.B. Atwood et al. The large area telescope on the Fermi Gamma-ray space telescope. 2009.

G. D. Badhwar and S. A. Stephens. Gamma ray production in interstellar space. *International Cosmic Ray Conference*, 1:198–202, 1977.

T.S. Bastian, D.A. Dulk, and G. Chanmugam. Radio flares from AE Aquarii: A low-power analog to Cygnus X-3? *ApJ*, 324:431–440, 1988.

K. Bernlöhr, A. Barnacka, Y. Becherini, O. Blanch Bigas, E. Carmona, P. Colin, G. Decerprit, F. Di Pierro, F. Dubois, C. Farnier, S. Funk, G. Hermann, J. A. Hinton, T. B. Humensky, B. Khélifi, T. Kihm, N. Komin, J.-P. Lenain, G. Maier, D. Mazin, M. C. Medina, A. Moralejo, S. J. Nolan, S. Ohm, E. de Oña Wilhelmi, R. D. Parsons, M. Paz Arribas, G. Pedaletti, S. Pita, H. Prokoph, C. B. Rulten, U. Schwanke, M. Shayduk, V. Stamatescu, P. Vallania, S. Vorobiov, R. Wischnewski, T. Yoshikoshi, A. Zech, and CTA Consortium. Monte Carlo design studies for the Cherenkov Telescope Array. *Astroparticle Physics*, 43:171–188, March 2013. doi: 10.1016/j.astropartphys.2012.10.002.

N. G. Beskrovnaya, N. R. Ikhsanov, A. Bruch, and N. M. Shakhovskoy. Photometric and polarimetric analysis of the flaring activity in AE Aqr. *AAP*, 307: 840–848, Mar 1996.

N.G. Beskrovnaya and N.R. Ikhsanov. On the origin of the peculiar cataclysmic variable AE Aquarii. 2014.

George R. Blumenthal and Robert J. Gould. Bremsstrahlung, Synchrotron Radiation, and Compton Scattering of High-Energy Electrons Traversing Dilute Gases. *REV-MOD-PHYS*, 42(2):237–270, April 1970.

J.A. Bookbinder and D.Q. Lamb. Discovery of Radio emission from AE Aquarii. *ApJ*, 323:L131–L135, 1987.

J.J. Calitz. The development of an UFS-Boyden photometric pipeline to facilitate the observational study of accretion driven systems. Master's thesis, University of the Free State, South Africa, 2005.

Celestron. *NexStar Communications Protocol*. Celestron, 2835 Columbia Street, Torrance, CA 90503, April 2005. URL `www.celestron.com/c3/images/files/downloads/1154108406_nexstarcommprot.pdf`.

P.M. Chadwick, J.E. Dickinson, M.R. Dickinson, N.A. Dipper, J. Holder, T.J.L. McComb, K.J. Orford, S.M. Rayner, I.D. Roberts, M.D. Roberts, S.P. Tummy, and K.E. Turver. A burst of pulsed VHE gamma rays from AE Aquarii. *Astroparticle Physics*, 4:99–111, 1995.

A. Chen, A. Bulgarelli, T. Contessi, A. Giuliani, S. Mereghetti, A. Pellizzoni, A. Trois, and S. Vercellone. *GRID Scientific Analysis User Manual*. AGILE-IFC-OP-09, November 2011.

A.W. Chen et al. Calibration of AGILE-GRID with in-flight data and Monte Carlo simulations. *A&A*, (558):A37, 2013.

C. Choi, T. Dotani, and P.C. Agrawal. A study of the X-ray emission of the Magnetic Cataclysmic Variable AE Aquarii. *ApJ*, 525:399–406, 1999.

C. Clapham. *Concise Dictionary of Mathematics*. Oxford University Press, Oxford, second edition, 1996.

R. Coppejans and A. Gulbis. *SHOCnhelpful, a guide to the Sutherland high-speed optical cameras*. South African Astronomical Observatory, SAAO, Cape Town, South Africa, June 2014.

J. A. Crawford and R. P. Kraft. An Intrepretation of AE Aquarii. *ApJ*, 123:44, Jan 1956. doi: 10.1086/146128.

M. Cropper. Polarization observations of DQ HER stars and other cataclysmic variables. *MNRAS*, 222:225–233, September 1986.

O. C. De Jager, B. C. Raubenheimer, and J. W. H. Swanepoel. A poweful test for weak periodic signals with unknown light curve shape in sparse data. *A&A*, 221:180–190, Aug 1989.

O.C. De Jager and P.J. Meintjes. Short optical bursts and acceleration to TeV energies in AE Aquarii. *A$A*, 268:1.1–1.4, 1993.

O.C. De Jager, P.J. Meintjes, D. O'Donoghue, and E.L. Robinson. A discovery of a brake on the white dwarf in AE Aquarii. *MNRAS*, (267):577–588, 1994.

G. Dubus, R. Campbell, B. Kern, R.E. Taam, and H.C. Spruit. Excess mid-infrared emission in cataclysmic variables. *MNRAS*, 349:869–881, 2004.

G. Dubus, R.E. Taam, C. Hull, D.M. Watson, and J.C. Mauerhan. *Spitzer Space Telescope* observations of the Magnetic Cataclysmic Variable AE Aquarii. *ApJ*, 663:516–521, 2007.

J. Echevarria, F. Diego, D. Mills, and R.C. Smith. High resolution time-resolved UCLES spectroscopy of AE Aqr: I. The secondary star revealed. *JAAVSO*, 35: 136B, 2006.

M. Eracleous, J. Halpern, and J. Patterson. X-ray spectra of cataclysmic variables from the Einstein Observatory. *ApJ*, 382:290–300, Nov 1991. doi: 10.1086/170716.

M. Eracleous, K. Horne, E.L. Robinson, E. Zhang, T.R. Marsh, and J.H Wood. The ultraviolet pulsations of the cataclysmic variable AE Aquarii as observed with the *Hubble Space Telescope*. *ApJ*, 433:313–331, 1994.

Fermi at ASDC. http://fermi.asdc.asi.it/.

Fermi Science Support Center at HEASARC. http://fermi.gsfc.nasa.gov/ssc/.

G.B. Folland. *Fourier analysis and its applications*. Brooks/Cole Publishing Company, Pacific Grove, California, USA, 93950, 1992.

M. Friedjung. The characteristics of the cool component of the cataclysmic binary AE Aquarii derived from its HIPPARCOS parallax. *NA*, 2:319–322, October 1997. doi: 10.1016/S1384-1076(97)00024-9.

G. Ghisellini. *Radiative processes in high energy astrophysics*. INAF - Osservatorio Astronomico di Brera, 2012.

J.Y. Guo, H. Greiner-Mai, O. Dierks, L. Ballani, J. Neumeyer, and C.K. Shum. Application of the Folding-Averaging Algorithm for the Determination of the Periods of the Earth's Free Oscillation Using Superconducting Gravimeter Data. *Bulletin d'Information des Mares Terrestres*, 139:11025–11036, 2005.

HEASARC. *CFITSIO User's Reference Guide, An Interface to FITS Format Files for C Programmers*. HEASARC, Code 662, Goddard Space Flight Center, Greenbelt, MD 20771, USA, Version 3.0 edition, August 2007.

C. Hellier. *Cataclysmic Variable Stars: How and why they vary.* Praxis Publishing Ltd., Chichester, UK, first edition, 2001.

K. G. Henize. Rapid variation of AE Aquarii. *AJ*, 54:89, March 1949. doi: 10.1086/106203.

C.A. Hill, C.A. Watson, T. Shahbaz, D. Steeghs, and V.S. Dhillon. Roche tomography of cataclysmic variables - VI. Differential rotation of AE Aqr - Not tidally locked! *MNRAS*, 2014.

S. Hoenen, M. Schimmel, and M.D. Marques. Rescuing Rhythms from Noise: A new method of analysis. *Biological Rhythm Research*, 32(2):271–284, 2001.

N.R. Ikhsanov, V.V. Neustroev, and N.G. Beskrovnaya. A white dwarf in the State of an Ejector. *Astronomy Letters*, 30(10):675–684, 2004.

IRAF.Net. IRAF software and user support. `http://iraf.net/`.

K. Itoh, S. Okada, M. Ishida, and H. Kunieda. Density Diagnostics of the Hot Plasma in AE Aquarii with XMM-Newton. *ApJ*, 639:397–404, March 2006. doi: 10.1086/499152.

R.F. Jameson, A.R. King, and M.R. Sherrington. The UV spectrum of AE Aqr. *MNRAS*, 191:559–569, 1980.

A. H. Joy. Spectroscopic Observations of AE Aquarii. *ApJ*, 120:377, November 1954. doi: 10.1086/145928.

W. J. Karzas and R. Latter. Electron Radiative Transitions in a Coulomb Field. *ApJS*, 6:167, May 1961. doi: 10.1086/190063.

E. Kellogg, J. R. Baldwin, and D. Koch. Studies of cluster X-ray sources, energy spectra for the Perseus, Virgo, and Coma clusters. *ApJ*, 199:299–306, Jul 1975. doi: 10.1086/153692.

M. Kotze. *A data reduction pipeline for SHOC: Manual*, June 2013.

P. Kumar, R. A. Hernández, Ž. Bošnjak, and R. B. Duran. Maximum synchrotron frequency for shock-accelerated particles. *MNRAS*, 427:L40–L44, Nov 2012.

P. Lamb and P. W. Sanford. Compton scattering effects observed in SCO X-1 and similar sources. *MNRAS*, 188:555–563, Aug 1979.

M.J. Lang, J.H. Buckley, D.A. Carter-Lewis, M. Catanese, M.F. Cawley, E. Colombo, E. Connaughton, D.J. Fegan, J.P. Finley, J.A. Gaidos, G.A. Gillanders, A.M. Hillas, M.P. Kertzman, F. Krennrich, R.W. Lessard, P. Moriarty, J. Quinn, H.J. Rose, G. Sembroski, and T.C. Weekes. A search for TeV emission from AE Aquarii. *Astroparticle Physics*, 9:203–211, 1998.

D. A. Liedahl, A. L. Osterheld, and W. H. Goldstein. New calculations of Fe L-shell X-ray spectra in high-temperature plasmas. *ApJL*, 438:L115–L118, Jan 1995. doi: 10.1086/187729.

N.R. Lomb. Least-squares frequency analysis of unequally spaced data. *ApSS*, 39: 447–462, 1976.

M.S. Longair. *High-energy astrophysics*, volume 1. Cambridge University Press, 2nd edition, 1992.

R. Lopez-Coto, O. Blanch Bigas, J. Cortina, D. Hadasch, L. Takalo, D. Torres, M. Bogosavljevic, Z. Ioannou, C. W. Mauche, E. V. Palaiologou, M. A. Perez-Torres, and T. Tuominen. Search for TeV γ-ray emission from AE Aqr coincident with high optical and X-ray states with the MAGIC telescopes. *ArXiv:1309.2503v1 [astro-ph.HE]*, September 2013.

K.V. Mardia. *Statistics of Directional Data*. Academic Press Inc. (London) Ltd., London, UK, 1972.

C.W. Mauche. The white dwarf in AE Aqr brakes harder. *MNRAS*, (369):1983–1987, 2006.

P. J. Meintjes. Magnetized fragmented mass transfer in cataclysmic variables: AE Aquarii, a trial case. *MNRAS*, 352:416–426, August 2004. doi: 10.1111/j.1365-2966.2004.07898.x.

P. J. Meintjes and L. A. Venter. Modelling the continuous radio outbursts in AE Aquarii. *MNRAS*, 341:891–900, May 2003. doi: 10.1046/j.1365-8711.2003.06459.x.

P.J. Meintjes. *Search for TeV Gamma-ray emission from cataclysmic variables.* PhD thesis, University of Potchefstroom, South African, 1990.

P.J. Meintjes and L.A. Venter. The diamagnetic blob propeller in AE Aquarii and non-thermal radio to mid-infrared emission. *MNRAS*, (360):573, 2005.

P.J. Meintjes, B.C. Raubenheimer, O.C. de Jager, C. Brink, H.I. Nel, A.R. North, G. van Urk, and B. Visser. AE Aquarii: An emitter of pulsed TeV Gamma rays resembling optical emission during flares. *ApJ*, 401:325–336, 1992.

P.J. Meintjes, O.C. de Jager, B.C. Raubenheimer, H.I. Nel, A.R. North, D.A.H. Buckley, and C. Koen. Simultaneous optical and TeV gamma-ray observations of the cataclysmic variable AE Aquarii. *ApJ*, 434:292–305, 1994.

P. Melchior. *The tides of the planet earth*. Pergamon Press, Oxford, UK, 1978.

R. Mewe, E. H. B. M. Gronenschild, and G. H. J. van den Oord. Calculated X-radiation from optically thin plasmas. V. *A&AS*, 62:197–254, Nov 1985.

R. Mewe, J. R. Lemen, and G. H. J. van den Oord. Calculated X-radiation from optically thin plasmas. VI - Improved calculations for continuum emission and approximation formulae for nonrelativistic average Gaunt factors. *A&AS*, 65: 511–536, Sep 1986.

B. Oruru and P.J. Meintjes. X-ray characteristics and the spectral energy distribution of AE Aquarii. *MNRAS*, (421):1557–1568, 2012.

D.M. Palmer. A fast chi-squared technique for period search of irregularly smapled data. *AJ*, 695:496–502, 2009.

J. Patterson. Rapid oscillations in cataclysmic variables. III. An oblique rotator in AE Aquarii. *ApJ*, 234:978–992, 1979.

J. Patterson, D. Branch, G. Chincarini, and E. L. Robinson. 33 second X-ray pulsations in AE Aquarii. *ApJ*, 240:L133–L136, September 1980.

Physical Geography. `http://www.physicalgeography.net/fundamentals/images/helions.jpg`, Retrieved June 2013.

W.H. Press, S.A. Teukolsky, W.T. Vetterling, and B.P. Flannery. *Numerical Recipes. The art of scientific computing*. Cambridge University Press, 32 Avenue of the Americas, New York, NY 10013-2473, USA, 3rd edition, 2007.

J.A. Rice. *Mathematical Statistics and Data Analysis*. Wadsworth Publishing Company, Belmont, California, USA, 94002, second edition, 1995.

I. Ridpath. *Dictionary of Astronomy*. Oxford University Press, Oxford, 1997.

E.L. Robinson, A.W. Shafter, and S. Balachandran. The pulse-timing and emission-line orbits of the white dwarf in the cataclysmic variable AE Aquarii. *ApJ*, 374:298–306, 1991.

B.G. Rybicki and P.A. Lightman. *Radiative Processes in Astrophysics*. Wiley, 1979.

SAAO 1.9 m telescope. `http://www.saao.ac.za/science/facilities/telescopes/1-9m/`.

SBIG Astronomical Instruments. *SBIG Class Library*. Santa Barbara Instruments Group, Santa Barbara, CA 93117, USA, Version 1.2 edition, September 2006.

SBIG Astronomical Instruments. *SBIG Universal Driver/Library*. Santa Barbara Instruments Group, Santa Barbara, CA 93117, USA, Version 4.57 edition, September 2007.

J.D. Scargle. Studies in astronomical time series analysis. II. Statistical aspects of spectral analysis of unevenly spaced data. *ApJ*, 263:835–853, 1982.

M.A. Seeds. *Foundations of Astronomy*. Brooks/Cole Thomson Learning, USA, sixth edition, 2001.

N. Sidro, J. Cortina, C.W. Mauche, E. de Ona, J. Rico, D.F. Torres, and The MAGIC collaboration. Observation of AE Aquarii with the MAGIC telescope. In D'Olivo J.C. Medina-Tanco G. Nellen L. Sanchez F.A. Caballero, R. and J.F. Valdes-Galicia, editors, *Proceedings of the 30th International Cosmic Ray Conference*, volume 2 (OG part 1), pages 715–718, Mexico City, Mexico, 2008. Universidad Nacional Autonoma de Mexico.

Y. Terada, M. Ishida, K. Mukai, K. Makishima, T. Dotani, L. Gallo, S. Naik, T. Hayashi, S. Okada, R Nakamura, and T. Enoto. A high-sensitive Suzaku observation of possible non-thermal emission from a white dwarf, 2007.

Y. Terada, T. Hayashi, M. Ishida, K. Mukai, T. Dotani, S. Okada, R. Nakamura, S. Naik, A. Bamba, and K. Nakamura. Suzaku discovery of hard X-ray pulsations from the rotating magnetized white dwarf, AE Aquarii. *PASJ*, 2008. Retrieved as arXiv:0711.2716v2 [astro-ph] 24 Jan 2008.

H.J. Van Heerden. The development of an IRAF-based scientific photometric package for the UFS-Boyden 1.5-m telescope. Master's thesis, University of the Free State, South Africa, 2008.

H.J. Van Heerden. *Observing Procedures and Celestron Telescope Manual*. Astrophysics Group, Dept. of Physics, UFS, September 2010.

H.J. Van Heerden and J.J. Calitz. *Observing Procedures and 1.52 m Telescope Manual*. Astrophysics Group, Dept. of Physics, UFS, September 2010.

J. E. Van Zyl. *Ontsluier die Heelal*. Protea Boekhuis, Pretoria, South Africa, second edition, 2002.

L.A. Venter and P.J. Meintjes. Kelvin-Helmholtz and the turbulance driven magnetoshperic propeller and non-thermal flares of AE Aqurii. *MNRAS*, (366): 557–565, 2006.

A.A. Wachmann. Neue Veränderliche. *Astronomische Nachrichten*, 242:382, 1931.

P.T. Wallace. *SLALIB - Positional Astronomy Library, Programmers Manual*. CCLRC, Rutherford Appleton Laboratory, Starlink Project, October 2003.

C.A. Watson and V.S. Dhillon. Roche tomography of cataclysmic variables - I. Artefacts and techniques. *MNRAS*, (326):67–77, 2001.

C.A. Watson, V.S. Dhillon, and T. Shahbaz. Roche tomography of cataclysmic variables - III. Star-spots on AE Aqr. *MNRAS*, (368):637–650, 2006.

C.A. Watson, D. Steeghs, V.S. Dhillon, and T. Shahbaz. Imaging the cool stars in the interacting binaries AE Aqr, BV Cen and V426 Oph. *AN*, 328(8):813–816, 2007.

W. F. Welsh, K. Horne, and R. Gomer. Doppler signatures of Hα flares in AE Aquarii. *MNRAS*, 298:285–302, July 1998. doi: 10.1046/j.1365-8711.1998.01643.x.

W.F. Welsh, K. Horne, and R. Gomer. On the location of the oscillations in AE Aquarii. *ApJ*, 410:L39–L42, 1993.

W.F. Welsh, K. Horne, and R. Gomer. A study of the absorption lines from the donor star in the exotic cataclysmic variable AE Aquarii. *MNRAS*, (275): 649–670, 1995.

H. Worters and S. Potter. *1.9-m Telescope Control Software: A user's guide*, November 2011.

G. A. Wynn, A. R. King, and K. Horne. A magnetic propeller in the cataclysmic variable AE Aquarii. *MNRAS*, 286:436–446, April 1997.

R.K. Zamanov, G.Y. Latev, K.A. Stoyanov, S. Boeva, B. Spassov, and S.V. Tsvetkova. Simultaneous UBVRI observations of the cataclysmic variable AE Aquarii: Temperatures and masses of fireballs. *AN*, (8):736–743, 2012.

E. Zinner. Mitteilungen über veränderliche und verdächtige Sterne. *Astronomische Nachrichten*, 265:345, May 1938.

Appendix A

Time Series Analysis Techniques

A.1 Introduction

Time series analysis is the study of a set or sequence of observations taken over a period of time (usually at equal intervals), with the aim to identify the characteristics that define the phenomenon being observed. The main characteristics are then the variation and trend, which can be used to possibly predict the future behaviour of the observed phenomenon. The variation is usually the shorter term change in the time series: i.e. is there a periodic change or is it random, while the trend is the long term change in the time series: i.e., the variation or "signal" increasing or decreasing in amplitude or strength (Refer to Clapham (1996) for additional discussion).

One of the main tools used during time series analysis is the power spectrum or periodogram. The power spectrum of the phenomenon being studied is the graphical representation of the power or strength of the different detected signals in frequency space, while the periodogram is the graphical representation of the power or strength of the different detected periodicities in time space. The relevance of each graph that is produced or used during time series analysis depends on the type of data, analysis methods and the required resultant format.

One of the purposes of astronomical time series analysis is the detection and anal-

ysis of periodic events in astronomical sources. These include transient events, spin and orbital periods of stellar systems, inter- and extra-galactic phenomena and even phenomena in the solar system.

For accurate time series analysis, an accurate frame of reference is required to measure the phenomena against. In the case of periodic signal detection or analysis of astronomical sources, an accurate clock is required for an accurate time-stamp for the signal being measured. With this in mind, all external influences that might have an effect on the accuracy of the reference clock need to be taken into consideration. One of the ways to correct for this is to use a so-called "Standard Clock", just like standard stars are used to correct photometric or spectroscopic measurements and Standard Candles are used to calibrate distance measurements.

To understand why and how a "Standard Clock" is used the different time systems involved have to be referenced. The following discussions are referenced mainly from Ridpath (1997). The time system used on earth to measure astronomical events is the Julian Day (JD) which is the number of days and fractions of days as measured from *mean noon* on 4713 BC, with the fractions defined as the Universal Time (UT) in terms of a fraction of a day. The Julian day time system is designed to give unambiguous dates and times. Another reference frame used to measure astronomical sources is the Julian epoch. The Julian epoch is a set date that is specified as a year with a decimal part, with the year specified as the Julian year of 365.25 days, and the time-scale used the Barycentric Dynamical Time (TDB). Thus J2000.0 is 1.5 January 2000 or 12 h TDB on January 1 the year 2000. For example, J1999.0 is exactly 365.25 days earlier, i.e. 1.25 January 1999.

To correct for the JD or date in terms of the time-stamp is therefore relatively easy because it is referenced to a set year value, but to correct the fractional component is more difficult, because as seen above different time systems are used, i.e. UT and TDB. To therefore correct the fractional component, the observation time-stamp has to start with an accurate time value. Time on earth is measured using different systems or reference frames, depending on position and purpose. The earth is split into 24 time zones with the time zones centred on the Greenwich

meridian, where time is defined as Greenwich Mean Time (GMT), with the time set as the Greenwich hour angle of the mean sun plus 12 h. Therefore the day starts at 12:00 midnight. South African Standard Time (SAST) for instance is defined as GMT + 2, i.e. if it is 10:00 at Greenwich then SAST will be 12:00.

A specially corrected version of UT, Coordinated Universal Time (UTC), is used to define modern civil time signals, and is linked with International Atomic Time (TAI). The differences between UT and UTC that has to be corrected for is the difference between GMT and Greenwich Mean Sidereal Time (GMST), the variation in longitude due to the Chandler wobble of the earth and the dependence on the observing site location, as well as the difference between UT and TAI, which is approximately 1 second per year. The link between TAI and UTC is kept at a whole number of seconds, and between UT and UTC at 0.9 s. Because of the differences, sometimes leap seconds has to be used to correct the offset.

Because of the technical nature of using civil time signals to get an accurate time-stamp, a relatively new time system is used that does not have so many corrections. Global Positioning System (GPS) time is based on the atomic time scale implemented by the GPS ground control systems, as well as the satellites themselves. GPS time is not perturbed by leap seconds, because it is directly linked to atomic time and was zero at 00:00 on 6th January 1980. The difference between TAI and GPS is set at 19 seconds. Therefore the local time at an observatory can be set using a GPS receiver system. The accuracy of the time signal from the GPS receiver then only depends on how many satellites it picks up and how long it remains in a stationary position. Thus the longer it remains stationary and the more satellites it can pick up to triangulate its position, the more accurate will be its time signal in terms of sub-second accuracy. Most scientific stations nowadays use GPS as the primary or secondary system to correct or set their time signal or time-stamp during observational work.

Two time systems that can briefly be mentioned at this stage is Ephemeris Time (ET) and Terrestrial Time (TT), also known as Terrestrial Dynamical Time. Ephemeris time was the time system used to calculate the orbits of objects within

the solar system from 1960 to 1984, but was dropped because of being inconvenient, in that it used the ephemeris second which was based on a tropical year. TT, which replaced it from 1984 onwards, uses as its fundamental unit the day of 86400 SI seconds. Through their definitions there is a difference of 32.184 seconds between TT and TAI. ET and TT are mentioned to exclude possible confusion with the so-called ephemeris of an astronomical object. The ephemeris of an astronomical object by definition is a table giving the predicted positions of said object for a given time. The ephemeris can therefore also be described by an ephemeris equation, which then describes the positional motion of an astronomical object through time, and could also be used to describe said motion, i.e. is the orbital or spin motion of an object constant or variable, and is the variation cyclic or linear.

Getting back to time series analysis of an astronomical object with the aim of defining or refining variables that can be used to define or refine ephemerides for said object that could in turn be used to prove, explain or refine models of said object, there is one final obvious correction that could or should be made in terms of the time-stamp. As mentioned above, to do accurate time series analysis of an astronomical object, a standard clock has to be used as a time-stamp of measured events. Also, as mentioned, the JD is used as the time-stamp reference, but by definition it uses TDB as the fractional component. Therefore the difference between TDB and GPS time has to be defined, and how to correct for this difference.

Even though the GPS satellites orbits the earth, GPS time is still an earth or terrestrial based system. Thus any measurements made from earth predefines the measured events to a geocentric system. This leads to a few problems: Because the earth is moving the light path (the path travelled by the emitted radiation from the object, including total distance) is constantly changing, which means that the arrival times of the measured events are influenced by the orbital and spin motion of the earth, in the simple case of an earth-bound observatory. In the case of an satellite, the additional motion of the satellite should also be taken into account. For this reason the GPS time-stamp has to be corrected to TDB. In this case the barycentre of TDB refers to the barycentre of the solar system.

The reason why the time-stamp is corrected to a barycentric time is that to have an accurate time-stamp for the observed events which would enable accurate time series analysis, a stationary position is required from where the astronomical object is observed. This means that the light path remains relatively constant in terms of the distance between the observer and the object being observed. With the barycentre of the solar system being just outside the sun's surface, the relatively known periodic variations because of the earth's motion can be compensated for, or if the observations are satellite-based, the additional satellite orbital variations in addition to the earth's can be compensated for. Most satellite observational data therefore also include orbital motion files, that can be used in the barycentric corrections. An additional consideration that has to be compensated for is then also the location of the object observed in terms of the earth-barycentre position (See figure A.1 and figure A.2).

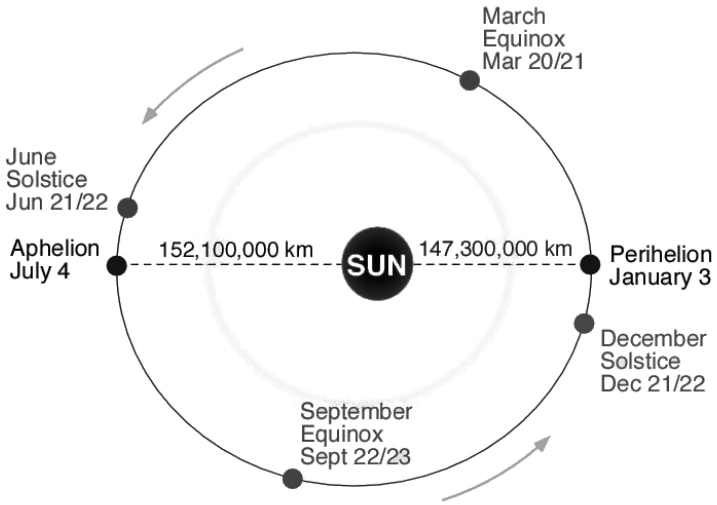

Figure A.1: Orbit of the earth around the sun (Physical Geography (2013)).

From the figures it can be seen that the light path can be corrected (depending upon position) by as much as 152 100 000 km or in terms of light time 507.351 seconds, given that the speed of light is c = 299 792.458 km.s^{-1}. See figure A.3 for a basic graph of the combined spin and orbital light time variation effect of the earth versus the barycentre of the solar system in terms of an observer, with the object

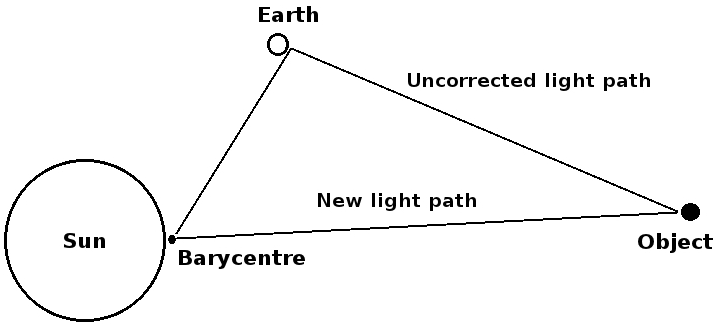

Figure A.2: Barycentric correction for light path distance and time.

being observed positioned parallel to the Aphelion-Perihelion axis. As can be seen the predominant variation is due to the orbital motion of the earth, but the spin of the earth also has a small effect. Additional effects not mentioned or shown are the small effects on the position of the barycentre due to the orbital positions of the other solar system bodies. Modern-day barycentric correction algorithms that are used in astronomical analysis software packages then not only include equations that model the orbital and spin variations and positional dependence of the earth-barycentre-object, but also include ephemerides for the different solar system bodies in addition to input for satellite orbital motion tables.

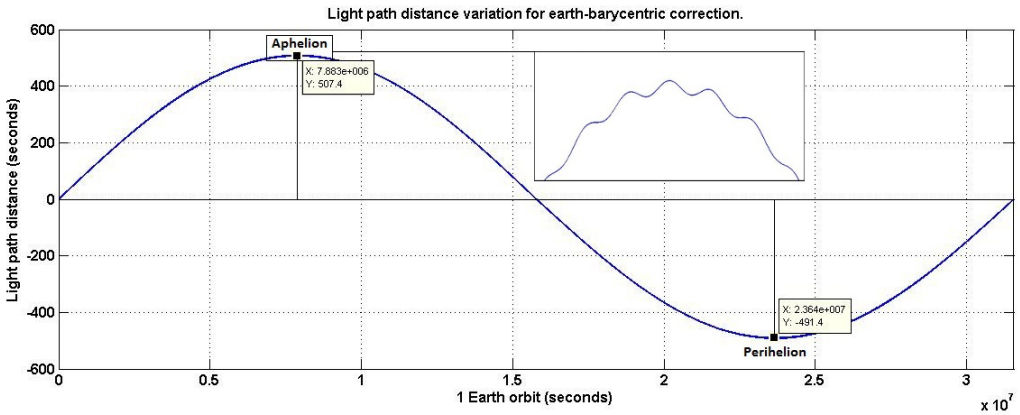

Figure A.3: Orbital and spin variation of Earth-Barycentre light path correction.

With all of the above-mentioned corrections applied to the time-stamp of the observations, an accurate time series is now ready for analysis. Additional manipulations that can also be performed on the time series are binning or re-sampling. This involves changing or combining the sampling rates of the measured events, with the event data then also being combined in order to have increased sampling rates, or through interpolation techniques, adding of additional artificial data for decreased sampling rates. Although this kind of approach can have positive results in terms of reduction of noise, or increase in resolution, it also inherently poses dangers in terms of false positives or artificial signals. Another technique that can be applied is de-trending of the time series. This consists of removal of large-scale structure or low frequencies in the time series data through the following method: Fitting and then subtracting of low order polynomials to the data set, or through mean averaging where section by section is normalised. A technique that is applied in electronics is band passing, where the lower frequencies are removed through filters, and only frequencies within a specified pass band are measured. These techniques can only be safely applied if one has a thorough understanding of the time series or signal being studied. The time series, being in an acceptable format, can then be used in power spectrum or periodogram analysis techniques.

A.2 Power spectrum or periodogram analysis techniques

A.2.1 The DFT and FFT

The predominant technique used in time series analysis of standard signals or time series is the Fourier transform. The following concise discussion is referenced mainly from Folland (1992). The Fourier transform is based on the assumption that all continuous time series that are functions of $\mathbf{R}$ can be represented by the sum of different sine and cosine series. This Fourier series thus represents the mathematical transform of the time series to frequency space. The continuum Fourier transform of an integrable function f on $\mathbf{R}$ is then $\hat{\mathrm{f}}$ on $\mathbf{R}$, and is defined

by

$$\hat{\mathrm{f}}(\xi) = \int \mathrm{e}^{-\mathrm{i}\xi\mathrm{x}}\mathrm{f}(\mathrm{x})\mathrm{dx}, \tag{A.1}$$

with the Fourier inversion theorem represented by

$$\mathrm{f}(\mathrm{x}) = \frac{1}{2\pi}\int \mathrm{e}^{\mathrm{i}\xi\mathrm{x}}\hat{\mathrm{f}}(\xi)\mathrm{d}\xi. \tag{A.2}$$

This inversion function can then be used to recover the mathematical form of the original time series data, based on the representative Fourier transform. The form of the Fourier transform used in signal analysis is then

$$\hat{\mathrm{f}}(\omega) = \int \mathrm{e}^{-\mathrm{i}\omega\mathrm{t}}\mathrm{f}(\mathrm{t})\mathrm{dt} \quad \text{and} \quad \mathrm{f}(\mathrm{t}) = \frac{1}{2\pi}\int \mathrm{e}^{\mathrm{i}\omega\mathrm{t}}\hat{\mathrm{f}}(\omega)\mathrm{d}\omega, \tag{A.3}$$

for all possible frequencies ω. In computational studies of time series, the discrete Fourier transform (DFT) is used. This is because in computational analysis, the numerical approximation of the Fourier transform has to be used. The analysis is thus performed over only a finite number of calculations for a finite number of data. The Fourier transform is thus limited from say $0 - \Omega$ for a data set of length Ω. With the integral becoming a Riemann sum with N equal intervals with endpoints $\mathrm{n}\Omega/\mathrm{N}$, the DFT can thus be represented by

$$\hat{\mathrm{a}}_{\mathrm{m}} = \sum_{\mathrm{n}=0}^{\mathrm{N}-1} \mathrm{e}^{-2\pi\mathrm{mn}/\mathrm{N}}\mathrm{a}_{\mathrm{n}} \qquad (0 \leq \mathrm{m} < \mathrm{N}), \tag{A.4}$$

where m is defined as $|\mathrm{m}| \leq \frac{\mathrm{C}\Omega}{2\pi}$, the integer cycle for the Fourier values. Thus a vector $\mathbf{a} = (\mathbf{a_0}, ..., \mathbf{a_{N-1}}) \in \mathbf{C^N}$ can be transformed into another vector $\hat{\mathbf{a}} = (\hat{\mathbf{a}}_\mathbf{0}, ..., \hat{\mathbf{a}}_\mathbf{N-1}) \in \mathbf{C^N}$. The inversion formula is then

$$\mathrm{a}_{\mathrm{n}} = \frac{1}{\mathrm{N}}\sum_{\mathrm{m}=0}^{\mathrm{N}-1} \mathrm{e}^{2\pi\mathrm{mn}/\mathrm{N}}\hat{\mathrm{a}}_{\mathrm{m}}. \tag{A.5}$$

The implementation of the DFT in computational algorithms is then the fast Fourier transform (FFT). In the calculation of $\hat{\mathbf{a}}$, a total number of N^2 operations is required. The FFT is a case where the DFT is represented by N values, and N is a power of 2, i.e. $\mathrm{N} = 2^{\mathrm{k}}$. N can thus be factorised, and it can be shown that this

N can then be factored from $2^{2k} = N^2$ to $k2^{k+1} = 2Nlog_2N$. This form of the DFT has been used as far back as Gauss in 1805. The computational FFT algorithm calculates both the Fourier transform as well as the inverse Fourier transform of the time series data to be analysed. The danger of the FFT is that the data has to be more or less continuous, with no large gaps present, and the data set must be a power of 2 in length. Zero padding can be used to complete the input vector to fill the gaps, and make the dataset a power of 2, but it comes with its own set of risks, in terms of false positives, and ringing at low frequencies due to the strengthening of low frequency noise. Aliasing can also occur due to leakage of power from high frequencies to much lower frequencies. The simple FFT also does not consider the nature of the data, specifically in terms of the statistics.

A.2.2 Lomb-Scargle method

A technique that considers the data as well as a measure of the statistics of the data is the Lomb-Scargle method. Lomb (1976) and Scargle (1982) developed the same method through independent means, which is based on least squares fitting of test frequencies to unequally spaced data. An additional reference used was Press et al. (2007). The periodogram or power spectrum can be constructed by calculating the normalised Lomb-Scargle power

$$P_x(\omega) = \frac{1}{2\sigma^2}\left(\frac{[\sum_j (X_j - \bar{X})\cos\omega(t_j - \tau)]^2}{\sum_j \cos^2\omega(t_j - \tau)} + \frac{[\sum_j (X_j - \bar{X})\sin\omega(t_j - \tau)]^2}{\sum_j \sin^2\omega(t_j - \tau)}\right), \tag{A.6}$$

where $\bar{X}$ is the data mean, and σ^2 the variance. The time lag τ between measurements is defined as

$$\tan 2\omega\tau = \frac{\sum_j \sin 2\omega t_j}{\sum_j \cos 2\omega t_j}. \tag{A.7}$$

The structures within the resultant periodogram can be considered as follows: The distribution of $P(\omega)$ can be used to analyse the chance that a detected peak is 'n signal or a spurious spectral peak due to noise. The maximum power Z for a pure

noise spectrum of N frequencies with independent powers will be

$$\langle \mathrm{Z(max)} \rangle = \sum_{\mathrm{k=1}}^{\mathrm{N}} 1/\mathrm{k}, \tag{A.8}$$

This means that if a large number of frequencies are inspected for a spectral peak, a large peak power can be found even if no signal is present. Because of this a false alarm probability has to be defined. If a power level z_0 is found, and claimed to be a signal, the probability p_0 that the claim is a false positive would be

$$\mathrm{z_0} = -\ln\left[1 - (1 - \mathrm{p_0})^{1/\mathrm{N}}\right], \tag{A.9}$$

where N is the number of frequencies considered for the maximum. Thus for example if N = 30, Z must be greater than 8 to report a signal with 99.0% ($\mathrm{p_0} = 0.01$) confidence.

A.2.3 Rayleigh test

The following concise discussion is referenced mainly from Mardia (1972) and De Jager et al. (1989). The Rayleigh test is a test for uniformity of a sample population that has a von Mises $\mathrm{M}(\mu_0, \kappa)$ distribution. For the null-hypothesis we have that

$$\mathrm{H_0} : \mathrm{f}(\theta) = 1/2\pi, \qquad 0 \leqslant \theta \leqslant 2\pi, \tag{A.10}$$

against the alternative

$$\mathrm{H_1} : \mathrm{f}(\theta) = \mathrm{g}(\theta), \tag{A.11}$$

where for $\mathrm{H_0} : \mu_0 = 0$ and $\kappa = 0$ against $\mathrm{H_1}$ where both μ_0 and κ are unknown. The likelihood function for $\mathrm{H_0}$ then becomes

$$\mathrm{L_0} = 1/(2\pi)^2, \tag{A.12}$$

while the maximum likelihood function for $\mathrm{H_1}$ becomes

$$\max \mathrm{L}_1 = \{2\pi \mathrm{I}_0(\hat{\kappa})\}^{-\mathrm{n}} \mathrm{e}^{(\mathrm{n}\hat{\kappa}\bar{\mathrm{R}})}. \tag{A.13}$$

The general function for $\bar{\mathrm{R}}$ (Rayleigh test statistic) for a dataset of n values, tested for l harmonics, is given by

$$2\mathrm{n}\bar{\mathrm{R}}_\mathrm{l}^2 = 2\mathrm{n}(\bar{\mathrm{C}}_\mathrm{l}^2 + \bar{\mathrm{S}}_\mathrm{l}^2), \tag{A.14}$$

with the sine and cosine components defined as

$$\bar{\mathrm{S}} = \frac{1}{\mathrm{n}} \sum_{\mathrm{i}=1}^{\mathrm{n}} \sin(2\pi \mathrm{l}\theta_\mathrm{i}) \quad \text{and} \quad \bar{\mathrm{C}} = \frac{1}{\mathrm{n}} \sum_{\mathrm{i}=1}^{\mathrm{n}} \cos(2\pi \mathrm{l}\theta_\mathrm{i}). \tag{A.15}$$

From De Jager et al. (1989) the Rayleigh power, which is analogue to the Fourier power in FFT analysis, can then be defined in terms of the signal strength p as:

$$\mathrm{n}\bar{\mathrm{R}}_\mathrm{l}^2 = \frac{\mathrm{np}^2}{4} + 1 \tag{A.16}$$

The significance of the Rayleigh power can be determined by calculating the logarithm of the Rayleigh probability, i.e.

$$-\mathrm{Log}_{10}\ \mathrm{Pr} = 0.434\mathrm{n}\bar{\mathrm{R}}_\mathrm{l}^2. \tag{A.17}$$

The probability that θ_i follows a uniform distribution, in the absence of a periodic signal, is then given by

$$\mathrm{Pr}(> \mathrm{n}\bar{\mathrm{R}}_\mathrm{l}^2) = \mathrm{e}^{-\mathrm{n}\bar{\mathrm{R}}_\mathrm{l}^2}, \tag{A.18}$$

with the Rayleigh statistic following a χ^2 distribution with 2 degrees of freedom. If the data follows a white noise distribution, the semi-logarithmic plot of the differential number distribution of the independent Rayleigh test statistics should show a linear dependence of gradient 0.5.

A.3 Additional notes

A.3.1 Additional spectral analysis techniques

Two additional spectral analysis techniques worth mentioning, that were examined but ultimately not used during the final data analysis processes of this thesis, are the Folding Averaging Algorithm (FAA) and Palmer's χ^2 method.

The FAA is an older method that was used in time series analysis, and is independent of the time of observation (Guo et al. (2005)). The method was used for instance by Darwin to analyse the tides of the oceans (Melchior (1978)), and was used widely before the use of computers in that the FAA method was used to analyse the DFT before the FFT was developed, even more widely to analyse non-harmonic signal analysis in biology (Hoenen et al. (2001)). The basic principle is to build a matrix consisting of small time series for each test period T, for which the mean is calculated from the test period sections of the original time series, i.e.

$$\bar{\mathrm{R}}_{\mathrm{j}} = \frac{1}{\mathrm{M}} \sum_{\mathrm{i}=0}^{\mathrm{M}-1} \mathrm{V}_{\mathrm{i}(\mathrm{T}/\Delta\mathrm{t})+\mathrm{j}}. \tag{A.19}$$

The completed matrix is then used to construct the periodogram by calculating the amplitude and phase for each test period, i.e.

$$\mathrm{a} \left\{ \begin{matrix} \cos \\ \sin \end{matrix} \right\} \phi = \frac{2}{\mathrm{T}} \Delta\mathrm{t} \sum_{\mathrm{i}=0}^{\mathrm{N_s}-1} \bar{\mathrm{R}}_{\mathrm{i}} \left\{ \begin{matrix} \cos \\ \sin \end{matrix} \right\} [(2\pi/\mathrm{T})(\mathrm{i}\Delta\mathrm{t})], \tag{A.20}$$

with the amplitude and phase given by

$$\mathrm{a} = \sqrt{(\mathrm{a}\sin\phi)^2 + (\mathrm{a}\cos\phi)^2} \quad \text{and} \quad \phi = \arctan 2(\mathrm{a}\sin\phi, \mathrm{a}\cos\phi). \tag{A.21}$$

Palmer's χ^2 method on the other hand has a very strong statistical approach, that allows the fitting of any amount of test harmonics to the data (Palmer (2009)). The method allows for detection of non-sinusoidal harmonic functions. It combines FFT and least squares fitting algorithms to determine the periodogram. The basics of the method consist of determining the model parameters $\mathbf{P}$ that minimize

$$\chi^2(\mathrm{P}) = \sum_{\mathrm{i}=1\ldots\mathrm{n}} \frac{(\mathrm{M}(\mathrm{P},\mathrm{t}) - \mathrm{x_i})^2}{\sigma_\mathrm{i}^2}, \tag{A.22}$$

with the model defined by a Fourier series limited to harmonic H, i.e.

$$\Phi_\mathrm{H}(\{\mathrm{A}_{0\ldots2\mathrm{H}}, \mathrm{f}\}, \mathrm{t}) = \mathrm{A}_0 + \sum_{\mathrm{h}=1\ldots\mathrm{H}} \mathrm{A}_{2\mathrm{h}-1}\sin(\mathrm{h}2\pi\mathrm{ft}) + \mathrm{A}_{2\mathrm{h}}\cos(\mathrm{h}2\pi\mathrm{ft}). \tag{A.23}$$

A.3.2 Statistics: mean, variance, distribution functions and confidence levels

The following concise discussion is referenced mainly from Mardia (1972) and Rice (1995). For statistical analysis of data samples it is important to know the type of distribution that the data follows. The type of distribution then determines how the mean, variance and confidence levels are to be determined. The data analyses in this thesis consist of three different types of distributions, e.g. Normal (or Gaussian), von Mises and Poisson.

The normal distribution plays a central role in data statistics, probability and measurement error analysis. It is based on the central limit theorem, that specifies that if a random variable X is the sum of a large number of independent random variables, the variable X will be approximately normally distributed, i.e. $\mathrm{X} \sim \mathrm{N}(\mu, \sigma^2)$. The parameters $\mu(-\infty < \mu < \infty)$ and $\sigma(\sigma > 0)$ then define the mean and standard deviation of the normal density. For n data-points of x random variables the mean and standard deviation are given by:

$$\mu = \frac{1}{\mathrm{n}}\sum_{\mathrm{i}=1}^{\mathrm{n}} \mathrm{x_i} \quad \text{and} \quad \sigma = \sqrt{\frac{1}{\mathrm{n}}\sum_{\mathrm{i}=1}^{\mathrm{n}} (\mathrm{x_i} - \mu)^2}. \tag{A.24}$$

The normal density function is defined as:

$$\mathrm{f(x)} = \frac{1}{\sigma\sqrt{2\pi}\mathrm{e}^{-(\mathrm{x}-\mu)^2/2\sigma^2}}, \qquad -\infty < \mathrm{x} < \infty. \tag{A.25}$$

The normal distribution can then be represented by Figure A.4.

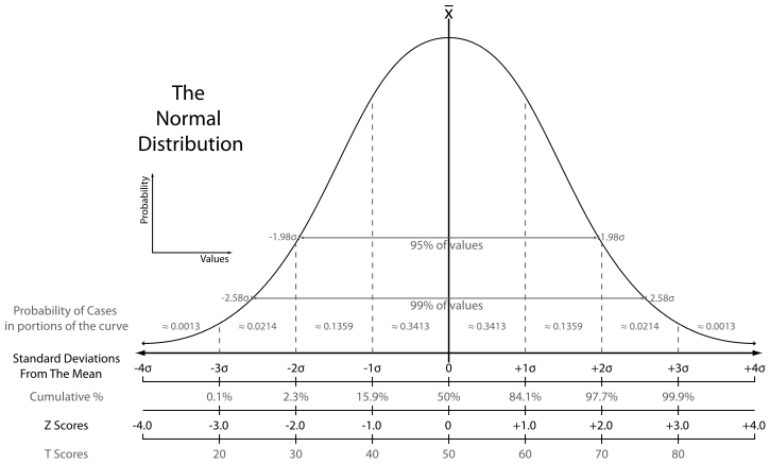

Figure A.4: Normal distribution diagram indicating standard deviation values (Adopted from www.commons.wikimedia.org).

The significance of an event measured in normally distributed data can then be determined from the confidence level chosen. The confidence level is determined from $\mu \pm \mathrm{x}\sigma$, which states that for an event to be considered as significant, it has to fall outside the confidence level, with the population that falls within determined from the error function, i.e. $\mathrm{erf}(\frac{\mathrm{x}}{\sqrt{2}})$. Thus for a confidence level of 3σ, the probability Pr that the percentage of sampled data points lies within 3σ is $\Pr(\mu - 3\sigma \leq \mathrm{x} \leq \mu + 3\sigma) \approx 0.9973$. The event thus has a $\Pr \geq 99.73\%$ that it is not a random variable. Table A.1 list the most frequently used confidence levels.

Table A.1: Selected confidence levels for normally distributed data.

Range	Population in range (%)	Expected frequency outside range
$\mu \pm 1\sigma$	68.2689	1 in 3
$\mu \pm 2\sigma$	95.4499	1 in 22
$\mu \pm 3\sigma$	99.7300	1 in 370
$\mu \pm 4\sigma$	99.9936	1 in 15 787
$\mu \pm 5\sigma$	99.9999	1 in 1 744 278

The von Mises distribution is an approximation of the circular form of the normal distribution. Per definition it is used for a circular random variable θ that has a probability density function of

$$g(\theta;\mu_0,\kappa) = \frac{1}{2\pi I_0(\kappa)} e^{\kappa\cos(\theta-\mu_0)}, \quad 0 < \theta \leqslant 2\pi, \quad \kappa > 0, 0 \leqslant \mu_0 < 2\pi, \tag{A.26}$$

where $I_0(\kappa)$ is the modified Bessel function of the first kind and order zero, i.e.

$$I_0(\kappa) = \sum_{r=0}^{\infty} \frac{1}{r!^2}(0.5\kappa)^{2r}. \tag{A.27}$$

The parameter μ_0 is then the mean direction, and κ the concentration parameter. The graphical representation of the von Mises distribution, for different κ values is given by Figure A.5.

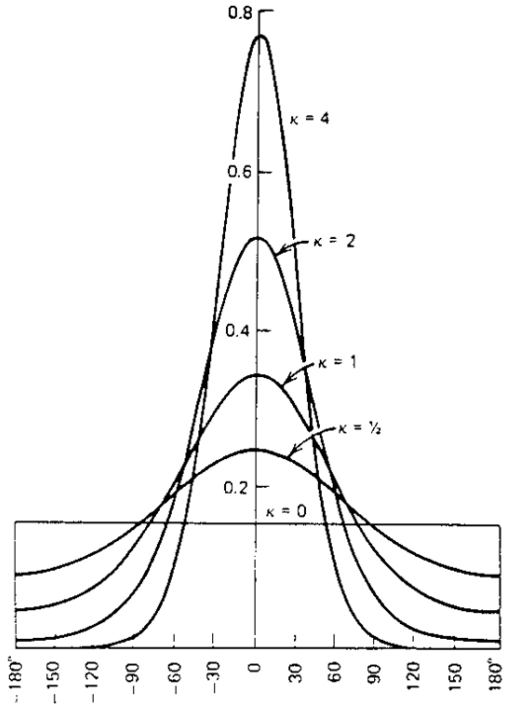

Figure A.5: von Mises distribution diagram indicating curves for different κ values (Adopted from www.what-when-how.com).

Lastly the Poisson distribution is derived from the limit of the binomial distribution where the number of trials $n \to \infty$, and the probability of success on each trail $p \to 0$, where $np = \lambda$. The Poisson frequency function is then given by

$$P(X = k) = \frac{\lambda^k}{k!} e^{-\lambda}, \qquad k = 0, 1, 2, ... \tag{A.28}$$

The estimate for the mean and the standard deviation, for n large enough ($n > 20$), is then approximately

$$\bar{\lambda} = n \approx \lambda \quad \text{and} \quad \sigma = \sqrt{\lambda} \approx \sqrt{n}. \tag{A.29}$$

The confidence interval for Poisson distributed data can thus for example be calculated as $I = n \pm 3\sqrt{n}$ for the 99.73% confidence interval. The graphical representation of the Poisson distribution, for different λ values is given by Figure A.6.

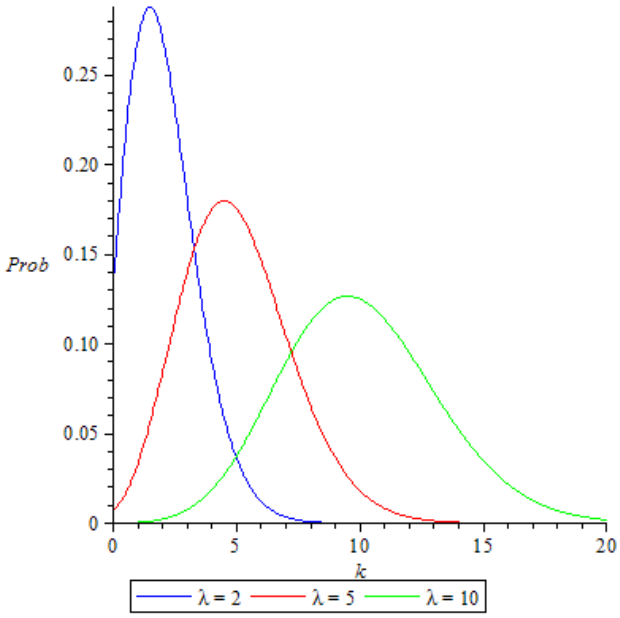

Figure A.6: Poisson distribution diagram indicating curves for different λ values (Adopted from www.historyofsci.blogspot.com).

Appendix B

Radiative processes

The following concise discussion on radiative processes is referenced mainly from Ghisellini (2012). There are two different types of plasmas that can produce radiation, thermal and non-thermal. Thermal plasmas can be described by a Maxwellian distribution of particles, while non-thermal is basically anything else and can mostly be described by some other form of spectrum, in most cases a power law.

The transport of the produced radiation from a spherical source is described by the transport equation,

$$\frac{\mathrm{dI}_\nu}{\mathrm{ds}} = -\alpha_\nu \mathrm{I}_\nu + \mathrm{j}_\nu, \tag{B.1}$$

where $\frac{\mathrm{dI}_\nu}{\mathrm{ds}}$ is the intensity per path length, $-\alpha_\nu \mathrm{I}_\nu$ the absorption intensity and j_ν the emission. But the absorption of radiation will be dependent on the optical depth of the source, i.e. $\mathrm{d}\tau_\nu = \alpha_\nu \mathrm{ds}$. The transport equation then becomes

$$\frac{\mathrm{dI}_\nu}{\mathrm{d}\tau_\nu} = -\mathrm{I}_\nu + \frac{\mathrm{j}_\nu}{\alpha_\nu}, \tag{B.2}$$

Solving this equation for optically thin ($\tau_\nu \ll 1$) sources, the source intensity for a specific frequency ν and source radius R becomes

$$\mathrm{I}_\nu(\tau_\nu) = \mathrm{j}_\nu \mathrm{R} \;\; (\mathrm{erg\ cm^{-2}\ s^{-1}\ Hz^{-1}\ sterad^{-1}}). \tag{B.3}$$

This is usually the case for high-frequency (i.e., high-energy) radiation. For optically thick sources ($\tau_\nu \gg 1$), the source intensity becomes

$$\mathrm{I}_\nu(\tau_\nu) = \frac{\mathrm{j}_\nu \mathrm{R}}{\tau_\nu} \ \ (\mathrm{erg\ cm^{-2}\ s^{-1}\ Hz^{-1}\ sterad^{-1}}). \tag{B.4}$$

Here $\frac{\mathrm{R}}{\tau_\nu}$ essentially represents the width of an outer shell which is optically thin to the radiation. This is usually the case for lower frequencies (i.e. lower-energy) radiation. The flux from the source can then be calculated using

$$\mathrm{F} = \int \mathrm{I} \cos\theta \mathrm{d}\Omega \ \ (\mathrm{erg\ cm^{-2}\ s^{-1}}). \tag{B.5}$$

For a source such as AE Aquarii, both thermal and non-thermal emission is observed. The known thermal emission is the expected stellar black-body spectrum dominated by the secondary star, as well as soft thermal X-ray emission. Non-thermal emission is in the form of synchrotron emission in the radio wavelengths from the propeller ejected blobs in the system. Based on a variety of studies (including this study), suspected very high energy (VHE) non-thermal emission might be possible and is still to be verified. For an extended discussion on AE Aquarii and studies conducted refer to Chapter 2. The radiative processes that can be responsible for the detection and characterization of VHE emission will therefore be highlighted and discussed.

VHE radiation can be produced by several different mechanisms, e.g. Bremsstrahlung, Synchrotron radiation, Inverse Compton scattering, interactions between particle pairs and decay of radioactive material in the from of γ-decay. The most likely detectable sources of astronomical $\gamma-$ rays would be through mechanisms involving charged particles (usually electrons) accelerated to very high energies that produce secondary $\gamma-$ rays.

Acceleration of VHE particles can be accomplished through the following mechanisms: Magnetic reconnection, charge separation (double layers), pulsar mechanisms (rotating B-fields, Poynting fluxes, jets), or first and second-order Fermi acceleration that occur in shocked regions of astrophysical plasmas.

B.1 Non-thermal Synchrotron emission in AE Aquarii

Synchrotron radiation occurs when charged leptons (usually electrons) move in a magnetic field at close to the speed of light. The nature of the emission process is such that it appears in a continues spectrum over a wide range of wavelengths (e.g. Ghisellini (2012)). The radially accelerated or spiralling particles also has a characteristic polarization, and can be detected from radio to hard X-rays and even $\gamma-$ rays. A feature of astronomically produced synchrotron radiation is a non-thermal power-law spectrum. Synchrotron radiation is observed in AE Aquarii between Radio and IR, and is produced from magnetized clouds with field strengths of $B \sim 300 - 1000$ G that contain relativistic electrons accelerated to $\epsilon_e \sim 150 - 10$ MeV. The accelerator responsible for the relativistic electron clouds is an MHD-driven propeller mechanism that converts thermal electrons to relativistic electrons through magnetic reconnection and pumping (Meintjes and Venter (2005); Venter and Meintjes (2006)). Circular polarization has also been detected in AE Aquarii. There is also a proposal that a component of the hard X-ray emission of AE Aquarii is from synchrotron radiation (Terada et al. (2008)).

The analysis of synchrotron emission can be considered with the simple case of a single electron. The Lorentz force causes the gyration of the relativistic particle around the magnetic field lines and induces acceleration in the particle, but hardly changes the velocity modules. Using the acceleration Lorentz transformation, where $a'_{||} = \gamma^3 a_{||}$ and $a'_{\perp} = \gamma^2 a_{\perp}$, for the relativistic particle the Larmor formula becomes

$$P_e = P'_e = \frac{2e^2}{3c^3}\left[a'^2_{||} + a'^2_{\perp}\right] = \frac{2e^2}{3c^3}\gamma^4\left[\gamma^2 a^2_{||} + a^2_{\perp}\right], \tag{B.6}$$

where P_e is the total "emitted" power radiated by the accelerated particle, and is Lorentz invariant. Through analysis of the parameters involved, such as the Lorentz force components, Larmor radius, fundamental frequency and pitch angles, the synchrotron power for an isotropic distribution of pitch angles (θ) over the solid angle becomes

$$\langle \mathrm{P} \rangle = \frac{4}{3}\sigma_{\mathrm{T}}\mathrm{c}\mathrm{U}_{\mathrm{B}}\gamma^2\beta^2, \tag{B.7}$$

where σ_{T} is the Thompson scattering cross section, c the speed of light, U_{B} the magnetic energy density, γ the Lorentz factor and $\beta = \frac{\nu}{\mathrm{c}}$, the velocity of the particle. Additional references include Blumenthal and Gould (1970) and Rybicki and Lightman (1979).

The characteristic spectrum emitted by a single electron can thus be derived through the following approach. The emitting time during which an electron will emit photons in a particular direction is described by $\Delta \mathrm{t}_{\mathrm{e}} \sim \frac{2}{2\pi}\frac{1}{\gamma\nu_{\mathrm{B}}}$, with ν_{B} the magnetic gyro frequency. The photon arrival time is then $\Delta \mathrm{t}_{\mathrm{A}} = \Delta \mathrm{t}_{\mathrm{e}}(1-\beta) = \frac{1}{2\pi\gamma^3\nu_{\mathrm{B}}}$. The synchrotron frequency, the frequency at which the particle emits most of its power, is then

$$\nu_{\mathrm{s}} = \frac{1}{2\pi\Delta \mathrm{t}_{\mathrm{A}}} = \gamma^2\frac{\mathrm{eB}}{2\pi \mathrm{m}_{\mathrm{e}}\mathrm{c}}. \tag{B.8}$$

The final derived results for the spectrum of a single electron is then:

$$\begin{aligned} \mathrm{P}_{\mathrm{s}}(\nu,\gamma,\theta) &= \frac{\sqrt{3}\mathrm{e}^3\mathrm{B}\sin\theta}{\mathrm{m}_{\mathrm{e}}\mathrm{c}^2}\mathrm{F}(\nu/\nu_{\mathrm{c}}) \\ \mathrm{F}(\nu/\nu_{\mathrm{c}}) &\equiv \frac{\nu}{\nu_{\mathrm{c}}}\int_{\nu/\nu_{\mathrm{c}}}^{\infty}\mathrm{K}_{5/3}(\mathrm{y})\mathrm{dy} \\ \nu_{\mathrm{c}} &\equiv \frac{3}{2}\nu_{\mathrm{s}}\sin\theta. \end{aligned}$$

The variable $\mathrm{K}_{5/3}$ in the flux function is the modified Bessel function of order 5/3. The flux function peaks at $\nu \sim 0.29\nu_{\mathrm{c}}$, with the low frequency part well approximated by a power law with a slope of 1/3:

$$\mathrm{F}(\nu/\nu_{\mathrm{c}}) \rightarrow \frac{4\pi}{\sqrt{3}\Gamma(1/3)}\left(\frac{\nu}{2\nu_{\mathrm{c}}}\right)^{1/3} \quad (\nu \ll \nu_{\mathrm{c}}). \tag{B.9}$$

At frequencies above ν_c, i.e. $\nu \gg \nu_c$, the spectrum decays exponentially, and can be approximated by:

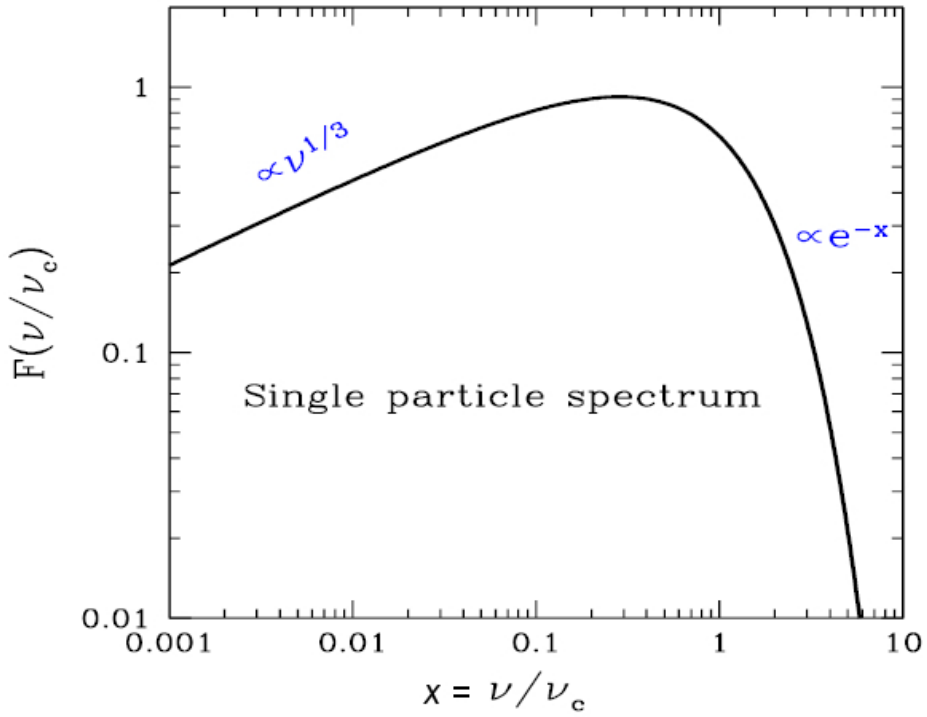

Figure B.1: Flux dependence upon frequency for a single particle (Adapted from Ghisellini (2012)).

$$\mathrm{F}(\nu/\nu_\mathrm{c}) \rightarrow \left(\frac{\pi}{2}\right)^{1/2} \left(\frac{\nu}{\nu_\mathrm{c}}\right)^{1/2} \mathrm{e}^{-\nu/\nu_\mathrm{c}} \quad (\nu \gg \nu_\mathrm{c}). \tag{B.10}$$

The emission spectrum for a single electron is represented in Figure B.1. The many-electron model for synchrotron emission is based on a power-law distribution, i.e.

$$\mathrm{N}(\gamma) = \mathrm{K}\gamma^{-\mathrm{p}} = \mathrm{N}(\mathrm{E})\frac{\mathrm{dE}}{\mathrm{d}\gamma} \quad (\gamma_{\mathrm{min}} < \gamma < \gamma_{\mathrm{max}}). \tag{B.11}$$

For a distribution of pitch angles being equal at low and high γ, the synchrotron emissivity for many electrons can be determined as follows. By integrating the power law density function over the γ range the power for a single electron times $N(\gamma)$ and dividing by 4π for isotropic emission (emissivity) gives

$$\epsilon_{\rm s}(\nu,\theta) = \frac{1}{4\pi}\int_{\gamma_{\rm min}}^{\gamma_{\rm max}} {\rm N}(\gamma){\rm P}(\gamma,\nu,\theta){\rm d}\gamma \;\; (\text{erg cm}^{-3}\ \text{s}^{-1}\ \text{Hz}^{-1}\ \text{sterad}^{-1}). \tag{B.12}$$

For an appropriate range of frequencies the integral becomes

$$\epsilon_{\rm s}(\nu,\theta) \propto {\rm KB}^{({\rm p}+1)/2}\nu^{-\alpha}, \tag{B.13}$$

with $\alpha = \frac{{\rm p}-1}{2}$ the spectral index of the radiation and B the magnetic field strength. The flux from a homogeneous and optically thin source of volume ${\rm V} \propto {\rm R}^3$ at a distance $\rm d_L$ is then

$$\begin{aligned} {\rm F_s}(\nu) &= 4\pi\epsilon_{\rm s}(\nu)\frac{\rm V}{4\pi {\rm d_L^2}} \\ &\propto \frac{\rm R^3}{\rm d_L^2}{\rm KB}^{1+\alpha}\nu^{-\alpha} \\ &\propto \theta_{\rm s}^2{\rm RKB}^{1+\alpha}\nu^{-\alpha}, \end{aligned} \tag{B.14}$$

where θ_s is the angular radius of the source. Unfortunately only the following values can be determined for the function. Through measurement of the source at different frequencies, the slope for the spectral index, as well as the radius R and the distance d_L can be determined. The only unknowns is then the particle density and magnetic field. To determine the rest of the system parameters the self-absorbed flux needs to be characterized.

The absorption for non-thermal particle distributions cannot be determined in the same manner as for Maxwellian distributions, but instead the relationship between the A and B Einstein coefficients has to be considered. Omitting the details, the source intensity for an absorbed source can be determined by equating the brightness temperature to the kinetic temperature of the emitting electrons,

i.e.:

$$\begin{aligned} \mathrm{I}(\nu) &\equiv 2\mathrm{kT}\frac{\nu^2}{\mathrm{c}^2} \quad (\text{for } \mathrm{kT} \sim \gamma \mathrm{m_e c^2}) \\ &\sim 2\mathrm{m_e}\nu^2 \left(\frac{\nu}{\nu_\mathrm{L}}\right)^{1/2} \\ &\propto \frac{\nu^{5/2}}{\mathrm{B}^{1/2}}. \end{aligned} \tag{B.15}$$

This approach to the intensity function is only valid if a specific γ can be associated to any ν. The flux can then be determined by integrating the intensity over the angular dimension (θ_s) of the source, giving:

$$\mathrm{F}(\nu) \propto \theta_\mathrm{s}^2 \frac{\nu^{5/2}}{\mathrm{B}^{1/2}} \tag{B.16}$$

Based on model fitting of a synchrotron spectrum of a partially self-absorbed source, the magnetic field B can be determined from the self-absorbed part, while the normalisation K and electron spectral index p can be determined from the thin part. Refer to Figure B.2.

The maximum energy for synchrotron emission can then also be shown to be 50 MeV for shock heated plasmas (e.g. Kumar et al. (2012)). It can be shown that the energy that electrons gain whenever they cross a relativistic shock front and are scattered back is a factor ~ 2. The time of this process is of the order of the Larmor time

$$\mathrm{t_L} = \frac{\mathrm{mc}\gamma_\mathrm{e}}{\mathrm{qB}}, \tag{B.17}$$

where B is the co-moving frame magnetic field strength, m the mass of the particle and q the particle charge. The Synchrotron losses during this time is

$$\delta \mathrm{E} \sim \frac{\mathrm{t_L}\sigma_\mathrm{T}\mathrm{B}^2\gamma_\mathrm{e}^2\mathrm{c}}{6\pi} \sim \frac{\sigma_\mathrm{T}\mathrm{B}\gamma_\mathrm{e}^3\mathrm{mc}^2}{6\pi\mathrm{q}}. \tag{B.18}$$

When $\delta \mathrm{E} \sim \gamma_\mathrm{e}\mathrm{mc}^2/2$, particle acceleration ceases and the maximum Lorentz factor a particle can attain is then

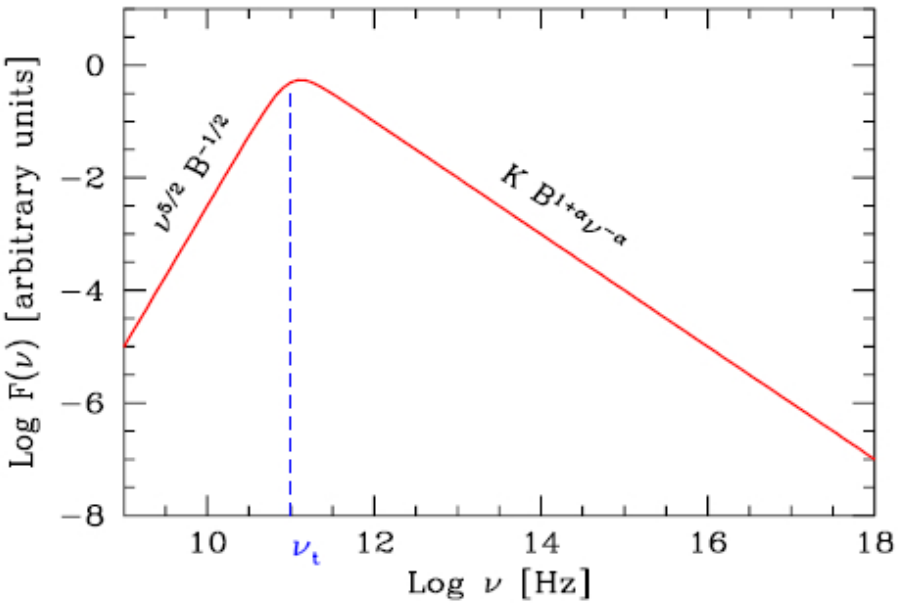

Figure B.2: Synchrotron spectrum for a partially self absorbed source (Adopted from Ghisellini (2012)).

$$\frac{\sigma_{\rm T} B \gamma_{\rm e}^2}{3\pi q} \sim 1 \quad \text{or} \quad \gamma_{\rm max}^2 \sim \frac{9 m^2 c^4}{8 B q^3}, \tag{B.19}$$

with $\sigma_{\rm T}$ the Thomson cross section. The synchrotron photon energy corresponding to $\gamma_{\rm max}$ is then

$$h\nu_{\rm max} \sim \frac{qB\gamma_{\rm max}^2 h}{2\pi mc} \sim \frac{9mc^3 h}{16\pi q^2}. \tag{B.20}$$

For electrons the maximum photon energy is thus $\sim$ 50 MeV, and for protons $\sim 10^2$ GeV. These upper limits can however be violated under certain conditions as presented by Kumar et al. (2012), with a maximum energy of $\lesssim$ 10 GeV observed in several gamma-ray bursts.

The synchrotron emission from AE Aquarii is unfortunately more complex in that it is from multiple expanding sources (blobs). The particle acceleration in the magnetised blobs is also described through magnetic reconnection, shock drift

acceleration and magnetic pumping. The basic model therefore had to be modified to compensate for this. The synchrotron emission from the expanding clouds of relativistic electrons were thus modelled by Meintjes and Venter (2003) using a Van der Laan (VDL) model. The VDL model gives a parametrisation of a single synchrotron flare from an ensemble of electrons. For the frequency regimes on either side of maximum the VDL model is virtually the same as for an expected synchrotron spectrum, i.e.

$$\mathrm{S}(\nu) = \mathrm{k}_1 \theta^2 \frac{\nu^{5/2}}{\mathrm{B}^{1/2}} \quad (\nu \ll \nu_\mathrm{m}) \tag{B.21}$$

and

$$\mathrm{S}(\nu) = \mathrm{k}_2 \mathrm{C} \theta^3 \mathrm{B}^{(\delta+1)/2} \nu^{-(\delta-1)/2} \quad (\nu \gg \nu_\mathrm{m}), \tag{B.22}$$

where k_1 and k_2 are constants, and C is the coefficient in the energy distribution equation

$$\mathrm{N(E)dE} = \mathrm{CE}^{-\delta}\mathrm{dE}. \tag{B.23}$$

Excluding the details (refer to Meintjes and Venter (2003)), the flux density equation can be determined as

$$\mathrm{S}(\nu, \rho) = \mathrm{S}_{\mathrm{m0}} \left(\frac{\nu}{\nu_{\mathrm{m0}}} \right)^{5/2} \rho^3 \frac{1 - \mathrm{e}^{-\tau_{\nu_\mathrm{m}} \left(\frac{\nu}{\nu_{\mathrm{m0}}} \right)^{-(\delta+4)/2} \rho^{-(2\delta+3)}}}{1 - \mathrm{e}^{-\tau_{\nu_\mathrm{m}}}}, \tag{B.24}$$

where S_{m0} is the maximum flux density at initial time t_0, ν_{m0} is the frequency at the maximum flux density, with τ_m the optical depth at ν_{m0}, and $\rho = \mathrm{r}/\mathrm{r}_0$ is the angular diameter ratio between the initial diameter and the expanded diameter. Although the optical depth is frequency dependent, most of the emission is emitted for $\tau_\nu \approx \tau_\mathrm{m} \approx 1$. The non-thermal flux $\mathrm{S}(\nu, \rho)$ can be seen to depend asymptotically on ν and ρ as

$$\mathrm{S}(\nu, \rho) = \begin{cases} \mathrm{S}(\nu)\rho^3, & \nu \ll \nu_m, \\ \mathrm{S}(\nu)\rho^{-2\delta}, & \nu \gg \nu_m. \end{cases} \tag{B.25}$$

Using this equation, the expected flux densities of individual flare events can be

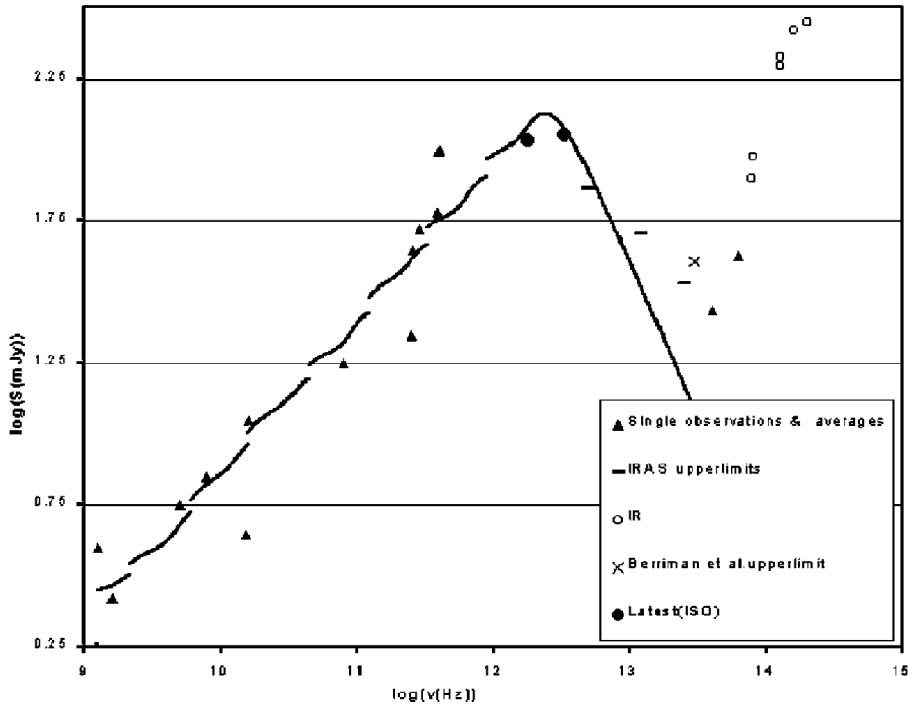

Figure B.3: Simulated VDL spectrum of AE Aquarii for 10 radio synchrotron blobs with $B_0 = 3000$G (Adopted from Meintjes and Venter (2003)).

modelled. Refer to Figure B.3 for a simulated VDL model for 10 blobs with $B_0 = 3000$G with measured radio observations of AE Aquarii also indicated. As can be seen the VDL is a close approximation of the measured radio emission from AE Aquarii.

B.2 Soft thermal X-ray emission from AE Aquarii

The most prominent X-ray emission mechanism in astrophysics is thermal Bremsstrahlung. Bremsstrahlung is radiation that occurs when charged particles (usually electrons) are decelerated due to electric fields (resulting in thermal Bremsstrahlung) or magnetic fields (resulting in magneto-Bremsstrahlung, i.e. synchrotron radiation) (e.g. Ghisellini (2012)). The bigger the change in energy of the accelerated particle the more the peak of the spectrum will shift to higher frequencies and

increased intensity. The dominant observable Bremsstrahlung in astrophysical sources is thermal Bremsstrahlung (also called free-free radiation) emitted from a plasma through the interactions between free electrons and ions. Another source of X-ray emission is through photo-ionization due to the interaction of high energy photons with electrons, with the atom connected to the electron becoming ionized. This process has been modelled for hot diffuse gas (e.g. stellar corona) and is known as the Mekal model. The emission lines for the ionized atoms is then present in the thermal X-ray emission spectra, and can be characterised using the Mekal model. For a brief description and references, refer to Section 4.4.

Plasma heating at the magneto-spheric radius or MHD pumping of the coronal envelope results in soft thermal X-rays in AE Aquarii. The most recent *Suzaku* soft X-ray spectra has also been modelled using multiple Mekal models, to compensate for multiple thermal X-ray emission regions observable in the X-ray spectra. However, the analysis of *Suzaku* spectra in this study found the possibility of an additional Bremsstrahlung component in the spectra. The Bremsstrahlung requires a population of free electrons for the X-ray production. This population can then later be re-utilized for the production of $\gamma-$ rays. Therefore a concise discussion of Bremsstrahlung is required.

A step by step approach as in Ghisellini (2012) will be presented. Considering an electron-proton plasma the first step would be to define the characteristic time of the interaction between the electron and proton when the electron passes close to the proton, i.e.

$$\tau \approx \frac{\mathrm{b}}{\mathrm{v}}, \tag{B.26}$$

with b the impact parameter and v the electron velocity. The acceleration during the interaction is then assumed to be constant and given by

$$\mathrm{a} \approx \frac{\mathrm{e}^2}{\mathrm{m_e b}^2}. \tag{B.27}$$

For the simplified case the Larmor equation becomes

$$P = \frac{2e^2a^2}{3c^3} \approx \frac{e^2}{c^3}\frac{e^4}{m_e^2c^3b^4} = \frac{e^6}{m_e^2c^3b^4}. \tag{B.28}$$

The characteristic time can be written as a characteristic frequency, i.e.

$$\omega \approx \frac{1}{\tau} = \frac{v}{b}. \tag{B.29}$$

The power at the characteristic frequency is then

$$P(\omega) \approx \frac{P}{\omega} = \frac{e^6}{m_e^2c^3vb^3}. \tag{B.30}$$

The impact factor can be estimated from the proton number density as

$$b \approx n_p^{-1/3} \rightarrow b^3 = \frac{1}{n_p}. \tag{B.31}$$

The emissivity will then be the power for a single electron times the electron number density, and considering an isotropic emission divided by 4π, giving $j(\omega)$ as

$$j(\omega) \approx \frac{n_e n_p}{4\pi}\frac{e^6}{m_e^2c^3}\left(\frac{m_e}{kT}\right)^{1/2}, \tag{B.32}$$

with kT the temperature of the plasma: $mv^2 \sim kT \rightarrow v \sim (kT/m)^{1/2}$. Integrating over frequencies, where $\omega_{max} = \frac{kT}{\hbar}$, and considering that $\nu = \omega/(2\pi)$ the exact result can be derived. Considering also that for the general case the plasma will consist of nuclei with atomic number Z and number density n. The acceleration of the electron will then be $a = Ze^2/(m_e b^2)$. The acceleration also has to be squared to get the power from the Larmor equation. The emissivity thus becomes:

$$\begin{aligned} j(\nu) &= 5.4 \times 10^{-39} Z^2 n_e n_i T^{-1/2} e^{-h\nu/kT} \bar{g} \quad (\text{erg cm}^{-3}\ \text{s}^{-1}\ \text{Hz}^{-1}), \\ j(\nu) &= 1.13 \times 10^{-28} Z^2 n_e n_i T^{-1/2} \bar{g} \quad (\text{erg cm}^{-3}\ \text{s}^{-1}\ \text{Hz}^{-1}), \end{aligned} \tag{B.33}$$

with $\bar{g}$ the Gaunt factor. The latter represents quantum mechanical corrections to the minimum impact parameter which determines the maximum frequency. The absorption part of the Bremsstrahlung spectrum, or free-free absorption can

be derived as follows. For thermal emission (i.e., Maxwellian distribution) the Kirchoff law can be used to determine the absorption using

$$S_\nu \equiv \frac{j_\nu}{\alpha_\nu} = B_\nu = \frac{2h\nu^3}{c^2}\frac{1}{e^{h\nu/kT}-1}. \tag{B.34}$$

If the emission is non-thermal however, the Kirchoff law cannot be used, but a more fundamental approach has to be used, i.e., the Einstein coefficients. The free-free absorption is given by

$$\alpha_\nu^{ff} = \frac{j_\nu}{B_\nu} = 3.7\times10^8\frac{Z^2 n_e n_i}{T^{1/2}}\frac{1-e^{-h\nu/kT}}{\nu^3}\bar{g}_{ff}. \tag{B.35}$$

For the Raleigh-Jeans regime ($h\nu \ll kT$) this simplifies to

$$\alpha_\nu^{ff} = 0.018\frac{Z^2 n_e n_i}{T^{3/2}\nu^2}\bar{g}_{ff}. \tag{B.36}$$

The complete Bremsstrahlung spectrum can now be modelled. Figure B.4 shows the Bremsstrahlung intensity from a source of radius $R = 10^{15}$cm, density $n_e = n_p = 10^{10}$cm^{-3} and varying temperature, with the Gaunt factor set to unity. The dependence on temperature can clearly be seen. The self-absorbed part of the emission spectrum can also be seen, with a slope of ν^2 which ends when the optical depth $\tau = \alpha_\nu R \sim 1$. There is then also a dependence on the optical depth, which can be seen from the absorption coefficient, in that the ν^{-3} term ensures that the absorption preferentially takes place at low frequencies. What this means is that for increasing emitting (and absorbing) particle densities, the spectrum will be self-absorbed to higher frequencies. This is clearly illustrated in Figure B.5, in that for increasing particle number densities, the spectrum approaches a black-body spectrum. When the spectrum reaches a black-body spectrum the intensity becomes constant, i.e.:

$$I_\nu = \frac{j_\nu R}{\tau_\nu} \propto \frac{n_e n_p R}{n_e n_p R} \rightarrow \text{constant} \qquad (\tau_\nu \ll 1). \tag{B.37}$$

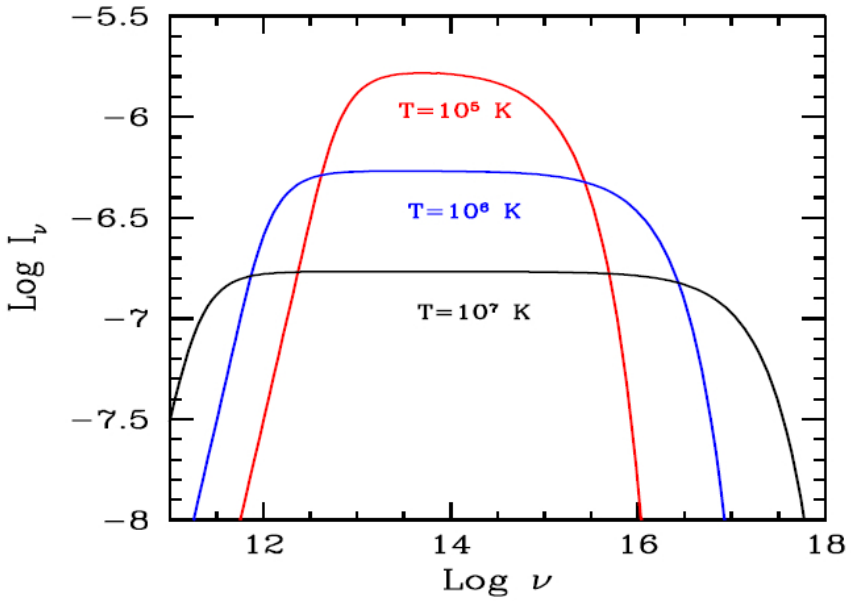

Figure B.4: The Bremsstrahlung intensity from a source of radius $R = 10^{15}$ cm, density $n_e = n_p = 10^{10} cm^{-3}$ and varying temperature (Adopted from Ghisellini (2012)).

B.3 Possible VHE emission mechanisms

The most likely VHE hard X-ray and $\gamma-$ray emission from AE Aquarii could be through synchrotron emission of relativistic electrons or inverse Compton processes. Inverse Compton scattering (ICS) occurs when a photon gains energy when struck by a fast-moving electron (Ghisellini (2012)), or more generally when a relativistic electron interacts with a photon field. It then also has a non-thermal power-law spectrum. Inverse Compton scattering that up-scatters soft photons from the secondary star or propeller outflow could therefore result in $\gamma-$ray emission in AE Aquarii. A variation on inverse Compton scattering is Synchrotron-Self-Compton (SSC) scattering. This is when photons produced by electrons during synchrotron processes are up-scattered by the very same electrons through inverse Compton processes.

Scattering is the simplest interaction between photons and free electrons. When the energy of the incoming photon is small, classical electro-dynamics can be used

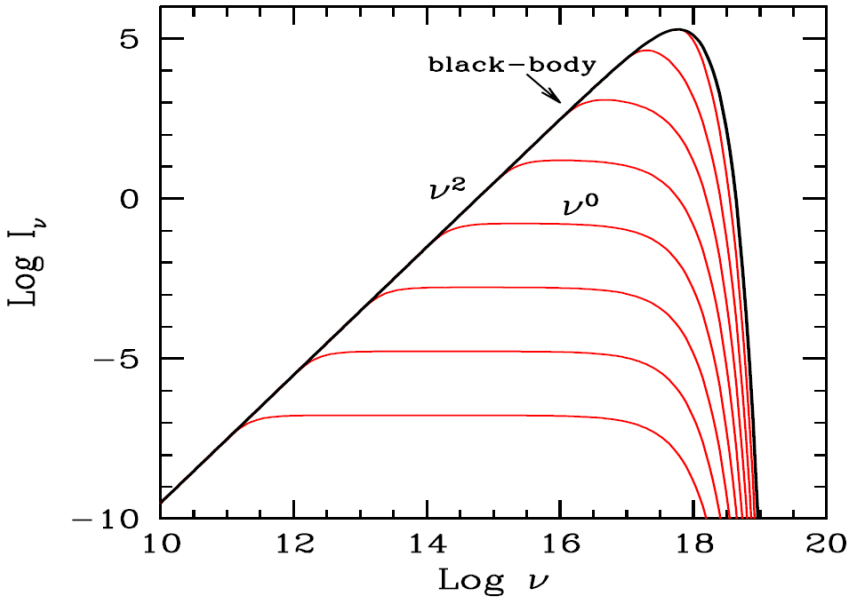

Figure B.5: Bremsstrahlung intensity spectrum for a source of radius R = 10^{15}cm, temperature T = 10^7 K and varying particle densities. The particle densities varies from 10^{10}cm^{-3} (bottem curve) to 10^{18}cm^{-3} (top curve), for $n_e = n_p$ at a density increase factor of 10 per curve (Adopted from Ghisellini (2012)).

to describe the scattering, and the process is called Thomson scattering. However, when the incoming photon has energies comparable to or greater than $m_e c^2$, a quantum treatment becomes necessary. This regime is called the Klein-Nishina regime. A detailed discussion of Compton scattering and the Klein-Nishina cross section is outside the scope of this discussion but a detailed presentation can be found in Ghisellini (2012). Full details on ICS is lengthy, therefore only the most important points will be noted.

Through relativistic analysis of the collision between a photon field and a relativistic electron field, the rate at which energy is removed from the electron field can be determined. The total loss rate is then (for the Thomson regime)

$$\mathrm{P_c}(\gamma) \equiv \frac{\mathrm{dE_e}}{\mathrm{dt}} = \frac{4}{3}\sigma_\mathrm{T}\mathrm{c}\gamma^2\beta^2\mathrm{U_r}, \tag{B.38}$$

where

$$\mathrm{U_r} = \int \epsilon \mathrm{n}(\epsilon)\mathrm{d}\epsilon \tag{B.39}$$

is the energy density of the ambient radiation field before scattering, σ_T is the Thompson cross section. The energy loss rate equation can be represented as follows:

$$\begin{aligned} \mathrm{P_c}(\gamma) &= \left(\frac{\sharp \text{ of collisions}}{\mathrm{sec}}\right) (\text{average photon energy after scattering}) \\ &= \left(\sigma_\mathrm{T}\mathrm{c}\frac{\mathrm{U_r}}{\langle \mathrm{h}\nu \rangle}\right)\left(\frac{4}{3}\langle \mathrm{h}\nu \rangle \gamma^2\right). \end{aligned} \tag{B.40}$$

Upon comparison, similarities between this equation to the synchrotron energy loss can be seen, i.e., the energy loss rates are identical. What this means is that if relativistic electrons are present in a region containing similar radiation and magnetic energy densities, the electrons will emit equally through both synchrotron and ICS processes. The ratio between the emitted luminosities would then be:

$$\frac{\mathrm{L_{sync}}}{\mathrm{L_{ICS}}} = \frac{\mathrm{P_{sync}}}{\mathrm{P_{ICS}}} = \frac{\mathrm{U_B}}{\mathrm{U_r}}. \tag{B.41}$$

The similarities between synchrotron and ICS results in the derivation of the ICS emissivity being done using the same method. Assume a power-law energy distribution for the relativistic electrons:

$$\mathrm{N}(\gamma) = \mathrm{K}\gamma^{-\mathrm{p}} = \mathrm{N(E)}\frac{\mathrm{dE}}{\mathrm{d}\gamma} \quad (\gamma_{\min} < \gamma < \gamma_{\max}). \tag{B.42}$$

The assumption can also be made that the seed photons are isotropic and monochromatic with frequency ν_0. There is also a strong link between the scattered frequency ν_c and the electron energy. The following can therefore be set:

$$\nu_\mathrm{c} = \frac{4}{3}\gamma^2\nu_0 \rightarrow \gamma = \left(\frac{3\nu_\mathrm{c}}{4\nu_0}\right)^{1/2} \rightarrow \left|\frac{\mathrm{d}\gamma}{\mathrm{d}\nu}\right| = \frac{\nu_\mathrm{c}^{-1/2}}{2}\left(\frac{3}{4\nu_0}\right)^{1/2} \tag{B.43}$$

Following the arguments used for synchrotron emission, the emissivity can then be shown to be

$$\epsilon_\mathrm{c}(\mathrm{h}\nu_\mathrm{c}) = \frac{1}{4\pi}\frac{(4/3)^\alpha}{2}\frac{\tau_\mathrm{c}}{\mathrm{R/c}}\frac{\mathrm{U_r}}{\mathrm{h}\nu_0}\left(\frac{\nu_\mathrm{c}}{\nu_0}\right)^{-\alpha}, \tag{B.44}$$

where $\tau_\mathrm{c} \equiv \sigma_\mathrm{T}\mathrm{KR}$ is the scattering optical depth and (for $\tau_\mathrm{c} < 1$) is the fraction of the seed photons $\mathrm{U_r/h}\nu_0$ undergoing scattering in a time R/c. The average gain of the scattered photons is then $\nu_\mathrm{c}/\nu_0 \sim \gamma^2$, and $\alpha = \frac{\mathrm{p}-1}{2}$. A typical ICS spectrum is illustrated in Figure B.6.

The Synchrotron self-Compton (SSC) process is a variant of the ICS process, in that there exists a possibility that the photons produced from the synchrotron process can interact with the same relativistic electron population through ICS, thus SSC. The scattering will be important for high electron and photon densities. Thus, if the electron distribution is a power law, the expectation is that the SSC flux will be $\propto \mathrm{K}^2$. The specific synchrotron radiation energy density can then be given by

$$\mathrm{U_s}(\nu) = \frac{3\mathrm{R}}{4\mathrm{c}}\frac{\mathrm{L_s}(\nu)}{\mathrm{V}} = 4\pi\frac{3\mathrm{R}}{4\mathrm{c}}\epsilon_\mathrm{s}(\nu), \tag{B.45}$$

where 3R/(4c) is the average photon source crossing time, and V is the volume of the source. With the specific synchrotron emissivity written as $\epsilon_\mathrm{s}(\nu) = \epsilon_{\mathrm{s},0}\nu^{-\alpha}$,

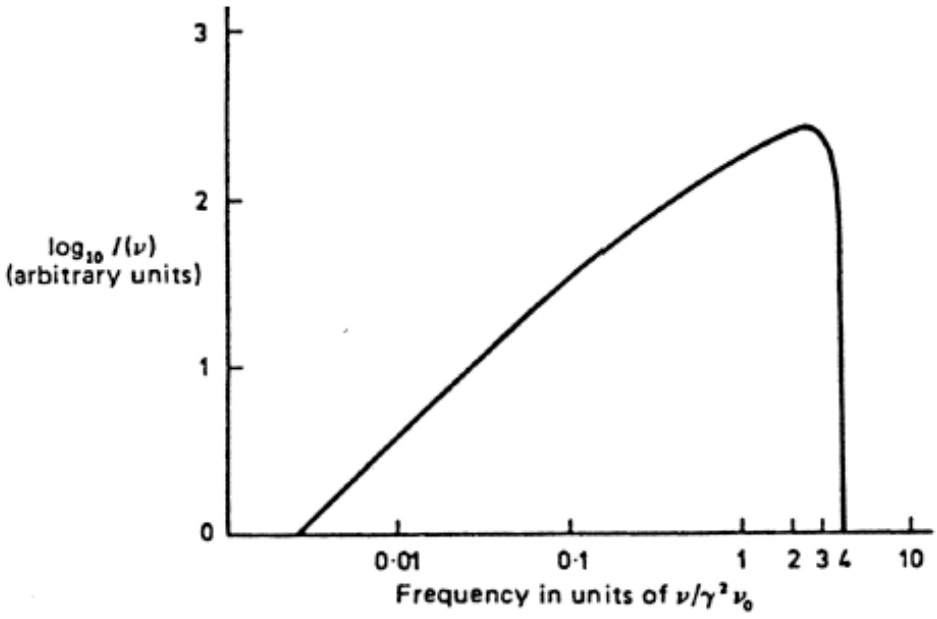

Figure B.6: Typical ICS spectrum (Adopted from Longair (1992)).

and comparing to the inverse Compton emissivity, it can be shown that

$$\epsilon_{\rm SSC}(\nu_{\rm c}) = \frac{(4/3)^{\alpha-1}}{2}\tau_{\rm c}\epsilon_{\rm s,0}\nu_{\rm c}^{-\alpha}\int_{\nu_{\rm min}}^{\nu_{\rm max}}\frac{{\rm d}\nu}{\nu}. \tag{B.46}$$

This equation can be simplified by defining the integral part as $\ln\Lambda$, and seeing that $\epsilon_{\rm s,0}\nu_{\rm c}^{-\alpha} = \epsilon_{\rm s}(\nu_{\rm c})$ is just the specific synchrotron emissivity at the Compton frequency $\nu_{\rm c}$. The final equation is then:

$$\epsilon_{\rm SSC}(\nu_{\rm c}) = \frac{(4/3)^{\alpha-1}}{2}\tau_{\rm c}\epsilon_{\rm s}(\nu_{\rm c})\ln\Lambda. \tag{B.47}$$

The ratio between the Synchrotron and SSC flux can be seen to be $[(4/3)^{\alpha-1}/2]\tau_{\rm c}\ln\Lambda \sim \tau_{\rm c}\ln\lambda$, with a typical SSC spectrum thus illustrated in Figure B.7.

Two more processes to take note of for the production of VHE $\gamma-$rays are relativistic Bremsstrahlung and the decay of neutral pions. The neutral pion decay process is very important as it is responsible for the continuum emission of the interstellar gas at energies $\epsilon \geq 100$ MeV. The following brief discussion is based

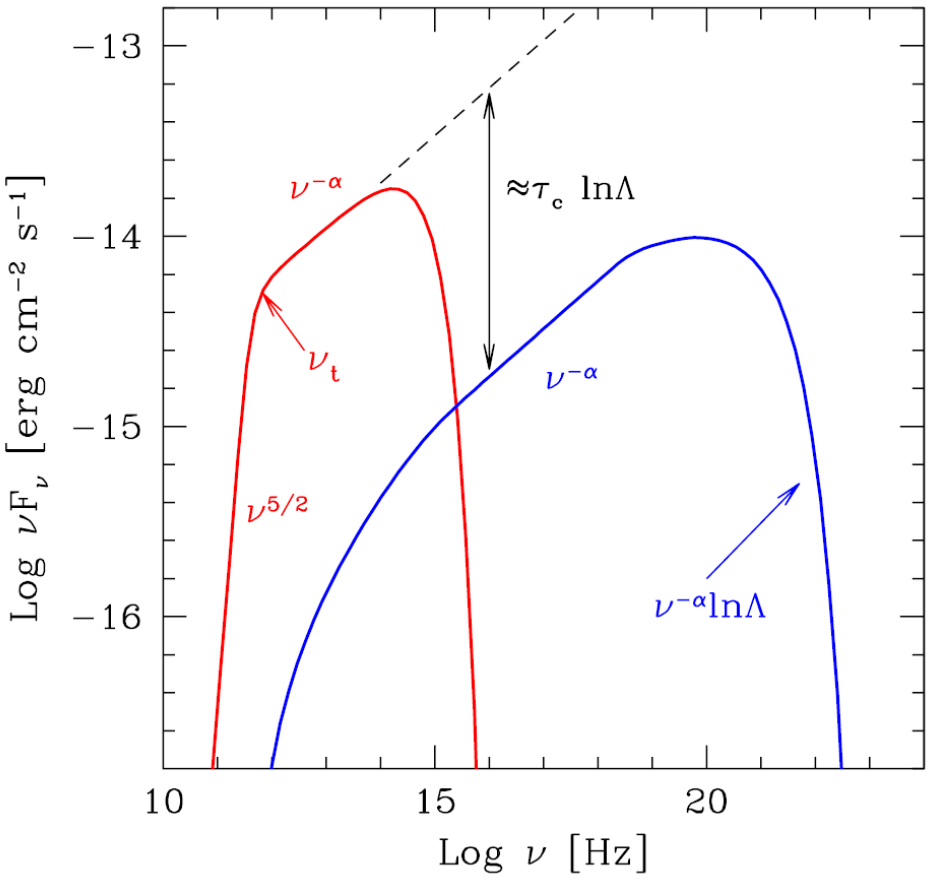

Figure B.7: Typical SSC spectrum, with a synchrotron spectrum shown for comparison (Adopted from Ghisellini (2012)).

on Longair (1992). The neutral pions are created during the collision between relativistic protons and nuclei of atoms and ions in the interstellar gas, i.e.

$$\mathrm{p} + \mathrm{p} \rightarrow \pi^{+}, \pi^{-}, \pi^{0}. \tag{B.48}$$

The charged pions decay into muons and neutrinos, with a mean lifetime of 2.552×10^{-8} s, i.e.

$$\pi^{+} \rightarrow \mu^{+} + \nu_{\mu}; \pi^{-} \rightarrow \mu^{-} + \bar{\nu}_{\mu}. \tag{B.49}$$

The charged muons then decay into electrons and positrons, with a mean lifetime of 2.2001×10^{-6} s, i.e.

$$\mu^{+} \rightarrow \mathrm{e}^{+} + \nu_{\mathrm{e}} + \bar{\nu}_{\mu}; \mu^{-} \rightarrow \mathrm{e}^{-} + \bar{\nu}_{\mathrm{e}} + \nu_{\mu}. \tag{B.50}$$

The neutral pions by contrast decay into pairs of $\gamma-$rays in only 1.78×10^{-16} s, i.e.

$$\pi^{0} \rightarrow \gamma + \gamma. \tag{B.51}$$

The cross section of this process is then $\sigma_{\mathrm{pp}\rightarrow\gamma\gamma} \approx 10^{-30}$ m^2, with the emitted spectrum of $\gamma-$rays having a broad maximum centred on a $\gamma-$ray energy of about 70 MeV. This maximum can clearly be seen in Figure B.8, which shows the calculated curves for $\gamma-$ray production. The differential spectra from observed cosmic-ray protons with hydrogen are represented by curve A, while curve B are from cosmic-ray nuclei with interstellar gas. Curve C is then the integral spectrum in interstellar space.

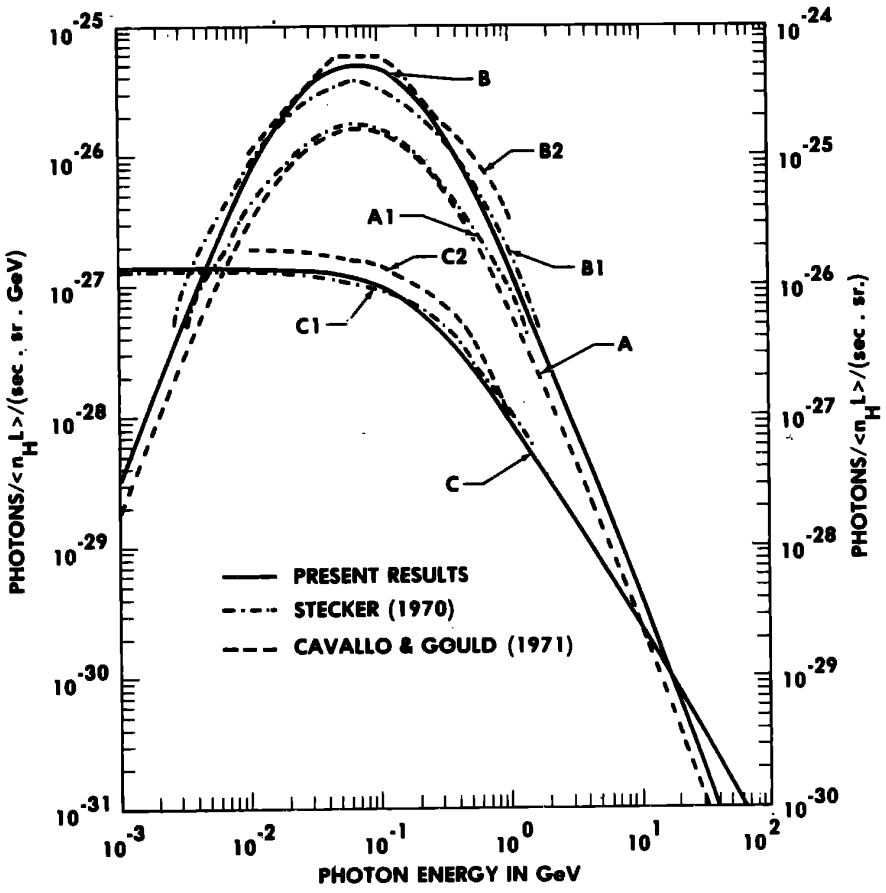

Figure B.8: Calculated curves for γ – ray production (Adopted from Badhwar and Stephens (1977)).

Appendix C

Spica - Custom data acquisition software for the UFS Boyden research telescopes

C.1 Introduction

The photometric analysis and characterisation of optical data to facilitate the search for pulsed Very High Energy (VHE) non-thermal emission from AE Aquarii required a general overhaul of the research equipment available at Boyden. The main telescope used was the 1.5 m Boyden Reflector. The CCD camera, filter-wheel system, telescope control and general data acquisition systems were adequate for the general use at that time, but some additional requirements (such as accurate GPS timing) were needed, which led to the upgrading and overhaul of the data acquisition system Spica in 2008 (See Figure C.1 for the main user interface).

Spica is a Windows XP based software package initially developed as a custom data acquisition system specifically for the Boyden 1.5 m Reflector during the PLANET program (1996-2004) by Hannes Calitz. This development was in response to problems that arose and shortcomings with customisation capabilities of the data acquisition software in use at that time. Because of the customisable nature of developing in-house data acquisition and instrumentation control

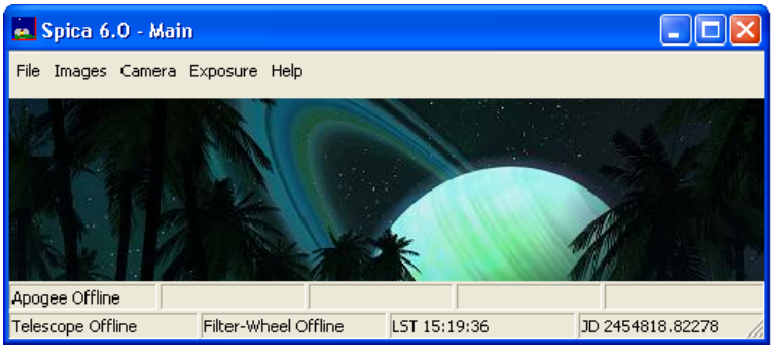

Figure C.1: Spica version 6.0 main user interface.

software, it was decided to continue with the development of Spica and to include additional requirements for the current project and future studies into the software already available. The current version of the software is Spica version 6.2.

C.2 Planning and layout of the software package

The planning and layout of the software required a basic knowledge of the capabilities of the software (Spica version 5.0), user interface layout, instrumentation control requirements and possible future capabilities. The software had to be user-friendly and logical first and foremost in such a way that any observer or user of the software should be able to control the telescope system after only a short introduction and a simple user manual. On the other hand, the software had to be powerful and robust enough to be able to run the complex telescope system continuously without interruptions or too much user maintenance or input.

The software planning and layout were therefore designed along a modular architecture. This approach guaranteed a highly customisable and robust system, without influencing or hamstringing the rest of the system when development was done on a specific component of the system. Keeping in mind these guidelines the system was redesigned during the upgrade with separate modules that control the telescope, filter-wheel, CCD camera, GPS system and FITS file management (Figure C.2 represents a general layout of the software and background structure).

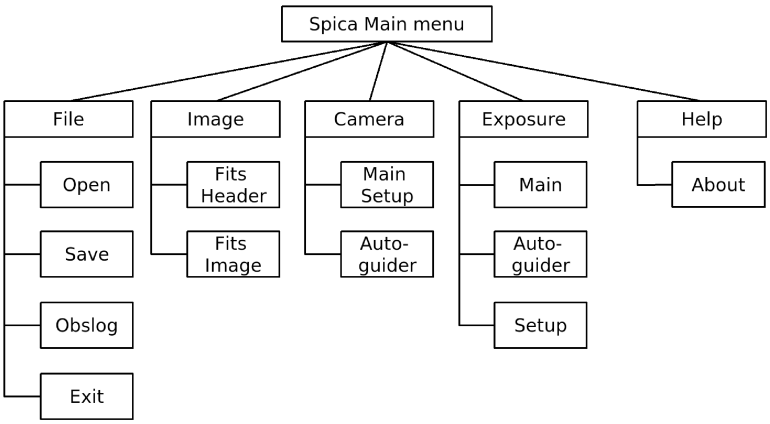

Figure C.2: Design and layout of the Spica menu system.

Spica was then also expanded to include control modules, not just for the 1.5 m Reflector Telescope system, but also for the new 14 inch Celestron Reflector system, and the additional camera and filter-wheel systems that became available in the last few years. Spica was initially developed in a C++ development environment, therefore upgrading and expansion were also done in C++. Additional reasons for keeping to a C++ environment were the increased power and speed that C++ offers, as well as cross-platform capabilities. This assured that less effort was needed for redeveloping the software package for different operating systems, e.g. Linux.

C.3 General capabilities of the software

C.3.1 FITS file management

Spica uses the CFitsio libraries as well as standard IO commands for the data file management. The filenames and directory structures are automatically generated and managed according to initial system parameters from the user. General save and open interface dialogues are built into the software for singular cases of manual file management, but in general the automated system is used.

The filenames and directories are structured according to Project->Object->Date->Filename. The filenames are generated as Object_Number_Filter.fit, where "Object" is the object observed, "Number" is the sequential number of the data frame taken and "Filter" the filter used for the frame observed. For example Galaxies_M87_0001_V.fit.

The FITS files are single frame files, although the FITS file structure as well as some CCD cameras do allow for block or multiple frame files (files where the data frames are in a matrix format). The FITS header structure includes all information required for general data analysis processes, for instance the data frame information, time parameters, CCD camera parameters, telescope parameters and observer information. The upgrade included restructuring of the FITS file control module into a separate module, as well as inclusion of error handling. The FITS header structure was also slightly adjusted, with additional header information included such as the the CCD GAIN, RDNOISE, and TEMPERATURE values as well as OBSERVER and OBSERVATORY values.

C.3.2 Telescope control

Spica interfaces with the DFM telescope control system through RS232 communications protocols. The commands available are telescope slew commands, telescope position commands and time sync commands.

The telescope slew command sends slew coordinates (Right Ascension (RA) and Declination (Dec)) to the telescope according to the specified object parameters to be studied. The object parameters are entered into Spica from a text file. This text file contains the parameters in the following sequence: Project Name, Object Name, RA, Dec and Epoch. This text file can then contain a whole list of objects to be used in an observational study.

The telescope position command is used to acquire the current telescope position in RA and Dec. The position parameters could then be used for inclusion into the

FITS header, or additional telescope control procedures.

The time sync command is used to sync the DFM telescope control system with the rest of the system. This is important not to just have all the computer systems synced on the same time-stamp for the FITS header frames, but for the accurate slewing of the telescope the telescope needs to know its position very accurately in both positional space and time. The recalculation of the positional coordinates (RA and Dec) from a different epoch (J2000 for instance) to the current epoch, requires the current JD down to the correct second value.

The upgrade included restructuring of the telescope control module into a separate module, as well as inclusion of error handling. Although there is a module available for control of the Celestron system, it is still under development and not used at this stage. The telescope is currently controlled by using secondary planetarium software like The Sky or Stallerium or Celestron's own control software. The communications interface is the same as with the DFM system and is through RS232 protocols.

C.3.3 CCD camera control

At this stage there are control modules for three different camera systems. The Apogee U55 (USB interface) camera, the Apogee AP6E (PCI control card interface) camera and the SBIG ST7 (Parallel Port interface) camera. During the upgrade the control module for the Apogee U55 was restructured, with some additional features (such as error handling and additional camera controls such as binning and bit depth) added. The control modules for the Apogee AP6E and SBIG ST7 are new.

The control modules, although using different drivers and libraries, have certain control commands in common. A camera can be connected or disconnected, the following camera parameters can be set: camera bit depth, camera control temperature, camera binning, camera frame type and camera exposure time, and all

relevant camera parameters acquired for camera control or inclusion into the FITS headers.

C.3.4 Filter-wheel control

Spica has control modules for the two different filter-wheel systems available at Boyden. The filter-wheel system on the 1.5 m telescope (UFS Filter-wheel), which is an 8 position filter-wheel containing Johnson UBVRI filters, a Clear filter, a Closed and a Hole position, is controlled using RS232 protocols. The control module and code for the UFS Filter-wheel was restructured with additional features (such as error handling and shut-down procedures) added during the upgrade. The upgrade also included a control module for the filter-wheel on the Celestron telescope, which is a 7 position Apogee (USB Interface) system and contains Johnson UBVRI filters, a Clear filter and a Closed position.

C.3.5 GPS and time controls

The upgrade included additions of GPS timing systems. These systems are available on both telescopes, although at this stage Spica only interfaces with the GPS system on the more complex 1.5 m telescope. The Spica GPS control modules allow monitoring of the time signal from the GPS system and sync command to sync the different system components (like the DFM system) with the GPS time signal. The accuracy of the time-signal on the 1.5 m telescope GPS system was tested against the time signal available at HRO with a difference in the signals on the nano-second scale.

C.4 Extended capabilities

During the upgrade, extended capabilities were build into the system, with additional capabilities and improvements made as they are required. Some of the

extended capabilities are the automation of the observing procedure. This is accomplished by using an expanded observation input list (as mentioned above) that additionally includes the frame type, filter, exposure time and number of exposures. This list is then used as part of an automated script.

Another capability is basic raw measurement of instrumental data frame parameters such as the stellar flux, fwhm and magnitude values. The displayed image data is also auto scaled, as well as the image column and row profiles displayed. A specific source can also be monitored in real-time for magnitude variations from frame to frame.

The exposure setup can also be set to a so called fast photometry mode, during which time all unnecessary background processes are shut down to make the exposure throughput time as fast as possible. In this mode the system can take an exposure (excluding exposure time) every $\sim$0.5 seconds, and is only limited to the physical read/write speed of the computer system used. The only other way to increase the frame rate for the current system is to use the frame stacking capability of the camera itself, but this capability has not yet been explored.

C.5 Testing and finalizing the software

The software was tested throughout the development stages, with the initial upgrading processes finalized approximately two years after starting. Additional testing and improvements are constantly made as more users/observers use the different systems and secondary requirements are identified. There are also user manuals for each of the two current systems that use Spica.

C.6 Conclusion

Thus far the upgraded system proved to be a success, and was used successfully each observational season on multiple projects. The modular system setup also proved to be the correct choice, as the constant development continues without any loss in productivity, and the different system components (hardware) can be interchanged without resulting in a system crash, or having to redo the system from scratch. Additional capabilities that have been partially developed is a module for auto-tracking, although time and hardware constraints have hampered this side project at this stage. But this has been identified as a critical future capability, especially for very deep field or very faint object observational projects, which require very long exposure times and very accurate telescope position control.

The next stage in development of the system would be to convert the software and operating system (OS) environment from a Windows-based system to a Linux OS system. This would be a project on its own, which would require a complete redesign/redevelopment of the graphical user interface (GUI) modules, with a reintegration of the different drivers and libraries and control modules with the GUI and the Linux OS. The argument behind such a project would be for the increased speed and stability of a correctly set up Linux system, improved real-time processing, and possibly linking Spica with photometry packages like IRAF for real-time photometry reduction and analysis procedures.

C.7 Additional references

Additional references for background into Spica and the specific systems used at Boyden are: Apogee Instruments Inc., Apogee Instruments Inc (2006), Calitz (2005), HEASARC (2007), Celestron (2005), IRAF.Net, SBIG Astronomical Instruments (2006), SBIG Astronomical Instruments (2007), Van Heerden (2008), Van Heerden and Calitz (2010) and Van Heerden (2010).